Università degli Studi di Palermo

AREA RICERCA E TRASFERIMENTO TECNOLOGICO
SETTORE DOTTORATI E CONTRATTI PER LA RICERCA
U. O. DOTTORATI DI RICERCA

Dottorato di Ricerca in Scienze Fisiche
Dipartimento di Fisica e Chimica-Emilio Segré
Settore Scientifico Disciplinare – FIS/05 – Astronomia e Astrofisica

Outflows in Black Hole X-ray binaries

IL DOTTORE
CARLOTTA MICELI

IL COORDINATORE
PROF. MARCO CANNAS

IL TUTOR
MELANIA DEL SANTO

CO TUTOR
JULIEN MALZAC

CICLO XXXVIII
ANNO CONSEGUIMENTO TITOLO 2026

Université Fédérale
Toulouse Midi-Pyrénées

THÈSE

En vue de l'obtention du

DOCTORAT DE L'UNIVERSITÉ DE TOULOUSE

Délivré par :

Université Toulouse 3 Paul Sabatier (UT3 Paul Sabatier)

Cotutelle internationale avec Université de Palerme

Présentée et soutenue par :
Carlotta Miceli
le 04/03/26

Titre :
Outflows in Black Hole X-ray Binaries

École doctorale et discipline ou spécialité :
ED SDU2E : Astrophysique, Sciences de l'Espace, Planétologie

Unité de recherche :
IRAP - Institut de Recherche en Astrophysique et Planetologie

Directeur/trice(s) de Thèse :
Julien Malzac and Melania Del Santo

Jury :
Mme Barbara De Marco, Rapperteur
M. Stephan Corbel, Rapperteur
M. Marco Miceli, Examinateur
M. Jonatan Ferreira, Examinateur
M. Julien Malzac Directeur de Thèse
Mme Melania Del Santo, Co-directrice de Thèse

Contents

Abstract

Outflows are among the most important and complex phenomena shaping both the evolution and the observational appearance of black hole X-ray binaries (BH XRBs). In these systems, accretion onto a compact object is often accompanied by powerful mass-loss processes in the form of disk winds and relativistic jets, whose presence and properties strongly depend on the accretion state. Understanding the physical origin of these outflows and their connection to the accretion flow is therefore essential to build a coherent picture of accretion–ejection coupling in XRBs. This thesis is devoted to the investigation of outflows in BH XRBs through a multi-approach study combining multi-wavelength observations with physically motivated modelling. The main goal is to constrain the geometry, physical conditions, and variability of winds and compact jets, and to assess their impact on the observed emission across different spectral states.

The first project described in the thesis focuses on the study of cold disk winds through high-resolution optical spectroscopy of the BH XRB MAXI J1305–704. While clear and unambiguous wind signatures could not be firmly established in the optical band, the analysis revealed absorption and emission features whose properties are consistent with a complex and variable environment. In the second part of the project, I show how a new approach that use X-ray modelling on optical spectra can provide constraints on the inclination of the system.

The second project is dedicated to the analysis of an obscured spectral state in the highly variable BH XRB GRS 1915+105. Using broadband X-ray spectroscopy, I study the effects of absorption and scattering on the observed emission and explore the physical origin of the obscuring material. The results favour an interpretation in which the obscuring medium is best explained by a warped accretion disk, rather than by a uniform absorber or a purely wind-driven structure, in agreement with theoretical and observational expectations for systems accreting at high luminosities.

The third project investigates compact jets, the most persistent form of outflow in BH XRBs during hard intermediate states. I model the broadband spectral energy distribution (SED) of the BH XRB MAXI J1535–571 using an updated internal shocks code, which links the observed X-ray variability to the dissipation of kinetic energy along the jet. By exploring different jet geometries, this work finds that a parabolic jet geometry provides the best description of the broadband emission of MAXI J1535–571. The possible contribution of the jet to the soft gamma-ray emission is also investigated. Although a jet origin cannot be formally excluded from spectral modelling alone, the required physical conditions are extreme, favouring instead a non-thermal Comptonization origin of the high-energy tail in the corona.

Résumé

Les écoulements sortants (i.e. les vent et jets de matiere) constituent parmi les phénomènes les plus importants et les plus complexes qui façonnent à la fois l'évolution et l'apparence observationnelle des binaires X à trou noir (BH XRBs). Dans ces systèmes, l'accrétion sur l'objet compact s'accompagne fréquemment de processus de perte de masse puissants, sous la forme de vents de disque et de jets relativistes, dont la présence et les propriétés dépendent fortement de l'état d'accrétion. Comprendre l'origine physique de ces écoulements et leur lien avec le flot d'accrétion est donc essentiel pour établir une vision cohérente du couplage accrétion–éjection dans les binaires X. Cette thèse est consacrée à l'étude des écoulements sortants dans les BH XRBs à travers une approche multi-méthodes combinant des observations multi-longueurs d'onde et une modélisation physiquement motivée. L'objectif principal est de contraindre la géométrie, les conditions physiques et la variabilité des vents et des jets compacts, et d'évaluer leur impact sur l'émission observée à travers différents états spectraux.

Le premier projet présenté dans cette thèse se concentre sur l'étude des vents froids du disque à l'aide de la spectroscopie optique à haute résolution de la BH XRB MAXI J1305–704. Bien que des signatures de vent claires et sans ambiguïté n'aient pas pu être fermement établies dans le domaine optique, l'analyse a révélé des structures d'absorption et d'émission dont les propriétés sont compatibles avec un environnement complexe et variable. Dans la seconde partie du projet, je montre comment une nouvelle approche, consistant à appliquer des techniques de modélisation X aux spectres optiques, permet d'obtenir des contraintes sur l'inclinaison du système.

Le deuxième projet est dédié à l'analyse d'un état spectral obscurci dans la BH XRB hautement variable GRS 1915+105. À l'aide de la spectroscopie X à large bande, j'étudie les effets de l'absorption et de la diffusion sur l'émission observée et j'explore l'origine physique du milieu obscurcissant. Les résultats privilégient une interprétation dans laquelle ce milieu est le mieux expliqué par un disque d'accrétion déformé, plutôt que par un absorbeur uniforme ou une structure uniquement entraînée par un vent, en accord avec les attentes théoriques et observationnelles pour des systèmes accrétant à haute luminosité.

Le troisième projet porte sur les jets compacts, la forme d'écoulement sortant la plus persistante dans les BH XRBs durant les états durs et intermédiaires. Je modélise la distribution spectrale d'énergie à large bande de la BH XRB MAXI J1535–571 à l'aide d'une version mise à jour d'un modèle de chocs internes, qui relie la variabilité X observée à la dissipation de l'énergie cinétique le long du jet. En explorant différentes géométries de jet, ce travail montre qu'une géométrie parabolique fournit la meilleure description de l'émission à

large bande de MAXI J1535–571. La contribution possible du jet à l'émission en rayons gamma mous est également examinée. Bien qu'une origine liée au jet ne puisse être formellement exclue sur la seule base de la modélisation spectrale, les conditions physiques requises apparaissent extrêmes, ce qui favorise plutôt un scénario dans lequel la queue à haute énergie est produite par une Comptonisation non thermique dans la couronne.

Acknowledgements

At the end of this journey, marked by both highs and lows, I would like to express my heartfelt gratitude to all the people who have supported me and made it possible for me to reach this point.

In roughly chronological order, I would like to begin by thanking my astrophysics professors, Tiziana and Rosario, who first inspired in me a passion for this field. During my university years, they encouraged me through difficult moments and, throughout my PhD, they continued to guide and motivate me, always ready to answer my countless questions and involve me in their projects. I am also grateful to Luciano for the times he would unexpectedly enter the office with stimulating physics questions and exercises that pushed us to think further.

I would like to sincerely thank my supervisors, Melania and Julien, for giving me this unique opportunity and for supporting (and sometimes patiently putting up with me) throughout these years. They have helped me grow both personally and academically, and opened the path for me to continue in the world of research. I am also grateful to Marco, director of the PhD in Palermo, for his patience with deadlines and his constant support over the years. My thanks also go to Geneviève, director of the École Doctorale in Toulouse, for her availability and for helping me navigate the many bureaucratic aspects along the way.

I would like to thank my colleagues in Palermo, especially both Alessino and Alessio; in Tenerife, Emma, Teresa, Vanessa, and Rosa; and all the new colleagues I have met along the way, for making each working day lighter and more enjoyable. I am also deeply grateful to those who are giving me the opportunity to continue my path in research and who have placed their trust in me at this important stage of my career. I would also like to thank Manuel and Marga for welcoming me and making this new beginning feel easier and more familiar.

My deepest thanks go to my friends — Andrea, Eva, Aileen, Jean Christophe and Sophie, Debora, Montse, Cati, Inés and many others — who have been fundamental throughout these years, sharing moments of joy and helping me through the more challenging times.

I am profoundly grateful to my family for supporting me in every decision and for always believing in me. I would also like to thank my church community, especially Ilaria, Viviana and Lollo, Epi, Maria, and Antonio, for their presence in my daily life, for listening to me, accompanying me, and helping me find lightness during the heaviest moments. A special thank you goes to my godmother, Valentina, for always

being a constant and caring presence in my life.

Finally, my deepest and most heartfelt thanks go to my best friend, Esther, who has always been close to me despite the distance, with a bond that time and space have only made stronger.

Last but not least, I would like to thank my future husband, Gabriel, who fills my life with love, strength, and serenity, and who has been by my side every step of the way.

Introduction

BH XRBs are among the most powerful laboratories for investigating the physics of accretion and outflows under extreme conditions. These systems consist of a stellar-mass BH accreting matter from a companion star through Roche-lobe overflow or stellar winds. As matter spirals towards the compact object, gravitational potential energy is released and converted into radiation, predominantly emitted in the X-ray band. A fraction of this matter is expelled from the system in the form of relativistic jets and disk winds. While this basic picture is conceptually simple, the physical processes governing accretion, mass loss, and energy release in BH XRBs are complex and remain only partially understood.

Unlike isolated BHs, which are observationally elusive, accreting BHs reveal their presence through luminous and highly variable emission across the electromagnetic spectrum. X-ray observations provide direct access to the innermost regions of the system, where relativistic effects and extreme physical conditions dominate. Over the past decades, advances in X-ray instrumentation have enabled high-quality spectral and timing studies, allowing increasingly detailed investigations of accreting BH systems. At the same time, coordinated multi-wavelength campaigns have revealed that accretion is almost never an isolated process, but is instead accompanied by powerful outflows in the form of jets and disk winds.

The X-ray spectra of BH XRBs are typically characterized by two main components. At soft X-ray energies (below $\sim$ 10 keV), a quasi-thermal component is commonly observed and interpreted as emission from an optically thick, geometrically thin accretion disk. In addition, a non-thermal, power-law-like component extending to hard X-rays is frequently detected and is generally attributed to inverse Compton scattering of soft photons by a population of hot electrons in a tenuous, optically thin region often referred to as the corona. The relative contribution of these components varies with time and defines the so-called spectral states of BH XRBs.

Transient BH XRBs undergo episodic outbursts during which they evolve through different spectral states. These systems typically rise in luminosity in a hard state dominated by Comptonized emission, transition to a soft state where the disk emission prevails, and eventually return to the hard state at lower luminosity before fading back into quiescence. This evolution follows a characteristic hysteretical pattern, indicating that spectral states cannot be described by the mass accretion rate alone. Instead, changes in the physical conditions and structure of the accretion flow, as well as the onset or suppression of outflows, play a fundamental role.

Outflows are a defining feature of accreting BH systems. In the hard state, BH XRBs commonly produce

compact, steady jets that emit synchrotron radiation from radio to infrared frequencies and, in some cases, contribute to higher-energy emission. These jets are quenched during the transition to the soft state, pointing to a strong coupling between accretion and ejection processes. The existence of correlations between radio and X-ray luminosity in BH XRBs, and their extension to supermassive BHs in active galactic nuclei (AGN), further supports the idea of a fundamental link between inflow and outflow across a wide range of scales.

Despite extensive observational and theoretical efforts, the physical mechanisms responsible for launching jets, determining their geometry, and regulating their radiative output remain poorly constrained. In particular, the origin of the high-energy emission observed in some BH XRBs, including the soft gamma-ray tail extending beyond the standard thermal Comptonization cutoff, is still debated. Whether this emission arises from non-thermal processes in the corona or from synchrotron and inverse-Compton emission within the jet itself is an open question that has important implications for our understanding of energy dissipation and particle acceleration in these systems.

In addition to jets, accreting BHs can also drive disk winds, powerful outflows that remove mass, angular momentum, and energy from the system. Disk winds are most commonly detected during soft spectral states through blue-shifted absorption lines in high-resolution X-ray spectra, tracing highly ionized plasma launched from the accretion disk. However, growing observational evidence suggests that the phenomenology of winds is more complex. Their presence, strength, and ionization structure may vary across spectral states, and in some systems wind signatures have been proposed even during non-canonical or obscured accretion regimes.

Optical spectroscopy provides a complementary window onto disk winds, particularly in high-inclination systems where cooler and denser outflowing material may imprint detectable features on emission and absorption lines. Studying how these signatures evolve across accretion states offers a unique opportunity to test whether winds are confined to the soft state or whether they can persist under different physical and geometric conditions. Since winds imply non-conservative accretion, their presence has important consequences for the energetics of BH XRBs and for the long-term evolution of the binary system.

This thesis is devoted to the investigation of outflows in BH XRBs, with a particular focus on disk winds and jets and their connection to the accretion flow. Through detailed spectral analysis of X-ray, optical, and multi-wavelength data, this work aims to constrain the physical properties and geometries of outflows, explore their dependence on accretion state, and assess their impact on the observed emission. By combining high-quality spectroscopy with physically motivated modelling, the thesis addresses several open problems related to the accretion–ejection interplay in BH XRBs.

The main scientific questions addressed in this thesis can be summarized as follows:

- What are the physical properties and geometries of outflows in accreting BH XRBs?
- Under which accretion states and physical conditions are cold disk winds launched, and can they persist outside canonical soft states?
- How do outflows interact with the accretion flow, and how do they shape the observed X-ray and optical spectra?
- How do compact jets evolve across accretion states, and what constraints can broadband spectral modelling place on their geometry and properties?

- What is the origin of the soft gamma-ray emission observed in BH XRBs, and can it be explained within jet-based scenarios or does it require non-thermal Comptonization processes?

Thesis outline

Chapter 1 reviews the observational and spectral properties of accreting BH XRBs, focusing on the diagnostics used to identify and characterise disks, coronae, and outflows. The chapter summarises the current understanding of the open questions introduced above and provides the methodological framework adopted throughout the thesis.

Chapter 2 addresses the question of whether disk winds in BH XRBs can be detected at optical wavelengths and how their properties depend on accretion state and system geometry. Using optical spectroscopy of MAXI J1305−704 during its 2012 outburst, this chapter investigates the presence of wind signatures in the soft state and explores how emission-line properties can be used to constrain inclination of the system through a new modelling approach.

Chapter 3 addresses the question of how obscured accretion states in BH XRBs can be used to probe the structure of the inner accretion environment and the presence of dense outflows. Focusing on the peculiar absorption-dominated state of GRS 1915+105, this chapter investigates whether extreme absorption and reflection features encode information on the inclination and physical conditions of the circumnuclear material. To address this, quasi-simultaneous *XMM-Newton* and *NuSTAR* observations are used to model the broadband X-ray spectrum, attempting the properties of the absorber, reflector, and illuminating source to be constrained within a unified framework.

Chapter 4 focuses on the compact jet in the BH XRB MAXI J1535−571 and addresses two closely related questions: how the jet geometry and energetics evolve during an outburst, and whether the jet can contribute significantly to the emission at soft gamma-ray energies and beyond. These questions are investigated by modelling a set of quasi-simultaneous multi-wavelength SEDs using the ISHEM internal-shock jet framework. By exploring different assumptions on jet geometry and particle acceleration, this approach allows the jet contribution to the broadband emission to be quantitatively tested.

Chapter 5 summarises the main results of the thesis and places them in a broader context. The chapter revisits the open questions introduced in Chapter 1 and discusses how the results obtained on disk winds, obscured accretion states, and compact jets improve our understanding of outflows in BH XRBs. In addition, this chapter discusses how the conclusions reached in the previous chapters naturally lead to new open questions. I then outline several directions for future work, including the exploitation of upcoming high-resolution X-ray missions, coordinated multi-wavelength campaigns, and the development of more self-consistent models of outflows in accreting BH systems.

Introduction

Les binaires X à trou noir (BH XRBs) constituent parmi les laboratoires astrophysiques les plus puissants pour étudier la physique de l'accrétion et des écoulements sortants dans des conditions extrêmes. Ces systèmes sont constitués d'un trou noir de masse stellaire accrétant de la matière à partir d'une étoile compagne, soit par débordement du lobe de Roche, soit par capture du vent stellaire. À mesure que la matière spiralise vers l'objet compact, l'énergie potentielle gravitationnelle est libérée et convertie en rayonnement, principalement émis dans le domaine des rayons X. Une fraction de cette matière est cependant expulsée du système sous la forme de jets relativistes et de vents de disque. Si ce schéma général est conceptuellement simple, les processus physiques gouvernant l'accrétion, la perte de masse et la dissipation d'énergie dans les BH XRBs restent complexes et encore imparfaitement compris.

Contrairement aux trous noirs isolés, qui sont difficiles à détecter observationnellement, les trous noirs accrétants révèlent leur présence par une émission lumineuse et fortement variable sur l'ensemble du spectre électromagnétique. Les observations en rayons X offrent un accès direct aux régions les plus internes du système, où dominent les effets relativistes et des conditions physiques extrêmes. Au cours des dernières décennies, les progrès de l'instrumentation X ont permis des études spectrales et temporelles de haute qualité, ouvrant la voie à des investigations de plus en plus détaillées des systèmes à trou noir accrétants. Parallèlement, les campagnes multi-longueurs d'onde coordonnées ont montré que l'accrétion n'est presque jamais un processus isolé, mais qu'elle s'accompagne au contraire d'écoulements sortants puissants, sous la forme de jets et de vents de disque.

Les spectres X des BH XRBs sont généralement caractérisés par deux composantes principales. Aux énergies X molles (en dessous de $\sim$ 10 keV), une composante quasi thermique est fréquemment observée et interprétée comme l'émission d'un disque d'accrétion optiquement épais et géométriquement mince. À cela s'ajoute une composante non thermique, de type loi de puissance, s'étendant vers les hautes énergies et attribuée à la diffusion Compton inverse de photons mous par une population d'électrons chauds dans une région ténue et optiquement mince, souvent désignée sous le terme de couronne. La contribution relative de ces composantes évolue au cours du temps et définit les différents états spectraux des BH XRBs.

Les BH XRBs transitoires connaissent des épisodes d'éruption au cours desquels ils évoluent à travers plusieurs états spectraux. Ces systèmes voient typiquement leur luminosité augmenter dans un état dur dominé par l'émission Comptonisée, puis transitent vers un état mou où l'émission du disque devient prépondérante, avant de retourner à l'état dur à plus faible luminosité et de replonger finalement dans la quiescence. Cette

évolution suit un schéma hystérétique caractéristique, indiquant que les états spectraux ne peuvent pas être décrits uniquement par le taux d'accrétion. Des changements dans les conditions physiques et la structure du flot d'accrétion, ainsi que l'apparition ou la suppression des écoulements sortants, jouent un rôle fondamental.

Les écoulements sortants constituent une caractéristique essentielle des systèmes à trou noir accrétants. Dans l'état dur, les BH XRBs produisent couramment des jets compacts et quasi stationnaires, émettant un rayonnement synchrotron des ondes radio jusqu'à l'infrarouge et, dans certains cas, contribuant à des énergies plus élevées. Ces jets sont fortement atténués lors de la transition vers l'état mou, ce qui souligne l'existence d'un couplage étroit entre les processus d'accrétion et d'éjection. L'existence de corrélations entre les luminosités radio et X dans les BH XRBs, ainsi que leur extension aux trous noirs supermassifs des noyaux actifs de galaxies, renforce l'idée d'un lien fondamental entre les écoulements entrants et sortants sur une large gamme d'échelles.

Malgré d'importants efforts observationnels et théoriques, les mécanismes physiques responsables du lancement des jets, de la détermination de leur géométrie et de la régulation de leur émission radiative restent encore mal contraints. En particulier, l'origine de l'émission à haute énergie observée dans certains BH XRBs, notamment la queue en rayons gamma mous s'étendant au-delà du seuil de coupure de la Comptonisation thermique standard, demeure débattue. La question de savoir si cette émission provient de processus non thermiques dans la couronne ou d'une émission synchrotron et Compton inverse au sein même du jet reste ouverte et revêt des implications majeures pour notre compréhension de la dissipation d'énergie et de l'accélération des particules dans ces systèmes.

Outre les jets, les trous noirs accrétants peuvent également produire des vents de disque, des écoulements puissants qui extraient masse, moment angulaire et énergie du système. Les vents de disque sont le plus souvent détectés durant les états spectraux mous au moyen de raies d'absorption décalées vers le bleu dans des spectres X à haute résolution, traçant un plasma fortement ionisé lancé depuis le disque d'accrétion. Toutefois, des observations récentes suggèrent que la phénoménologie des vents est plus complexe. Leur présence, leur intensité et leur structure d'ionisation peuvent varier selon l'état spectral, et dans certains systèmes des signatures de vent ont été proposées même dans des régimes d'accrétion non canoniques ou obscurcis.

La spectroscopie optique offre une fenêtre complémentaire sur les vents de disque, en particulier dans les systèmes à forte inclinaison, où un matériau sortant plus froid et plus dense peut laisser des signatures détectables dans les raies d'émission et d'absorption. L'étude de l'évolution de ces signatures au cours des différents états d'accrétion constitue une opportunité unique pour tester si les vents sont confinés aux états mous ou s'ils peuvent persister dans d'autres conditions physiques et géométriques. Étant donné que les vents impliquent une accrétion non conservative, leur présence a des conséquences importantes sur le bilan énergétique des BH XRBs et sur l'évolution à long terme du système binaire.

Cette thèse est consacrée à l'étude des écoulements sortants dans les BH XRBs, avec un accent particulier sur les vents de disque et les jets, ainsi que sur leur lien avec le flot d'accrétion. À travers une analyse spectrale détaillée de données X, optiques et multi-longueurs d'onde, ce travail vise à contraindre les propriétés physiques et les géométries des écoulements sortants, à explorer leur dépendance vis-à-vis de l'état d'accrétion et à évaluer leur impact sur l'émission observée. En combinant une spectroscopie de haute qualité à une modélisation physiquement motivée, cette thèse aborde plusieurs questions ouvertes relatives au couplage accrétion–éjection dans les BH XRBs.

Les principales questions scientifiques abordées dans cette thèse peuvent être résumées comme suit :

- Quelles sont les propriétés physiques et les géométries des écoulements sortants dans les BH XRBs accrétants ?
- Dans quels états d'accrétion et sous quelles conditions physiques les vents de disque sont-ils lancés, et peuvent-ils persister en dehors des états mous canoniques ?
- Comment les écoulements sortants interagissent-ils avec le flot d'accrétion et comment façonnent-ils les spectres X et optiques observés ?
- Comment les jets compacts évoluent-ils au cours des différents états d'accrétion, et quelles contraintes la modélisation spectrale à large bande peut-elle apporter sur leur géométrie et leur bilan énergétique ?
- Quelle est l'origine de l'émission en rayons gamma mous observée dans les BH XRBs, et peut-elle être expliquée dans des scénarios dominés par le jet ou nécessite-t-elle des processus de Comptonisation non thermique ?

Organisation de la thèse

Le Chapitre 1 présente une revue des propriétés observationnelles et spectrales des BH XRBs accrétants, en mettant l'accent sur les diagnostics utilisés pour identifier et caractériser les disques, les couronnes et les écoulements sortants. Ce chapitre résume l'état actuel des connaissances sur les questions ouvertes introduites précédemment et fournit le cadre méthodologique adopté dans l'ensemble de la thèse.

Le Chapitre 2 aborde la question de la détection des vents de disque des BH XRBs dans le domaine optique et de la dépendance de leurs propriétés vis-à-vis de l'état d'accrétion et de la géométrie du système. À partir de spectres optiques de MAXI J1305–704 obtenus lors de son éruption de 2012, ce chapitre étudie la présence de signatures de vent dans l'état mou et explore comment les propriétés des raies d'émission peuvent être utilisées pour contraindre l'inclinaison du système à l'aide d'une nouvelle approche de modélisation.

Le Chapitre 3 s'intéresse aux états d'accrétion obscurcis dans les BH XRBs comme sondes de la structure de l'environnement interne et de la présence d'écoulements denses. En se concentrant sur l'état dominé par l'absorption observé dans GRS 1915+105, ce chapitre examine si les caractéristiques extrêmes d'absorption et de réflexion permettent de contraindre l'inclinaison et les conditions physiques du milieu environnant. Pour ce faire, des observations quasi simultanées de *XMM-Newton* et *NuSTAR* sont utilisées afin de modéliser le spectre X à large bande dans un cadre unifié.

Le Chapitre 4 est consacré au jet compact de la BH XRB MAXI J1535−571 et aborde deux questions étroitement liées : l'évolution de la géométrie et du bilan énergétique du jet au cours d'une éruption, et la contribution potentielle du jet à l'émission en rayons gamma mous et au-delà. Ces questions sont étudiées à travers la modélisation d'un ensemble de distributions spectrales d'énergie multi-longueurs d'onde quasi simultanées, à l'aide du cadre de chocs internes ISHEM. En explorant différentes hypothèses sur la géométrie du jet et l'accélération des particules, cette approche permet de tester quantitativement la contribution du jet à l'émission à large bande.

Le Chapitre 5 synthétise les principaux résultats de la thèse et les replace dans un contexte plus large. Il revient sur les questions ouvertes introduites au Chapitre 1 et discute comment les résultats obtenus sur les vents de disque, les états d'accrétion obscurcis et les jets compacts améliorent notre compréhension des écoulements sortants dans les BH XRBs. Ce chapitre discute également les nouvelles questions soulevées par ce travail et esquisse plusieurs perspectives futures, incluant l'exploitation de futures missions X à

haute résolution, des campagnes multi-longueurs d'onde coordonnées et le développement de modèles plus auto-cohérents des écoulements sortants dans les systèmes accrétants.

1 X-ray Binaries

In this chapter, I provide a phenomenological introduction to BH X-ray binaries (XRBs), focusing on their formation, structure, and multi-wavelength behaviour. I first outline the basic properties of interacting binaries that host compact objects, emphasizing why systems containing neutron stars (NSs) or BHs are among the most efficient engines of accretion-powered emission. I then introduce Low-Mass X-ray Binaries (LMXBs) on which I focus in my thesis and in particular system with a BH as compact object, describing how these systems form, how mass is transferred from a low-mass donor through Roche-lobe overflow, and why LMXBs represent excellent laboratories for studying accretion under extreme physical conditions.

A concise overview of the main components of an LMXB—the donor star, the accretion disc, the inner hot flow or corona, and the associated outflows in the form of winds and jets—is presented to set the stage for the rest of the thesis. I also summarize the phenomenology of accretion states and their characteristic transitions, which regulate the appearance and disappearance of these components across the electromagnetic spectrum.

This chapter therefore provides the conceptual framework for the three main topics explored in the thesis: the physics of accretion and X-ray spectral components (Chapter 2), the properties of disc winds and their optical signatures (Chapter 3), and the origin and modelling of relativistic jets (Chapter 4).

1.1 How does a star end its life?

A natural question that arises when studying stellar evolution is: *what happens at the end of a star's life?* Although stars appear immutable on human timescales, each of them follows a well-defined evolutionary path governed by the balance between gravity and the internal pressure generated by nuclear fusion. As long as hydrogen burning proceeds in the core, this equilibrium keeps the star stable during the main sequence phase. Eventually, however, nuclear fuel becomes depleted. When hydrogen is exhausted, the core can no longer sustain the outward pressure required to counteract gravity, leading to contraction and heating.

More massive stars ignite successive stages of fusion, producing heavier elements until reaching iron, beyond which further fusion becomes energetically unfavourable. At this point, gravity inevitably wins, driving the star toward collapse. Depending primarily on the initial mass, this terminal stage leads to one of three types of compact remnants: white dwarfs (WDs), NSs, or BHs (Shapiro & Teukolsky 1983; Tauris &

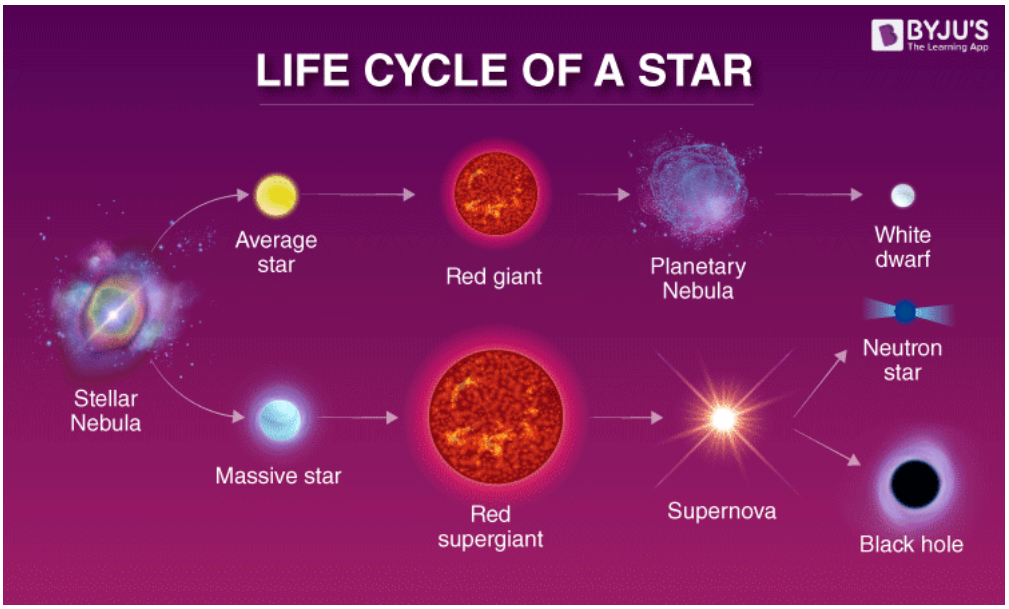

Figure 1.1: Sketch representing the main evolutionary stages of the stars and their final form as compact objects.

van den Heuvel 2006). These compact objects represent the final products of stellar evolution and play a central role in high-energy astrophysics—including the systems discussed in this thesis (see Fig. 1.1 for a summary sketch of stellar evolution).

Stars with initial masses below $\sim 8\,M_\odot$ end their lives as WDs (Heger et al. 2003), supported by electron degeneracy pressure (Chandrasekhar 1931). When nuclear burning ceases in the stellar core, the star is no longer able to counteract gravitational collapse through radiation pressure. The remaining compact object is then sustained by electron degeneracy pressure. At the extremely high densities reached in the stellar remnant, the electrons form a degenerate Fermi gas that can no longer be described by classical physics, while the much heavier ions (nuclei) still behave approximately as an ideal gas. As the particles are fermions, the Heisenberg uncertainty principle ($\Delta x\,\Delta p \sim \hbar$) implies that, as their spatial separation decreases, their momenta must increase. Moreover, the Pauli exclusion principle prevents two fermions from occupying the same quantum state. This leads to a quantum mechanical pressure, known as *degeneracy pressure*, which counterbalances gravity (e.g. Chandrasekhar 1931; Shapiro & Teukolsky 1983). The derivation of the pressure equation, and hence the equation of state of degenerate matter, reveals two distinct regimes depending on the electron velocities:

- In the non-relativistic regime, it scales as $P_d \propto n_e^{5/3}$;
- In the relativistic regime, the pressure scales as $P_d \propto n_e^{4/3}$,

where n_e is the electron number density. In typical WDs the pressure is dominated by non-relativistic electron degeneracy, but in the most massive WDs, approaching the Chandrasekhar limit, the electron momenta become relativistic and the relativistic form of the equation of state becomes increasingly important (Kippenhahn et al. 2013).

WDs are therefore extremely dense objects, with a mass comparable to that of the Sun and a radius of only about the size of the Earth, while their surface temperature can reach up to $\sim 10^4$ K (Lattimer & Prakash 2004). It is worth noting that our own Sun will eventually evolve into a WD after exhausting its nuclear fuel.

Then, if the progenitor star has a mass higher than about $8\,M_\odot$ (Heger et al. 2003), the density in the collapsing core becomes so high that the electrons reach relativistic velocities. In this case, the pressure follows the relativistic relation and increases more slowly with density than in the classical regime. As a consequence, electron degeneracy pressure can no longer support the star against gravitational collapse. The core contracts further until protons and electrons combine through inverse β-decay, forming neutrons. This process gives rise to an extremely dense object, mainly composed of neutrons, with a typical radius of ~ 10 km and a mass close to $1.4\,M_\odot$: a NS (Baade & Zwicky 1934).

If the progenitor star is even more massive (typically $M \gtrsim 15\,M_\odot$), the neutrons themselves become relativistic, and neutron degeneracy pressure can no longer balance gravity. In this case, the collapse continues inexorably, leading to the formation of a BH (Oppenheimer & Snyder 1939). The balance between gravitational pressure and degeneracy pressure allows us to define the limiting for the cores of compact objects. By equating the two, one obtains a critical mass of about $1.44\,M_\odot$, the well-known **Chandrasekhar limit** (Chandrasekhar 1931). Cores below this mass will stabilize as WDs, while more massive cores collapse further. An analogous limiting value exists for NSs: following similar arguments, Oppenheimer & Volkoff (1939) derived the **Oppenheimer–Volkoff limit**, corresponding to a maximum mass of about $0.7\,M_\odot$ for a NS composed of a cold, non-interacting degenerate neutron gas. Above this limit, no stable equilibrium configuration can exist. This relatively low value arises from the simplified equation of state adopted in their calculation, which neglected the effects of strong nuclear interactions that provide additional pressure support at high densities. Rhoades & Ruffini (1974) later provided a more general upper bound of $\sim 3\,M_\odot$, while more realistic equations of state suggest maximum NS masses in the range 2–$2.5\,M_\odot$ (see e.g. Lattimer & Prakash 2004).

1.2 Neutron stars

NSs were first proposed by Baade & Zwicky (1934) shortly after the discovery of the neutron (Chadwick 1932), as the compact remnants left behind after the core collapse of massive stars. Despite early claims that such objects would be too small and faint to ever be observed, Pacini (Pacini 1967) proposed that a rapidly spinning NS endowed with a strong magnetic field could manifest observationally as a pulsed radio signal. Remarkably, around the same time, an unusual train of short, regularly spaced radio bursts was independently discovered at Cambridge by Jocelyn Bell and her supervisor Antony Hewish. Initially dubbed the "Little Green Men" signal due to its puzzling periodicity, the emission was soon identified as originating from the first known pulsar, PSR B1919+21 (Hewish et al. 1968). NSs are extreme objects in every respect. A typical NS packs mass of $\sim 1.4\,M_\odot$ into a radius of only ~ 10–14 km, reaching central densities several times higher than the nuclear saturation density. Its structure is traditionally described in terms of different layers (Longair 2011): a thin atmosphere, a solid crust composed of increasingly neutron-rich nuclei, and an inner core whose composition is still debated. At such extreme densities, matter may exist in forms not accessible in our laboratories. The relation between pressure and energy density—the *Equation of State* (EoS)—remains one of the central open questions in modern astrophysics (for a review, see Özel & Freire 2016).

Progress over the last decade has been driven by high-precision X-ray observations and gravitational-wave measurements. NICER, operating on board the International Space Station, has provided the first simultaneous mass–radius constraints from pulse-profile modelling of a class of pulsars, called millisecond pulsars, e.g. PSR J0030+0451 and PSR J0740+6620 (Miller et al. 2019b, 2021). These results favour relatively stiff EoS,

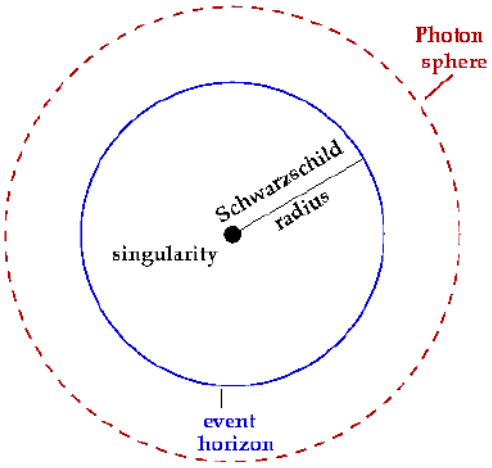

Figure 1.2: Schematic view of a Schwarzschild (non-rotating) BH. The event horizon forms a spherical surface with radius equal to the Schwarzschild radius. Just outside it lies the photon sphere, a region where light can orbit the BH on unstable circular trajectories.

implying radii of $R \approx 12$–13 km for a $1.4\,M_\odot$ NS. A detailed exploration of NS physics is beyond the scope of this thesis. For a more comprehensive treatment, the reader is referred to standard textbooks such as Longair (2011) and to recent dedicated reviews (e.g. Di Salvo et al. 2023).

1.3 Black holes

BHs were first recognised as physical solutions of general relativity soon after the theory was formulated. In 1916, Karl Schwarzschild derived the metric describing a static, spherically symmetric BH (Einstein 1916), while the rotating generalisation was obtained by Roy Kerr in 1963 (Kerr 1963) and later extended to include electric charge by Newman (Newman et al. 1965). These solutions showed that a sufficiently compact mass can curve spacetime to such an extent that a "no–return" surface appears: the *event horizon*. Its radius, the Schwarzschild radius,

$$R_{\rm Sch} = \frac{2GM}{c^2}, \tag{1.1}$$

scales linearly with BH mass M. For a non-spinning BH, photons moving on tangential orbits at $1.5\,R_{\rm Sch}$ form the so-called photon sphere; in Kerr BHs this radius depends on spin and photon trajectory (see Fig. 1.2). In physical terms, a BH is a region of spacetime from which nothing, not even light, can escape. Although quantum field theory predicts that BHs emit Hawking radiation (Hawking 1975), the corresponding temperature for stellar-mass BHs ($\sim 10^{-9}$ K) is far too low to be detectable. BHs are commonly classified by mass into three main categories:

- **Stellar-mass BHs** ($3\,M_\odot \lesssim M \lesssim 50\,M_\odot$) are generally thought to originate from the core collapse of massive stars. Stellar evolution models predict that pair-instability processes limit the maximum mass of BHs formed through standard single-star evolution to ~ 40–$50\,M_\odot$, depending on metallicity and mass-loss rates (Bambi 2025). Most dynamically confirmed stellar-mass BHs have been identified in X-ray binaries, where accretion from a companion star reveals their presence (see Remillard & McClintock 2006; Casares & Jonker 2014 for a review). The advent of gravitational-wave astronomy has revolutionised this field: LIGO and Virgo have detected dozens of mergers involving stellar-mass

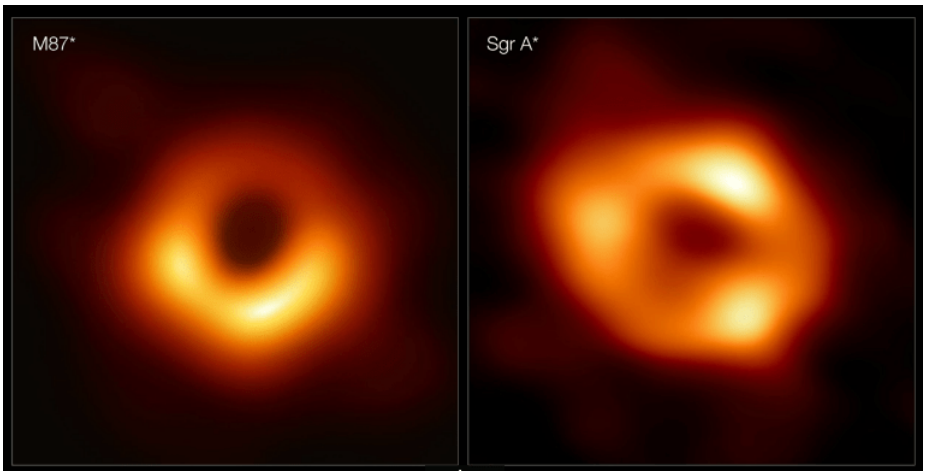

Figure 1.3: The first image of a BH: the supermassive BH at the center of Messier 87, obtained by the Event Horizon Telescope (Event Horizon Telescope Collaboration et al. 2019, 2022).

BHs, including systems with component masses extending into the so-called pair-instability mass gap, suggesting alternative formation channels such as low-metallicity progenitors, Population III stars, or hierarchical mergers (Abbott et al. 2016; Vink et al. 2021; Abbott et al. 2023).

- **Supermassive BHs** ($M \gtrsim 10^6\,M_\odot$) reside in the centres of galaxies. Their presence is established through stellar and gas kinematics, and—when they are actively accreting matter—they appear as luminous *AGN*, outshining their entire host galaxy. Observations of stars orbiting around Sgr A* provided the most compelling dynamical evidence for a supermassive BH in the Milky Way (Ghez et al. 2008; Gillessen et al. 2009; GRAVITY Collaboration et al. 2019). The Event Horizon Telescope (EHT) recently imaged the shadows of the BHs in M87 and Sgr A* (Event Horizon Telescope Collaboration et al. 2019, 2022), offering the first horizon-scale view of these objects (see Fig. 1.3).

- **Intermediate-mass BHs** ($50\,M_\odot \lesssim M \lesssim 10^6\,M_\odot$) bridge the gap between the two classes above and may represent the remnants of early Universe BH seeds. Although candidates have been identified in dwarf galaxies, star clusters, and through gravitational waves (e.g. the $\sim 142\,M_\odot$ remnant of Abbott et al. 2020), their existence is still under debate (Mezcua 2017; Greene et al. 2020).

But how can BHs be observed? Because Hawking radiation is far too weak to be detectable for astrophysical BHs, they cannot be observed directly. Instead, their presence must be inferred through indirect tracers: their gravitational influence on nearby matter or the dynamical motion of companion stars (see review by e.g. Casares & Jonker 2014). **Gravitational waves** also provide a powerful tool for identifying BHs. During the inspiral, merger, and ringdown of compact binaries, strong gravitational-wave signals are emitted. The first direct detection of such a signal from a binary BH merger (Abbott et al. 2016) inaugurated the era of gravitational-wave astronomy, and dozens of additional mergers have since been observed (Abbott et al. 2023).

Finally, BHs can reveal themselves through the *electromagnetic radiation* produced when they accrete material from their surroundings. In binary systems, a BH can exert a strong gravitational pull on its companion star, stripping and capturing part of its gas. As we will discuss extensively in the next Chapter, the accreted material heats up and emits copious X-rays, making these systems among the brightest sources in the X-ray sky: such objects are known as X-ray binaries (XRBs).

1.4 X-ray Binaries

Binary stars are a natural outcome of stellar formation, as the fragmentation of molecular clouds frequently produces pairs or higher-order multiple systems (Tohline 2002; Duchêne & Kraus 2013). As the system evolves, the two components generally follow different evolutionary paths and, in sufficiently massive binaries, one of the stars can end its life as a compact object. If the binary remains bound after this phase, mass transfer may occur through Roche-lobe overflow or via a stellar wind from the companion star. The accretion of this material onto the compact object releases gravitational potential energy, which is efficiently converted into electromagnetic radiation.

The development of X-ray astronomy began in the early 1960s. Because the Earth's atmosphere is opaque to X-rays, the first observations had to be carried out using sounding rockets equipped with simple detectors. A major breakthrough came in 1962, when an Aerobee rocket detected soft X-rays from outside the Solar System (Giacconi et al. 1962). The source responsible for this emission, later named *Scorpius X-1*, was recognized as the first extra-solar X-ray source in history. Its discovery demonstrated that the Universe hosts objects capable of releasing enormous amounts of high-energy radiation, inaugurating the field of X-ray astronomy and transforming our understanding of compact objects.

The launch of *Uhuru* in 1970—the first satellite dedicated entirely to X-ray observations marked the beginning of systematic surveys of the high-energy sky. Subsequent observations revealed that Scorpius X-1 is a binary system (Giacconi 1974) composed of a low-mass ($\lesssim 1\,M_\odot$) donor star transferring matter onto a NS. This identification provided the first clear evidence that compact binaries can efficiently convert gravitational potential energy into intense X-ray emission. Since then, similar systems have been recognized as among the most luminous X-ray sources in the Galaxy, establishing accreting NSs and BHs as key astrophysical laboratories.

A first classification of interacting binaries is based on the nature of the compact object. Systems hosting WDs are known as cataclysmic variables (CVs), typically reaching luminosities of 10^{29}–$10^{33}\,\mathrm{erg\,s^{-1}}$. When the accretor is a NS or a BH, the system is classified as an XRB, with luminosities extending up to 10^{38}–$10^{39}\,\mathrm{erg\,s^{-1}}$ (Lewin et al. 1996; Charles & Coe 2006). The large compactness and deep gravitational potentials of NSs and BHs naturally explain their enhanced radiative efficiency and strong multiwavelength variability compared to CVs.

A second distinction concerns the nature of the donor star. High-Mass X-ray Binaries (HMXBs) host early-type O/B companions and are relatively young systems, usually 10^7 years old and typically found in the Galactic disc. Low-Mass X-ray Binaries (LMXBs), instead, contain solar or sub-solar donors with mass $M \lesssim 1\,M_\odot$ and belong to an older stellar population (10^{9-10} years old). LMXBs are usually more compact—with shorter orbital periods—and their NSs exhibit weaker magnetic fields than those in HMXBs (with values of B around 10^8–10^9 G and 10^{12} G, respectively). As a result, coherent pulsations are common in NS HMXBs, whereas only a minority of NS LMXBs are X-ray pulsators forming the group of the Accreting Millisecond X-ray Pulsars (AMXPs, (Di Salvo & Sanna 2022)). A further distinction among NS LMXBs separates the so-called *atoll* and *Z* sources. These labels derive from the characteristic patterns these systems trace in a colour–colour diagram (see Fig. 1.4), where the intensity in a hard band is plotted against that in a softer one. Atolls typically follow fragmented, island-like tracks and are, on average, less luminous than Z sources, which instead describe smoother, Z-shaped paths.

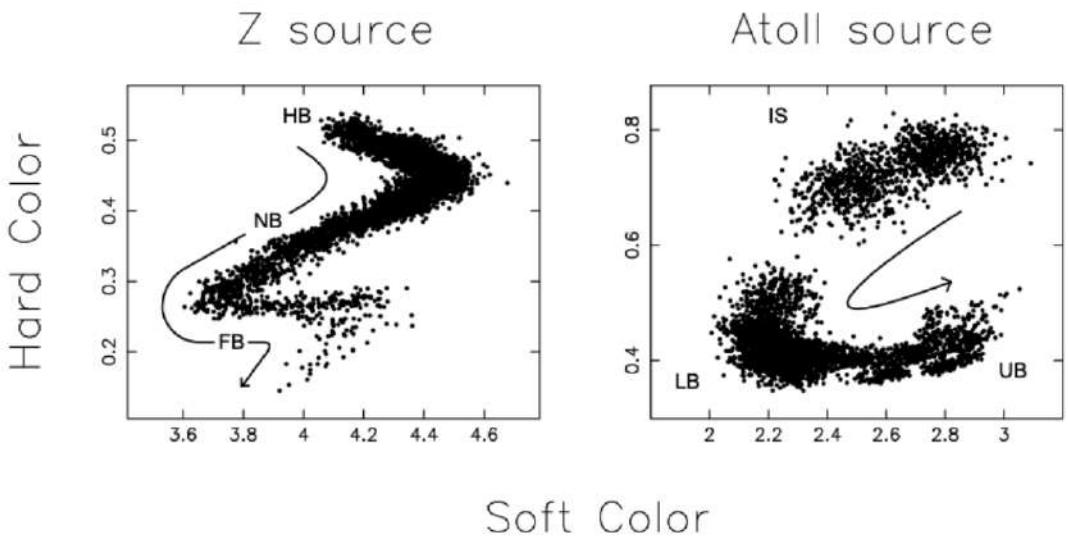

Figure 1.4: Typical X-ray colour–colour diagrams for sources classified as Z systems (left) and atolls (right). The arrows indicate the evolutionary tracks followed as the mass-accretion rate increases (Wijnands 2001). In Z sources, the three main branches are the horizontal branch (HB), the normal branch (NB), and the flaring branch (FB). In atoll sources, the track includes the island state (IS) and the banana branch, which is commonly subdivided into the lower banana (LB) and upper banana (UB).

When NS signatures such as pulsations or Type I X-ray bursts [1], providing a clear observational signature of a solid surface and distinguishing them from BH systems, are absent, the nature of the compact object can be determined through dynamical mass measurements. The mass function,

$$f(M) = \frac{P_{\rm orb} K_2^3}{2\pi G} = \frac{(M_2 \sin i)^3}{(M_1 + M_2)^2}, \tag{1.2}$$

with $P_{\rm orb}$ the orbital period of the system, K_2 the half-amplitude of the velocity curve, M_1 (M_2) the mass of the primary (secondary) star, and i the inclination of the system with respect to our line of sight. This function provides a lower limit to the mass of the accretor (e.g. Casares & Jonker 2014). Values of $M_1 \gtrsim 3\,M_\odot$ imply the presence of a BH. Although NS and BH systems share overlapping luminosity ranges, differences in their spectral and timing behaviour further assist in identifying the nature of the compact object, as discussed later in this thesis.

1.5 Accretion

As diverse as the family of XRBs may be, all systems share one fundamental characteristic: they are bright in X-rays. The mechanism responsible for this emission is accretion, an exceptionally efficient process through which gravitational potential energy is converted into radiation. In an XRB, a fraction of the mass of the companion star is transferred to the compact primary and falls into its deep gravitational potential well. As matter spirals inward through progressively smaller circular orbits, its gravitational potential energy is released in the form of thermal, kinetic, and radiative energy. Because of the high temperatures reached in the proximity of the accretor, much of this radiation emerges in the X-ray band.

[1] Many NS–LMXBs exhibit recurrent flashes in the X-ray band. These so-called type-I X-ray bursts are produced by unstable thermonuclear burning of the accreted material on the neutron-star surface; see Galloway et al. (2019) for a review.

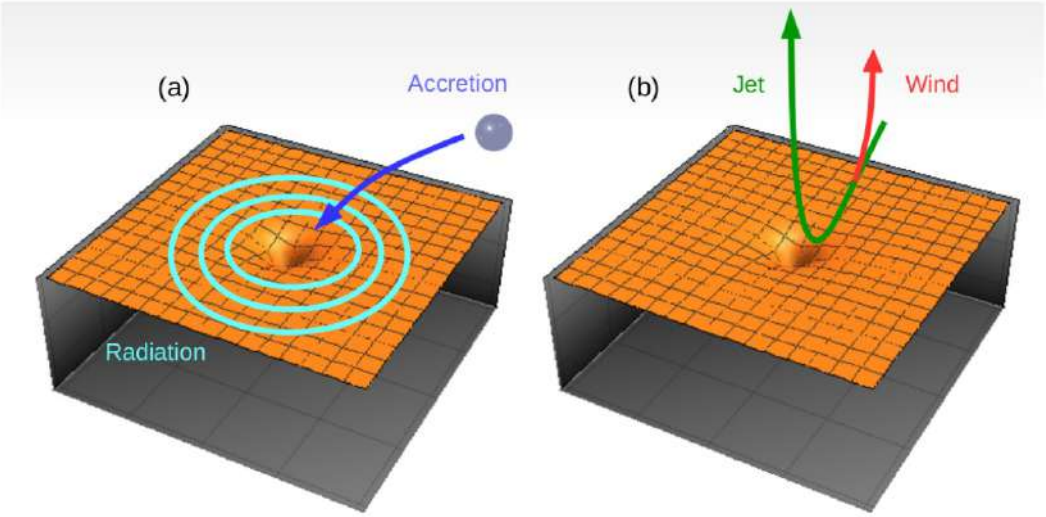

Figure 1.5: Schematic representation of accretion and ejection around a compact object. Matter falling into the gravitational potential well releases energy that can emerge as radiation, jets, or winds. In the inner regions, part of the accretion power may be channelled into relativistic, collimated jets, while further out, slower and more massive disc winds can be launched, providing feedback to the surrounding environment (adapted from Fender & Muñoz-Darias 2016).

Accretion is therefore central not only to the phenomenology of XRBs, but also to a wide range of astrophysical and fundamental physics questions. Accretion flows allow us to probe strong-field gravity, investigate the behaviour of matter at extreme densities, and study the coupling between inflow and powerful outflows such as jets and winds. More broadly, accretion and its feedback are now understood to play a key role in the growth of cosmic structures across the Universe (see, e.g. Fender & Muñoz-Darias 2016).

Accretion onto a compact object proceeds as matter is gravitationally captured and loses energy while moving inward. The gravitational energy released by a mass m falling from infinity to a radius R can be approximated as

$$\Delta E = -\frac{GMm}{R}, \tag{1.3}$$

where G is the gravitational constant, M the mass of the compact object, and the radius R which accretes a mass-test m, initially at infinity. This simple relation illustrates that the more compact the object, the more efficiently it can convert accreted mass into radiative and kinetic output (see Fig. 1.5).

To understand how powerful accretion can be in interacting binaries, it is useful to introduce the radiative efficiency, η, defined as the fraction of the rest–mass energy of the accreted material that is converted into radiation. A simple estimate can be obtained by comparing the gravitational potential energy released to the rest–mass energy mc^2:

$$\eta = \frac{GM}{Rc^2}, \tag{1.4}$$

which immediately implies that the efficiency increases with the compactness of the accretor. For a canonical NS of 1.4 $M_\odot$ and radius $\sim$ 10 km, one obtains $\eta \approx 0.15$, indicating that NSs can convert a significant fraction of the accreted mass into radiation. WDs, with similar masses but radii $\sim 10^3$ times larger, have efficiencies orders of magnitude lower and therefore power much fainter X-ray sources. For BHs, the efficiency depends sensitively on the spin: values between $\eta \sim 0.1$ and ~ 0.4 are expected (Frank et al. 2002), with the upper end corresponding to a maximally rotating Kerr BH.

Using this definition, the gravitational energy release associated with accretion can be written as

$$\Delta E_{\rm acc} = \eta\, mc^2, \tag{1.5}$$

and differentiating with respect to time yields the accretion luminosity,

$$L_{\rm acc} = \frac{GM\dot{M}}{R}, \tag{1.6}$$

where $\dot{M}$ is the mass-accretion rate. In a simplistic picture where gravity is the only relevant force, variations in the X-ray luminosity would directly trace variations in $\dot{M}$. In practice, however, the luminosity is only a non-linear proxy for the accretion rate, as mass losses, advection of energy, and magnetic stresses all modify the radiative output (Agol & Krolik 2000).

1.5.1 The Eddington limit

Accretion luminosities in NS and BH XRBs seldom exceed $\sim 10^{38}$–10^{39} erg s^{-1}, reflecting the existence of an upper limit known as the *Eddington luminosity*. This is defined as the radiative output at which the outward force exerted by photons on electrons balances the inward gravitational pull acting predominantly on protons. This condition is derived under the assumptions of steady, spherically symmetric accretion of fully ionised hydrogen and Thomson scattering as the dominant opacity source.

Since Thomson scattering has the smallest cross-section among typical matter–radiation interactions, the Eddington limit represents a true upper bound on the luminosity that can be radiated while maintaining stable accretion. In this framework, accretion is regulated by a competition between gravity and radiation. Gravity acts mainly on protons—being roughly 2000 times more massive than electrons—tending to draw material inward, while radiation pressure acts mainly on electrons, because the Thomson cross-section scales as m^{-2}, pushing matter outward. Although these forces act on different particles, their effects propagate to the entire plasma through Coulomb coupling between electrons and protons.

Radiation pressure at radius r can be expressed as $P_{\rm rad} = \frac{U}{c}$, where U is the photon energy flux. The flux is simply the luminosity crossing the spherical surface of radius r and gravity, on the other hand, exerts an inward force per proton of

$$F_{\rm grav} = \frac{GMm_{\rm p}}{r^2}. \tag{1.7}$$

The outward radiative force acting on an electron is

$$F_{\rm rad} = \sigma_{\rm T}\frac{L}{4\pi r^2 c}. \tag{1.8}$$

Equating the two forces, $F_{\rm grav} = F_{\rm rad}$, and assuming electrons and protons remain coupled, one obtains the well-known Eddington limit:

$$L_{\rm Edd} = \frac{4\pi GMm_{\rm p}c}{\sigma_{\rm T}} \simeq 1.3\times10^{38}\left(\frac{M}{M_\odot}\right)\ {\rm erg\,s^{-1}}. \tag{1.9}$$

At luminosities approaching or exceeding $L_{\rm Edd}$, radiation pressure may halt or even reverse the accretion flow, unless the geometry or opacity differ substantially from the assumptions above. For these reasons, the

Eddington luminosity serves as a fundamental reference scale for accretion physics in both NSs and BHs. Although widely used, this limit should be regarded as an order of magnitude estimate, since the assumptions of spherical symmetry, pure hydrogen composition, and Thomson scattering opacity are not always fulfilled in real accretion flows. For instance, a handful of sources, such as GRS 1915+105 (Fender & Belloni 2004) or Cir X-1 (Done & Gierliński 2003), have been observed to exceed the Eddington limit by factors of a few. Even more extreme are extragalactic *off-nuclear* sources known as Ultra-Luminous X-ray Sources (ULXs; Kaaret et al. 2017), which shine at $L_X \sim 10^{39}$–10^{42} erg s^{-1}. Their location outside galactic nuclei rules out an AGN origin and indicates accretion onto a stellar-mass compact object operating at, or well above, the Eddington limit.

1.6 Mass-transfer mechanism

In order for material to be accreted onto the compact object and produce X-ray emission, the companion star must transfer mass to the primary. In XRBs, two main channels enable mass transfer: (1) stellar-wind capture and (2) Roche-lobe overflow. The first mechanism is effective primarily in HMXBs, where massive O/B stars possess strong winds. Low-mass stars, on the other hand, produce negligible winds, making Roche-lobe overflow the dominant mechanism in LMXBs. Since this thesis focuses on LMXBs, I concentrate here on the physics of Roche-lobe overflow, setting aside the discussion related to HMXBs (to delve dipper into mass transfer processes in HMXBs see Frank et al. 2002).

1.6.1 Roche lobe overflow

The gravitational interaction between two stars in a binary is complex, and describing the resulting flow of matter requires understanding the effective gravitational potential of the system. In 1879, Édouard Roche formalized this problem by introducing the concept of gravitational equipotential surfaces—now known as **Roche lobes**—in his work *Sur l'équilibre des satellites et sur leur figure*. Roche's approach consists in studying the motion of a test particle in the combined gravitational and centrifugal potential generated by two orbiting point masses.

Assuming the binary follows a circular orbit[2], the fluid motion in a frame co-rotating with angular frequency ω is governed by the Euler equation:

$$\frac{\partial \mathbf{v}}{\partial t} + (\mathbf{v}\cdot\nabla)\mathbf{v} = -\nabla\Phi_R - 2\,\omega \wedge \mathbf{v} - \frac{1}{\rho}\nabla P, \tag{1.10}$$

where P is the pressure, ρ the gas density, and the term $-2\,\omega \wedge \mathbf{v}$ is the Coriolis force. The function Φ_R is the **Roche potential**, incorporating the gravitational fields of both stars and the centrifugal contribution (Frank et al. 2002):

$$\Phi_R(\mathbf{r}) = -\frac{GM_1}{|\mathbf{r}-\mathbf{r}_1|} - \frac{GM_2}{|\mathbf{r}-\mathbf{r}_2|} - \frac{1}{2}(\omega \wedge \mathbf{r})^2. \tag{1.11}$$

A three-dimensional representation of this potential is shown in Fig. 1.6, where the locations of Lagrange points are highlighted. The geometry of the equipotential surfaces is determined by the mass ratio $q = M_1/M_2$ and by the binary separation a, which follows from Kepler's third law, $a^3 = P^2 M/4\pi^2$, with $M = M_1 + M_2$.

[2]This is often a good approximation, as tidal forces efficiently circularize most initially eccentric binaries (Frank et al. 2002).

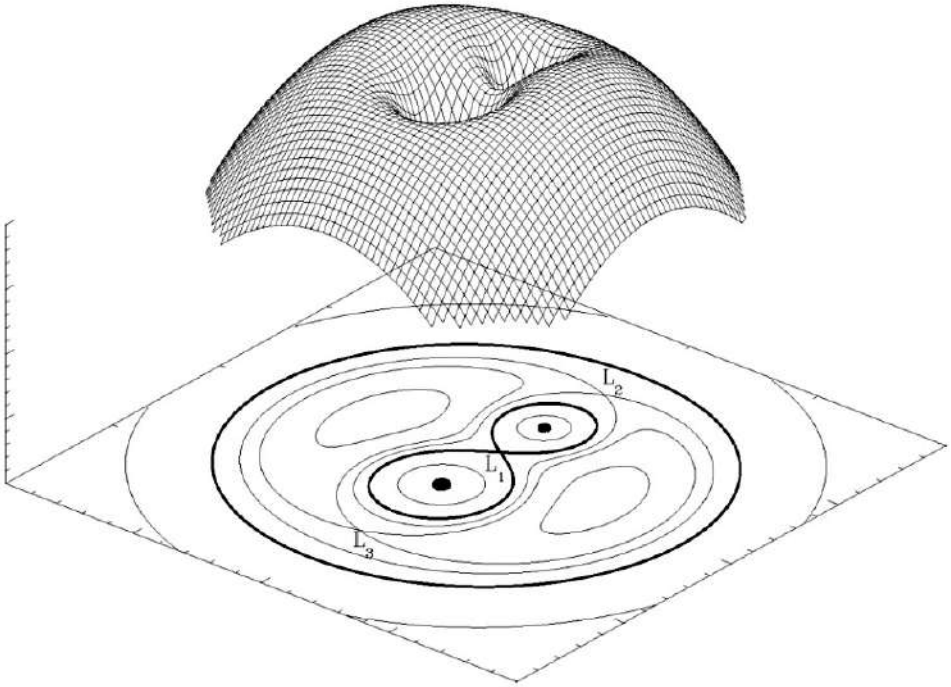

Figure 1.6: 3D representation of the Roche potential in a binary system. Three of the five Lagrange points, L_1, L_2, L_3, are highlighted (https:www.heaven.waarnemen.com).

If we consider a test mass located significantly far from the binary, it experiences approximately the gravitational field of a single body with mass $M_1 + M_2$. Instead, close to one star, its gravity dominates. At intermediate distances, however, an eight-shaped equipotential surface appears, forming two distinct lobes—each surrounding a star—and connected at a saddle point. These lobes are the **Roche lobes**, and the saddle point corresponds to the **inner Lagrange point** L_1. Matter near L_1 is in unstable equilibrium: a small perturbation can push it toward either star. If both stars lie within their respective Roche lobes, the system is said to be *detached*, and no mass transfer takes place. Over time, however, the secondary can grow relative to its lobe. In LMXBs, this usually happens because the orbital separation shrinks due to angular-momentum losses—primarily *magnetic braking* and *gravitational-wave radiation*—causing the lobe to contract until it meets the stellar surface. In other systems, the donor may evolve off the main sequence and expand to fill its lobe, a mechanism more relevant for high-mass stars (Kippenhahn & Weigert 1990). When the stellar surface reaches L_1, the system becomes *semi-detached*: gas at the outer layers of the donor can flow through L_1 into the potential well of the compact object, initiating **Roche-lobe overflow**. If, for some reason, both stars simultaneously fill their Roche lobes, the binary enters a *contact* configuration (e.g. Jayasinghe et al. 2020), though such systems are not relevant for LMXBs.

Because Roche lobes do not possess a simple analytic shape, it is convenient to define an effective radius corresponding to that of a sphere with the same volume. Several approximations exist. For moderate mass ratios ($0.1 \lesssim q \lesssim 0.8$), the expression by Paczyński (1971) is useful:

$$\frac{R_2}{a} = 0.462 \left(\frac{M_2}{M_1 + M_2} \right)^{1/3}, \tag{1.12}$$

where R_2 describes the radius of the Roche lobe of the companion star, and a denotes the orbital separation[3]

[3]The radius of the primary object lobe R_1 can be determined by replacing q with q^{-1}.

An even more general relation—accurate to within 1% over the entire range of q—is given by Eggleton (1983):

$$\frac{R_2}{a} = \frac{0.49\, q^{2/3}}{0.6\, q^{2/3} + \ln(1 + q^{1/3})}. \tag{1.13}$$

Mass transfer modifies both the mass ratio and the orbital separation, since angular momentum is exchanged together with mass. The determination of the Roche geometry by a and q, as evident from equation 1.13, implies that the Roche lobe of the mass-losing star undergoes either contraction or expansion during the process. It is natural to question whether such a variation of the Roche lobe could affect the mass transfer process. The outcome largely depends on the angular momentum of the binary which is $J = (M_1 a_1^2 + M_2 a_2^2)\, \omega,$, where a_1 and a_2 denote the relative distances of the stars from the centre of mass. If all transferred mass is accreted by the compact object (**conservative** mass transfer), $\dot{J} = 0$. If part of the mass is lost from the system, for instance via winds or jets (di Salvo et al. 2008), the transfer is **non-conservative**.

To understand how the temporal evolution of a, J, and M_2 occurs in the system, it is useful to apply the logarithmic derivative to the angular momentum J:

$$\frac{\dot{a}}{a} = \frac{2\dot{J}}{J} + \frac{2(-\dot{M}_2)}{M_2}(1 - q). \tag{1.14}$$

For conservative transfer ($\dot{J} = 0$), the contraction or expansion of a depends on q: the orbital separation increases when $q < 1$—the typical case for LMXBs—and decreases when $q > 1$. Physically, as mass flows toward the compact object near the system's centre of mass, the donor must move outward to conserve angular momentum.

The size of the Roche lobe evolves accordingly. Differentiating Eq. 1.12 and combining it with Eq. 1.14 gives:

$$\frac{\dot{R}_{2,\mathrm{L}}}{R_{2,\mathrm{L}}} = \frac{2\dot{J}}{J} + \frac{2(-\dot{M}_2)}{M_2}\left(\frac{5}{6} - q\right). \tag{1.15}$$

If $\dot{J} = 0$, the lobe shrinks when $q > 5/6$ and expands when $q < 5/6$. In this regime, the lobe grows faster than the donor can respond, eventually detaching from the stellar surface and bringing Roche-lobe overflow to an end. Mass transfer can then resume only if the companion star subsequently expands—typically by evolving off the main sequence—or if additional angular-momentum losses shrink the orbit again. In LMXBs, donor evolution is generally slow, so sustained mass transfer typically requires additional continued angular-momentum loss. In particular this can happen through two well-established mechanisms:

- **Magnetic braking**: here late-type, convective stars exhibit magnetic activity that couples their stellar wind to the magnetic field, forcing the wind to co-rotate with the star at large distances. This produces an efficient angular momentum drain, spinning down the star (Verbunt & Zwaan 1981; Rappaport et al. 1983). In tidally locked binaries, this angular momentum loss is communicated to the orbit, driving the system towards shorter separations.
- **Gravitational wave emission**: in very compact systems, the varying quadrupole moment of the binary produces gravitational radiation, removing both energy and angular momentum (Kraft et al. 1962). This effect is particularly relevant for ultracompact binaries with orbital periods of $\lesssim 1$ hr, where it dominates the evolution (Nelemans & Jonker 2010).

In LMXBs — particularly in compact and ultra-compact systems — angular-momentum losses are

dominated by gravitational radiation, as both the stellar wind and the associated removal of angular momentum are essentially negligible (Nelson & Rappaport 2003). Conversely, in systems with a more massive donor and/or a wider orbital separation, gravitational-wave emission becomes less effective, and magnetic braking provides the primary mechanism for driving orbital evolution. Recent observational work has shown that orbital period decay in some LMXBs occurs significantly faster than predicted by standard models (Jain et al. 2007; Burderi et al. 2010). This discrepancy points to additional processes at play, such as cyclic variations in $P_{\rm orb}$ driven by magnetic activity in the donor star that alters its gravitational quadrupole moment (the so-called Applegate mechanism; Applegate 1992). Overall, the relative contribution of these mechanisms remains an open question.

1.7 Accretion disc

In the previous sections, I examined the geometry of the Roche lobes and the conditions under which the companion star fills its own lobe, thereby enabling the onset of mass transfer and subsequent accretion. When matter escapes the donor star through the L_1 point, it carries a substantial amount of specific angular momentum. This prevents a direct, radial infall onto the compact object. Instead, the trajectory of the gas stream closely resembles that of a test particle launched from L_1: it follows an elongated, precessing orbit within the orbital plane, influenced by the gravitational field of both components of the binary. Because the stream is continuous, the incoming gas intersects previously ejected material, leading to shocks, collisions between parcels moving at different velocities, and more generally to dissipative processes that progressively remove orbital energy. Although the stream loses energy, it retains essentially the same specific angular momentum it had at L_1. As a result, the gas settles onto the circular orbit of minimum energy for that angular momentum. The radius of this orbit defines the *circularization radius*, $R_{\rm circ}$, which typically lies a factor of 2–3 smaller than the Roche-lobe radius of the accretor (Frank et al. 2002). The transferred material therefore collects into a ring at $R_{\rm circ}$, where dissipative processes convert gravitational potential energy into heat, part of which is radiated away. Because this energy loss forces the gas to move inward, but angular momentum must be conserved, the excess angular momentum is transported outward. The outermost annulus at $R_{\rm circ}$ is thus pushed to slightly larger radii. This feedback between energy dissipation and angular momentum redistribution causes the ring to spread on both sides, ultimately forming a geometrically thin, nearly Keplerian **accretion disc** composed mainly of hydrogen and helium (see Fig. 1.7). Applying the virial theorem to matter in circular Keplerian orbits shows that only half of the gravitational energy released during accretion is radiated by the disc. The other half is dissipated in the boundary layer (in NS systems) or is advected inward (in BH systems). The energy released through this process is thus expressed as $\Delta E = \Delta E_{acc}/2$. This, in turn, leads to a **disc Luminosity** equal to $L_{\rm disk} = GM\dot{m}/2R = L_{\rm acc}/2$. The disc extends outward until limited by tidal torques from the companion star; the corresponding *tidal radius* is close to $R_{\rm T} \simeq 0.9\,R_1$ (Frank et al. 2002).

Within the disc, matter orbits with differential Keplerian velocity,

$$\Omega_{\rm K}(R) = \sqrt{\frac{GM}{R^3}},$$

so neighbouring annuli shear against one another. Microscopic viscosity is far too small to account for the observed mass-transfer rates, but turbulent or magnetic stresses act as an effective viscosity. These stresses generate *viscous dissipation*, which converts orbital kinetic energy into heat. Despite the uncertainty in the

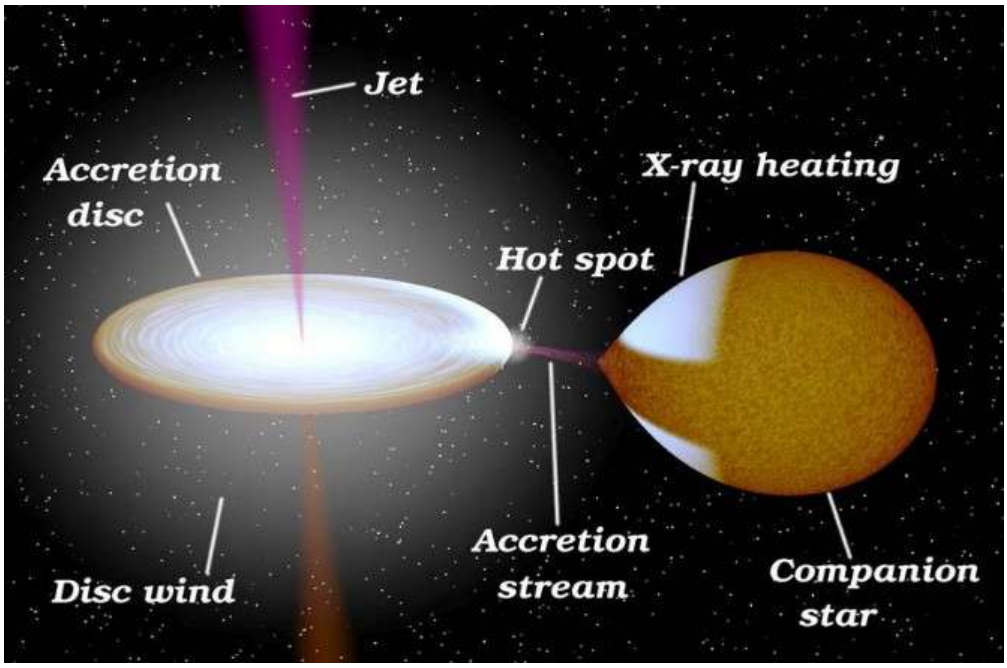

Figure 1.7: Schematic representation of the accretion disc in a LMXB binary system. Matter is transferred from the companion star through an accretion stream toward the accretion disc, where it heats up and emits X-rays. Part of the accreted material is expelled in the form of a disc wind and a relativistic jet, while X-ray irradiation heats the surface of the companion star, producing a localized hot spot.

microphysical origin of viscosity, the dissipation rate per unit surface area in a steady disc can be written analytically (Frank et al. 2002):

$$D(R) = \frac{3GM\dot{M}}{8\pi R^3}\left[1 - \left(\frac{R_*}{R}\right)^{1/2}\right], \tag{1.16}$$

where R_* is the radius of the compact object, or the ISCO in the case of a BH. In the Shakura & Sunyaev (1973) prescription, viscosity is parametrised as $\nu = \alpha c_s H$, where c_s is the sound speed and H the scale height of the disc. The α parameter enters only with weak powers in the disc equations, enabling a consistent phenomenological description even without specifying the exact physical origin of viscosity. More recently, some steps away from this simple phenomenological picture have been made: magneto-rotational instability (MRI) (see,e.g. Balbus 2005; Martin et al. 2019 for a review) is now recognised as the most promising driver of angular-momentum transport in ionised discs.

1.7.1 Disc spectral properties

In steady disks, each annulus radiates approximately as a blackbody with temperature set by the local dissipation rate, so that

$$\sigma T^4(R) = D(R),$$

leading to the standard radial temperature profile,

$$T(R) = \left[\frac{3GM\dot{M}}{8\pi\sigma R^3}\left(1 - \sqrt{\frac{R_*}{R}}\right)\right]^{1/4}. \tag{1.17}$$

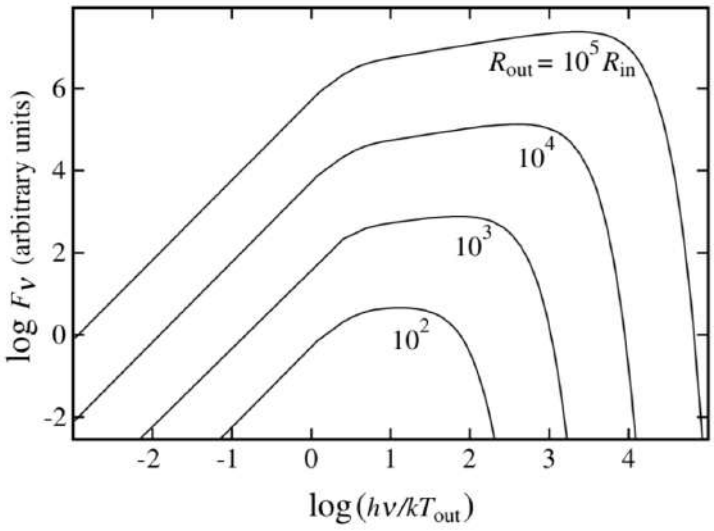

Figure 1.8: Multi-colour disc blackbody spectra computed for different outer disc radii. As R_{out} increases, the characteristic flat portion of the spectrum becomes progressively more pronounced, while it is essentially absent for discs with $R_{out} = 10^2 R_{in}$, as typically observed in cataclysmic variables. Adapted from Frank et al. (2002).

Consequently, for radii well outside the inner boundary, $T(R) \propto R^{-3/4}$ (Pringle 1981). This radial dependence produces a wide range of temperatures across the disc: in the outer regions, where T_{eff} drops to about 10^3–10^4 K, hydrogen may remain partially neutral, whereas in the innermost radii temperatures can reach 10^6–10^7 K, giving rise to thermal soft X-ray emission.

Approximately, the radiation emerging from an accretion disc can be viewed as the sum of blackbody spectra produced at its various radii, each characterized by a different temperature. The overall emission is largely governed by the hottest regions closest to the inner edge of the disc. Indeed, the flux at frequency ν from the disc is obtained by integrating the blackbody contribution emitted at each radius:

$$F_\nu \propto \nu^3 \int_{R_*}^{R_{out}} \frac{R\,dR}{\exp\left(\frac{h\nu}{kT(R)}\right) - 1}, \tag{1.18}$$

where R_* is the inner disc radius and R_{out} its outer radius. At low frequencies, the emission follows the Rayleigh–Jeans law ($F_\nu \propto \nu^2$), while at high energies it exhibits an exponential cutoff corresponding to the Wien tail. In the intermediate range where $kT(R_{out}) \ll h\nu \ll kT(R_*)$, one obtains $F_\nu \propto \nu^{1/3}$, yielding the well-known "flat-top" section of the disc spectrum (see Fig. 1.8). This effect is almost absent in CVs, that have disks smaller by two-three orders of magnitude with respect to disks in BH/NS systems.

The result neglects the irradiation from the central source and from the innermost disc regions, which modifies the temperature profile by heating a broad range of intermediate radii, leading to $kT(R) \propto R^{-1/2}$. Thus from 1.18 one finds that the flux, in the intermediate-frequency regime, no longer scales as $\nu^{1/3}$ but instead becomes proportional to ν^{-1}. This effect is particularly relevant in LMXBs, where the discs are large enough for irradiation to significantly alter their spectral shape. The resulting "flat" component is detectable primarily at UV–optical wavelengths and only when the companion contributes negligibly in this range, such as in systems with evolved, degenerate, or very low-mass donors. While classical, non-irradiated disc models (e.g. Mitsuda et al. 1984) successfully reproduce the X-ray spectra, irradiated disc models are essential for interpreting the combined optical-to-X-ray emission of LMXBs (Gierliński et al. 2008).

1.7.2 Beyond the disc

The accretion flow in XRBs is not limited to the geometrically thin, optically thick disc described in the previous sections. Close to the compact object, additional structures arise and profoundly affect the emerging spectrum. In systems hosting a NS (or, similarly, a WD) with a relatively weak magnetic field, the accretion disc is expected to extend down to radii very close to the stellar surface. In practice, however, the innermost region of the flow cannot join the compact object smoothly. Two conditions would be required for such a direct transition: (i) the magnetic pressure must be everywhere lower than the ram pressure of the accreting flow, defined as $P_{\rm ram} = \rho v^2$, where ρ and v are, respectively, the density and velocity of the infalling gas; it quantifies the dynamical force exerted by the material as it impacts the magnetosphere. (ii) The stellar rotation should match the local Keplerian angular velocity at the stellar radius. The latter condition is almost never met. As the disc approaches the surface of a NS, the gas must slow down from nearly Keplerian orbital velocities to match the much slower rotation of the stellar surface. This transition occurs within a compact and extremely hot region referred to as the *boundary layer*. A substantial fraction of the accretion power—comparable to or even exceeding the luminosity produced in the disc—is released in this narrow zone, and relativistic effects further enhance its contribution (Sibgatullin & Sunyaev 2000). Such an additional radiative component is a distinctive feature of NS accretors, since BHs lack a solid surface and the inflowing material simply crosses the event horizon with its remaining energy advected inward. The presence or absence of a boundary layer therefore represents a fundamental observational discriminator between NSs and BHs.

At the same time, both classes of compact accretors frequently display a hard X-ray component, often extending to hundreds of keV, which cannot be produced by the standard disc emission. This high-energy tail is well described by Comptonization in a tenuous, hot plasma surrounding the innermost flow: the *corona*. Indeed, in order for an optically thick but geometrically thin disc to exist, protons and electrons must interact sufficiently to maintain thermal coupling, and electrons must efficiently cool via repeated collisions with photons. At low mass-accretion rates, however, the density of the flow may drop below the threshold required for frequent Coulomb interactions. In this regime, the gravitational energy gained by the much heavier protons is only partially transferred to electrons, which cool predominantly by inverse Compton scattering. The outcome is a *two-temperature plasma* (Shapiro et al. 1976), with protons remaining extremely hot while electrons settle at temperatures of tens to hundreds of keV. If the cooling becomes inefficient, most of the gravitational energy is advected inward with the protons rather than being radiated away. This leads to a radiatively inefficient, optically thin accretion flow, whose structure is commonly referred to as an *Advection-Dominated Accretion Flow* (ADAF; Narayan & Yi 1995; Yuan 2001). Building upon this scenario, Esin et al. (1997) proposed that the Shakura-Sunyaev disc may truncate at a transition radius, inside which the flow switches to a hot, advection-dominated configuration. The resulting spectrum combines multicolour disc photons with a Comptonized component produced in the inner hot flow. Subsequent work has explored alternative or complementary mechanisms, including convection-dominated flows (CDAFs; Blandford & Begelman 1999; Abramowicz & Igumenshchev 2001), magnetically dominated configurations (MDAFs; Meier 2005), and models in which part of the high-energy emission is linked to the base of the jet (Falcke et al. 2004).

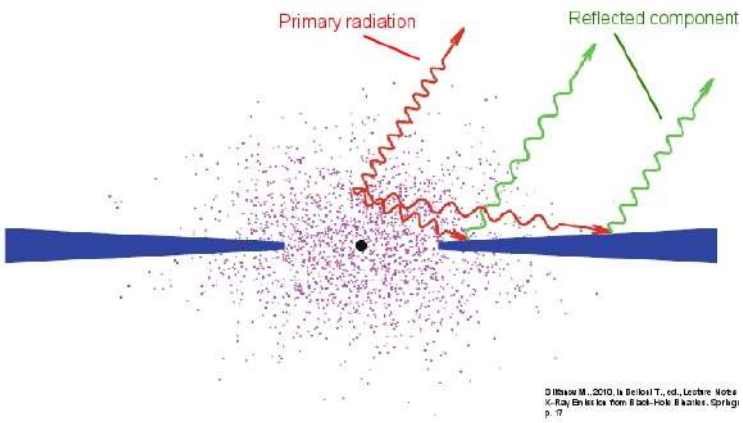

Figure 1.9: A schematic view of the innermost regions of a LMXB. A fraction of the high-energy photons produced in the hot inner flow illuminates the accretion disc and the companion star, where they are reprocessed and give rise to the characteristic X-ray reflection features (Gilfanov 2010).

1.8 X-ray reflection

Although the geometry of the accretion flow remains a matter of active debate, it is generally accepted that at least part of the photons produced in the corona will inevitably illuminate the accretion disc. For this reason, in addition to the primary continuum produced in the innermost regions of the accretion flow, the observed X-ray spectra of compact objects often display a secondary component originating from the interaction between this radiation and the surface of the accretion disc. This process, broadly referred to as *reflection*, carries unique diagnostic power, as it encodes information on the geometry, ionisation state, and relativistic environment of the inner disc (see Fig. 1.9). High-energy photons emitted by the corona or the hot inner flow irradiate the optically thick disc. A fraction of this radiation is absorbed by the disc surface and re-emitted through a combination of fluorescence, Compton scattering, and thermal reprocessing. The remaining photons are either scattered back toward the observer or lost deeper within the disc. A fraction of the absorbed energy is subsequently reprocessed and re-emitted at lower X-ray energies as a quasi-thermal component (Zdziarski & De Marco 2020), although this emission is generally too weak to be detected. The most prominent feature of the reflected emission is the Fe Kα fluorescence complex around 6–7 keV, a component so informative and rich in physical diagnostics that it warrants a dedicated discussion in the following subsection. In addition to the iron line, a Compton hump appears at 20–40 keV. This excess results from the down-scattering of high-energy photons in the disc surface layers and is a characteristic signature of reflection in both stellar-mass and supermassive accreting systems. At lower energies, numerous soft X-ray emission lines and absorption edges arise from lighter elements, depending on disc composition and ionisation. The shape of the reflected spectrum is therefore mainly determined by four key ingredients: (i) the ionisation parameter of the disc surface, (ii) the chemical abundances (especially iron), (iii) the inclination of the system, (iv) and the geometry of the illuminating source.

1.8.1 Relativistic feature as inner disc diagnostics

First detected in AGNi (see the review by Fabian et al. 2000), the shape of the reflected iron line has soon proved to be a powerful diagnostic for inferring properties of the system as, e.g., the inner radius of the accretion disk (see, for a review, Reynolds & Nowak 2003). Indeed iron is abundant and has a high fluorescent

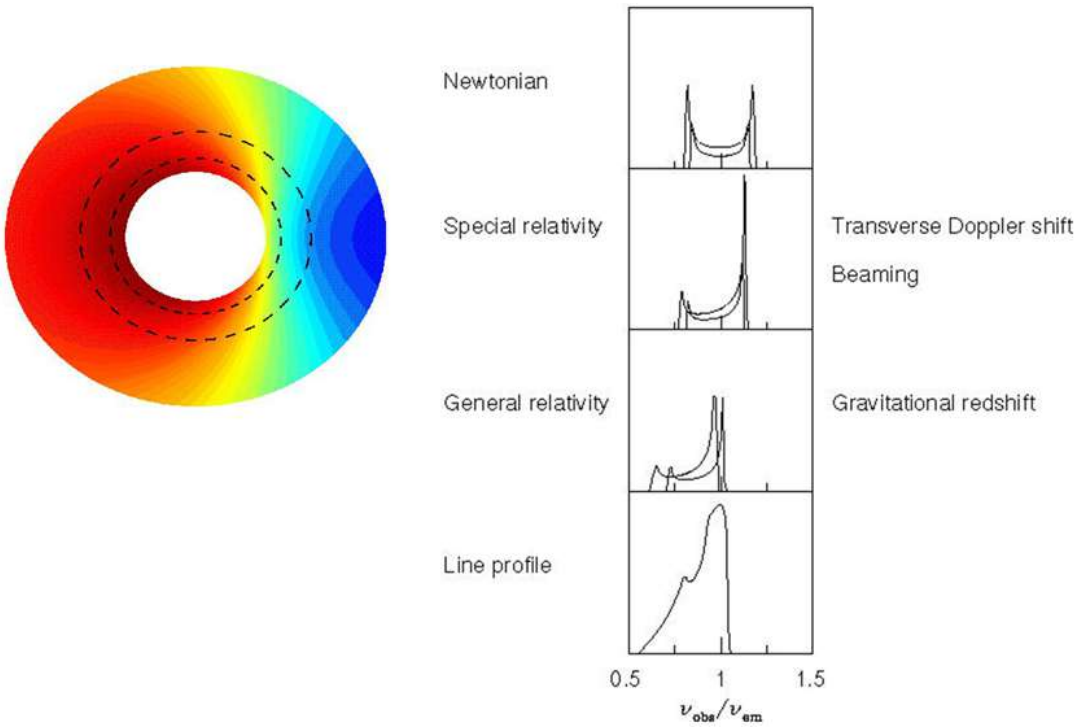

Figure 1.10: **Left panel**: Schematic top view of an accretion disc. The blue-shaded region corresponds to material moving toward the observer, while the red-shaded region marks the receding side. **Right panel**: Illustration of how the iron line profile is progressively modified by (from top to bottom) Newtonian Doppler shifts, relativistic beaming, and gravitational redshift, following Fabian et al. (2000).

yield (Kaastra 1999). But how does it arise? Whenever an incident photon with energy above the iron K-shell binding energy is absorbed by a disc atom, the subsequent electronic transition produces a line photon whose rest-frame energy depends on the ionisation state of iron: from 6.4 keV for neutral Fe to about 6.97 keV for H-like Fe. The physical appearance of the reflection spectrum depends strongly on the disc ionisation. In the *low-ionisation* regime, the surface remains partially neutral, producing strong fluorescence lines (especially Fe Kα) and sharp absorption edges. As ionisation increases, bound electrons are stripped, suppressing the line forest in the soft X-ray band and shifting the Fe K complex to higher energies. In the *highly ionised* regime, Compton scattering becomes dominant, smoothing line features and increasing the relative strength of the high-energy hump. The extreme case of a fully ionised disc erases all atomic features, leaving only a curved continuum.

Because reflection originates in the strong-gravity regime close to the compact object, the emerging signal carries the imprint of relativistic effects. Doppler boosting, gravitational redshift, and light bending distort the intrinsically narrow Fe K line into a broad, asymmetric profile. The degree of broadening provides a direct handle on the radius at which the line originates—hence on the location of the inner accretion disc—as well as offering valuable constraints on the system's inclination.

The Doppler effect shapes the line profile in two main ways. First, it produces the characteristic double-peaked structure: emission from material moving toward the observer is blue-shifted, while that from receding regions is redshifted. Second, it broadens the line, since each disc annulus contributes photons spanning a range of Doppler-shifted frequencies, with the largest spread coming from the fastest-moving inner regions. Relativistic aberration further skews the profile, typically enhancing the blue peak with respect to the red (see Fig. 1.10).

Because matter orbits with nearly Keplerian velocities, the width of the line reflects the orbital speed at the emission radius. Given that the disc emissivity peaks in the innermost region, the overall breadth of the profile provides an estimate of the inner disc radius. This information is crucial for constraining the BH spin, the extent (and possible truncation) of the disc, and—when the accretor is a NS—the stellar radius itself (e.g. Egron et al. 2011; Miller 2007; Sanna et al. 2014; Reynolds 2014).

Finally, the global shape of the line is not determined by relativistic effects alone: it also depends on the radial emissivity profile, the iron abundance, the inclination of the binary, and the disc geometry (particularly its inner and outer radii, $R_{\rm in}$ and $R_{\rm out}$). The influence of several of these parameters on the resulting line profile is illustrated in Fig. 1.11.

A more detailed overview of a typical X-ray spectrum of accreting BH binaries — including the main spectral components introduced above — will be presented in Chapter 3, where I will discuss the spectral analysis of GRS 1915+105 and show how these results advance our understanding of the geometry of the system.

1.9 Spectral states

In the previous sections, I have described the key physical processes that shape the radiation emerging from accreting compact objects, along with their characteristic spectral components. The thermal emission from the accretion disc and the Comptonized continuum produced in the hot inner flow constitute the fundamental building blocks of XRB spectra. Observationally, these components can be combined in different proportions, giving rise to the rich phenomenology of *spectral states*.

The first evidence for distinct states emerged from early X-ray observations of the archetypal BH binary Cyg X–1, which clearly displayed two different spectral behaviours: a "high" state, associated with a higher soft X-ray flux, and a "low" state, in which the flux was systematically reduced (e.g. Tananbaum et al. 1972; Holt et al. 1975). These two states were also spectrally different: the high state exhibited the expected disc blackbody shape, whereas the low state was instead dominated by a power-law continuum. However, the limited energy coverage of the first X-ray missions (typically 2–10 keV) hindered a proper interpretation of this dichotomy.

A clearer picture emerged in the 1990s thanks to the advent of broad-band observatories such as *BeppoSAX*, *RXTE*, and *CGRO*, which extended sensitivity well above 10 keV. These facilities revealed that the so-called "low" state is in fact characterized by a hard spectrum extending to ~ 100 keV and beyond, with a bolometric luminosity comparable to that of the high state in sources like Cyg X–1 (e.g. Nowak 1995; Zhang et al. 1997). As a consequence, the earlier terminology was superseded by the now-standard labels *soft state* (formerly "high") and *hard state* (formerly "low"). This spectral duality is naturally interpreted in terms of the two basic components of the accretion flow described in Section 2.7: a geometrically thin, optically thick Shakura–Sunyaev disc, and a hot, optically thin Comptonizing region. The balance between these components—and their geometry—determines whether the spectrum appears disc-dominated (soft state) or corona-dominated (hard state).

Although originally identified in BH XRBs, analogous behaviour is also present in NS LMXBs. In particular, atoll sources exhibit spectral states that broadly correspond to the hard and soft branches of BH systems, commonly referred to as the *island* and *banana* states, respectively (Hasinger & van der Klis 1989).

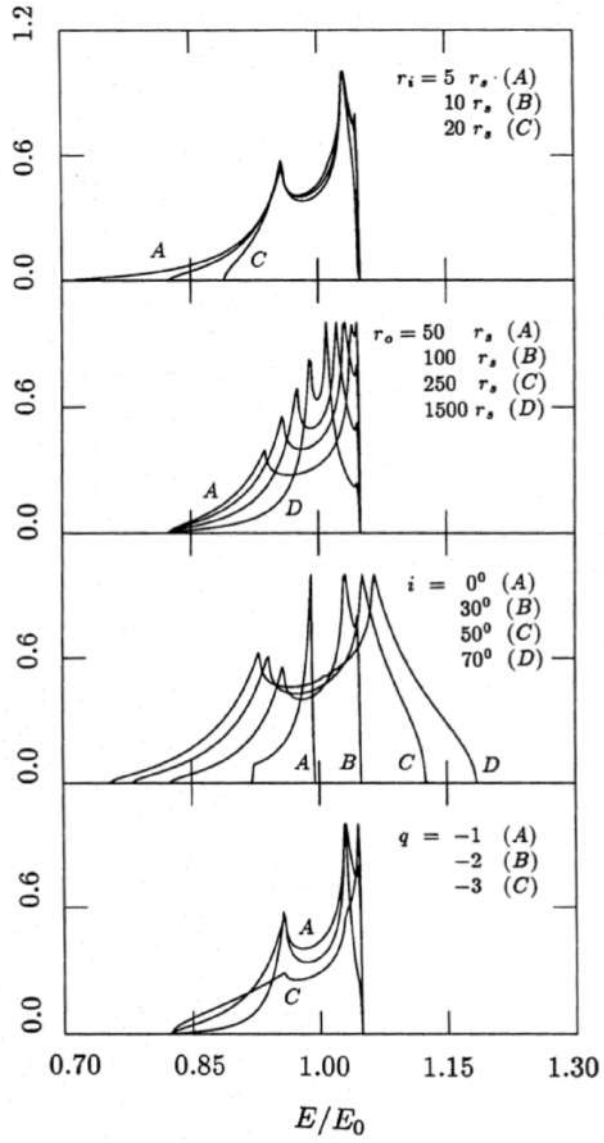

Figure 1.11: Iron line profiles computed for different values of the key disc parameters: from top to bottom, the inner and outer disc radii, the inclination angle, and the emissivity index (**denoted as e in this thesis to avoid confusion with the mass ratio**). Unless otherwise stated, the models assume $R_{\rm in} = 10\,R_{\rm G}$, $R_{\rm out} = 100\,R_{\rm G}$, $i = 30°$, and $e = -2$ (Fabian 1989).

Except where explicitly required, in this thesis I adopt the BH nomenclature (hard/soft) to refer to both classes, to facilitate comparison.

In the rest of paragraph that follows, I discuss the observational properties of each spectral state, the leading physical scenarios proposed to explain them, and the phenomenology of transitions between them. Particular emphasis is placed on BH binaries, while highlighting the key similarities and differences with NS accretors where relevant.

Soft state

In BH LMXBs, the *soft state* is characterised by a spectrum overwhelmingly dominated by thermal emission from the accretion disc. In the soft X-ray band (roughly 0.1–10 keV), these spectra are well described by multi-colour disc blackbody models, consistent with an optically thick, geometrically thin disc extending down to the innermost stable circular orbit (ISCO). Several works have shown that, in this state, the bolometric luminosity scales approximately as $L_{\rm bol} \propto T^4$ (Kubota et al. 2001; Kubota & Done 2004; Davis et al. 2005). If the spectrum is indeed disc-dominated, such that

$$L_{\rm bol} = 4\pi R_{\rm in}^2 \, \sigma T^4,$$

the observed relation $L_{\rm bol} \propto T^4$ naturally implies that $R_{\rm in}$ remains nearly stable—consistent with the disc extending down to the ISCO (Done et al. 2007). NS LMXBs in soft states share several similarities, although their spectra can include additional contributions from the stellar surface or boundary layer. In these systems, the soft emission is sometimes described as the superposition of two saturated Comptonized components, one associated with the disc and the other with the boundary layer or NS surface (Lin et al. 2007; Armas Padilla et al. 2017).

The advent of hard X-ray and soft γ-ray missions such as *CGRO* and *INTEGRAL* revealed that soft-state spectra do not end at a few keV. Instead, they often exhibit a high-energy component extending to hundreds of keV with a power-law index $\simeq 2$ (Gierliński et al. 1999). Although the exact origin of this component is still debated, it is commonly attributed to Comptonization by a non-thermal population of electrons. Hybrid thermal/non-thermal electron distributions likely coexist in the corona, producing the observed high-energy behaviour in both soft and hard states (Poutanen & Coppi 1998; Coppi 1999). This additional component is often referred to in the literature as the *hard tail*. Such high-energy tails have been detected not only in BH LMXBs (e.g. Malzac et al. 2006; Del Santo et al. 2008) but also in several NS systems, including Z-sources (Di Salvo et al. 2006) and bright atoll sources (Paizis et al. 2006). Importantly, hard tails are observed across different accretion regimes and are not exclusive to the soft state (e.g. Fiocchi et al. 2006; Paizis et al. 2006; Bouchet et al. 2009; Del Santo et al. 2013).

Hard state

In the hard state, the X-ray spectra of accreting compact objects are typically described by a power-law with photon index $\Gamma \simeq 1.5$–2.0, often accompanied by a high-energy cutoff above ~ 10 keV. In BH LMXBs, these spectral properties are well reproduced by thermal Comptonization models, with coronal electron temperatures $kT_{\rm e} \sim 70$–120 keV (see, e.g. Done et al. 2007). In contrast, NS systems generally exhibit cooler coronae (e.g. Done & Gierliński 2003; D'Aì et al. 2010; Di Salvo et al. 2019), partly due to the additional

soft-photon reservoir provided by the stellar surface and boundary layer. The seed photons participating in the Comptonization process may originate from several regions: synchrotron photons generated within the corona itself (this possibility has been discussed in various hybrid coronal models), the thermal emission of the accretion disc, or—when the accretor is a NS—the boundary layer and the stellar surface.

In systems hosting a NS, two broad interpretations were originally proposed for the accretion geometry: one in which a compact corona surrounds the star and comptonizes seed photons from the surface and boundary layer (Mitsuda et al. 1989), and another in which the corona is more extended and primarily intercepts disc photons (White et al. 1988), with later revisions including an additional contribution from the stellar surface (Church & Bałucińska-Church 2004). Timing studies generally favour the former scenario (Churazov et al. 2001), and the presence of a hot stellar surface provides an extra cooling mechanism that naturally produces softer spectra than in BH systems (Done & Gierliński 2003). Since my focus in this thesis is on BH accretors, I do not explore these models in detail here, and refer the interested reader to the above works for a more comprehensive discussion.

At soft X-ray energies, the spectrum sometimes includes a cool blackbody-like component. In BH LMXBs, this is usually interpreted as emission from a truncated accretion disc with $kT_{\rm disk} \lesssim 0.5$ keV (e.g. Di Salvo et al. 2001; Miller et al. 2006; Buisson et al. 2019). For NS systems, the same soft component may instead arise from the boundary layer or the stellar surface (e.g. Lin et al. 2007; Armas Padilla et al. 2017). The overall spectral behaviour in the hard state is commonly explained for BH LMXBs, within the framework of the *truncated disc* paradigm. In this scenario, the optically thick disc retreats to radii significantly larger than the ISCO, contributing mainly as a provider of seed photons, while the innermost region is filled with a hot, optically thin and radiatively inefficient flow (Esin et al. 1997), as illustrated in Fig. 1.12. This model is supported by spectral fits (e.g. Gilfanov et al. 1999; Basak et al. 2017), as well as by timing diagnostics such as X-ray reverberation lags (De Marco et al. 2015, 2021) and the behaviour of type-C quasi-periodic oscillations (QPOs) (e.g. Ingram et al. 2016).

However, the truncated-disc scenario is not universally accepted. Several studies have reported the presence of broad Fe K emission lines in hard-state BH LMXBs, implying very small inner disc radii—sometimes consistent with the ISCO—thus suggesting that the accretion disc may extend close to the compact object even in the hard state (e.g. Miller et al. 2006; Tomsick et al. 2008; García et al. 2015; Kara et al. 2019). Within this framework, a variety of alternative coronal geometries have been proposed. These include compact X-ray sources located on the rotational axis above the BH (the so-called lamppost geometry; Matt et al. 1991), magnetically heated and spatially inhomogeneous active regions distributed above the disc surface (the "patchy corona"; Haardt et al. 1994; Nayakshin 2000), as well as more extended slab- or wedge-like coronae. In some models, part of the hard X-ray emission may also originate from the base of a relativistic jet.

Recent X-ray polarimetric measurements have provided new and independent constraints on the coronal geometry. Krawczynski et al. (2022), using IXPE observations of Cygnus X–1, found that the polarization properties are inconsistent with a compact, vertically collimated corona, instead favouring a configuration in which the corona is extended parallel to the accretion disc. Consistently, Mastroserio et al. (2025) showed that the coronal emission is best described by a horizontally extended structure lying in the plane of the accretion disc. A schematic overview of these proposed configurations and their possible combinations is shown in Fig. 1.13.

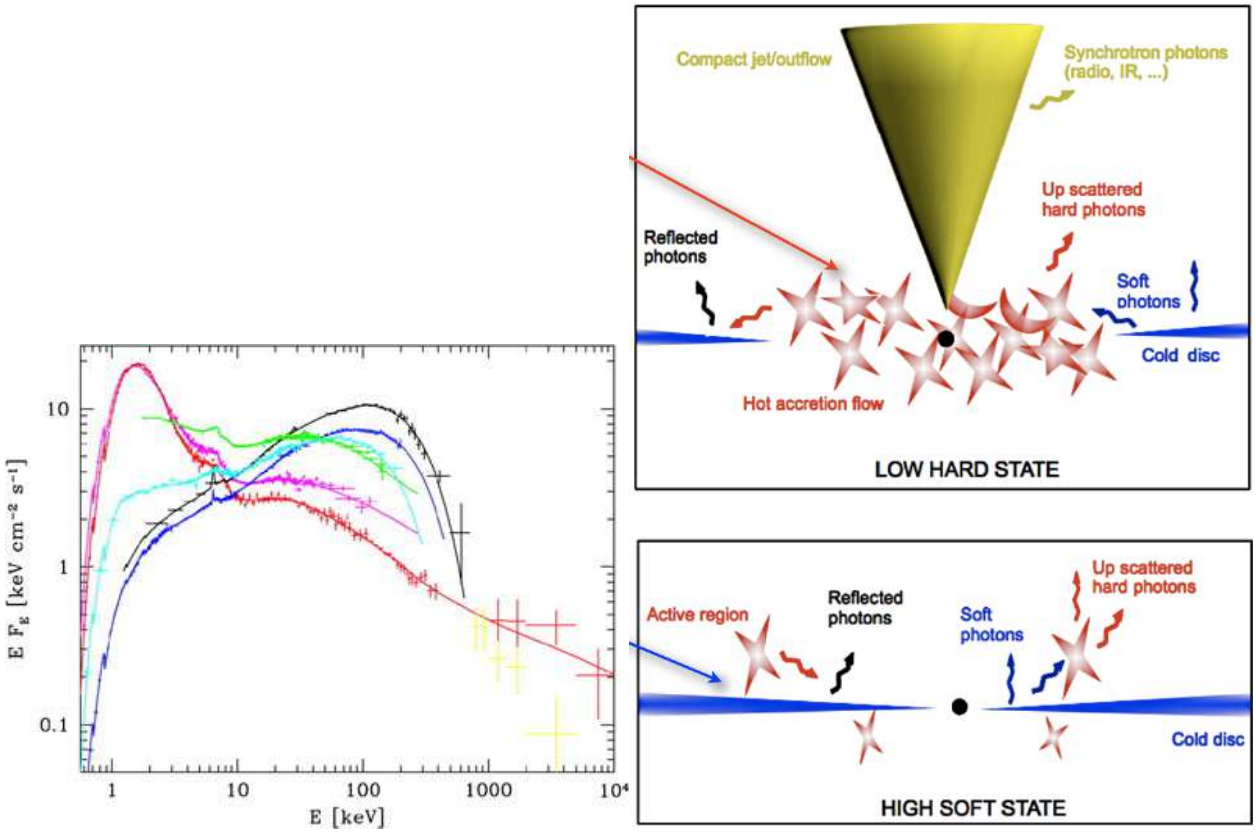

Figure 1.12: Broadband X-ray spectra and schematic accretion geometries for a black-hole XRB in the *low/hard* and *high/soft* states. **Left:** representative SEDs, where the black and blue spectra correspond to the low/hard state, dominated by hard Comptonized emission, while the magenta and red spectra represent the high/soft state, characterized by a strong thermal disc component. **Right:** qualitative cartoons of the corresponding configurations, with a truncated cold disc and hot inner flow (often associated with a compact jet/outflow) in the low/hard state, and a disc extending close to the compact object with a weaker coronal region in the high/soft state. Adapted from Zdziarski et al. (2002).

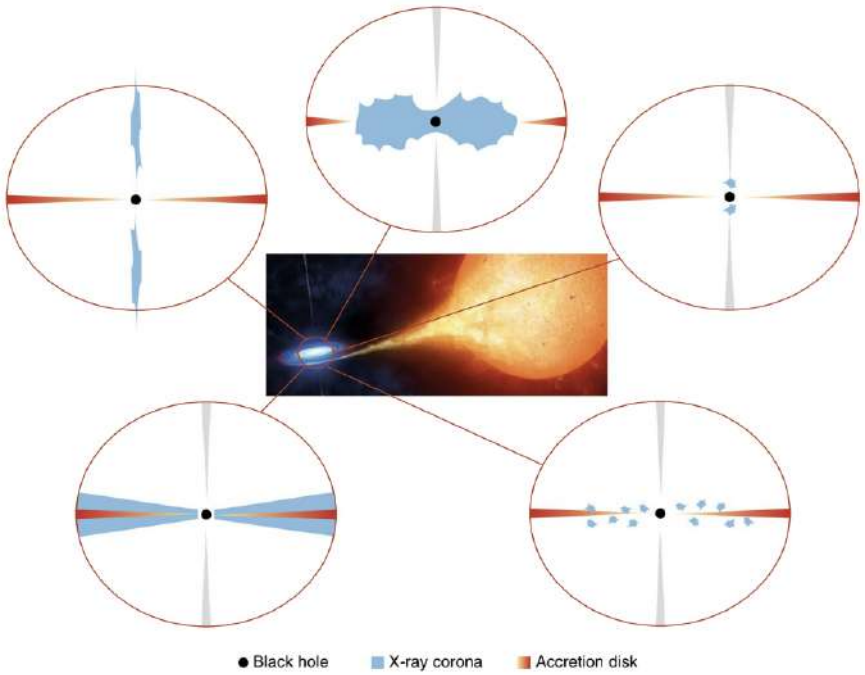

Figure 1.13: Examples of proposed geometries for the inner accretion flow in XRBs and AGNs. Clockwise from the top: a hot inner flow surrounded by a truncated accretion disk, a compact lamppost geometry, compact magnetically active regions distributed across the disk, an extended slab or wedge-shaped corona, and extended jet emission. In all panels, the non-thermal X-ray–emitting region is shown in light blue, the accretion disk in red and yellow, and the jet in grey. Various combinations of these geometrical configurations have also been explored. Credit: central image courtesy of Stocktrek Images, Inc. / Alamy Stock Photo.

Intermediate states

Between the hard and soft states, LMXBs often pass through an *intermediate state*, during which the spectral properties display a mixture of the two regimes. In this phase, the spectrum typically shows thermal Comptonization produced in a corona cooler than in the hard state, together with a disc component that is present but not yet dominant (e.g. Done et al. 2007). Within the framework of the truncated-disc scenario, this behaviour can be interpreted as a gradual inward motion of the disc. As the inner radius decreases, the geometrically thin disc increasingly overlaps with the hot inner flow, enhancing Compton cooling and progressively reducing the coronal temperature. Once the inner disc reaches the ISCO, the optically thin plasma collapses into an optically thick configuration, and the system settles into the soft state. In BH binaries, the transition through the intermediate state is also tied to a critical luminosity threshold: once the accretion power exceeds $\sim 0.1\, L_{\rm Edd}$, both thermal and non-thermal components contribute significantly to the spectrum. Although NS systems are believed to undergo qualitatively similar transitions, intermediate states are detected far less frequently (e.g. Marino et al. 2019). Their outbursts evolve more rapidly than those of BHs—often on timescales of only a few days (Muñoz-Darias et al. 2014)—which likely hampers the observational coverage required to characterise these phases. The physical origin of this difference remains a topic of active investigation.

Recent developments have further refined our understanding of transitional behaviour. X-ray reverberation studies, for instance, have shown that the corona can contract markedly during the hard-to-soft transition (e.g. Kara et al. 2019; De Marco et al. 2021; Wang et al. 2021), while multi-wavelength campaigns have revealed complex coupling between disc, and corona on short timescales. These results point toward a dynamic

restructuring of the innermost accretion flow as systems progress through the intermediate state.

1.10 Outflows in LMXBs

Accretion is only one side of the life cycle of X-ray binaries. These systems also expel matter through powerful outflows, most notably disc winds and relativistic jets. Such ejection processes influence the long-term evolution of the binary and, in some cases, impact the surrounding medium. Observationally, some form of outflow is detected in nearly every accretion state, underscoring the close coupling between accretion and ejection. High-inclination XRBs accreting at luminosities of $L_{\rm X} \gtrsim 0.5\,L_{\rm Edd}$—typically during soft spectral states—frequently show narrow absorption features from highly ionised species, most prominently He-like and H-like iron (Done et al. 2007). The blue shifts of these lines, corresponding to outflow velocities of a few hundred km s^{-1}, provide direct evidence for accretion-disc winds. Such winds have been observed across a wide variety of systems, including both high- and low-mass XRBs, and in binaries hosting either NSs or BHs (e.g. Ueda et al. 1998; Díaz Trigo et al. 2006; Ponti et al. 2014; Pinto et al. 2020). Their appearance at high luminosities, when the thermal disc emission dominates the X-ray spectrum, strongly suggests a disc origin. The physical origin of these winds is still debated: they may arise from thermal driving (Begelman & McKee 1983) or from magnetocentrifugal acceleration (e.g. Proga 2003). Recent radiation-MHD simulations further indicate that multiple driving mechanisms may coexist, with magnetic launching becoming increasingly important at higher accretion rates or in the presence of strong magnetic fields (see Chapter 3).

A second major channel of mass ejection is represented by relativistic jets, which dominate the broadband emission of XRBs from the radio to the IR. The SED of LMXBs extends far below the optical and X-ray bands, into the radio regime, where the emission cannot be produced by the accretion disc or, in the case of NS systems, by the stellar surface. Instead, the radio–IR component is now firmly established as synchrotron radiation from relativistic particles in a collimated outflow, called jets (Baade & Minkowski 1954), (usually) along the axis of rotation of the system. The "jet interpretation" is supported by the non-thermal shape of the radio–IR spectrum and by the very high brightness temperatures inferred, which require emission regions far bigger than the size of the binary itself. High-resolution radio imaging has directly resolved such jets in several systems: compact, elongated structures extending over tens of astronomical units have been observed in BH binaries like Cyg X–1 (Stirling et al. 2001) and GRS 1915+105 (Dhawan et al. 2000; Fuchs et al. 2003), as well as in NS systems such as Sco X–1 (Fomalont et al. 2001).

Jets are present during most phases of outburst evolution: steady, compact jets are typically associated with hard spectral states, while transient, highly relativistic ejections are often launched during intermediate states. I will discuss winds and their launching mechanisms in more detail in Chapter 3, and I will treat jet formation and properties in Chapter 4.

1.10.1 Traces of jets: the radio–X-ray correlation

Even though jets and accretion flows dominate different regions of the electromagnetic spectrum, they remain tightly connected. In BH LMXBs—and in a subset of NS systems (e.g. Gusinskaia et al. 2017)—compact, steady jets are observed only in the hard and intermediate states, while the radio emission is strongly suppressed in the soft state (Fender et al. 1999; Corbel et al. 2000). This "quenching" is generally interpreted as the disappearance (or radiative dimming) of the compact jet during the soft state (Drappeau et al. 2017).

Only a handful of BH systems appear to deviate from this behaviour (e.g. Gallo et al. 2004; Brocksopp et al. 2005). In contrast, neutron-star LMXBs often retain radio emission even in soft states (e.g. Migliari et al. 2004), although typically at a lower level than BHs. Despite these differences, a broad connection between accretion and ejection is evident across LMXBs. The jet is believed to originate within a few hundred gravitational radii of the compact object (Gandhi et al. 2017), i.e. the same region responsible for most of the X-ray emission. A powerful way to investigate this coupling is through radio–X-ray luminosity diagrams ($L_{\rm R}$–$L_{\rm X}$). While such empirical correlations provide strong evidence for a coupling between accretion and ejection, their physical interpretation remains debated. In particular, standard hot-flow models developed to explain the X-ray emission, such as ADAFs, do not naturally predict the presence, suppression, or scaling of jets with accretion power. This limitation becomes especially relevant when addressing the radio–X-ray correlation and the quenching of compact jets in soft states. In this context, the Jet Emitting Disc–Standard Accretion Disc (JED–SAD) framework (Ferreira et al. 2006; Marcel et al. 2018b,a, 2019, 2022) offers a physically motivated approach to link accretion and jet production. In this model, the accretion flow is radially stratified into an outer, radiatively efficient Shakura–Sunyaev disc and an inner, strongly magnetized jet-emitting disc capable of launching magneto-centrifugal outflows. Variations in the relative radial extent of these two regions and in the mass accretion rate naturally regulate both the X-ray emission and the jet power, providing a unified framework to interpret the observed radio–X-ray coupling and jet quenching across spectral states. Two decades of coordinated multi-wavelength monitoring, predominantly for BHs, have produced an increasingly rich dataset (e.g. Bassi et al. 2019; Gallo et al. 2018). In BH LMXBs, sources typically cluster along two tracks of the form $L_{\rm R} \propto L_{\rm X}^{\beta}$, with $\beta \simeq 0.6$ for "radio-loud" systems and $\beta \simeq 1.4$ for "radio-quiet" ones (Corbel et al. 2013). This dichotomy may reflect differences in the accretion flow (Coriat et al. 2011) or in the jet physics (Espinasse & Fender 2018). NS systems show a similar behaviour but with larger scatter and systematically weaker radio output, being typically ∼30 times fainter in the radio band than BHs at the same $L_{\rm X}$ (Fender 2001; Gallo et al. 2018). Whether this reflects intrinsically weaker jets, or instead differences in compact-object mass, spin (e.g. Migliari et al. 2011), or radiative efficiency (Körding et al. 2006), remains unclear.

1.10.2 Transient sources and the *q*-diagram

As discussed in Section 1.9, XRBs exhibit a range of spectral states that reflect changes in the geometry, luminosity and optical depth of the accretion flow. Each state is also associated with a specific pattern of mass ejection, such as disc winds in the soft state and compact or transient jets in hard and intermediate states, respectively. Having outlined these building blocks, it is now possible to describe how accreting systems evolve through them over an outburst cycle.

Most X-ray binaries (XRBs) do not accrete persistently; instead, they spend the majority of their lifetime in a faint, low-luminosity phase known as *quiescence*, typically characterized by $L_{\rm X} \lesssim 10^{34}\,{\rm erg\,s^{-1}}$ for NS LMXBs and $L_{\rm X} \lesssim 10^{33}\,{\rm erg\,s^{-1}}$ for BH XRBs. During quiescence, accretion onto the compact object is strongly suppressed and the inner accretion flow is expected to be radiatively inefficient and geometrically thick. Occasionally, these systems undergo dramatic episodes of enhanced accretion, known as *outbursts*, during which the X-ray luminosity can increase by several orders of magnitude. Transient sources are thus observed to alternate between quiescence and outburst phases (last from weeks to months). An outburst typically follows a well-defined evolutionary pattern, during which the source transitions through distinct accretion states. These state changes are commonly interpreted in terms of progressive modifications of

the geometry of the inner accretion flow, involving a reconfiguration of the relative extent of the accretion disc, hot flow, corona, and jet. As the outburst develops, the accretion disc is thought to move inward toward the compact object, while the hot inner flow or corona changes its size, shape, and coupling to the disc. Conversely, during the decay phase, the system gradually returns to a geometry resembling that of quiescence. Although the physical drivers of these transitions—such as variations in the mass accretion rate and the presence of hysteresis—will be discussed in detail later, this geometric evolution provides a useful framework to describe the phenomenology of outbursts in XRBs. This behaviour is usually interpreted within the framework of the Disc Instability Model (DIM; see Lasota 2001 for a review), in which a cool, partially neutral accretion disc gradually accumulates mass transferred from the companion star. As the surface density and temperature increase, the disc undergoes a thermal–viscous instability: a sudden rise in temperature and opacity triggers a heating front that propagates through the disc, driving a rapid increase in the mass-accretion rate $\dot{M}$ and launching the system into outburst. The increase in $\dot{M}$ is expected to be accompanied by a substantial reconfiguration of the inner accretion flow. At low $\dot{M}$, the accretion disc is thought to be truncated at large radii and replaced in the inner regions by a hot, radiatively inefficient flow or an extended corona. As $\dot{M}$ rises during the outburst, the disc progressively moves inward toward the compact object, while the hot flow or corona becomes more compact and more efficiently coupled to the disc. During the decay phase, as $\dot{M}$ decreases, the inner disc is expected to recede again, and the system gradually returns to a geometry characteristic of quiescence (Fig. 1.12). Although this picture provides a useful qualitative framework, it is insufficient to fully explain the observed phenomenology of XRB outbursts. In particular, the fact that state transitions occur at different luminosities during the rise and decay phases—commonly referred to as hysteresis (Zdziarski et al. 2004)—cannot be naturally reproduced within the standard DIM. This indicates that, in addition to changes in $\dot{M}$, other physical processes and geometric effects must play a key role in governing the evolution of the inner accretion flow. These issues will be discussed in detail in the following sections.

BH LMXBs are almost exclusively transient (Remillard & McClintock 2006), while NS LMXBs may be either persistent or transient depending on their mass-transfer rate and disc size. When a transient source leaves quiescence, it usually follows a characteristic sequence of spectral states. The rise begins in the hard state (i), with the luminosity increasing by several orders of magnitude ($L_X \sim 10^{36-39}$ erg s^{-1} for BHs, while slightly lower values are typically reached by NSs, $L_X \sim 10^{36} - 2 \times 10^{38}$ erg s^{-1}). The source then moves to an intermediate state (ii), and eventually reaches a soft state (iii) at roughly the same bolometric luminosity. As the outburst decays, the path is retraced in reverse order—soft (iv), intermediate, and finally hard (v)—but at *lower* luminosity. This asymmetric behaviour is showed in Fig. 1.14.

In a hardness–intensity diagram (HID), where the X-ray count rate is plotted against a hard-to-soft colour ratio, this evolution traces the so-called q-shaped (Homan et al. 2001; Belloni et al. 2006) which is always run anti-clockwise (see Fig. 1.14). The jet properties follow this path as well: compact, steady jets are present during the hard and hard-intermediate states and are suppressed upon entering the soft state. During the return to the hard state, the system crosses the so-called "jet line", where the compact outflow reappears (Homan & Belloni 2005; Fender et al. 2005). A similar hysteretical behaviour emerges in the rms–intensity diagram (RID), where variability amplitude replaces spectral hardness (Muñoz-Darias et al. 2011 and see Fig. 1.15).

Since most of the aperiodic variability originates in the hot inner flow or corona (e.g. Done et al. 2007), hardness and variability remain strongly correlated. QPOs (i.e. narrow peaks in the power density spectrum indicating variability components with preferred characteristic frequencies) also evolve systematically along the loop and are central to state identification (I will discuss it in the next section). Atoll sources exhibit

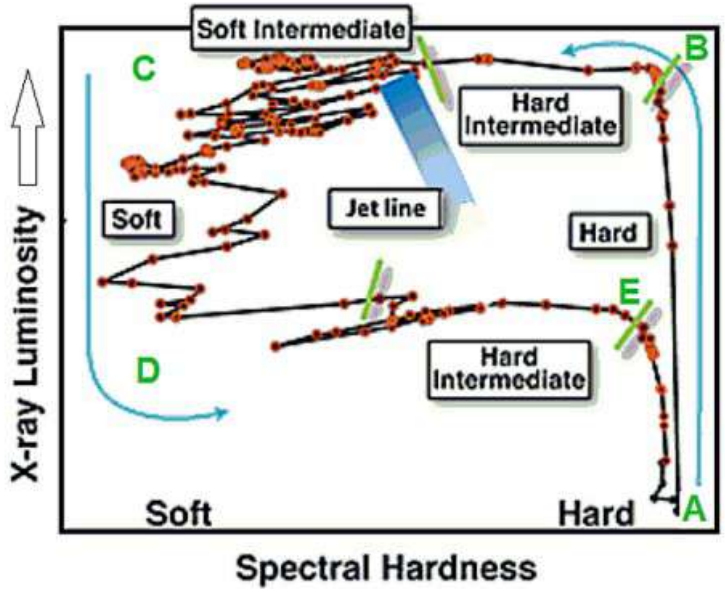

Figure 1.14: Schematic representation of the "q"-shaped curve in a hardness intensity diagram for black-hole X-ray binaries (adapted from Homan & Belloni 2005).

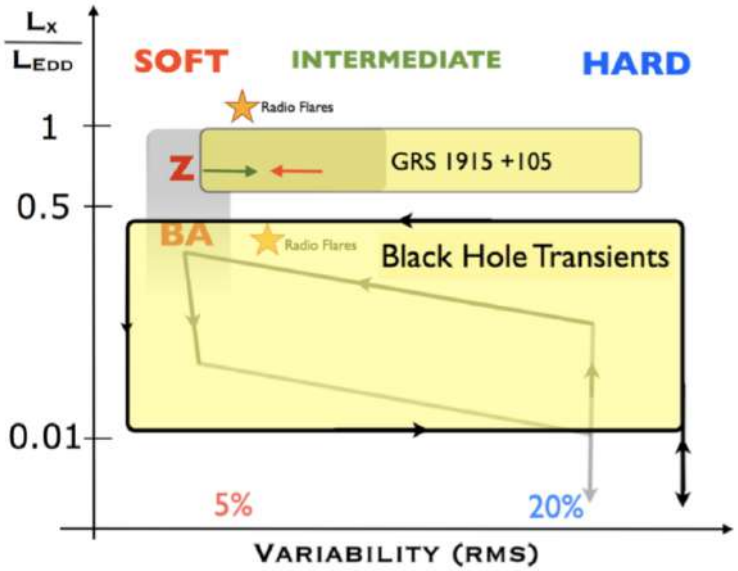

Figure 1.15: Sketch describing the qualitative behaviour of atolls (labelled as A), bright atolls (BA), Z sources (Z) and BH transients in RID (Muñoz-Darias et al. 2014)

analogous hysteretical cycles—both in transient and persistent NS LMXBs—but with notable differences (Muñoz-Darias et al. 2014): their tracks are often more diagonal than horizontal, hard states are less variable than in BH binaries, and transitions occur on much shorter timescales. A plausible explanation is the additional cooling provided by the NS surface, which reduces the coronal temperature and suppresses variability. While most BH XRBs follow the full q-diagram, several BH systems have displayed "failed outbursts", never reaching the soft or even the hard-intermediate state (e.g. Ferrigno et al. 2012; Del Santo et al. 2016; Bassi et al. 2019). The physical origin of these incomplete cycles as well as that of the canonical outburst, remains an open question.

New observations suggest that large-scale magnetic flux may strongly influence outburst evolution. MAXI J1820+070 exhibited optical and radio delays relative to X-rays, interpreted as evidence for Magnetically Arrested Discs (MADs) formation during the hard-to-intermediate transition (You 2024). This introduces magnetic flux accumulation as a potential regulator of state transitions. High-throughput timing missions (NICER, XMM-Newton, NuSTAR) now detect X-ray reverberation lags even in the early hard state of BHs, implying a disc extending close to the ISCO earlier than previously thought. Time-resolved reverberation has measured evolution in coronal height throughout outbursts (Kara et al. 2019; De Marco et al. 2021). This directly probes the geometry changes that drive the q-diagram evolution.

1.11 Timing analysis

XRBs are characterized by an extraordinary level of variability on very short time-scales, down to milliseconds in the case of stellar-mass BHs and NSs. Such rapid variability, extensively revealed by missions like *RXTE* (Bradt et al. 1993), indicates that a significant fraction of the X-ray emission originates in the innermost regions of the accretion flow, close to the compact object. Importantly, both the amplitude and characteristic time-scales of the variability are found to depend strongly on the spectral state of the source, pointing to a close connection between variability properties and the geometry and physical conditions of the accretion flow. In particular as shown in the RID (Fig. 1.15), during hard and hard-intermediate states, XRBs exhibit strong aperiodic variability, with fractional rms amplitudes typically reaching ~20–40%, together with prominent QPOs. As the source transitions toward softer states, the overall variability level decreases dramatically: in the soft state, the fractional rms is usually below a few per cent, and the Power Density Spectrum (PDS) is dominated by weak, steep red noise (e.g. Belloni et al. 2005; Remillard & McClintock 2006; Gilfanov 2010). The investigation of both periodic and aperiodic variability—generally referred to as *timing analysis* (see the review by Gilfanov 2010)—is therefore a key diagnostic tool in the study of XRBs. Timing analysis is commonly performed through the construction of PDS, in which the variability power (i.e. the amplitude of variability) of a light curve is decomposed as a function of Fourier frequency. This approach enables the identification of coherent or quasi-coherent signals, such as QPOs, as well as broad-band noise components associated with stochastic accretion processes.

Mathematically, if a source is observed for a time interval Δt divided into N bins, the Fast Fourier Transform is defined as (van der Klis 1989):

$$X_j = \sum_{k=0}^{N-1} x_k \, e^{2\pi j k/N}, \qquad j = -\frac{N}{2}, \ldots, \frac{N}{2} - 1, \tag{1.19}$$

where x_k is the number of counts in the k-th bin and X_j is the Fourier coefficient at frequency $\omega_j = 2\pi j/(N\Delta t)$.

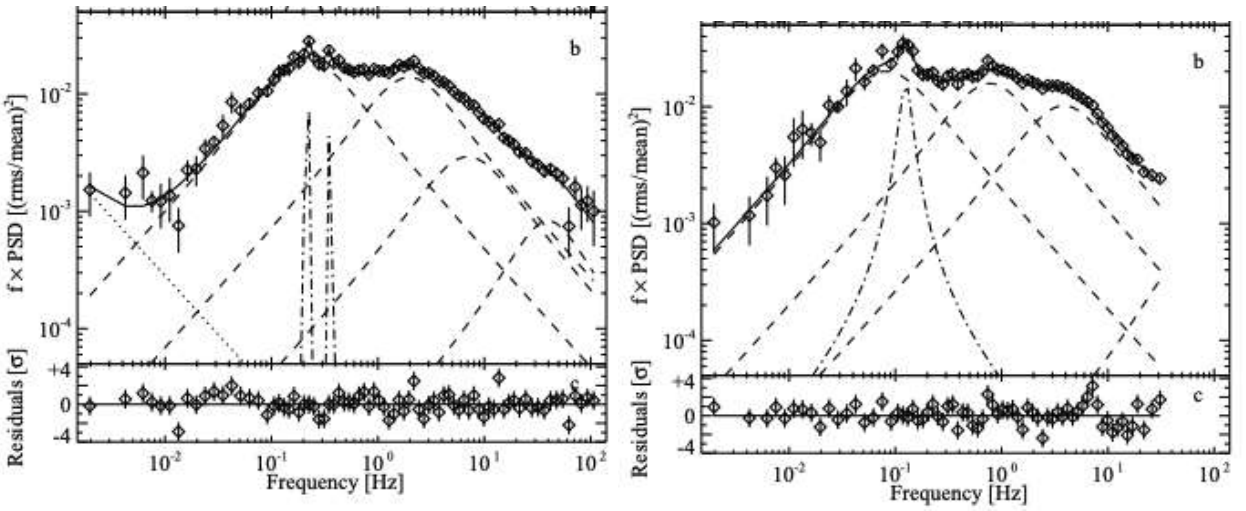

Figure 1.16: **Left:** Examples of PDS of Cyg X–1 in the hard state. The upper panel shows the $\nu P(\nu)$ representation, where the characteristic peak frequencies of the broad and narrow Lorentzian components become evident; the lower panel displays the corresponding residuals of the multi-Lorentzian fit. **Right:** Another representative hard-state PDS from Cyg X–1, modelled with a combination of broad and narrow Lorentzian components. Both examples are adapted from Pottschmidt et al. (2003).

The PDS is then given by $P_j = A|X_j|^2$, with A a normalisation factor. Each spectral state exhibits characteristic timing signatures (see van der Klis 2004). In the hard state of BH LMXBs, PDS typically show broad, flat-topped noise in $\nu P(\nu)$, with a low- and high-frequency breaks and several (usually 4–5) Lorentzian components (Psaltis et al. 1999). NS XRB systems displaying flatter BH-like PDS and particularly strong hard-state variability occupy an extension of the island branch in the color–color diagram and are sometimes classified as *Extreme Island State* (EIS; Méndez & van der Klis 1997; van Straaten et al. 2003). During the transition from hard to soft state, both in BH and NS LMXBs, the characteristic frequencies of the Lorentzians shift progressively to higher values. Once they reach ~ 5 Hz, the corresponding components sharply decrease in amplitude and width (e.g. Pottschmidt et al. 2003; Kalemci et al. 2006). In addition to broad-band noise, PDS often exhibit narrow peaks—*QPOs*—detected in both BH and NS binaries (for a recent overview, see Ingram & Motta 2019). In BH systems, QPOs are commonly divided into *low-frequency* (below 30 Hz) and *high-frequency* (above 60 Hz), with low-frequency QPOs further classified into three types (A, B, C) according to their coherence, amplitude, and spectral state (Casella et al. 2005). Type–A QPOs are detected during the soft end of hard–to–soft transitions, type–B QPOs are typically associated with soft–intermediate states, whereas type–C QPOs—the most frequent and widely studied class—are observed in hard and hard–intermediate states (see e.g. Fig. 1.16).

NS systems display analogous behaviour, but also show additional variability components, such as hectohertz QPOs and kilohertz QPO pairs, the latter never observed in BH binaries (van der Klis 2006).

I refer the reader to Ingram & Motta (2019) for a comprehensive overview of the current theoretical framework for QPOs. A detailed treatment of variability in X-ray binaries lies beyond the scope of this thesis; however, it is important to highlight that the observed evolution of timing properties closely follows the expected behaviour within the truncated–disc scenario. If the characteristic Lorentzian frequencies correspond to dynamical timescales at specific radii in the flow, their shift to higher frequencies during the hard-to-soft transition implies that the truncation radius decreases, i.e. the disc gradually approaches the ISCO.

1.12 X-ray polarimetry as a probe of accretion geometry

Until recently, the geometry of the inner accretion flow in XRBs could only be inferred indirectly through spectroscopy, timing, and occasionally reverberation mapping. A major breakthrough came with the launch of the *Imaging X-ray Polarimetry Explorer* (IXPE; Weisskopf 2022), which opened a completely new observational window: X-ray polarimetry. By measuring the degree and angle of linear polarization, IXPE allows us to directly probe the geometry, optical depth, and emission mechanisms of accretion flows, coronae, and jets.

Thermal emission from a geometrically thin accretion disc is predicted to be weakly polarized ($\sim 1-5\%$) with a polarization angle perpendicular to the disc plane due to electron scattering in a plane-parallel atmosphere (Chandrasekhar 1960). In contrast, Comptonized emission from an optically thin corona produces higher polarization degrees whose angle depends sensitively on the coronal geometry. For instance, slab-like coronae yield polarization vectors parallel to the disc, while compact or spherical coronae produce lower polarization fractions and weaker angular dependence (Poutanen & Svensson 1996). IXPE observations have now directly confirmed these expectations. In the hard state of several BH XRBs, the measured polarization angle is aligned with the radio jet axis, supporting models in which the corona is elongated or vertically extended in a plan perpendicular to the jet axis, i.e. above the disc (see e.g. Krawczynski et al. 2022; Veledina et al. 2023). In soft states, polarization degrees drop significantly, consistent with domination by thermal disc photons (e.g. Chandrasekhar 1960; Titarchuk et al. 2025).

Polarimetric studies also provide insight into how geometry evolves during state changes. For example, a comparative IXPE study of the HMXB Cyg X–1 and the LMXB Swift J1727.8–1613 across different accretion states showed that in addition to the increase of the polarization degree with energy, the polarization angle remains remarkably stable and aligned with the radio jet in both states (Brigitte & Svoboda 2025). The similar polarimetric behaviour observed in systems with very different donor stars suggests that the geometry of the innermost accretion flow and corona is largely independent of the nature of the companion.

Regarding the X-ray polarimetry in NS systems, a highly significant polarization signal has been detected in the accreting pulsar Hercules X–1, allowing constraints on the spin and magnetic geometry (Doroshenko et al. 2022), while spectro-polarimetric measurements of the atoll source 4U 1820–303 reveal an energy-dependent polarization pattern consistent with a geometrical separation between disc emission and a harder component likely produced in the boundary or spreading layer (Di Marco et al. 2023).

2

Accretion disk and optical Spectroscopy of MAXI J1305–704

2.1 Accretion disk winds

In Sect. 2.10, I introduced disc winds as one of the principal mass-loss channels in accreting XRBs, alongside relativistic jets. In this chapter, I focus explicitly on disc winds, discussing their observational properties and physical interpretation in BH systems. Relativistic jets, which dominate the hard state and carry energy through highly collimated outflows, will instead be addressed in detail in Chapter 4.

High-resolution X-ray spectroscopy provides the most direct observational evidence for these winds, which manifest as blue-shifted absorption features of highly ionised species—most notably Fe XXV and Fe XXVI—with characteristic velocities of order 10^3 km s^{-1} (e.g. Lee et al. 2002; Neilsen et al. 2009; Ponti et al. 2012) as illustrated in Fig. 2.2. In several sources, including GRS 1915+105, the absorption profiles occasionally display P-Cygni signatures, consisting of a blue-shifted absorption component and a redshifted emission wing, is the hallmark of an expanding wind (Fig. 2.1). The absorption originates from material moving toward the observer, while the emission is produced by gas receding away, coming from reprocessed emission from the wind itself.

Disc winds are detected preferentially in high-inclination systems and are nearly ubiquitous during soft states, whereas they are strongly suppressed during hard states, supporting the picture of an equatorial geometry for the outflow (Ponti et al. 2012; Parra et al. 2024) and see Fig. 2.3. Moreover, their appearance is often anti-correlated with jet activity, suggesting that the accretion flow regulates the competition between different ejection channels.

As shown by Lee et al. (2002), simple calculations indicate that the wind could have a significant impact on the accretion process. The strength of an absorption line provides a direct estimate of the number of absorbing ions along the line of sight. In particular, from the measured equivalent width W_λ of a given transition, one can infer the ionic column density N_j pf every species (in cm^{-2}) through the relation:

$$\frac{W_\lambda}{\lambda} = 8.85 \times 10^{-13}\, \lambda\, f_{ij}\, N_j,$$

where λ is the transition wavelength (in centimetres) and f_{ij} is the oscillator strength describing the probability of absorption between the lower and upper energy levels i and j. This expression applies under the assumption

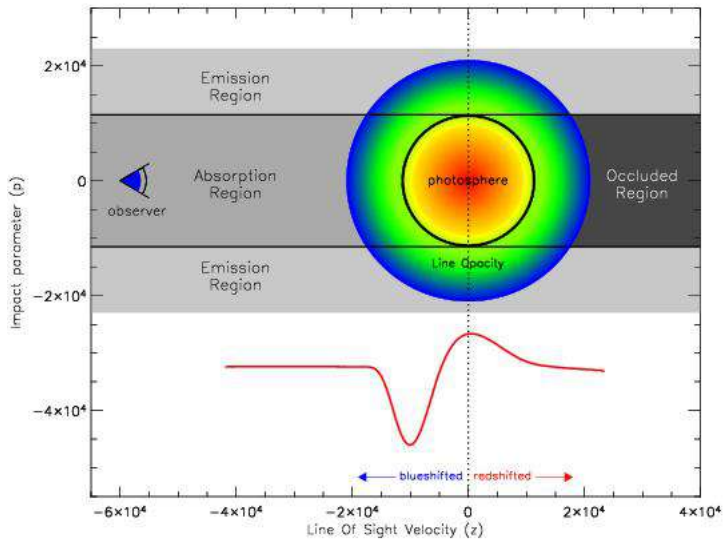

Figure 2.1: Schematic representation of the formation of P-Cygni profiles in an expanding outflow. Blue-shifted absorption arises from material moving toward the observer, while the red-shifted emission is produced by gas moving away.

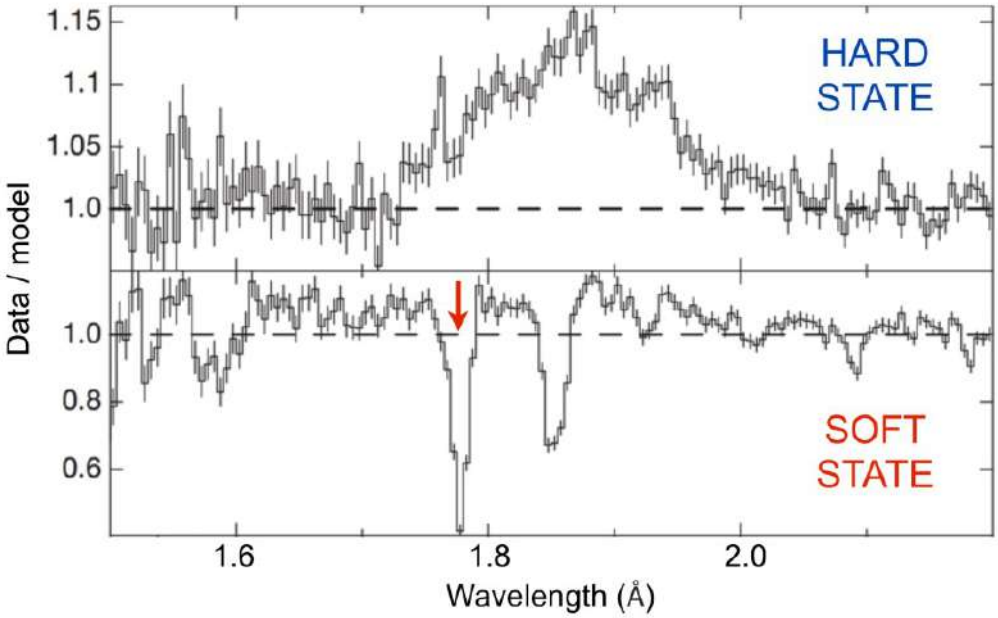

Figure 2.2: Example of accretion disc wind variability in the BH binary GRS 1915+105. During the soft state (middle and bottom panels), multiple absorption features are detected, including a prominent blueshifted Fe XXVI line (indicated by the red arrow). In contrast, the hard state spectrum (top panel) shows no absorption features but displays a broad Fe XXV emission line. Adapted from Fender & Muñoz-Darias (2016); see also Neilsen et al. (2012).

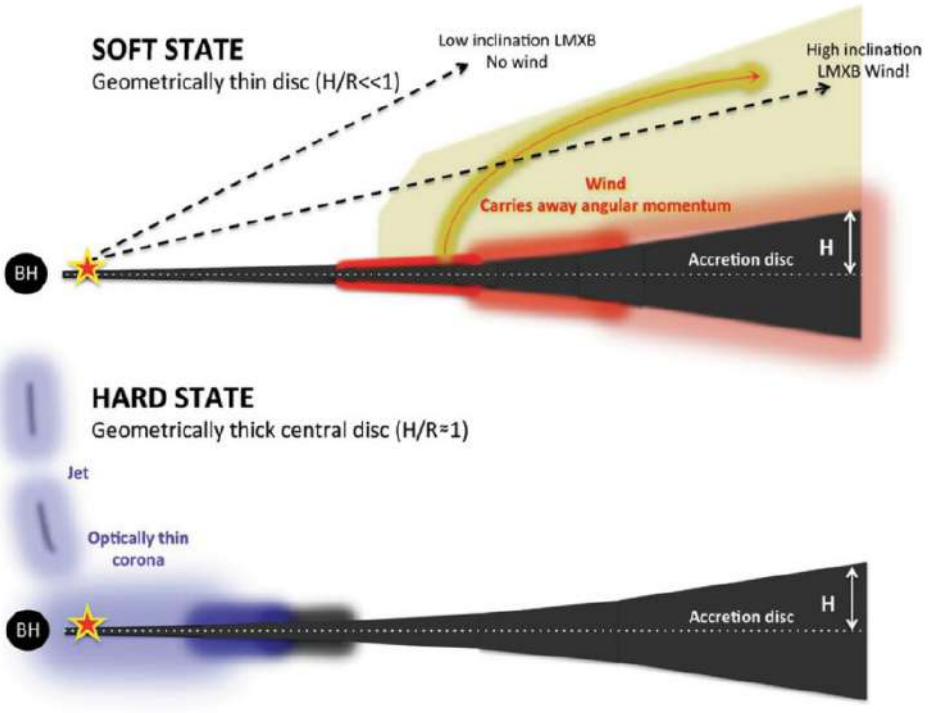

Figure 2.3: Schematic illustration of the thermal wind scenario across different accretion states. During the soft state, strong irradiation of the outer accretion disc heats the gas and drives a thermally induced wind, whereas in the hard state the reduced irradiation prevents significant outflow formation. Adapted from Ponti et al. (2012).

that the absorption line lies in the linear regime of the curve of growth, i.e. the line is optically thin and not saturated, so that the equivalent width increases linearly with column density. The relative strengths of the Fe XXV and Fe XXVI absorption lines can be used to constrain the physical conditions of the outflowing plasma. By comparing their measured ratio with photoionization models (e.g. Kallman & Bautista 2001), it is possible to estimate the ionization parameter, defined as

$$\xi = \frac{L}{n\, r^2},$$

where L is the ionizing luminosity, n the gas density, and r the distance from the illuminating source (Tarter et al. 1969). This parameter quantifies the degree of ionization of the plasma: higher values correspond to stronger radiation fields or lower densities. In typical disc winds from XRBs, inferred values are around $\xi \sim 10^4$, indicative of highly ionized gas with temperatures exceeding 10^6 K (Fender & Muñoz-Darias 2016).

Once the ionization state is known, one can estimate the amount of mass carried away by the outflow. The mass-loss rate associated with the wind can be expressed as

$$\dot{M}_{\rm wind} = 4\pi\, m_p\, v_{\rm wind}\, \frac{L}{\xi} \left(\frac{\Omega}{4\pi}\right),$$

where m_p is the proton mass, $v_{\rm wind}$ the outflow velocity, and $\Omega/4\pi$ represents the fraction of the sky covered by the wind as seen from the central source (Fender & Muñoz-Darias 2016). For typical wind velocities of the order of 10^3 km s^{-1} and covering angles spanning several tens of degrees, the inferred mass-loss rates can be comparable to, or even greater than the accretion rate itself (Neilsen et al. 2011; Ponti et al. 2012). Simulations

have confirmed this and show that winds have strong angular dependence (Luketic et al. 2010), even if many uncertainties remain. Despite this, the kinetic luminosity associated with the wind ($L_{\rm wind} \propto \dot{M}_{\rm wind} v^2_{\rm wind}/2$) usually remains much lower than the bolometric radiative output, implying that disc winds primarily affect the accretion process through mass removal rather than through their kinetic energy.

Wind launching mechanisms

Several physical mechanisms have been proposed to explain the launching of accretion disc winds in LMXBs, each of them potentially dominant under different accretion states and luminosity regimes (e.g. Begelman & McKee 1983; Proga et al. 2000; Miller et al. 2006; Muñoz-Darias et al. 2016; Tomaru et al. 2023). The three main mechanisms discussed in the literature are:

- **Radiation-pressure driven winds:** at luminosities approaching the Eddington limit, the radiation field can impart momentum to the plasma via thomson scattering. However, the optical and X-ray P-Cygni profiles observed in many systems occur at much lower Eddington ratios ($L \sim 10^{-3}$–$10^{-2} L_{\rm Edd}$), where radiation pressure alone cannot explain the observed outflow velocities ($v_{\rm wind} \sim$ 1000–3000 km s^{-1}). This suggests that radiative driving may only become relevant during brief super-Eddington phases, such as those preceding the so-called nebular stage (Muñoz-Darias et al. 2016).

- **Line-driven winds:** these outflows are accelerated by radiation pressure acting on resonance absorption lines in the UV band. In this mechanism, photons emitted from the disc or the central source transfer momentum to ions through line absorption, predominantly from partially ionized metals such as C IV, N V, and O VI. This process is highly effective in hot, UV-bright environments—such as those found in massive stars and AGN—where the radiation field can efficiently couple to the gas through thousands of metal lines. However, in LMXBs the strong X-ray illumination from the inner accretion flow tends to over-ionize the disc atmosphere, removing most bound electrons and thereby suppressing the UV resonance transitions necessary for line driving. As a result, radiative acceleration through line absorption is expected to be inefficient in these systems (e.g. Proga 2002).

- **Thermal (Compton-heated) winds:** this scenario, originally proposed by Begelman & McKee (1983), arises when the outer disc is irradiated by the central X-ray source, heating the gas until the thermal velocity exceeds the local escape velocity and allowing escape of the X-ray heated matter to infinity. The characteristic launching radius $R_{\rm L}$ corresponds to the region where the Keplerian velocity equals the measured terminal velocity of the wind. For typical velocities $v_{\rm wind}$ = 1500–3000 km s^{-1}, this yields $R_{\rm L} \sim (1.5\text{–}6) \times 10^5$ km. Assuming a standard irradiated disc temperature profile (Frank et al. 2002), the outer disc reaches effective temperatures of $T_{\rm d} \sim (5 \times 10^3\text{–}2 \times 10^4)$ K, consistent with the coexistence of neutral hydrogen and helium in the outflowing gas.

Besides theese mechanisms, **magnetic processes** may contribute to launching and accelerating disc winds. In magnetised accretion flows, large-scale ordered magnetic fields threaded through the disc can remove angular momentum vertically, naturally driving an outflow (Blandford & Payne 1982; Contopoulos & Lovelace 1994; Ferreira 1997; Miller et al. 2006). In this scenario, the wind is accelerated predominantly by the magnetic torque and Lorentz forces, with the poloidal field extracting angular momentum from the disc and the toroidal component providing additional collimation. A key feature of such magnetically–driven winds is that

they are intimately linked to the accretion flow: mass loading, acceleration efficiency and collimation are all controlled by the magnetic field strength and geometry at the disc surface. As a consequence, magnetic winds can in principle carry away a substantial fraction of the accreted mass and angular momentum, potentially exceeding the accretion rate itself at high efficiencies. This contrasts with purely thermal winds, where the mass flux is mainly regulated by the irradiation of the outer disc. However, more recent work by Tomaru et al. (2023) has shown, however, that in at least some cases (e.g. GRO J1655−40), thermal–radiative driving alone can reproduce the observed wind properties, questioning the need for purely magnetic models. Their results also highlight the key role of irradiation and radiative heating in powering disc winds and linking them to the spectral state transitions.

2.2 Optical winds

In the previous section, I introduced the concept of accretion disc winds, mostly traced in the X-ray band and primarily detected during soft accretion states of both BH and NS binaries (e.g. Ponti et al. 2019; Rogantini et al. 2025; Miller et al. 2016; Ponti et al. 2012). Despite their ubiquity at high luminosities, several key questions remained open. In particular, it was unclear whether such outflows persist, weaken, or fundamentally change in nature once the source transitions to the hard state, where X-ray wind features are generally absent. A major step forward has came from the discovery of *optical winds*. These were first unambiguously identified in the BH transient V404 Cygni during its 2015 outburst, when high-quality optical spectra revealed deep, blue-shifted P-Cygni profiles in hydrogen and helium lines (Muñoz-Darias et al. 2016). Crucially, these observations were obtained during phases in which X-ray winds were not detected, suggesting that powerful outflows can be present even when the classical X-ray tracers appear suppressed. Similar optical signatures have since been reported in other systems, predominantly during hard-state phases (e.g. Mata Sánchez et al. 2018; Muñoz-Darias et al. 2019; Cúneo et al. 2020; Mata Sánchez et al. 2022; Panizo-Espinar et al. 2022).

The optical wind phenomenon reveals that outflows can persist even during relatively low X-ray luminosity phases, when the outer disc remains only partially ionized. In this regime, gas temperatures of a few $\times 10^4$ K and terminal velocities of $v_{\rm T} \sim$ 1500–3000 km s^{-1} are typically inferred (Muñoz-Darias et al. 2016; Mata Sánchez et al. 2018). Such velocities are consistent with the escape speeds at radii of $R_{\rm l} \sim 10^5$–10^6 km, indicating that these winds are launched from the outer regions of the accretion disc rather than from its innermost parts. Their detection during the hard state, when X-ray–driven thermal winds are expected to be weak or absent, suggests that optical winds may represent a distinct mass-loss channel operating under cooler and less ionized conditions. The detection of the P-Cygni profiles is strongly modulated by the ionization state of the gas. When the central X-ray luminosity increases, the wind becomes highly ionized, reducing line opacity and causing the absorption components to weaken or disappear. As the flux drops and recombination sets in, the lines re-emerge, often developing into broad emission wings once the ejected material turns optically thin. This transition marks the onset of a so-called "nebular phase," characterized by strong recombination lines with large equivalent widths (up to several thousand Å), tracing the cooling and expansion of the outflowing plasma (Muñoz-Darias et al. 2016; Castro Segura et al. 2022).

The physical mechanism driving these optical winds is still under debate. Their relatively low ionization, large covering factors, and inferred launching radii make radiation pressure via Thomson scattering unlikely. Instead, a thermal wind scenario is favoured, in which the gas is heated by irradiation until its thermal velocity exceeds the local escape speed. The estimated mass-loss rates are substantial — in some cases comparable to

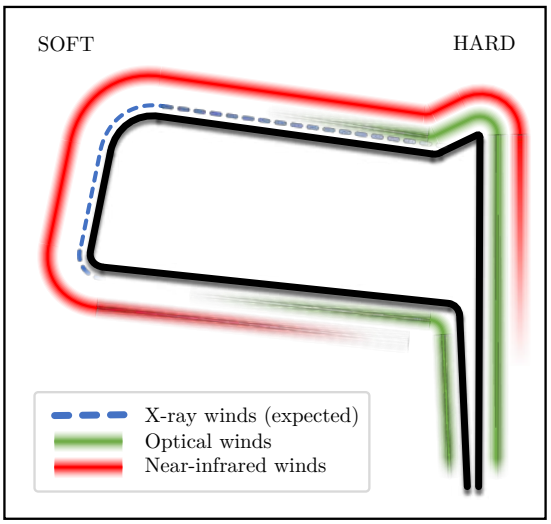

Figure 2.4: Schematic illustration of wind detectability across the hardness–intensity diagram of MAXI J1820+070, adapted from Muñoz-Darias et al. (2019) and Sánchez-Sierras & Muñoz-Darias (2020). The shaded regions indicate the approximate locations where wind signatures have been detected at optical and near-infrared wavelengths. The outburst phases most favourable to the detection of X-ray winds, based on Ponti et al. (2012), are highlighted by the dashed blue contour.

the contemporaneous accretion rate — suggesting that such winds can deplete the outer disc and even quench the outburst prematurely by disconnecting the inner accretion flow from its mass reservoir (Muñoz-Darias et al. 2016; Mata Sánchez et al. 2018; Tetarenko et al. 2018; Castro Segura et al. 2022).

Since this discovery, analogous features have been found in several systems, not only as P-Cygni profiles but also as broad wings (as I mentioned before) or flat-top lines, all signatures of out-flowing gas (see Panizo-Espinar et al. 2022). In particular, flat-top or box-shaped emission lines are naturally produced by radially expanding gas distributions. In such a geometry, each projected velocity between $-V_{\rm max}$ and $+V_{\rm max}$ corresponds to a constant emitting surface, thereby producing a plateau in the observed line profile (see Sects. 2.1.3–2.1.4 in Jerkstrand 2017). The interest generated by these detections has also fostered wind searches at other wavelengths, including the NIR during soft state (e.g. Sánchez-Sierras & Muñoz-Darias 2020;) and UV (Castro Segura et al. 2022). These detections naturally raise new questions about the physical origin of the outflows at different accretion states. In particular, the presence of NIR wind signatures during soft states, but the absence of clear optical counterparts in the same phases, suggests that distinct components of the outflow may dominate at different wavelengths (see Fig. 2.4 for a schematic and up-to-date representation of wind visibility across the HID). While the above studies show that both hot and cold winds appear to be common—possibly ubiquitous—in XRBs, it remains unclear whether these represent physically distinct types of outflows, or instead different manifestations of a single underlying phenomenon. A possible explanation is that LMXB winds are intrinsically multi-phase, with different temperature and ionisation layers contributing to the observed features across the electromagnetic spectrum (Muñoz-Darias & Ponti 2022). In what follows, I briefly summarise the main scenarios discussed in Muñoz-Darias & Ponti (2022), and I refer the reader to Fig. 2.5 for their schematic representation.

First, one possibility is that the optical and X-ray signatures come from *distinct* outflows that appear under different luminosity conditions. In this case, their similar velocities would simply reflect comparable system scales rather than a shared origin. This interpretation, however, requires a high degree of fine-tuning to reproduce the similar kinematic properties inferred from strictly simultaneous data, while keeping both

outflows as totally independent phenomena.

A second option is that there is a *single* wind whose ionisation state changes with the irradiating luminosity. In such a view, only one component (hot or cold) would be visible at any given time. Yet, optical spectroscopy suggests that lower-ionisation material may remain present even when X-ray wind tracers are absent, arguing against a purely single-phase picture.

Alternatively, one might consider a *static multi-phase* outflow in which hot and cold components always coexist with constant physical properties. This scenario is disfavoured by the clear luminosity-dependent variability seen across the available observations.

A more elaborate interpretation involves a *stratified* wind, in which the optical-emitting gas lies farther from the BH than the X-ray-emitting gas, due to their markedly different ionisation parameters. Simple estimates, however, imply very large radial separations unless the density profile is highly contrived, and even then it remains difficult to reproduce the observed rapid response of the optical lines to X-ray variability.

Finally, an alternative view is that the optical and X-ray components of the outflow do not only coexist over the same time intervals, but also originate from comparable radii, i. e. a *multi-phase dynamic wind*. In such a picture, the wind would consist of cooler and denser clumps embedded within a hotter and more tenuous medium. Configurations of this kind are commonly invoked in studies of the interstellar medium (e.g. McKee & Ostriker 1977), albeit at significantly lower densities, and have also been extensively applied to outflows in AGN, where large ranges in ionisation parameter appear to arise from spatially co-located gas phases (e.g. Krolik et al. 1981). If the irradiating X-ray source varies strongly, as is the case for V404 Cygni, this scenario naturally leads to a highly dynamic outflow, for which substantial variability in the observed wind signatures is expected across multiple wavebands. In this scenario, changes in the illuminating spectrum or in the local opacity would simply adjust the relative visibility of the hot and cold phases, without the need for the two components to be spatially distinct. In practical terms, this implies that at lower luminosities—as typically achieved in the hard state—the cooler, optically emitting gas would dominate the observable signatures, whereas at higher luminosities, characteristic of soft states, the hotter X-ray phase should become more prominent. This behaviour is fully consistent with current detections, where optical winds are mostly reported during hard states, while X-ray winds preferentially emerge at higher luminosities. Finally, multi-phase and clumpy winds, are also thought to be present in massive stars, where both theoretical modelling and observations suggest that density perturbations—ultimately responsible for clumping—originate very near the launching region (e.g. Sundqvist & Owocki 2013). In summary, even if some level of stratification is certainly plausible—for instance, hotter material is naturally expected closer to the ionisation front— a multi-phase outflow provides a far more satisfactory explanation of the observations. The comparable velocities inferred for both X-ray and optical winds (e.g. Ponti et al. 2015; Panizo-Espinar et al. 2022), together with their simultaneous detection in the optical–NIR (Sánchez-Sierras & Muñoz-Darias 2020) and optical–UV bands (Castro Segura et al. 2022), strongly support this view. At present, a multi-phase accretion disc wind therefore appears to be the most consistent interpretation of the available data in XRBs.

In this picture, one would then expect optical wind signatures to remain detectable during soft states as well, although the stronger X-ray emission in this regime could potentially outshine or mask the optical contribution. An another limitation, could be that only a few systems have been followed spectroscopically in the optical once they enter the soft state, which has so far precluded a systematic assessment of optical wind observability in this regime. In the next section, I address this question directly by investigating whether optical wind signatures can indeed be identified during soft-state phases, through an optical spectroscopic

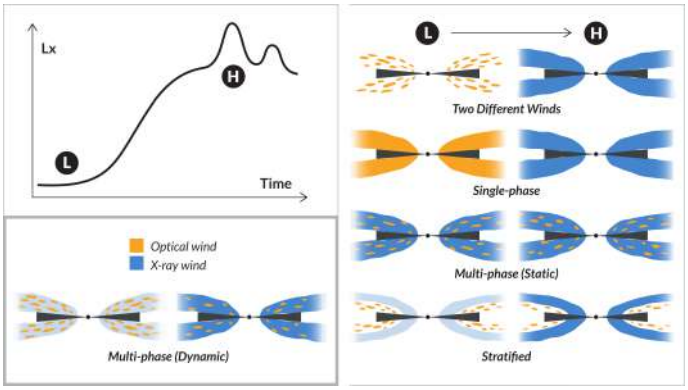

Figure 2.5: Schematic representation (adapted from Muñoz-Darias & Ponti 2022) illustrating the possible connections between the optical and X-ray wind components as the hard X-ray luminosity increases from low (L) to high (H) values. Observations support a dynamic, multi-phase configuration as the most plausible scenario.

study of the BH system MAXI J1305−704 (hereafter J1305).

2.3 MAXI J1305–704 analysis

This analysis is organised in two stages. First, I search for wind-related absorption signatures during the soft state of the source (hereafter referred to as CM24). I then exploit the properties of the optical emission lines to investigate the geometry and inclination of the accretion disc using a new diagnostic approach (AA24).

2.3.1 Source Overview

J1305 was proposed as a high-inclination BH XRB based on its X-ray properties during outburst, such as the presence of dips (Suwa et al. 2012, Kennea et al. 2012, Shidatsu et al. 2013, Morihana et al. 2013). The source was first detected on 2012 April 9 by the Monitor of All-sky X-ray Image instrument (*MAXI*; Matsuoka et al. 2009), equipped with the Gas Slit Camera (GSC; Mihara et al. 2011), as part of its transient alert system (Suwa et al. 2012). Subsequent follow-up observations with the Neil Gehrels *Swift* Observatory (Gehrels 2004) confirmed the presence of an uncatalogued bright X-ray source using both the on-board X-Ray Telescope (*XRT*; Burrows et al. 2005) and the UltraViolet and Optical Telescope (*UVOT*; Roming et al. 2005). Miller et al. (2014) reported evidence of a potential failed wind in the X-rays during the hard state, highlighting J1305 as a promising candidate for the search of multi-wavelength outflow signatures. An optical study carried out during quiescence provided dynamical confirmation of a BH accretor, determined the orbital period ($P_{\rm orb} = 0.394 \pm 0.004$ d), and further supported the high-inclination scenario measuring an inclination $i = 72^{+5}_{-8}$ deg (Mata Sánchez et al. 2021).

The 2012 outburst of J1305 was extensively studied in the X-ray band, but follow-up at other wavelengths has been limited. Shaw et al. (2017) presented the only published optical spectrum obtained during the outburst, with restricted spectral coverage during the hard-to-soft transition. In this work, I report the analysis of two optical spectroscopic epochs, which enable the study, for the first time, of possible outflow features in this high-inclination system during the soft state—a crucial step toward building a more complete understanding of outflow physics in X-ray binaries. The results presented here are based on my work of

Miceli et al. (2024) published in *Astronomy & Astrophysics* (CM24).

2.3.2 Observations and data reduction in CM24

J1305 was observed during its discovery outburst in 2012 with the 6.5-m Magellan Clay telescope (PI: Degenaar) at the Las Campanas Observatory (Chile) which is an optical/NIR telescope, recognized for its excellent seeing conditions and equipped with a suite of high-performance spectrographs. The observations were performed using the Low Dispersion Survey Spectrograph (LDSS-3), a high-efficiency optical spectrograph and imager mounted at the Nasmyth focus of the Clay telescope. LDSS-3 provides excellent sensitivity at red optical wavelengths and is optimized for faint-object spectroscopy, thanks to its efficient sky subtraction and large field of view.

In this case, the VPH-ALL grism configuration was employed, which offers broad wavelength coverage (approximately 3800–9400 Å) at moderate spectral resolution ($R \sim 700$). This setup allows simultaneous observation of multiple hydrogen and helium emission lines, crucial for tracing accretion and outflow signatures in X-ray binaries. The chosen configuration therefore ensured both high throughput and sufficient spectral resolution to resolve broad emission profiles typical of LMXB optical spectra. All observations used a 0.75″ slit, which resulted in a resolving power of R=826, measured as the full-width-at-half-maximum (FWHM) of the skylines from the background spectra. The system was observed during two consecutive nights, May 2nd (02:18:34 UTC to 02:56:41 UTC) and May 3rd (00:29:36 UTC to 01:09:03 UTC). The exposure time of each individual spectrum was fixed to 300s, amounting to six spectra per epoch. This setup allowed us to cover a broad wavelength range (4300–11000 Å). I reduced the data using standard procedures based on IRAF[1] software, MOLLY tasks and PYTHON packages from ASTROPY and PYASTRONOMY (Astropy Collaboration et al. 2022). These tools allowed us to correct the observed spectra from bias and flats, as well as to calibrate them in wavelength using Ne, He and Ar lamps.

2.3.3 X-ray data

To complement the optical dataset with simultaneous and multi-wavelength coverage, I also analysed publicly available data from the *Swift* observatory. I analysed *Swift/XRT* observations performed on May 3rd, 2012, coincident with the second night of our Magellan campaign. The data were processed following standard recipes using the *Swift* XRTPIPELINE v6.32.1[2]. From the processed event files, I extracted spectra using circular regions of radius 47″ for both the source and background, positioned around and away from the target, respectively. The tool XRTPRODUCTS was used to generate the source spectrum, which I then binned with GRPPHA to ensure a sufficient number of counts per bin. The spectra were analysed with the X-ray spectral-fitting program XSPEC (Arnaud 1996), employing the appropriate ancillary response file (ARF) and redistribution matrix file (RMF).

[1] IRAF is distributed by the National Optical Astronomy Observatories, operated by the Association of Universities for Research in Astronomy, Inc., under contract with the National Science Foundation.

[2] https://heasarc.gsfc.nasa.gov/lheasoft/download.html

2.3.4 UV/optical data

In addition, I analysed *Swift/UVOT* data covering 11 April to 14 July 2012, a time span that includes the May interval during which the optical spectra were obtained. *UVOT* observations were taken using three optical filters (U, B, and V) and three UV filters (W1, M2, and W2). Source extraction was performed using a circular region of 5″ radius centred on J1305, while background regions were defined using multiple small regions located away from the source. The task UVOTSOURCE was then applied to derive coincidence-corrected count rates, magnitudes, and flux densities.

2.4 Analysis and results in CM24

2.4.1 X-ray spectral state

I employed publicly available *MAXI*[3] data collected from April 5th to July 17th, 2012, corresponding to the initial and decay phases of the outburst (Morihana et al. 2013). In Fig. 2.10, I show the X-ray light curve and hardness ratio. I defined the soft and hard colours in the hardness ratio using the $2-4$ keV and $4-10$ keV bands, respectively, while I used the $2-10$ keV band to trace the source brightness. To improve the signal-to-noise ratio (SNR), I binned the data in one-day intervals during the brighter period (MJD 56022 to 56034), and in 5-day intervals during the fainter phases. A complete hardness–intensity diagram using these same energy bands is available in Morihana et al. (2013) (see their Fig. 3). The hard-to-soft transition occurred around 20 days before my optical observations (Suwa et al. 2012), which fall within interval D as defined in Morihana et al. (2013). X-ray spectra obtained roughly two weeks before my campaign already showed properties consistent with the soft state (Shidatsu et al. 2013). This interpretation is further supported by my analysis of a *Swift/XRT* observation on May 3rd, simultaneous with my optical dataset.

The X-ray spectrum (0.5–10.0 keV) was fitted using the model TBABS*(DISKBB+EXPABS* POWERLAW+GAUSSIAN), which provides an adequate description of the soft state in BH binaries (see Fig. 2.6 for the fitted spectrum and residuals). In this model, TBABS accounts for interstellar photoelectric absorption along the line of sight (Wilms et al. 2000), while DISKBB represents the multicolour blackbody emission from a geometrically thin, optically thick accretion disc (Mitsuda et al. 1984). The POWERLAW component models the high-energy tail produced by Compton up-scattering of soft photons in a hot corona, and the multiplicative term EXPABS introduces an exponential cutoff mimicking the effect of photoionized absorption or partial covering at higher energies. I also include a Gaussian in the model to reproduce a broad absorption feature at ~ 1 keV. This structure is reminiscent of the features reported by Miller et al. (2014) from *Chandra/HETG* observations, which were interpreted as signatures of a *failed wind* — that is, an outflow launched from the accretion disc that becomes overionized before reaching escape velocity and subsequently falls back onto the disc surface. Such phenomena may occur during transitions between accretion states, when changes in luminosity or spectral hardness alter the ionization balance of the disc atmosphere (e.g. Neilsen et al. 2011; Ponti et al. 2012). However, given the limited spectral resolution of our dataset, the identification of this feature with a failed X-ray wind remains uncertain, and I therefore focus primarily on the continuum emission.

The best-fit parameters are characteristic of a disc-dominated (soft) spectral state, with an inner disc temperature of $kT_{\rm in} = 0.91 \pm 0.03$ keV and a steep power-law index ($\Gamma > 3$). Assuming a BH mass

[3] http://maxi.riken.jp/pubdata/v7.7l/

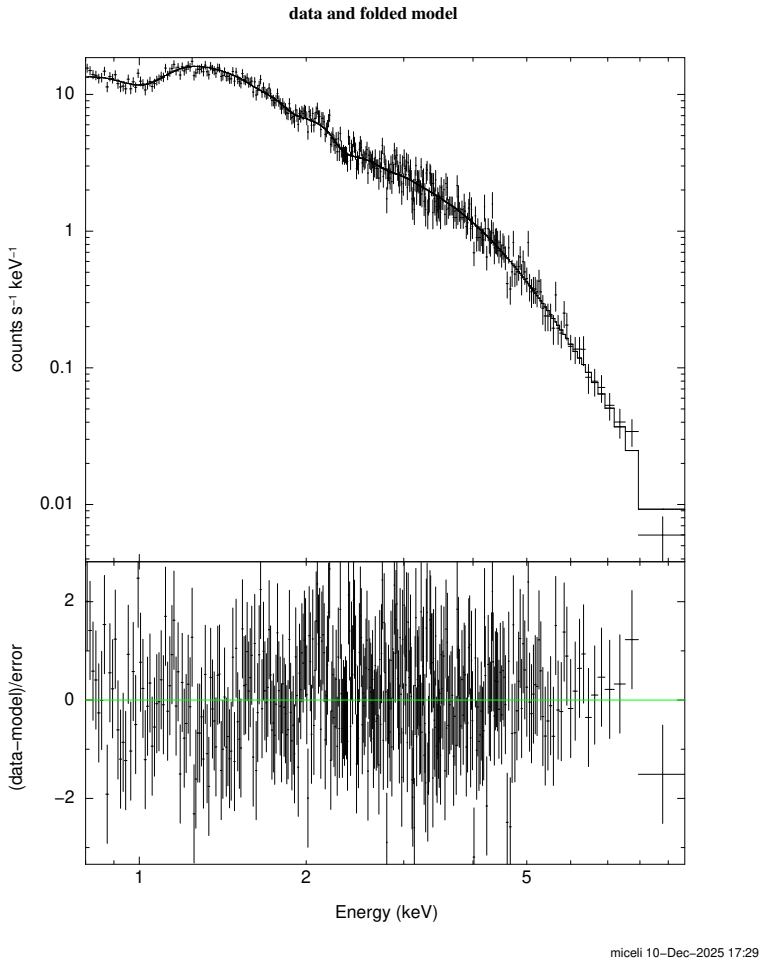

Figure 2.6: Swift/XRT spectrum of J1305 obtained on 3 May 2012, fitted with the model described in the text. Residuals are shown in the lower panel.

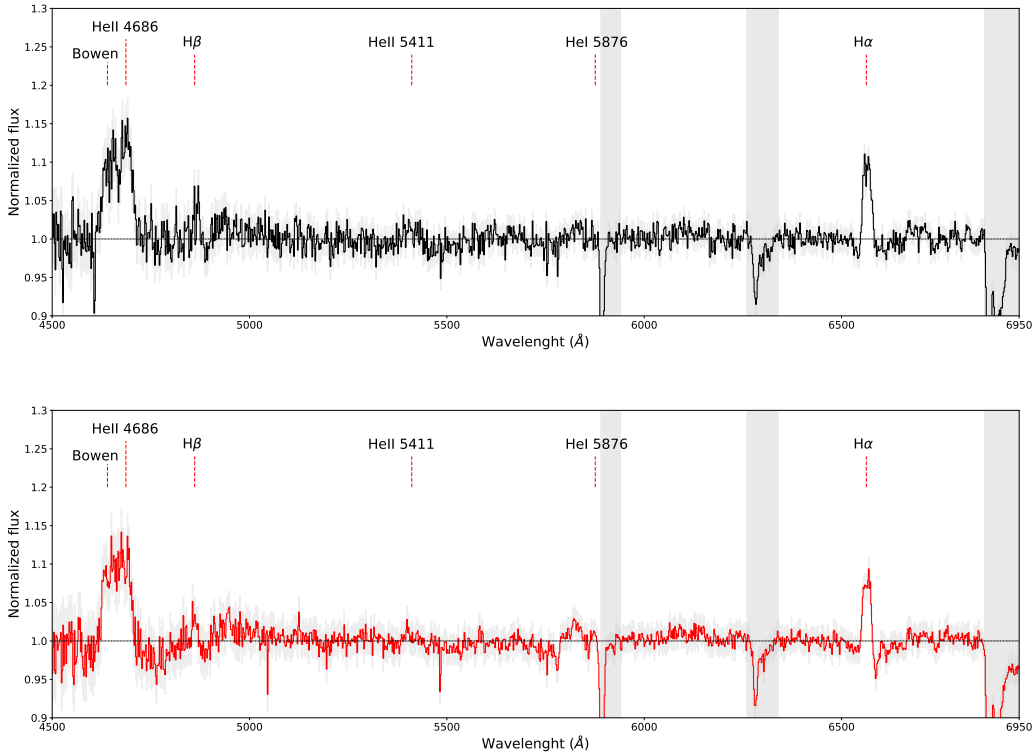

Figure 2.7: Average spectra of epoch A (black) and epoch B (red) of optical observations. The light-grey band on the left corresponds to the edge of the 5890 sodium D line, while the other two correspond to the strongest telluric (Miceli et al. 2024).

of $10\,M_{\odot}$ and a distance of 7.5 kpc (Mata Sánchez et al. 2021), the inferred bolometric luminosity is $L_{\rm bol} \simeq 8 \times 10^{38}$ erg s^{-1}, corresponding to about 40% of the Eddington limit.

2.4.2 Optical spectra

I reduced and normalised the observed spectra using tailored PYTHON routines. The data were stored in FITS format and consisted of two spectral segments recorded by separate CCDs: 4300–6600 Å (CCD2) and 6600–11,000 Å (CCD1). Standard reduction steps were first applied, including bias subtraction, flat-field correction, and wavelength calibration using comparison-lamp spectra (Ne, He, Ar).

Due to the use of two independent CCDs, the extracted spectra displayed a small offset in the continuum level around the overlap region (∼ 6600 Å). To correct this mismatch, I modelled the continuum of each spectrum using a fifth-degree polynomial—sufficiently flexible to capture the broad instrumental curvature—combined with a step function to account for the discontinuity between the CCDs. This approach allowed me to flatten the continuum across the full spectral range while preserving the intrinsic line profiles. The resulting averaged and normalised spectra for the two consecutive nights of observations (hereafter epoch A and epoch B) are shown in Fig. 2.7. Although the full range extended from 4300 to 11000 Å, I restricted the analysis to 4500–6950 Å, as this region is less affected by telluric absorption and SNR limitations, and it includes the relevant spectral features.

In these spectra, I identified hydrogen emission lines from the Balmer series, most prominently Hα (Fig. 2.9) and the weaker Hβ. High-excitation features were also present, such as the He II 4686 Å line

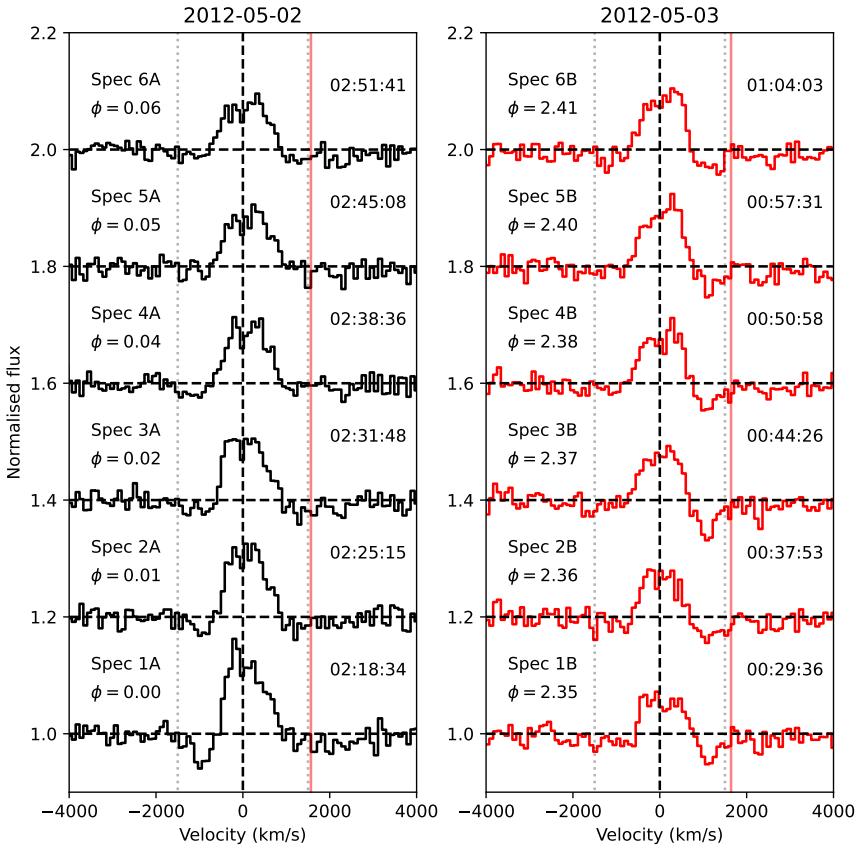

Figure 2.8: Individual Hα emission lines from the spectra obtained during epoch A (black) and epoch B (red) of the optical observations. Black dotted lines mark the maximum terminal velocity observed in both blue- and red-shifted absorption features ($\pm 1500\,\mathrm{km\,s^{-1}}$). The red solid line marks the intersection between CCDs, confirming that the red-shifted features, when present, are not due to a normalisation issue. The normalised profiles have been vertically offset for clarity. The phases shown here are relative phases as defined in the text (Miceli et al. 2024).

(Fig. 2.7) and the Bowen blend (a mixture of N III and C III emission lines produced by fluorescence cascades, see Steeghs & Casares 2002). These features are consistent with the soft-state classification inferred from X-ray analysis (Morihana et al. 2013).

I focused my detailed analysis on the Hα line, the strongest isolated feature in the spectra. Its profile displayed a clear evolution, both within each observed spectrum (Fig. 2.8) and between the two epochs (Fig. 2.9). The emission can be described as a double-peaked profile, as expected from a Keplerian accretion disc (Smak 1981), superimposed with a variable absorption component. During epoch A, some spectra (notably 1A, 2A, and possibly 4A) showed a blue-shifted absorption, whereas in epoch B the absorption appeared predominantly red-shifted.

To quantify these changes, I performed multi-Gaussian fits to the Hα line using the CURVE_FIT routine from the SCIPY package (Virtanen et al. 2020). For the emission, I used two Gaussians characterised by their height, a common FWHM, a centroid offset, and the double-peak separation (DP). To reproduce the absorption, I added a third Gaussian in absorption with free parameters depth, FWHM, and offset. The resulting fit parameters are summarised in Table 2.1, and an example of a fitted profile is shown in Fig. 2.9.

For reliability, I excluded absorption components shallower than 0.02, corresponding to less than twice the SNR measured on the nearby continuum (SNR $\sim$ 80 for individual spectra). With this criterion, spectrum

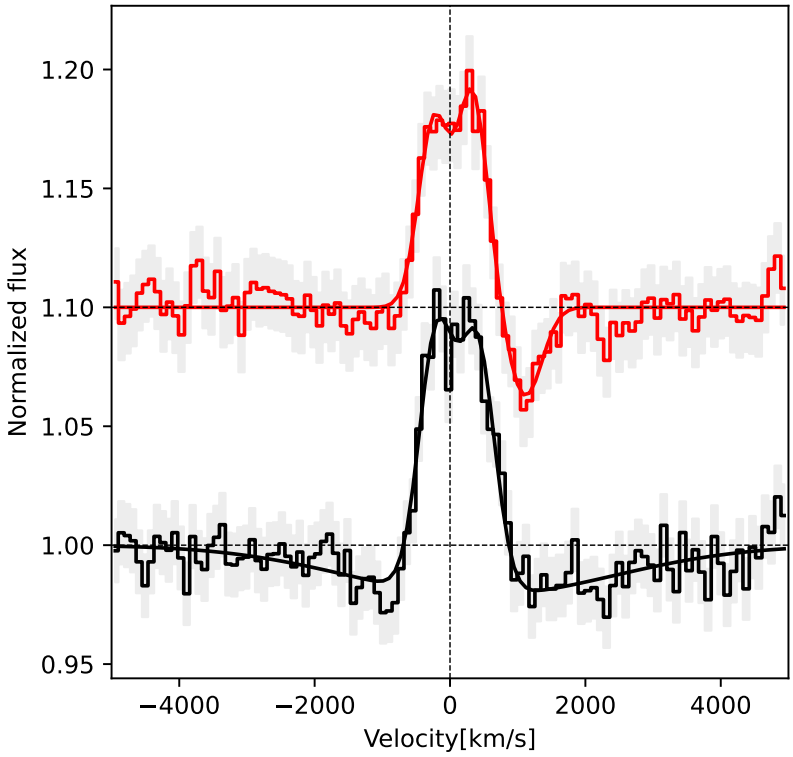

Figure 2.9: Average Hα emission line of epochs A (black, bottom) and B (red, top). The solid lines are the best fit to the nightly average (see Tab. 2.1 for the precise parameters). The normalised profiles have been separated vertically by a constant offset for visual purposes (Miceli et al. 2024).

Spectrum	Phase	Emission				Absorption			ML Class
		DP (km/s)	FWHM (km/s)	Height 1	Height 2	offset (km/s)	FWHM (km/s)	Depth	
1A	0.00	598 ± 73	420 ± 51	0.09 ± 0.01	0.14 ± 0.01	-845 ± 142	476 ± 175	-0.05 ± 0.01	Blue-abs/abs
2A	0.02	595 ± 49	500 ± 77	0.16 ± 0.07	0.17 ± 0.07	-73± 50	1146 ± 364	-0.09 ± 0.07	abs
3A	0.03	605 ± 39	421 ± 33	0.12 ± 0.01	0.11 ± 0.01	-	-	-	abs
4A	0.04	625 ± 47	453 ± 53	0.12 ± 0.03	0.12 ± 0.03	-93 ± 71	1288 ± 445	-0.04 ± 0.03	Blue-abs/abs
5A	0.05	633 ± 51	442 ± 40	0.09 ± 0.01	0.08 ± 0.01	-	-	-	abs
6A	0.06	672 ± 41	452 ± 33	0.10 ± 0.01	0.08 ± 0.01	-	-	-	abs
average A		603 ± 29	428 ± 25	0.10 ± 0.01	0.11 ± 0.01	-	-	-	abs
1B	2.35	608 ± 47	348 ± 34	0.06 ± 0.01	0.07 ± 0.01	1133 ± 38	280 ± 66	-0.04 ± 0.01	abs
2B	2.36	582 ± 51	433 ± 51	0.10 ± 0.02	0.11 ± 0.02	324 ± 145	1397 ± 276	-0.05 ± 0.02	abs
3B	2.38	553 ± 52	385 ± 43	0.09 ± 0.01	0.07 ± 0.01	1075 ± 35	352 ± 63	-0.06 ± 0.01	abs
4B	2.39	638 ± 39	464 ± 49	0.18 ± 0.05	0.13 ± 0.04	283 ± 134	1397 ± 276	-0.09 ± 0.07	abs
5B	2.40	616 ± 52	468 ± 54	0.17 ± 0.04	0.11 ± 0.03	336 ± 190	1113 ± 228	-0.06 ± 0.05	abs
6B	2.41	618 ± 45	461 ± 57	0.19 ± 0.07	0.14 ± 0.06	-	-	-	abs
average B		574 ± 29	428 ± 25	0.09 ± 0.01	0.07 ± 0.01	1112 ± 40	411 ± 69	-0.04 ± 0.01	abs

Table 2.1: Best fit parameters of the multi-Gaussian model described in the text, applied to our two epochs of observations. Uncertainties are at the 68% confidence level. The FWHM of both emission components are linked. We do not report absorption components whose depth was shallower than 2% of the continuum, in order to assure a 2-sigma detection over the signal-to-noise ratio measured on the nearby continuum. We include the results from the Machine Learning classification algorithm in the final column for reference (Miceli et al. 2024).

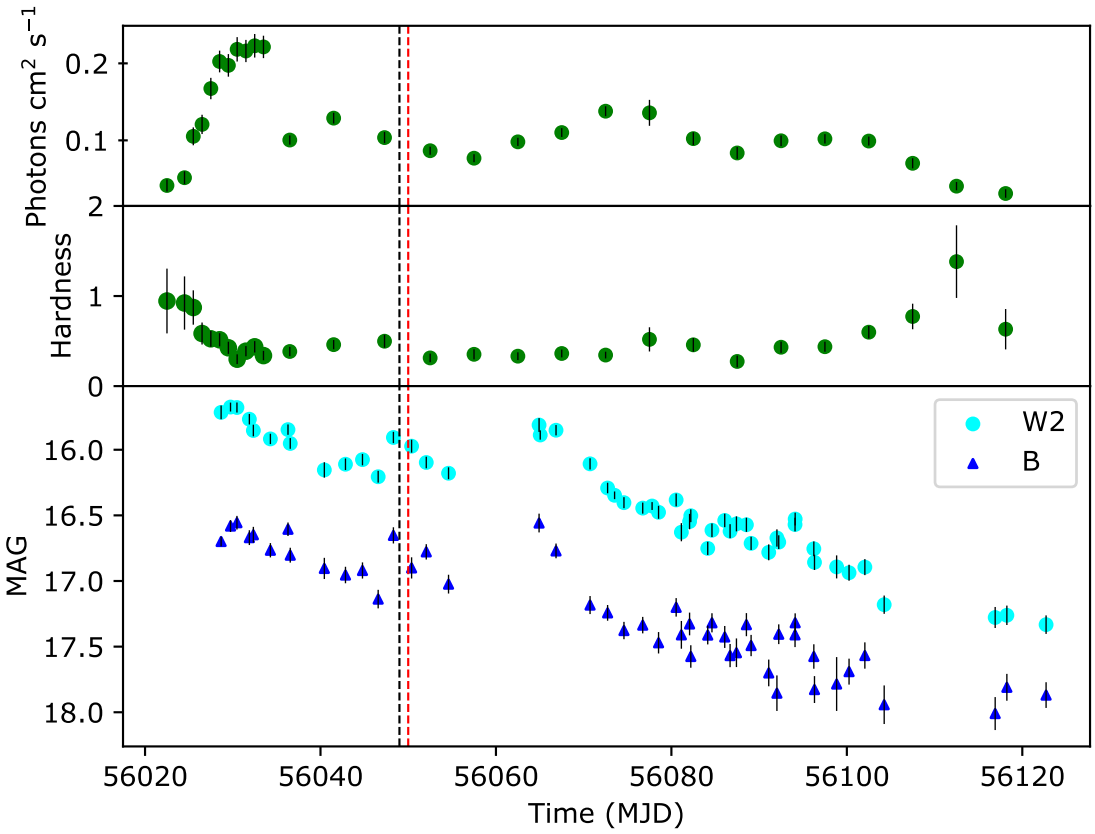

Figure 2.10: Top panel: light-curve of MAXI J1305-704 from 2 – 10 keV band count rate provided by *MAXI*. Middle panel: Hardness ratio data constructed from the 2 – 4 keV and 4 – 10 keV energy bands count rate provided by *MAXI*. Bottom panel: *UVOT* light curve in W2 UV and B optical band. The black and red dashed lines represent our optical observations of epochs A and B respectively (Miceli et al. 2024).

1A emerged as the clearest case of a narrow, blue-shifted absorption. In contrast, most spectra from epoch B displayed significant red-shifted absorptions with depths exceeding the 3σ threshold. The terminal velocity of these absorptions—defined as one FWHM from the absorption centroid—was comparable in both epochs ($\sim$ 1300–1600 km s^{-1}), though with opposite signs.

I also analysed the nightly averaged spectra of the Hβ line, which showed FWHM and DP consistent with those of Hα. However, due to the lower SNR of Hβ, I restricted the detailed discussion to the Hα line.

2.4.3 Swift/UVOT: search for orbital UV modulation

The Hα line profile in my spectra displayed rapid changes, both on timescales of a few minutes and between consecutive nights (see Fig. 2.8). Although the double-peaked emission was not strongly asymmetric, the varying peak intensities suggested the possible presence of a hot spot on the accretion disc. To investigate this scenario further, I analysed publicly available *Swift*/UVOT data obtained between April 11th and July 14th, 2012. From these observations, I extracted light curves in all available bands, binning the data in one-day intervals. Photometric light curves in the B and W2 filters are shown in Fig. 2.10 (bottom panel), serving as proxies for the system brightness at optical and UV wavelengths during the outburst.

I specifically searched for superhumps near the orbital period ($P_{\rm orb}$ = 0.394 ± 0.004 d; Mata Sánchez et al. 2021), as such modulations are often linked to hot spot structures on the disc. For this purpose, I used dedicated timing tools such as EFSEARCH and EFOLD available from the HEASARC suite. However, no significant periodic modulation was detected.

A limitation of this analysis comes from the temporal gap between the quiescence observations that established the orbital ephemeris (Mata Sánchez et al. 2021) and the earlier outburst data-set analysed here. Combined with the uncertainty in $P_{\rm orb}$, this prevented me from maintaining phase coherence and calculating absolute orbital phases. Instead, I defined relative orbital phases with respect to the first epoch of observations. Using this convention, the spectra of epoch A correspond to orbital phases 0.0–0.06, while those of epoch B span 2.35–2.41.

Although this coverage is too limited to robustly test for orbital modulation of the line profile, the fact that the profile peaks evolve significantly even within a single epoch suggests that a single hot spot is unlikely to explain the observed variability.

2.5 Discussion in CM24

In this section, I explore the possible association of the features analysed above with out-flowing phenomena.

2.5.1 Search for optical wind features

The most characteristic optical signatures of cold winds in LMXBs are P-Cygni profiles, although other features—such as flat-top profiles or broad wings—have also been traditionally considered as reliable tracers of outflows (see Panizo-Espinar et al. 2022 for a compilation).

The spectra from epochs A and B display significant differences, with the Hα line profile showing variability even on timescales of only a few minutes. Upon individual inspection, I find a clear blue-shifted absorption in at least one spectrum (1A, Fig. 2.8), extending down to ∼5% below the continuum. While such a feature could suggest the presence of a P-Cygni profile, several arguments prevent me from adopting this interpretation.

First, only a single spectrum in the data-set shows a clear detection of this blue-shifted absorption, whereas deep red-shifted absorptions are consistently observed during epoch B. If the former truly traced an outflow, the latter would imply the presence of inverted P-Cygni profiles—rare signatures associated with inflows and reported in only one LMXB so far (Cúneo et al. 2020). This possibility is intriguing, particularly given the evidence for failed X-ray winds in this system during its hard state (Miller et al. 2014). However, the terminal velocities inferred from the X-ray features are about an order of magnitude larger than those measured in the optical. This mismatch suggests that the two sets of features are unlikely to trace the same phenomenon, since systems with both X-ray and optical winds typically display comparable terminal velocities (e.g. Muñoz-Darias & Ponti 2022).

Furthermore, a comparison of the blue-shifted and red-shifted absorption components in my optical spectra reveals that they are remarkably consistent in both depth and terminal velocity (∼ 1300–1600 km s^{-1}). The multi-Gaussian fits compiled in Table 2.1 confirm that many of the spectra contain broad absorption

components with large FWHMs (e.g. spectrum 2B), while others exhibit narrower features with consistent velocities (e.g. spectrum 3B). Taken together, these results suggest that all of the observed absorptions likely share a common physical origin.

On this basis, and considering the absence of other wind-sensitive features with sufficient SNR in the spectra (e.g. He I 5876 Å), I disfavour a wind-driven interpretation. Instead, I propose that an underlying broad and rapidly varying absorption component is the main driver of the observed profile changes across the data-set. Such a component could produce both the apparent narrow red-shifted absorptions observed in epoch B and the occasional blue-shifted absorption seen in epoch A, depending on the relative offsets between the emission and absorption contributions.

The absence of clear optical wind signatures is consistent with the current paradigm, according to which winds have not been detected at optical wavelengths during the soft state of LMXBs, likely due to ionisation conditions in the outflow (Muñoz-Darias & Ponti 2022). Nevertheless, wind-related features have been reported in the NIR, where they remain detectable even in the soft state (Sánchez-Sierras & Muñoz-Darias 2020).

Finally, I note that my results do not allow me to conclusively rule out the presence of winds during the outburst of J1305, since the temporal coverage of the spectra is limited and does not span a full orbital phase. Indeed, some of the observed flat-top profiles (e.g. spectra 2A and 3A) could tentatively be linked to outflow activity. However, given that my analysis is restricted to a single emission line, a definitive confirmation cannot be established.

2.5.2 Machine Learning test

The analytical fits to the spectra, while informative, are not fully conclusive and do not allow me to efficiently distinguish between the outflow and broad absorption scenarios. In order to reduce potential biases associated with the observer's interpretation, I employed the Deep Neural Network classifier ATM (Mata Sánchez et al. 2023). This independent method is trained to classify any given spectrum into one of five categories: disc (no outflows), blue-absorption, broad, P-Cygni (three classes representing different types of outflow features), and absorbed (a class specifically dedicated to broad absorption features).

It is important to note that ATM is trained to recognise spectral features with a relative strength of at least 3σ above the local noise level ($\sigma = 0.01$). Because the reliability of line detection depends strongly on the signal-to-noise ratio (SNR), I tested the robustness of the classification results through a Monte Carlo simulation. Following the procedure described in Sec. 4.3 of Mata Sánchez et al. (2023), I generated 1000 realisations of each spectrum by adding Gaussian noise consistent with the measured uncertainties and re-ran the ATM analysis on every realisation. This allowed me to quantify how noise fluctuations affect the identification of individual lines and to estimate the probability that each detected feature remains significant. The resulting distributions provide a direct measure of the confidence level associated with the ATM classification.

The application of ATM to the J1305 data identified two potential blue-absorption profiles during epoch A (spectra 1A and 4A). However, for both cases the classifier also assigned a similar probability to the absorbed class. All remaining spectra were classified as absorbed, suggesting that broad absorption features are ubiquitous in the data-set. Since the absolute terminal velocities of all absorption features, whether blue-

or red-shifted, are consistent between epochs A and B, I again favour the broad absorption interpretation for this system.

This conclusion is further reinforced by the application of ATM to the nightly averaged spectra, where both epochs were consistently classified as absorbed type. Taken together, these results support the view that the profile variability is dominated by an underlying, broad and variable absorption component rather than by transient outflow features.

2.5.3 On the origin of the broad absorption features

The origin of the broad absorption features observed in J1305 is not yet well understood, although similar signatures have been reported in several other LMXBs (e.g., GRS 1009–45, della Valle et al. 1997; GRO J1655-40, Soria et al. 2000; MAXI J1807+132, Jiménez-Ibarra et al. 2019). The most widely discussed interpretation was first proposed by Dubus et al. (2001), who suggested that the broad absorption could originate in a partially neutral atmosphere, extended above the accretion disc. In this picture, the upper disc layers are heated by irradiation from the central X-ray source to temperatures of $\sim 10^4$–10^5 K, producing a stratified structure with a hot, ionised skin overlaying cooler, denser material. Radiation from the underlying disc passes through these outer layers, imprinting broad absorption components on the optical emission lines. The neutral gas therefore acts similarly to a stellar photosphere, while the irradiated layer still contributes to the double-peaked Balmer emission.

As discussed by Psaradaki et al. (2018), a configuration of this kind can be sustained by X-ray illumination of the outer disc, which drives vertical expansion and forms an extended, two-phase atmosphere. The low-ionisation component is denser and more clumpy, likely produced near the stream–disc impact region, whereas the highly ionised gas occupies a larger volume above the disc surface. This naturally explains the coexistence of emission and absorption features in the spectra, as well as their variability with orbital phase. Clumpy or inhomogeneous regions within the atmosphere can lead to asymmetric line profiles, consistent with the irregular absorption structures observed in J1305 (see Fig. 2.11). Therefore, here the complex line profiles can be naturally explained with an emission from the optically thick disc surface, and an absorption from a cooler, extended atmosphere lying above it.

The observed absorption velocities ($\sim$1500 km s^{-1}) are comparable to those of the Hα emission, suggesting that both originate from similar disc radii. The inclination of the system further enhances the visibility of these features, since they are most prominent when the line of sight crosses the upper layers of the disc.

Another key question concerns the unusually broad width of the absorption components. Several mechanisms could, in principle, account for such profiles. A first possibility is Doppler broadening, which would imply that the absorbing gas is located at relatively small radii, where the Keplerian velocities are higher than in the region producing the double-peaked emission lines. In this case, the line width directly reflects the rotational velocity field of the inner disc atmosphere. However, the strong variability of the absorption depth and shape suggests that the absorbing material is not confined to a single radius, but instead extends over a range of disc heights or azimuths, possibly in a clumpy or turbulent layer above the disc surface.

A second mechanism is pressure (collisional) broadening as originally proposed by Dubus et al. (2001). In this scenario, the line wings arise from the high electron densities ($n_e \gtrsim 10^{13}$ cm^{-3}) in the irradiated disc atmosphere, where frequent collisions perturb the atomic energy levels and broaden the transitions. While

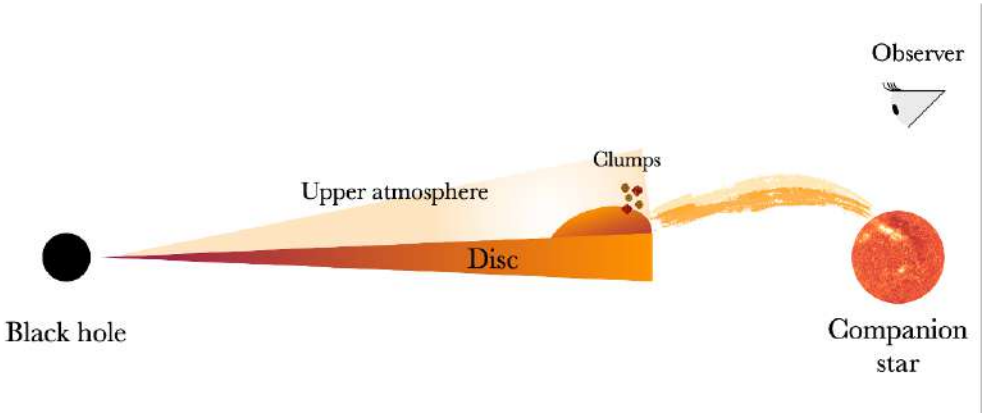

Figure 2.11: Possible schematic representation of the MAXI J1305-704 system, with the presence of an atmosphere.

this model can qualitatively reproduce the observed line shapes, it also predicts that such features should be most prominent in systems seen at low inclination, where the line of sight crosses a larger column of the dense disc atmosphere. Observationally, the opposite trend is found: all systems exhibiting broad absorption components are high-inclination binaries ($i \gtrsim 65°$). This includes the well-studied sources XTE J1118+480 (i = 68–79°; Dubus et al. 2001; Khargharia et al. 2013), MAXI J1659–152 (i = 70–80°; Kaur et al. 2012; Torres et al. 2021), and, as shown in this work, J1305 ($i = 72^{+5}_{-8}$ °; Mata Sánchez et al. 2021). If we further consider systems showing X-ray dipping behaviour (a robust indicator of high orbital inclination) the sample expands to include, for instance, MAXI J1803–298 (Mata Sánchez et al. 2022).

An alternative explanation is that some vertically extended disc structure, such as a thickened rim or a warped outer disc, partially obscures the emission region, producing complex absorption features. This could occur if the outer disc is inflated by irradiation or by the impact of the accretion stream, as proposed for dipping sources (e.g. White & Holt 1982; Psaradaki et al. 2018). However, no detailed modelling of this scenario has yet been carried out, and the relative contribution of geometrical versus thermal effects remains an open question.

To make progress in understanding these features and reconcile theory with observations, two complementary approaches are needed. On one hand, new physical models are required to provide testable predictions. On the other hand, systematic follow-up of future outburst events will be crucial to investigate whether the evolution of broad absorptions depends on orbital phase, and to search for simultaneous outflow signatures in multiple lines. In my J1305 spectra, I also detect He II 4686 Å and a weaker Hβ emission line (see Fig. 2.7). However, contamination from the nearby Bowen blend in the case of He II, and the low SNR in the case of Hβ, prevent me from drawing firm conclusions about the presence of outflows in these lines. This highlights that observations with at least 8-m class telescopes are necessary to achieve the required sensitivity for future detailed studies.

2.6 Conclusions in CM24

In this section, I have presented the analysis of the optical spectroscopy obtained during the 2012 outburst of J1305. I reduced and analysed data collected during two consecutive nights when the source was in the soft state (Morihana et al. 2013), consistent with the overall properties of the optical spectra, which display

high-excitation emission lines such as He II 4686 and the Bowen blend.

I focused my analysis on the Hα line, the strongest isolated feature in the spectra. By modelling it with a multi-Gaussian approach, I showed that its profile can be described as a double-peaked emission component, consistent with disc origin, superimposed on a broad and variable absorption feature. This scenario is favoured over a P-Cygni interpretation for those epochs where blue-shifted absorptions are present. An independent classification using the ATM machine learning algorithm further supports the broad absorption scenario. The detection of such broad absorptions in J1305 adds to a growing sample of high-inclination systems showing this behaviour, challenging traditional theoretical models that predicted these features to arise more readily in low-inclination binaries.

The absence of conclusive outflow features in the soft state of J1305 remains in line with the general picture emerging in recent years. Nevertheless, the issue is far from settled, and progress will require systematic, multi-epoch observations of outbursting systems. My results emphasise the importance of temporal coverage: without sufficient cadence, transient and variable features may be misinterpreted. In this sense, this study highlights the role of detailed optical spectroscopy as a diagnostic tool and underscores the need for high-SNR, time-resolved observations—ideally with 8-m class telescopes—to clarify the nature of the absorption features and to probe the elusive signatures of optical winds in the soft state of LMXBs.

2.7 Constraining the accretion disc geometry in AA24

As an extension of this investigation, I worked on a complementary optical study aimed at constraining the structure and orientation of the accretion disc in J1305 through emission-line spectroscopy in collaboration with Dr. Alessio Anitra. In this work, we applied for the first time the DISKLINE model to optical emission lines, testing whether the disc parameters inferred from the optical domain are consistent with those derived from X-ray analyses of the same source. This approach provides an independent way to probe the disc geometry and dynamics, thus strengthening our overall understanding of the system. The full results of this study are presented in Anitra et al. (2024), and a summary is provided in the following section. As outlined in Chapter 2, one of the most powerful observational diagnostics of accretion discs in LMXBs comes from the analysis of double-peaked emission-line profiles in the X-ray band. The overall morphology of these features encodes information on the radial velocity semi–amplitude, the orbital period, and the system inclination. The same diagnostic applies to optical spectra, which frequently show analogous structures. In particular, the Hα line exhibits a characteristic double-peaked shape with a central depression between the two velocity maxima (the so-called core), whose depth increases with the disc inclination, becoming especially pronounced for viewing angles above $\sim 67°$ (Horne & Marsh 1986). This effect arises because, at higher inclinations, the observer's line of sight intercepts a larger velocity gradient across the disc, enhancing the Doppler separation of the peaks and suppressing the relative flux at the line centre, which corresponds to material moving perpendicular to the line of sight. More recently, Casares et al. (2022) demonstrated a quantitative correlation between the depth of this central depression and the orbital inclination in a sample of quiescent BH LMXBs, allowing robust empirical constraints on this parameter. Additional work, such as the study of SDSS J102347.6+003841 by Wang et al. (2009), has shown that detailed modeling of the double-peaked profiles provides insights into the accretion disc geometry and physical conditions, including disc radii, temperature ranges, and total disc mass.

In this work we tested whether the inclination angle of transient BH candidates can be constrained by applying the relativistic DISKLINE model to optical emission lines. Although originally developed for

X-ray spectroscopy, this model describes Keplerian, axisymmetric disc emission under the assumption of a power-law emissivity profile. While optical lines can be more affected by asymmetries, hot spots, tidal distortions, and deviations from purely Keplerian flow, we found that the quiescent spectra of the BH systems Swift J1357.2−0933 and MAXI J1305−704 are sufficiently symmetric for the model to provide meaningful results. This work, published in Anitra et al. (2024), demonstrates the potential of DISKLINE as a new tool to extract geometric information from optical spectroscopy of LMXBs.

2.7.1 Data used in A24

Here I will describe only the application of this model to the source analysed in the previous section (J1305). In doing so, I will make use of both the optical spectra obtained during the 2012 outburst, presented in Sect. 3.3.2, and the quiescent data of J1305, which I introduce below. On 31 March 2016, the source was monitored with the Very Large Telescope (VLT) Unit Telescope 1 at Paranal Observatory (Chile), using the FORS2 instrument in long-slit mode (Appenzeller et al. 1998). A total of 16 spectra were acquired with individual exposure times of 1800 s, providing nearly 9 hours of continuous coverage and thus sampling almost one full orbital cycle (Mata Sánchez et al. 2021). The spectra cover the 5800–7300 Å wavelength range with a spectral resolution of $R \sim 2140$, as measured from the width of skylines in the background.

The data were reduced following standard procedures, including bias subtraction, flat-fielding, and wavelength calibration, making use of IRAF, MOLLY, and dedicated PYTHON routines from ASTROPY and PYASTRONOMY. Additional corrections were applied to account for cosmic-ray contamination using the L.A. COSMIC algorithm (van Dokkum et al. 2012). Optimal extraction techniques were employed to obtain one-dimensional spectra (Naylor 1998).

It is worth noting that the quiescent spectra may contain a small contribution from the donor star. However, as reported by Mata Sánchez et al. (2021), this contamination is likely below 10% of the total flux and does not significantly affect the accretion-disc dominated features, making the data reliable for studying the double-peaked emission lines characteristic of quiescent discs.

2.7.2 Diskline model applied to optical spectra

The Balmer emission lines, produced by hydrogen transitions in the accretion disc, often appear as broad double-peaked profiles in high-inclination systems. As explained in Chapter 2, this shape arises because gas at a given disc radius R_D orbits with the local Keplerian velocity $V_{Kep}(R_D)$: for a distant observer, part of the disc moves towards the line of sight while the opposite side recedes, producing simultaneous blue- and red-shifted components. The velocity distribution across the disc further broadens the line, while the separation of the two peaks depends on the outer radius of the emitting region and the wings reflect the emissivity profile (Smak 1981; Horne & Marsh 1986). The observed velocity component is given by $V_D = \pm V_{Kep}(R_D) \sin i$, showing the strong dependence on the orbital inclination. Additionally, the resulting profile is influenced by various other effects. For instance, self-absorption by an optically thick disc atmosphere can contribute to deepening the inner core of the line. Simultaneously, disc precession may play a significant role in determining the orbital-averaged velocity shifts observed in the emission line centroid (Torres et al. 2002), while the presence of a hot spot can enhance one of the two peaks of the line.

In XSPEC (Arnaud 1996), one of the most widely used models to describe such Doppler-shaped emission

lines is DISKLINE (Fabian 1989). It was originally developed for the relativistically broadened Fe Kα line in X-ray spectra of LMXBs (e.g. Di Salvo et al. 2009), but it can also be applied to optical Balmer profiles. The model includes as free parameters the inner and outer radii of the emitting region (in units of gravitational radii, $R_g = GM/c^2$), the system inclination, and the emissivity index β, which defines the radial dependence of the emission ($E \propto R^{-\beta}$).

At X-ray energies, relativistic effects such as beaming and gravitational redshift strongly distort the line shape, enhancing the blue peak and shifting the centroid to lower energies. However, if the emission arises from farther out in the disc, relativistic corrections become negligible and the line is dominated only by Newtonian Doppler broadening (see Fig. 2.12). In this regime, the DISKLINE model reduces to the optically thin solution of Horne & Marsh (1986) and can represent the shape of the hydrogen Balmer series lines in optical spectra, only affected by Newtonian Doppler shift.

For this analysis, in order to isolate the emission line profile, we normalised the spectra of J1305 using polynomial fits (fifth-order) and imported them into the XSPEC environment by creating unit diagonal response matrices. Finally, to better interpret the inferred disc radii, we expressed them in terms of the expected tidal radius, that is, the truncation radius set by the companion's tidal torque (Frank et al. 2002). This radius can be approximated as $R_T \simeq 0.9\,R_1$, where R_1 is the Roche-lobe radius of the compact object, derived using the Eggleton (1983) formula:

$$\frac{R_1}{a} = \frac{0.49\,q^{-2/3}}{0.6\,q^{-2/3} + \ln\left(1 + q^{-1/3}\right)}, \tag{2.1}$$

with $q = M_1/M_2$ the binary mass ratio and a the orbital separation obtained from Kepler's third law. This is the same Roche–lobe prescription introduced in Eq. 2.13 of Chapter 2 for the companion star, but rewritten here for the primary by replacing q with q^{-1}. Adopting BH masses of $\sim 8.9\,M_\odot$ for J1305 (Mata Sánchez et al. 2021), the corresponding gravitational radius is $R_g \approx 13$ km. This leads to orbital separations and tidal radius of $a = (2.52 \pm 0.002) \times 10^5\,R_g$ and $R_T = (1.45 \pm 0.06) \times 10^5\,R_g$ for J1305.

2.7.3 J1305 spectroscopy

Among the emission features present, I focused on Hα, which is the strongest isolated feature and is clearly detected in all spectra in both outburst and quiescent spectra.

Outburst

I decide to analyse separately the two days of observations. For the first night of observations, I analysed four out of six spectra, excluding those dominated by strong absorption or showing flat-top profiles suggestive of outflow-related features (see Miceli et al. 2024; Cúneo et al. 2020). These data were modelled with a power-law component to represent the normalised continuum (whose parameters are not physically meaningful), on top of which I added the DISKLINE model to fit the Hα line profile (hereafter MODEL 1). Given that the observations were obtained within a time interval of only one orbital period, I expect minimal spectral variations among the different spectra. For this reason, I constrained parameters such as the inclination angle, emissivity index, and inner and outer radii to remain the same for all spectra, while allowing the line energy to vary freely. On the second night, an additional absorption component was evident at wavelengths longer than the rest-frame Hα

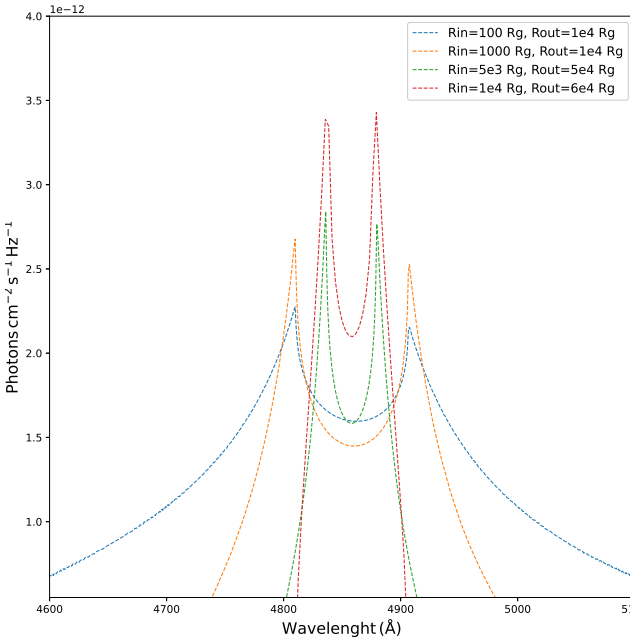

Figure 2.12: Line profile simulations obtained with the DISKLINE model, from Anitra et al. (2024). The inclination (i = 83°), emissivity index (β = 2.5), and line centroid (E = 4857.5 Å) are kept fixed, while the inner and outer radii are systematically varied in the ranges $(100 - 10^4)\,R_g$ and $(10^4 - 6 \times 10^4)\,R_g$, respectively. The figure illustrates how changes in the disc geometry affect the line profile shape. Model normalisations are scaled for visual clarity.

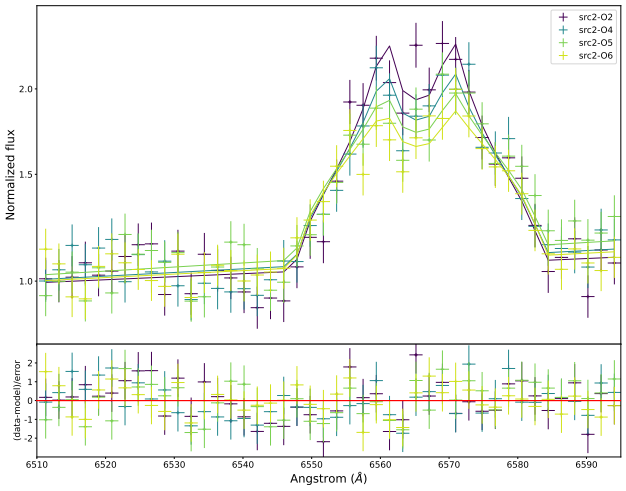

Figure 2.13: J1305 spectra obtained during the outburst phase and corresponding residuals (in units of sigma) with respect to the DISKLINE fit (MODEL 1), for the first night of observations. Figure adapted from Anitra et al. (2024).

(6563 Å, see previous section). To reproduce this feature, I complemented MODEL 1 with a Gaussian absorption component (MODEL 2), in which the centroid and FWHM were tied across spectra while the depth was allowed to vary. Both models yielded statistically acceptable results with a $\chi^2/\mathrm{dof} = 139.4/153$ (first day) and $\chi^2/\mathrm{dof} = 149.0/222$ (second day). The spectrum aand residuals are shown in Figs. 2.13 and 2.14, with best-fit parameters reported in Anitra et al. (2024). In both epochs, the inclination angle was constrained to $i \sim 70°$, consistent with the dynamical estimate of $i = 72^{+5}_{-8}$ deg by Mata Sánchez et al. (2021). Additionally, for the first day, I derived inner and outer radii values of $1.20^{+0.09}_{-0.07} \times 10^5$ Rg and $1.96^{+0.32}_{-0.27} \times 10^5$ Rg, respectively. For the second day, these values were $1.66^{+0.10}_{-0.08} \times 10^5$ Rg and $2.73^{+0.9}_{-0.6} \times 10^5$ Rg. Further discussion of these parameters is presented in the following section.

Quiescence

During quiescence, I analysed 10 out of 16 spectra collected with VLT/FORS2 (see Fig. 2.15), preferentially selecting symmetric double-peaked profiles to minimise the influence of asymmetries caused by hot spots or other disc structures. Fits with MODEL 1 alone left significant residuals in the line core, while MODEL 2 provided a more satisfactory description, ensuring a χ^2/dof of 4161.1/2620 (see Fig. 2.16). The final best-fit parameters, reported in Anitra et al. (2024), yield an inclination of $i = 72.6^{+1.4}_{-1.3}$ deg (90% c.l.), in excellent agreement with the independent dynamical constraint. The corresponding inner and outer radii of the Hα emitting region extend from $\sim 0.1 R_T$ to $\sim 1.3 R_T$.

2.8 Discussion in AA24

In this section I summarise the consistency checks we carried out for J1305, focusing on the independent tests that support the robustness of the spectral interpretation.

First, we examined whether the best-fit disc radii inferred from the modelling are consistent with the expected geometrical configuration of the system. A useful reference scale is the tidal radius, which sets the outer edge of the disc and is determined by the tidal torque exerted by the companion star (Frank et al. 2002).

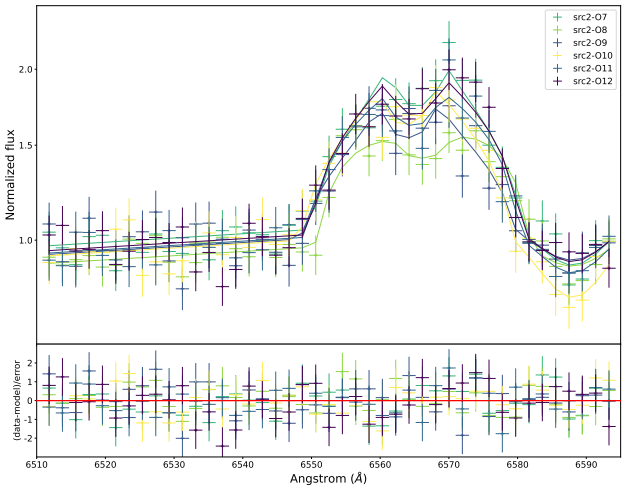

Figure 2.14: J1305 spectra obtained during the outburst phase and residuals (in units of sigma) relative to the DISKLINE model with an additional Gaussian absorption component (MODEL 2), for the second night of observations. Figure adapted from Anitra et al. (2024).

Although the exact value depends on several binary parameters, it is typically close to $R_T \simeq 0.9\,R_1$. I obtain an orbital separation of

$$a = (2.524 \pm 0.002) \times 10^5\,R_g,$$

which corresponds to a tidal radius of

$$R_T = (1.45 \pm 0.06) \times 10^5\,R_g.$$

The best-fit value of the outer disc radius obtained for the quiescent spectra is broadly consistent with the expected geometry of the system (although slightly larger than the tidal radius), whereas the radius inferred from the outburst spectra is entirely unphysical. In particular, the fitted value of $\sim 2 \times 10^6\,R_g$ exceeds the orbital separation by more than an order of magnitude. This discrepancy is not due to a computational mistake nor to a limitation inherent to the DISKLINE model. As reported by Miceli et al. (2024), the peak separation during outburst corresponds to a Doppler velocity of about $400\,km\,s^{-1}$. Assuming a Keplerian disc and applying Kepler's third law, the implied emitting radius is still larger than the orbital separation, reaching $\sim 5.49 \times 10^5\,R_g$. Such behaviour suggests that physical processes active during the outburst may modify the line-emitting region or its velocity field. One possibility is that the gas does not follow Keplerian motion. Under certain circumstances, a significant fraction of the dissipated energy can be advected into the BH, giving rise to an ADAF (see Chapter 2). Although ADAFs may arise at large radii (Narayan et al. 1997), they are typically associated with inner disc regions (Abramowicz et al. 1988; Chakrabarti & Titarchuk 1995). Even in standard accretion discs (Shakura & Sunyaev 1973), a local increase in viscosity could enhance the radial velocity component, causing departures from purely Keplerian rotation. Another possible explanation involves the presence of a circumbinary disc. At high accretion rates, outflows may expel material that subsequently accumulates around the binary, forming a viscous torus (Chen & Podsiadlowski 2019). Although such structures are usually cold, the intense X-ray luminosity during outburst ($L_X \sim 10^{37}\,erg\,s^{-1}$; Miller et al. 2014) may irradiate the circumbinary material sufficiently to power the atomic transitions responsible for the Hα emission. This could naturally produce an emitting region larger than the orbital separation itself. These possibilities remain speculative, and a more comprehensive analysis will be required to assess which mechanism, if any, is responsible for the anomalous radius inferred during the outburst.

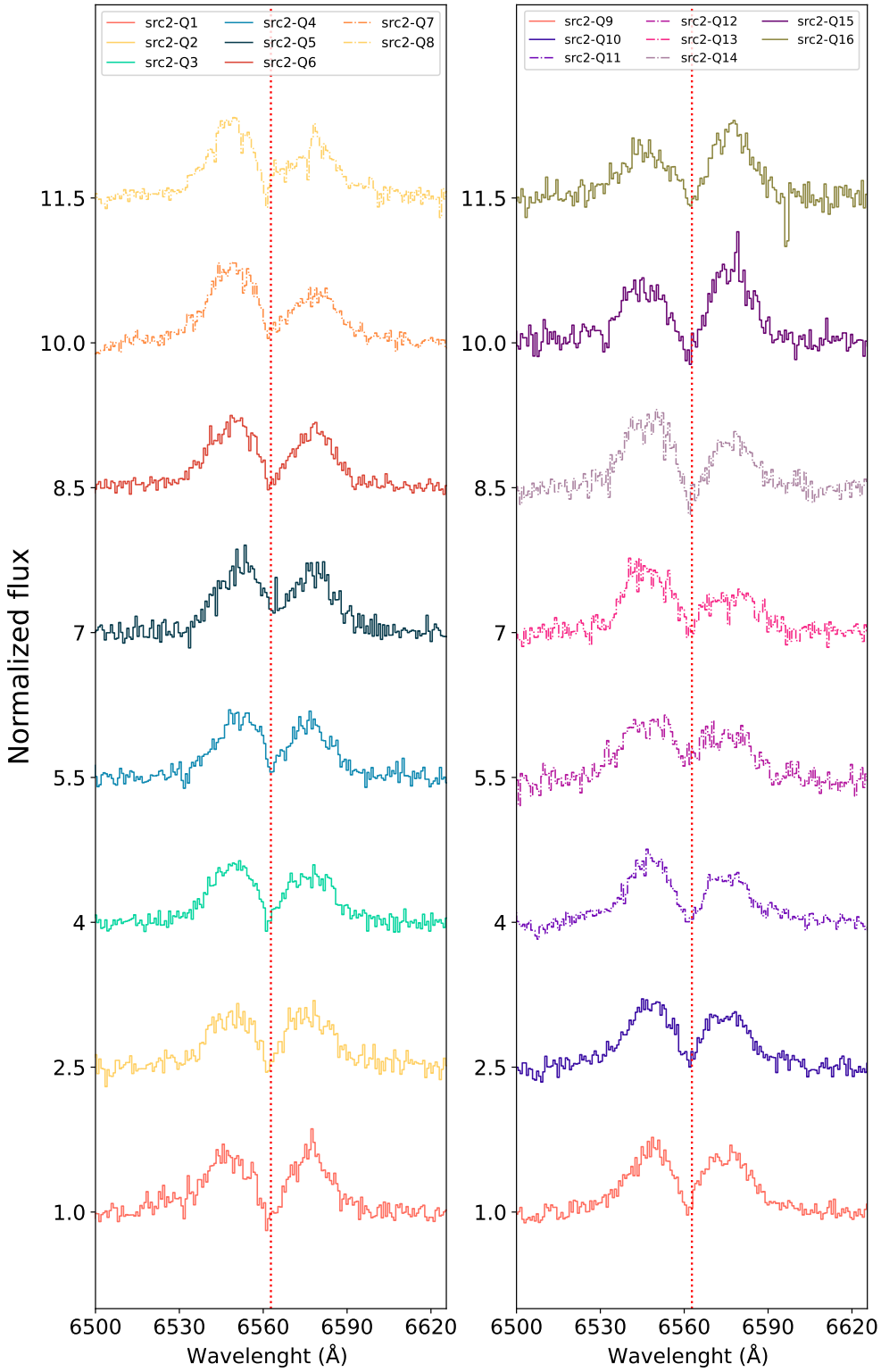

Figure 2.15: Individual Hα emission lines extracted from the spectra collected during the quiescent phase. The solid lines represent the spectra selected for the analysis, whereas the dashed lines correspond to those spectra that have been discarded. For visual clarity, the normalized profiles have been vertically separated by a constant offset.

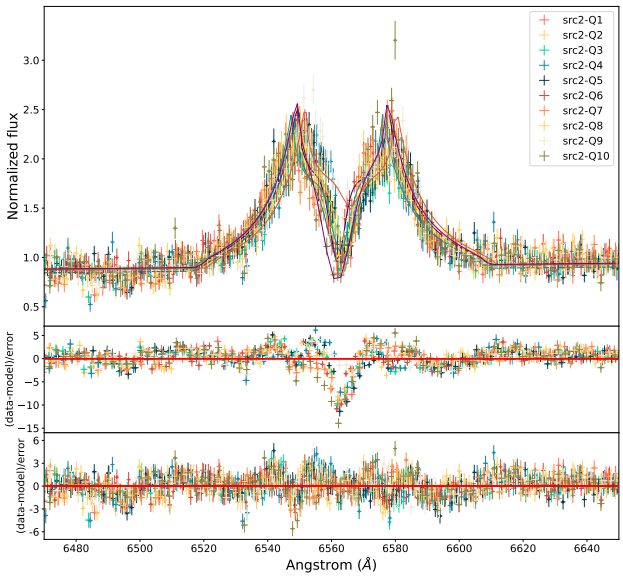

Figure 2.16: J1305 spectra obtained during the quiescent phase and residuals (in units of sigma) with respect to the DISKLINE model. The top panel shows the best fit including the Gaussian absorption component (MODEL 2), while the middle and bottom panels illustrate the residuals with MODEL 1 (diskline only) and with MODEL 2, respectively. Figure adapted from Anitra et al. (2024).

Second, although the inferred emitting radii for J1305 during quiescence appear consistent with the disc geometry, it is important to assess whether the gas at those distances can effectively host neutral hydrogen. Since the Hα lines arises from transitions in neutral H, excessively high temperatures would fully ionise the gas and suppress these features. The accretion disc structure can be described within the optically thick, geometrically thin approximation of Shakura & Sunyaev (1973). In the outer disc, the mid-plane temperature is given by

$$T = 8.6 \times 10^7 \, \alpha^{-1/5} \dot{m}^{3/10} m^{-1/5} r^{-3/4} (1 - r^{-1/2})^{3/10}, \tag{2.2}$$

where m, $\dot{m}$, and r are the dimensionless mass, accretion rate, and radius, and α is the viscosity parameter (here set to 0.1). The accretion rate for J1305 was estimated using its quiescent X-ray luminosity (Armas Padilla et al. 2014). At these large radii, the vertical structure is nearly isothermal, so the surface and central temperatures can be considered comparable. Using the inner and outer radii derived for J1305 in quiescence, the corresponding temperature range spans approximately 2081 ± 255 K down to 353 ± 40 K. To assess the ionisation state of hydrogen at these temperatures, I applied the Saha equation:

$$\log\left(\frac{H^+}{H}\right) = \log\frac{u^+}{u} + \log 2 + \frac{5}{2}\log T - 5040\,\frac{\chi_{\rm ion}}{T} - \log P_e - 0.48, \tag{2.3}$$

assuming an electron density $n_e = 10^{18}\,\mathrm{cm}^{-3}$ (Sincell & Krolik 1998). The resulting ionisation fractions range from 10^{-45} to 10^{-186}, indicating that hydrogen remains overwhelmingly neutral across the relevant radii. Therefore, the temperatures and ionisation conditions derived for J1305 are fully compatible with the formation of the Hα emission lines at the radii inferred from the disc-line modelling.

2.9 Conclusions in AA24

In this work we explored a complementary approach for studying the emission lines observed in the optical spectra of accreting binaries, making use of the DISKLINE model to place constraints on the geometry of the system. Although the DISKLINE model simplifies the physics of line formation—ignoring, for example, the effects of self-absorption in an optically thick atmosphere—its application in the optical band has proven useful for providing independent and physically consistent constraints on the disc geometry, including inclination, radial extent of the emission region, and the associated temperatures and ionisation conditions.

Future progress requires extending this methodology to a larger sample of sources. For this reason, we have submitted a VLT proposal aimed at applying the same strategy to additional XRBs, including eclipsing systems, where the comparison between different observational constraints would provide a robust test of the method. Access to multiple emission lines in the same object will also help to probe distinct disc annuli and refine our understanding of the complex physics behind optical emission in accreting compact objects.

3

Peculiar obscured Spectral State in GRS 1915+105

After discussing accretion disc winds in Chapter 3, with a particular focus on my investigation of outflow signatures through optical spectroscopy, this chapter turns to a complementary observational perspective. Here, I present an X-ray spectroscopic study of **GRS 1915+105**, a source that remains enigmatic in many respects and is characterized by extreme accretion rates, complex variability, and the persistent presence of powerful disc winds. In particular, the source exhibits episodes in which the inner regions of the system appear heavily obscured, offering a unique opportunity to investigate the structure and inclination of the accretion environment under conditions of high mass inflow. Before addressing the specific properties of GRS 1915+105 and presenting the results of the X-ray spectral analysis, it is useful to place this study within a broader context. As discussed in Chapter 1, the accretion flow in LMXBs involves multiple radiative and dynamical processes occurring in distinct regions of the system. These processes give rise to complex X-ray spectra shaped by the interplay of several physical mechanisms. Below, I summarize the main spectral components relevant for the analysis presented in this chapter.

3.1 X-ray Spectral Modeling

Interstellar absorption

Before modelling the intrinsic emission components of an X-ray spectrum, it is necessary to account for the effects of interstellar absorption, which primarily affects the spectrum at soft X-ray energies, typically below ~2–3 keV, where photoelectric absorption by neutral gas and dust is most effective. This absorption arises from photoelectric interactions between X-ray photons coming from the system and the intervening interstellar medium (ISM) along the line of sight and affects all spectral components in a multiplicative manner. Within the XSPEC (Arnaud 1996) spectral fitting framework, interstellar absorption is commonly modelled using dedicated components such as `phabs`, `wabs`, `tbabs`, and their variants. These models differ primarily in the assumed elemental abundances and photoelectric cross-sections. Earlier formulations, such as `wabs`, rely on outdated abundance tables, while more recent models provide a more accurate description of the ISM composition. In this work, interstellar absorption is modelled using the `tbabs` component (Wilms et al. 2000), which incorporates updated photoelectric cross-sections and interstellar abundances. The model is characterized by a single parameter, the equivalent hydrogen column density $N_{\rm H}$, which quantifies the amount of absorbing material along the line of sight.

Partial covering absorption

In addition to the interstellar absorption, X-ray spectra of accreting systems may be affected by local absorption arising within the binary system itself. This form of absorption can be associated with inhomogeneous or clumpy material located close to the X-ray source, the nature of which is still under debate (e.g., V404 Cyg Życki et al. 1999; Motta et al. 2017, and SS 433, (Fabrika 2004)). Unlike interstellar absorption, which uniformly attenuates all emission components along the line of sight, local absorbers may only partially cover the X-ray emitting region. Within the XSPEC framework, this scenario can be modelled using the `pcfabs` component, which describes a neutral partial covering absorber. The model is characterized by two main parameters: the equivalent hydrogen column density of the absorber, $N_{\mathrm{H,pc}}$, and the covering fraction, f_{cov}, which represents the fraction of the X-ray source obscured by the absorbing material. The remaining fraction of the emission is transmitted without additional local absorption. Alternative models are also available to describe more complex absorption scenarios, including ionized partial covering components such as `zxipcf` or absorbers based on photoionization grids generated with XSTAR. These models provide a more physical description of ionized winds but require higher spectral resolution and signal-to-noise to be reliably constrained. In this work, `pcfabs` is adopted as an effective phenomenological approach to account for the obscuration observed in GRS 1915+105.

Thermal blackbody-like component

At low X-ray energies (approximately 0.5–2 keV), the X-ray spectrum of BH XRB is generally dominated by a thermal blackbody-like component, originating from the accretion disc. The physical origin of this component, its formation mechanisms, and its main properties have been discussed in detail in Section 1.7. In the context of this chapter, the focus shifts from the underlying physical interpretation to the practical modelling of this emission. This component is typically described within XSPEC using a variety of phenomenological and physically motivated models, depending on the nature of the compact object and the quality of the data.

For BH systems, the thermal disc emission is commonly modelled using multicolour blackbody models, such as `diskbb`, which approximates the accretion disc as a superposition of blackbody spectra at different temperatures. The main parameters of this model are the inner disc temperature, T_{in}, and a normalization that is related to the apparent inner disc radius[1] and the source distance. More advanced models, including `diskpn`, `kerrbb`, and `bhspec`, incorporate additional physical effects such as relativistic corrections, inner boundary conditions, and spectral hardening; however, a detailed discussion of these models lies beyond the scope of this thesis. The choice of model and parametrization plays a crucial role in shaping the inferred physical picture and must be carefully adapted to the source state and observational constraints.

Comptonization

At higher energies, up to a hundred of keV, a hard Comptonized component typically becomes dominant. This emission is usually described by a power-law with a high-energy cutoff and is produced by Compton up-scattering of soft photons (e.g. Poutanen & Coppi 1998). The physical origin and properties of this process have been discussed in Chapter 1. In X-ray spectral fitting, Comptonization spectrum is modelled within the XSPEC framework using both phenomenological and physically motivated models. Simple representations

[1] on the correction factor between the apparent inner disk radius and the realistic radius, see e.g. Kubota et al. 1998

include a cutoff power-law (`cutoffpl`), characterized by a photon index and an exponential cutoff energy, which provides a convenient but approximate description of the spectrum. More physically motivated models explicitly account for the Comptonization process and its underlying parameters, including `comptt`, `compPS`, and `nthcomp`. In this work, the hard X-ray component is modelled using the `nthcomp` model, which provides an accurate description of the continuum shape produced by thermal Comptonization while remaining relatively simple in terms of parameterization. Compared to an exponentially cutoff power law, `nthcomp` reproduces a sharper high-energy rollover, which is directly parameterized by the electron temperature kT_e. While a rough correspondence between the exponential cutoff energy and the electron temperature can be expressed as $E_c \simeq 2\text{–}3\,kT_e$, the spectral shape around the cutoff is markedly different, with important implications for the inferred reflection fraction. In addition, `nthcomp` naturally incorporates the low-energy rollover of the Comptonized spectrum, which arises because hot electrons up-scatter seed photons, resulting in a deficit of scattered photons below the characteristic seed photon energy. This behaviour is particularly relevant for XRBs and cannot be captured by a simple power-law model. The seed photon spectrum in `nthcomp` can be specified as either a single-temperature blackbody or a multicolour disc blackbody, parameterized by the seed photon temperature kT_{seed}. This flexibility allows the Comptonized component to be consistently linked to thermal emission originating from the NS boundary layer or the accretion disc. Between the low- and high-energy rollovers, the spectral shape is determined by the combination of the electron temperature and the optical depth of the scattering medium. Although the resulting spectrum is not strictly a power law, it can be conveniently characterized by an asymptotic photon index Γ, which describes the slope of the spectrum in this intermediate energy range. A detailed discussion of the underlying formalism is provided in Życki et al. (1999).

Reflection

The presence of a reflection component in X-ray spectra of accreting BH systems arises from the reprocessing of hard X-ray photons by the accretion disc. The physical origin and diagnostic power of reflection features have been discussed in Chapter 2. X-ray reflection spectra are commonly modelled using the `xillver` family of models (García et al. 2013), which compute the reflection spectrum produced by an optically thick, ionized accretion disc illuminated by an external continuum. Relativistic effects arising in the inner regions of the disc are incorporated through convolution with relativistic blurring kernels, such as `relline`. These two components are combined self-consistently in the `relxill` suite of models (García 2014; Dauser 2014). Within this framework, several variants are available depending on the assumed shape of the illuminating continuum. In this work, the reflection component is modelled using the `relxillCp` model, in which the incident spectrum is described by a thermal Comptonization continuum consistent with the `nthcomp` model. In this formulation, the reflection spectrum includes both the reflected continuum and the associated fluorescent emission lines of the iron Kα. The `relxillCp` model includes a set of parameters describing both the properties of the accretion disc and the illuminating source. These include the inner disc radius (R_{in}), the BH spin parameter (a^*), the disc inclination angle (i), the ionization parameter of the reflecting material (ξ), the iron abundance (A_{Fe}), and the emissivity profile of the disc. The reflection fraction (R_f) quantifies the relative contribution of the reflected emission with respect to the direct Comptonized continuum.

In addition to self-consistent reflection models, it is useful to consider dedicated models for relativistic emission lines. In this context, the `diskline` model in XSPEC provides a relativistic description of an emission line originating from an accretion disc around a compact object, following the formulation of Fabian

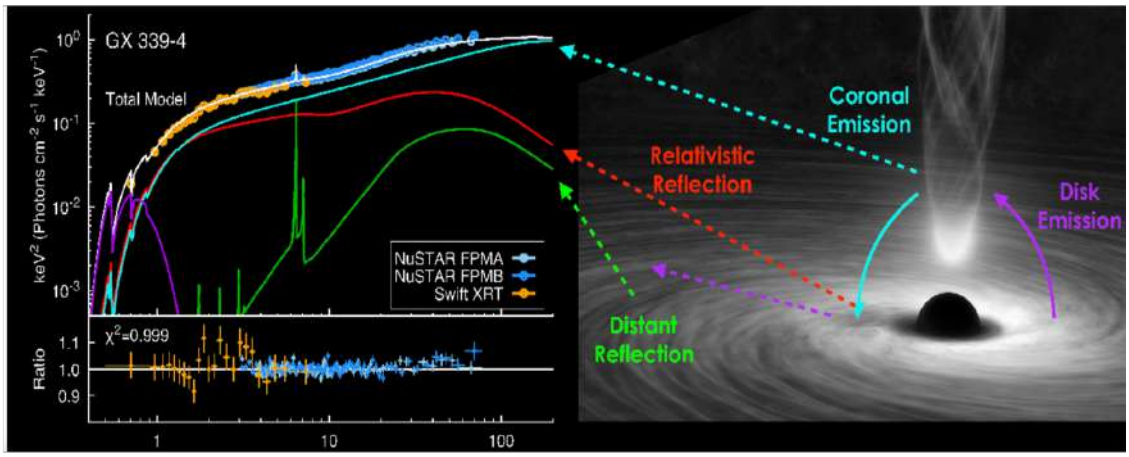

Figure 3.1: Broadband X-ray spectral modeling of the BH XRB GX 339–4. *Left panel:* Joint *NuSTAR* (FPMA and FPMB) and *Swift*/XRT spectrum fitted with a multi-component model. The total model (white solid line) and its individual components are shown: thermal disc emission (`diskbb`, purple), coronal Comptonized emission (`nthComp`, cyan), relativistic reflection from the inner disc (`relxilllpCp`, red), and distant reflection (`xillverCp`, green). The lower panel shows the data-to-model ratio. *Right panel:* Schematic view of the accretion geometry illustrating the origin of the different spectral components. Adapted from García et al. (2019)

(1989). While modern reflection models such as `relxill` compute the iron line self-consistently as part of the reflected spectrum, in practice the observed Fe Kα profile in complex or heavily absorbed spectra may not always be fully reproduced by the reflection continuum alone. In such cases, a relativistic line model offers additional flexibility in capturing structured residuals in the Fe–K band and allows the line properties to be constrained more directly. The `diskline` model assumes a geometrically thin, optically thick disc extending between an inner and outer radius, and subject to relativistic Doppler shifts and gravitational redshift. Its key parameters include the rest-frame line energy $E_{\rm line}$, the inner and outer disc radii ($R_{\rm in}$ and $R_{\rm out}$), the disc inclination i, and the emissivity index q, which describes how the line emissivity scales with radius ($\epsilon \propto r^{-q}$). The line normalization sets the total emitted flux. Owing to its simplicity and computational efficiency, `diskline` is often employed to provide a description of the relativistic line component.

Figure 3.1 shows an example of an accreting BH X-ray spectrum, illustrating the main spectral components discussed above. However, the relative strength and observational visibility of each component strongly depend on the accretion state of the system. In particular, transitions between hard and soft spectral states are accompanied by significant changes in the dominant emission mechanisms and in the geometry of the accretion flow. In the soft state, the spectrum is typically dominated by the thermal emission from the accretion disc, while the Comptonized component is weaker and characterized by a steeper spectral slope. Conversely, in the hard state the spectrum is dominated by the Comptonized continuum, with the thermal disc component becoming fainter or detectable only at lower energies. Reflection features are expected to be present in both states, as they arise from the reprocessing of the primary X-ray emission by the accretion disc; however, their prominence and spectral imprint depend on the illumination geometry, ionization state of the disc, and the properties of the primary continuum. Figure 3.2 schematically illustrates the main spectral components in the hard and soft states, highlighting their relative contributions across the X-ray band.

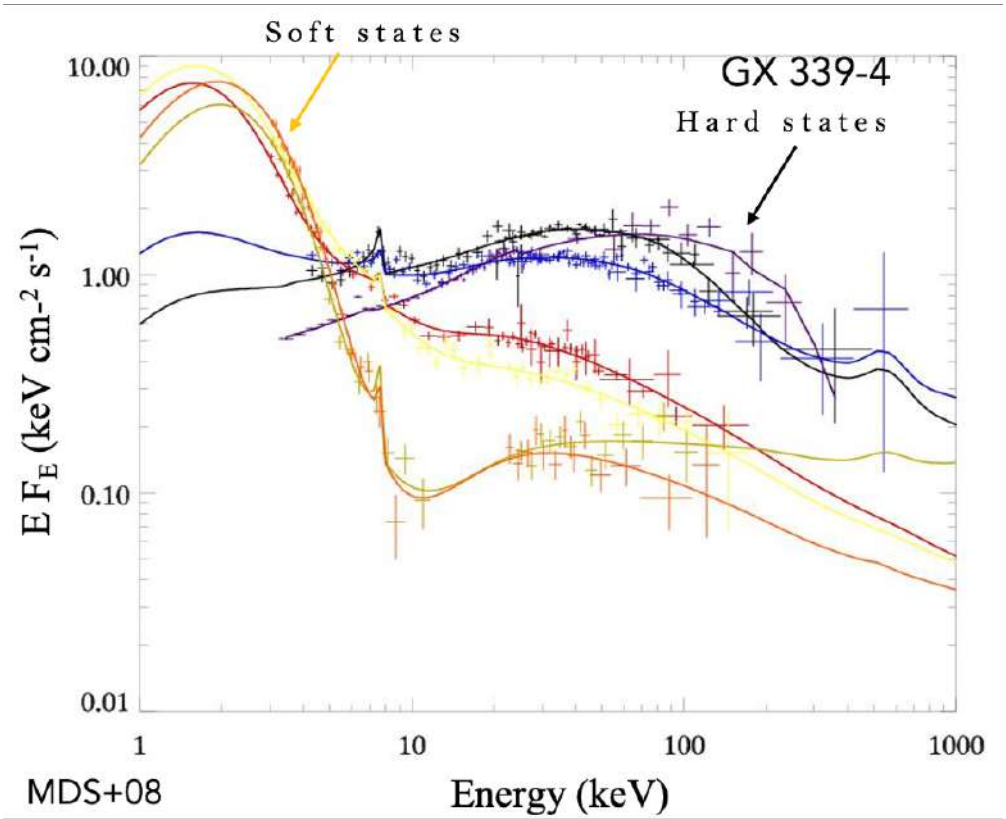

Figure 3.2: Joint JEM-X, IBIS, and SPI broadband X-ray spectra of the BH XRB GX 339−4 observed during different accretion states, illustrating the evolution of the relative contributions of the main spectral components across the X-ray band. The figure highlights the contrast between soft and hard spectral states. Adapted from Del Santo et al. (2008).

3.2 GRS 1915+105: source overview

GRS 1915+105 is one of the most extensively studied Galactic BH XRBs and represents an extreme laboratory for investigating accretion and ejection processes across a wide range of physical regimes. First detected as a bright X-ray transient in August 1992, the source remained persistently luminous in both X-rays and radio until recently (Negoro et al. 2018), exhibiting a phenomenology unmatched by any other known Galactic BH system. It was the first Galactic source in which apparent superluminal radio motions were observed (Mirabel & Rodríguez 1994), firmly establishing GRS 1915+105 as the prototypical "microquasar" and a cornerstone for studies of relativistic jets.

Radio parallax measurements place GRS 1915+105 at a distance of $d = 9.4 \pm 0.6$ kpc (Reid & Miller-Jones 2023), implying a BH mass of $M = 11 \pm 2\ M_{\odot}$ and a relatively high inclination, $\theta = 64 \pm 4^{\circ}$ when combined with optical radial velocity constraints. The inclination value is consistent with independent constraints from reflection spectroscopy (Miller et al. 2013; Draghis et al. 2024). Jet velocities inferred from radio observations range between $0.68 \lesssim v/c \lesssim 0.91$, highlighting the highly relativistic nature of the outflows (Reid & Miller-Jones 2023).

One of the defining characteristics of GRS 1915+105 is its extraordinary X-ray variability. The source displays at least twelve distinct variability classes, originally classified by Belloni et al. (2000), which are thought to reflect different configurations of the accretion disc, corona, and jet. Unlike canonical BH transients, whose behaviour is typically organized into a small number of spectral states, GRS 1915+105 exhibits transitions between three accretion states—two soft and one hard—that do not map cleanly onto the standard hard and soft states observed in other BH binaries (Motta et al. 2021). The soft states are generally characterized by thermal disc-dominated spectra with temperatures reaching ~2 keV and low variability, while the hard state shows strong aperiodic variability, a dominant Comptonized component, and a reduced or absent disc contribution. A notable system displaying phenomenology closely resembling that of GRS 1915+105 is IGR J17091–3624, which exhibits similarly complex variability patterns and heartbeat oscillations, albeit at significantly lower luminosities (Altamirano et al. 2011).

GRS 1915+105 is also a key system for studying the interplay between disc winds and relativistic jets. The properties of the winds appear to depend on spectral state and jet activity (Neilsen et al. 2009), although some level of wind activity may persist across all states (Neilsen et al. 2018). In soft, sub-Eddington, disc-dominated states, highly ionized winds with velocities as high as $v \simeq 0.03c$ have been detected (Miller et al. 2016), placing them in close analogy with ultra-fast outflows observed in Seyfert galaxies and quasars (see e.g. Tombesi et al. 2010; Gallo et al. 2023). This striking similarity reinforces the role of GRS 1915+105 as a Galactic analogue of accreting supermassive BHs.

In recent years, however, the phenomenology of GRS 1915+105 has undergone a dramatic transformation. After approximately 26 years of sustained high activity, the source entered an extended low-flux state in July 2018 (MJD 58300) (Negoro et al. 2018; Motta et al. 2019). However on 2019 May 14 (MJD 58617), renewed flaring activity across multiple wavelengths challenged the interpretation of the source having entered quiescence. X-ray observations revealed hard spectra affected by exceptionally strong and sometimes partially covering absorption, with intrinsic column densities exceeding $N_{\rm H} \gtrsim 3 \times 10^{23}$ cm^{-2}, more than an order of magnitude higher than the Galactic line-of-sight value (Miller et al. 2019a; Miller et al. 2020; Balakrishnan et al. 2021). This "obscured state" had never previously been observed in GRS 1915+105 and is rare among XRBs.

Comparable levels of intrinsic obscuration have only been observed in a handful of systems, most notably V404 Cyg during its major outbursts (Życki et al. 1999; Motta et al. 2017) and SS 433, which is believed to be persistently obscured by its inflated accretion disc (Fabrika 2004). In all cases, the obscuration is thought to be linked to extreme, possibly super-Eddington accretion and strong outflows, often accompanied by intense jet activity (Spencer 1979; Miller-Jones et al. 2019). In this context, GRS 1915+105 has transitioned from resembling an unobscured Seyfert-like system to exhibiting properties more akin to highly obscured Seyfert 2 or even Compton-thick AGN (CTAGN), with internal column densities approaching or exceeding $N_{\rm H} \sim 10^{24}$ cm^{-2} (Miller et al. 2020).

The obscured state has been further confirmed by multi-wavelength observations. Chandra grating spectra indicate that the obscuration may arise from dense, possibly failed disc winds (Miller et al. 2020), while *JWST*/MIRI observations reveal mid-infrared fluxes an order of magnitude higher than previously recorded, consistent with a large obscuring structure surrounding a still actively accreting central engine (Gandhi et al. 2025). Despite the strong X-ray obscuration, the source continues to accrete at ∼5–30% of its Eddington luminosity. Radio observations further indicate that the compact jet remains active, undergoing structural or energetic changes during the obscured phase (Rodríguez & Mirabel 2025).

GRS 1915+105 is a wide binary system, with an orbital period of $P = 33.85 \pm 0.16$ days (Steeghs et al. 2013). In other wide binaries, super-orbital periods are often attributed to the precession of a warped accretion disc. Recent changes in the position angle of the radio jet in GRS 1915+105 may also confirm this hypothesis (Rodríguez & Mirabel 2025), offering a natural geometrical mechanism for producing dramatic changes in obscuration. Within the framework of AGN unification models (Antonucci 1993), such a geometrical evolution would effectively transform a "microquasar" into a "micro-Compton-thick AGN".

Considerable effort has been devoted to measuring the BH spin in GRS 1915+105, motivated by its extreme jets and the possibility that they are powered by rotational energy extraction (Blandford & Znajek 1977). Reflection modelling of *NuSTAR* spectra yields a high spin parameter, $a \simeq 0.98 \pm 0.02$ (Miller et al. 2013; Draghis et al. 2024). Independent measurements based on disc continuum fitting and QPOs yield values ranging from $a \gtrsim 0.7$ to near-maximal spin (McClintock et al. 2006; Middleton et al. 2006; Motta & Belloni 2024), underscoring both the extreme nature of the system and the ongoing refinement of its fundamental parameters.

Recent high-resolution X-ray spectroscopy with the *XRISM* Resolve calorimeter of GRS 1915 +105 reveals that the central engine in its obscured state is covered by a layer of warm, Compton-thick gas, effectively acting as a coronagraph that obscures direct continuum emission (Miller et al. 2025). The spectrum is dominated by numerous strong, narrow emission lines from He-like and H-like charge states of elements ranging from Si to Ni, as well as prominent radiative recombination continuum (RRC) features, indicating that a large portion of the emitting gas is photoionized. Their findings support a scenario in which the observed obscuration arises from a warped or thickened outer disk brought into the line of sight, emphasizing complex disk geometry in the heavily absorbed state of this system.

In this work, I present a phenomenological X-ray spectral study of GRS 1915+105 during its obscured state, focusing on data obtained with *NuSTAR* and *XMM-Newton* during the 2021 soft X-ray re-brightening episode. The X-ray evolution of GRS 1915+105 around the obscured phase provides an important context for interpreting the nature of this peculiar state. In July 2021, a soft X-ray re-brightening was observed with MAXI/GSC, NICER, and AstroSat (Neilsen et al. 2021; Ravishankar et al. 2021), marking the second such event during the low-flux phase that followed the 2018 transition (see Fig.3.3. During this episode,

the spectrum displayed numerous absorption lines from highly ionized elements (e.g., Si, S, Ar, Ca, Fe, Ni), together with an Fe Kα emission feature, indicating the presence of a dense ionized absorber with column densities exceeding $N_{\rm H} \gtrsim 5 \times 10^{23}\,{\rm cm}^{-2}$. At the same time, the detection of a low-frequency QPO at ~ 0.17 Hz revealed the coexistence of wind signatures and timing features that are typically associated with different accretion states. As discussed by Kong et al. (2024), this re-brightening phase appears to trace transitions between thermally and magnetically driven outflows. In their interpretation, these changes can lead to the formation of a dense, Compton-thick structure produced by a low-velocity "failed wind," with periods of enhanced ionization and column density linked to magnetic activity. Perturbations in the magnetic field may propagate into the obscuring material and trigger low frequency QPOs, providing a possible connection between disk winds, magnetic processes, and rapid variability. Within this broader evolutionary picture, the obscured state studied in this work may represent a phase in which complex, dense outflow structures temporarily reshape the inner accretion environment. Placing the observations in the context of the long-term X-ray evolution therefore supports a scenario in which the obscuration is not an isolated phenomenon, but part of a dynamic sequence of accretion-driven structural changes occurring during the low-flux state.

In particular, while joint X-ray analyses involving other instruments have been reported in the literature, a dedicated broadband spectral study combining *NuSTAR* and *XMM-Newton* observations during this specific obscured phase has not been presented so far. While *XMM-Newton* provides high sensitivity and spectral resolution in the soft X-ray band, enabling a detailed characterization of absorption features and emission lines, *NuSTAR* extends the spectral coverage to hard X-rays, allowing the continuum shape to be robustly constrained. The aim of this analysis is to constrain the geometry of the inner accretion flow and to investigate the nature of the obscuring structure responsible for the complex absorption observed during the 2021 re-brightening.

3.3 Observations and data reduction

The data used for this analysis were quasi-simultaneous and obtained during its 2021 soft X-ray re-brightening phase (Neilsen et al. 2021). In particular, I used data from *XMM-Newton*, taken on 9 October 2021, and from *NuSTAR*, taken on 30 September 2021 (MJD 59487). The two observations were separated by less than ten days and were performed during a period of enhanced soft X-ray activity reported by several monitoring instruments (Neilsen et al. 2021; Kong et al. 2024) and see Fig. 3.3.

3.3.1 XMM-Newton

The *XMM-Newton* observation (ObsID: 0864960101) was performed with the European Photon Imaging Camera (EPIC), using the pn detector in Timing mode (Strüder et al. 2001), which provides high throughput and moderate spectral resolution in the 0.3–10 keV energy band. Data reduction was carried out using the Science Analysis Software (SAS) version 20.0.0, following the standard SAS analysis threads.

The Observation Data Files (ODFs) were processed using the `epproc` task to generate calibrated event files. An image in the 2–10 keV energy band was extracted to locate the source, and the position was refined via point spread function (PSF) fitting. Source events were extracted using `evselect` from a rectangular region defined by CCD RAWX columns 30–44, centred on the source position along the readout direction.

The background spectrum was extracted from a nearby source-free region on the same CCD, selecting

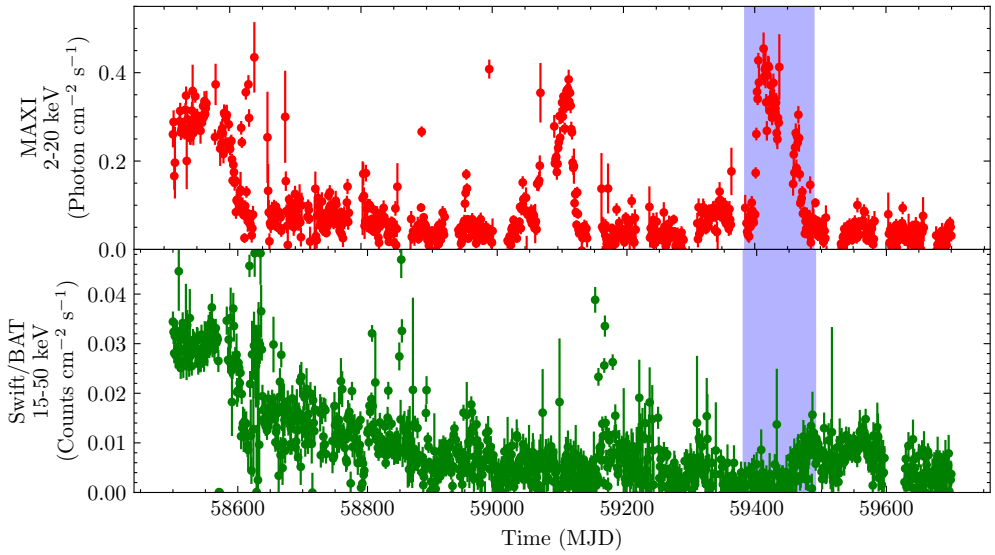

Figure 3.3: Light curves of GRS 1915+105 obtained with the MAXI all-sky monitor in the 2–20 keV energy range and with *Swift*/BAT in the 15–50 keV band, showing the transition into a prolonged low-flux state. The re-brightening episode observed in 2021, which constitutes the primary focus of this work, is highlighted in blue. Adapted from Kong et al. (2024).

RAWX columns 2–10. Standard filtering criteria were applied, retaining only single and double pixel events (`PATTERN ≤ 4`) and excluding bad pixels and columns (`FLAG == 0`). The response matrix file (RMF) and ancillary response file (ARF) were generated using the `rmfgen` and `arfgen` tasks, respectively. Finally, the spectrum was grouped to a minimum of 25 counts per bin using `grppha`.

3.3.2 NuSTAR

NuSTAR observed GRS 1915+105 on 30 September 2021 (ObsID: 90701332002). The raw data were reprocessed using the `nupipeline` task included in the *NuSTARDAS* software package (version 2.1.2), distributed with HEASoft version 6.31, and the most recent calibration database (CALDB).

Standard screening criteria were applied to remove events recorded during passages through the South Atlantic Anomaly (SAA), Earth occultation, and periods of invalid star tracker data, producing cleaned Level 2 event files for both focal plane modules, FPMA and FPMB.

Science products were extracted using the `nuproducts` task. Source and background regions were defined using *ds9*, adopting circular extraction regions with radii of 50″ and 100″, respectively, and applied consistently to both modules. The attitude and housekeeping files were specified through the `attfile` and `hkfile` parameters. This procedure generated source and background spectra, light curves, and the corresponding response files (ARF and RMF).

The spectra were finally grouped using the `ftgrouppha` tool from the FTOOLS package, adopting the optimal binning scheme (`grouptype=opt`) and specifying the background spectra to guide the grouping process (Harrison et al. 2013).

3.4 Spectral analysis

After data reduction, I performed a simultaneous spectral fit of the *XMM-Newton*/EPIC-pn and *NuSTAR* FPMA/FPMB spectra using XSPEC v12.12.0. The EPIC-pn data were fitted in the 2–10 keV band, while the *NuSTAR* spectra were fitted in the 3–70 keV range. These choices minimize calibration uncertainties at low energies and ensure sensitivity to the Fe–K band and to the high-energy curvature associated with reflection.

Given the spectral complexity of GRS 1915+105 in the obscured state, I adopted an incremental approach to build the spectral model, adding components only when required by statistically significant residuals. As a starting point, I modelled the continuum with interstellar absorption and a partially covered spectrum,

$$\texttt{constant} \times \texttt{TBabs} \times \texttt{pcfabs} \times \texttt{relxillCp}, \tag{3.1}$$

where `TBabs` accounts for absorption along the line of sight and `pcfabs` describes additional dense material local to the source that only partially covers the X-ray emitting region. The `relxillCp` component provides a physically motivated description of the primary continuum and relativistic disc reflection, including the Fe K emission line computed self-consistently with the reflection continuum.

This baseline model captures the overall broadband shape but leaves structured residuals in two main regions. First, significant curvature is present at low energies around ~2.5 keV. This feature is well described by adding a multiplicative absorption edge,

$$\texttt{constant} \times \texttt{TBabs} \times \texttt{edge} \times \texttt{pcfabs} \times \texttt{relxillCp}. \tag{3.2}$$

The `edge` component models the increase in photoelectric opacity above a threshold energy $E_{\rm edge}$, parameterized by $E_{\rm edge}$ and by the optical depth at threshold $\tau_{\rm max}$. In the present case, the best-fitting edge energy is consistent with inner-shell absorption from sulphur, suggesting additional opacity associated with locally ionized material.

Second, the Fe–K band shows line-like residuals both in emission and absorption. For this reason, I added narrow Gaussian components representing discrete emission and absorption lines, primarily constrained by the EPIC-pn spectrum owing to its superior spectral resolution at soft X-ray energies. In practice, these Gaussians model narrow features attributable to highly ionized species (e.g. Fe XXV/Fe XXVI in the Fe–K band and lower-energy transitions from lighter elements), as reported in Tables 3.1 and 3.2.

Finally, an additional broad relativistic line component was required to reproduce the remaining structured residuals in the Fe–K region. Although `relxillCp` includes a relativistic iron line self-consistently, the inclusion of a standalone `diskline` component significantly improves the fit and provides additional flexibility in capturing excess broad line-like emission not accounted for by the reflection continuum alone. The final model therefore takes the form `constant`×`TBabs`×`edge`×`pcfabs` (`diskline`+`gaussians`+`relxillCp`) shown schematically in Fig. 3.4. A multiplicative constant was included to account for cross-calibration differences between instruments.

As a first working hypothesis, all spectral parameters were initially tied between the two observations. Although the *XMM-Newton* and *NuSTAR* datasets are not strictly simultaneous, they are separated by only ~9 days, and it is therefore reasonable to test whether a single set of spectral parameters can describe both spectra. Within this framework, interstellar absorption (`TBabs`), the energy of the edge, and the centroid energies

and widths of the narrow Gaussian lines were kept tied across the two observations. These parameters were ultimately retained as linked, since primarily constrained by the *XMM-Newton* data, which provide superior spectral resolution in the soft X-ray band and therefore dominate the determination of their energies and widths. I also kept tied the inclination, inner radius, and emissivity indices of the relativistic components (`diskline` and `relxillCp`), ensuring a consistent geometrical description of the accretion flow.

The remaining parameters such as the column density and covering fraction of the local, partially covering absorber (`pcfabs`), the normalizations of both the relativistic line and the reflection continuum, and the spectral slope of the Comptonized emission (`relxillCp` Γ) were also initially linked between the two datasets. However, allowing them to vary independently resulted in a significant improvement of the fit, revealing that these quantities differ between the *XMM-Newton* and *NuSTAR* spectra. Such differences can be attributed to the short-timescale spectral variability that characterizes GRS 1915+105 (Athulya & Nandi 2023), especially in its obscured state. For this reason, these parameters were ultimately left free to vary between the two observations.

3.4.1 XMM-Newton results

The fit to the EPIC-pn spectrum (see Tables 3.1 and 3.2) yields an interstellar hydrogen column density of $N_{\rm H}^{\rm ISM} = (9.7^{+0.8}_{-1.0}) \times 10^{22}$ cm^{-2}, consistent with previous results (Balakrishnan et al. 2021). In addition, a dense partially covering absorber is required, with a column density of $N_{\rm H}^{\rm pcf} \sim 7.9 \times 10^{23}$ cm^{-2} and a covering fraction of 0.95 ± 0.01, confirming the presence of strong local obscuration (Miller et al. 2025).

A significant low-energy absorption edge is detected at $E_{\rm edge} = 2.50^{+0.05}_{-0.04}$ keV with an optical depth of $\tau_{\rm edge} = 0.51^{+0.21}_{-0.23}$. This energy is consistent with the K-shell absorption threshold of sulphur (e.g. S XV–S XVI, around 2.47–2.62 keV), suggesting that part of the obscuring material contains moderately ionized S. Such features are commonly associated with dense, locally ionized absorbers (Díaz Trigo & Boirin 2016).

We found several Gaussian components in both emission and absorption. Gaussian emission lines are in the 2.6–3.2 keV energy range, consistent with light elements such as S and Ar, respectively. In addition, Gaussian absorption features are found at 6.67 keV and 6.97 keV, likely associated with resonant absorption from highly ionized iron.

The emission feature at 6.81 keV shows significant relativistic broadening and was therefore modelled using a `diskline` component. The best-fit parameters imply an inclination angle of 42^{+2}_{-7} degrees and constrain the inner disc radius to $R_{\rm in} < 10\,R_{\rm g}$, indicating an origin in the inner regions of the accretion disc, close to the innermost stable circular orbit.

Allowing the inclination angle to vary independently in the `diskline` and `relxillCp` components yields best-fit values of $41.7^{+3.8}_{-5.4}$ and $36.7^{+4.7}_{-9.3}$ degrees, respectively. These values are statistically consistent within uncertainties, indicating that the inclusion of both reflection components is supported by the data and not driven by parameter degeneracies. For these reasons I then tied the inclination parameter between the two dataset.

The `relxillCp` component yields a high ionization parameter of $\log \xi = 3.6^{+0.4}_{-0.3}$, consistent with reflection from a highly ionized disc surface. The photon index of the illuminating continuum is $\Gamma = 1.79 \pm 0.14$, while the reflection fraction was not constrained.

3.4.2 NuSTAR results

The *NuSTAR* spectra (see Table 3.3) confirm the presence of strong reflection features and provide tighter constraints on the high-energy continuum. I found both a lower ionization parameter, $\log \xi = 2.3 \pm 0.3$, and a `diskline` component centered at 6.49 keV in the *NuSTAR* spectrum, indicating emission from less ionized iron. Taken together, these results may suggest that the reflection arises from slightly larger disc radii, or that the ionization state of the absorbing and reflecting material evolved between the two observations.

The photon index measured with *NuSTAR* is $\Gamma = 1.67^{+0.03}_{-0.02}$, which is statistically consistent with the value obtained from the EPIC-pn spectrum. The electron temperature is constrained to a lower limit $kT_e > 88$ keV (suggesting that the electron temperature is poorly constrained) while the obtained reflection fraction is $R_f = 0.65^{+0.09}_{-0.12}$ (I then fixed the XMM one to this value). The 6.97 keV absorption line detected with EPIC-pn is not required by the *NuSTAR* spectrum, possibly due to intrinsic variability of the absorber or to the lower spectral resolution of *NuSTAR*.

The fit statistics are acceptable for both datasets, with $\chi^2/\mathrm{dof} = 232.2/216$ for EPIC-pn and $650.3/528$ for *NuSTAR*.

3.4.3 Reflection geometry

I further explored the relative location of the line-emitting region and the reflection component by allowing the inner radii of the `diskline` and `relxillCp` components to vary independently, while keeping their inclination angles tied. This yields $R_{\rm in}^{\texttt{diskline}} = 9.3^{+2.0}_{-3.0}\, R_g$ and an upper limit of $R_{\rm in}^{\texttt{relxillCp}} < 6.3\, R_g$ (90% confidence). These results are consistent with the line-emitting region and the reflection-dominated disc region arising from comparable radii, within the limitations of the adopted phenomenological description.

Overall, the spectral analysis suggests that during the 2021 re-brightening phase GRS 1915+ 105 remained heavily obscured, yet still exhibited strong relativistic reflection signatures. This implies that, despite the extreme absorption, part of the inner accretion disc and the coronal emission region remained at least partially visible.

From the unabsorbed flux of $F = 2.79 \times 10^{-10}$ erg cm^{-2} s^{-1}, and assuming a BH mass of 11 $M_\odot$ and a distance of 9 kpc (Reid & Miller-Jones 2023), I derive an intrinsic luminosity of $L \simeq 2.7 \times 10^{36}$ erg s^{-1}, corresponding to approximately 0.2% of the Eddington luminosity.

3.5 Discussion

Despite the constraints obtained from spectral fitting, several aspects of the physical configuration remain uncertain. The complexity of the observed spectrum suggests a scenario that cannot be uniquely interpreted and is still the subject of ongoing discussion.

What I found is that both *XMM-Newton* and *NuSTAR* spectra require the presence of a dense, partially covering absorber, with column densities reaching $N_H \sim 10^{23}$–10^{24} cm^{-2} and covering fractions as high as $f_{cov} \sim 0.9$. This confirms that GRS 1915+105 remained in a heavily obscured state during the re-brightening phase, consistent with previous studies of this epoch (e.g. Kong et al. 2024). The differences observed in the

Table 3.1: Best-fit spectral parameters for the *XMM-Newton*/EPIC-pn observation of GRS 1915+105. Errors are quoted at the 90% confidence level. Fixed or tied parameters are indicated in parentheses.

Parameter	Value	Unit
`TBabs + pcfabs`		
$N_{\rm H}^{\rm ISM}$	$9.7^{+0.8}_{-1.0}$	$10^{22}\,{\rm cm}^{-2}$
$N_{\rm H}^{\rm pcf}$	79^{+11}_{-6}	$10^{22}\,{\rm cm}^{-2}$
Covering fraction	0.95 ± 0.01	–
`edge`		
$E_{\rm edge}$	$2.50^{+0.05}_{-0.04}$	keV
$\tau_{\rm edge}$	$0.51^{+0.21}_{-0.23}$	–
`diskline`		
$E_{\rm line}$	6.81 ± 0.02	keV
Inclination	42^{+2}_{-7}	deg
$R_{\rm in}$	< 10	$R_{\rm g}$
Emissivity index q	$3.10^{+0.25}_{-0.44}$	–
${\rm Norm}_{\rm diskline}$	$\left(1.44^{+0.30}_{-0.34}\right) \times 10^{-3}$	$\rm ph\,cm^{-2}\,s^{-1}$
`relxillCp`		
Inclination	(tied to `diskline`)	deg
Spin a_*	0.98 (fixed)	–
$R_{\rm in}$	(tied to `diskline`)	$R_{\rm g}$
$R_{\rm out}$	1000 (fixed)	$R_{\rm g}$
Emissivity indices $q_1 = q_2$	(tied to `diskline`)	–
Photon index Γ	1.79 ± 0.14	–
$\log \xi$	$3.6^{+0.4}_{-0.3}$	$\rm erg\,cm\,s^{-1}$
$\log n$	18 (fixed)	$\rm cm^{-3}$
$A_{\rm Fe}$	1 (fixed)	–
$kT_{\rm e}$	(tied to *NuSTAR*)	keV
Reflection fraction	(tied to *NuSTAR*)	–
${\rm Norm}_{\texttt{relxillCp}}$	1.69×10^{-3}	–
χ^2/dof	232.2/216	–

Table 3.2: Narrow emission and absorption features detected in the *XMM-Newton*/EPIC-pn spectrum of GRS 1915+105.

Parameter	Value	Unit
`Gaussian emission lines`		
E_1	$2.62^{+0.04}_{-0.03}$	keV
σ_1	$0.08^{+0.05}_{-0.03}$	keV
Norm_1	$(1.1^{+0.4}_{-0.3}) \times 10^{-4}$	$\mathrm{ph\,cm^{-2}\,s^{-1}}$
E_2	3.29 ± 0.02	keV
σ_2	0.04 ± 0.02	keV
Norm_2	$(6.2 \pm 0.9) \times 10^{-5}$	$\mathrm{ph\,cm^{-2}\,s^{-1}}$
`Gaussian Fe absorption lines`		
E_{abs1}	6.66 ± 0.007	keV
σ_{abs1}	0.066 ± 0.011	keV
$\mathrm{Norm}_{\mathrm{abs1}}$	$(-3.11 \pm 0.24) \times 10^{-4}$	$\mathrm{ph\,cm^{-2}\,s^{-1}}$
E_{abs2}	6.97 (frozen)	keV
σ_{abs2}	$= \sigma_{\mathrm{abs1}}$	keV
$\mathrm{Norm}_{\mathrm{abs2}}$	$(-2.13 \pm 0.29) \times 10^{-4}$	$\mathrm{ph\,cm^{-2}\,s^{-1}}$

Table 3.3: Best-fit spectral parameters for the *NuSTAR* observation of GRS 1915+105 (ObsID: 90701332002). Errors are quoted at the 90% confidence level. Parameters for FPMB are not shown, as they are tied to those of FPMA through a cross-normalization constant. Additional parameters not listed in the table were tied to the *XMM-Newton* ones.

Parameter	Value	Unit
`pcfabs`		
$N_{\mathrm{H,pcf}}$	49^{+3}_{-2}	$10^{22}\,\mathrm{cm^{-2}}$
Covering fraction	$0.850^{+0.016}_{-0.011}$	–
`diskline`		
E_{line}	$6.31^{+0.20}_{-0.08}$	keV
Norm	$(1.5^{+0.4}_{-0.5}) \times 10^{-3}$	$\mathrm{ph\,cm^{-2}\,s^{-1}}$
`Gaussian`		
Norm	$(-5.5^{+0.7}_{-0.9}) \times 10^{-4}$	$\mathrm{ph\,cm^{-2}\,s^{-1}}$
`relxillCp`		
Photon index Γ	$1.67^{+0.03}_{-0.02}$	–
$\log \xi$	2.0 ± 0.3	$\mathrm{erg\,cm\,s^{-1}}$
kT_e	< 88	keV
Reflection fraction	$0.65^{+0.09}_{-0.12}$	–
Normalization	$(2.20^{+0.30}_{-0.16}) \times 10^{-3}$	–
χ^2/dof	264.5/216	–

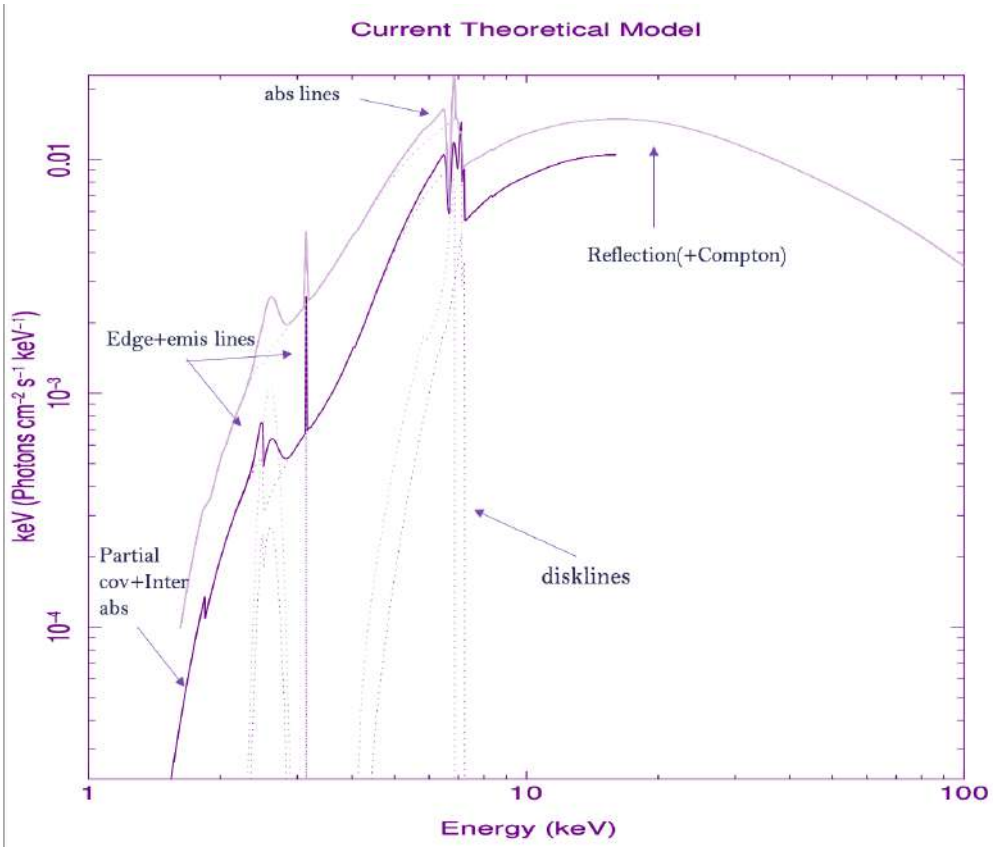

Figure 3.4: Schematic representation of the spectral model adopted in XSPEC for GRS 1915+105. The model includes a partially covering absorber, a Comptonized continuum, relativistic reflection, and additional Gaussian components to account for emission and absorption features.

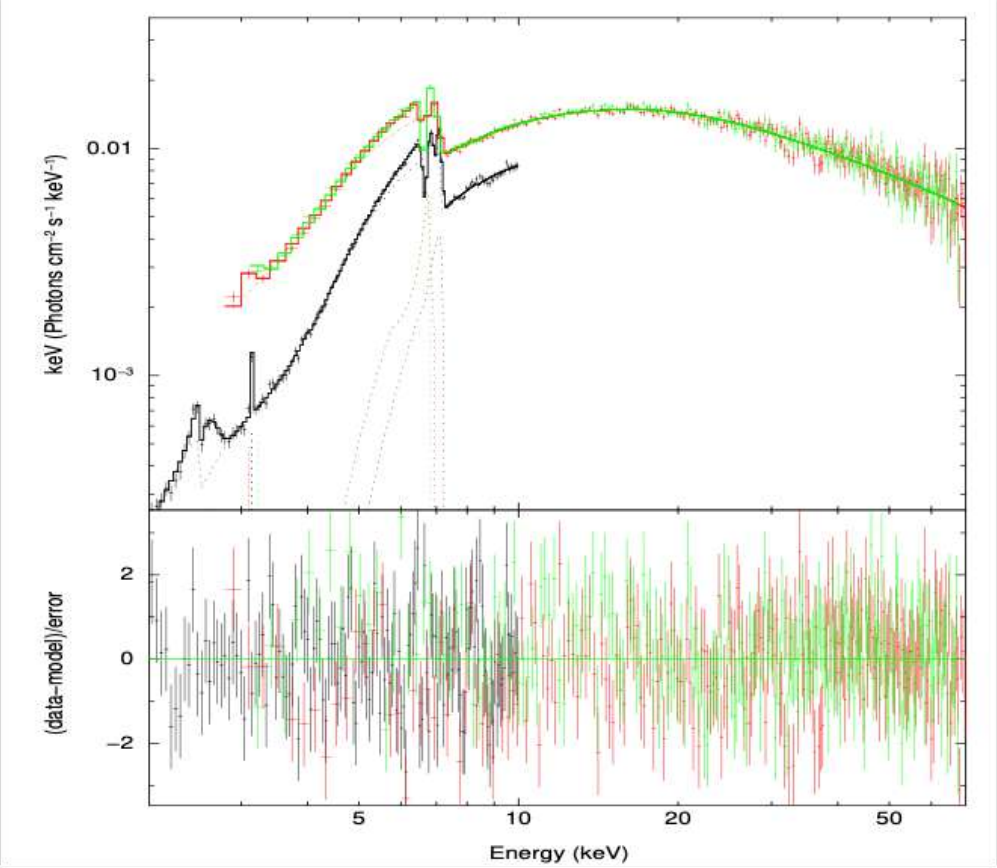

Figure 3.5: X-ray spectrum of GRS 1915+105 obtained with *XMM-Newton*/EPIC-pn during the 2021 rebrightening. The *XMM-Newton* data are shown in black, while *NuSTAR* FPMA and FPMB are shown in red and green, respectively. The model consists of a partially absorbed continuum, relativistic reflection (`relxillCp`), a relativistic Fe Kα line modeled with `diskline`, and several narrow Gaussian components. Residuals (in units of χ) are shown in the lower panel.

absorber properties between *XMM-Newton* and *NuSTAR*, separated by less than ten days, could point to a clumpy and rapidly variable absorbing medium, likely located close to the X-ray source.

Such behaviour can be explained in terms of inhomogeneous material associated with a thickened disc atmosphere or a failed disc wind, rather than by uniform interstellar absorption. Despite the extreme absorption, both datasets show strong reflection signatures, including a broadened Fe K emission line and a pronounced Compton hump detected by *NuSTAR*. The presence of the Compton hump, in particular, suggests the presences of reflection of optically thick material, as it cannot be reproduced by absorption effects alone. The detection of these features is indicative that the central engine is not intrinsically quenched during the obscured phase, but rather that its direct emission is partially hidden and observed primarily through reprocessing.

The spectral modelling points to the possibility that the reflection spectrum is best described by a relativistically blurred component (`relxillCp`), with an inner radius constrained to be within $\sim$ 6–10 R_g, indicating an origin in the inner accretion disc. The high ionization parameter inferred from the *XMM-Newton* data ($\log \xi \sim 3.5$) and the detection of highly ionized Fe XXV/XXVI features, support reflection from a highly ionized disc surface, while the lower ionization measured by *NuSTAR* suggests a stratified or time-variable disc atmosphere. In addition, the presence of narrow emission and absorption lines from highly ionized iron and lighter elements indicates that reprocessing also occurs in more distant regions, such as the outer disc atmosphere or a slow disc wind.

Nevertheless a complexity arises from the fact that the spectral description requires both a relativistically broadened Fe K emission line and a separate reflection component. While the `diskline` model captures the line profile alone and does not represent a full reflection spectrum, the need for both components may reflect the simplified nature of the adopted phenomenological approach, rather than implying physically distinct reflection regions. In addition, the `relxill` family of models assumes reflection from a relatively standard accretion disc geometry, an assumption that may not strictly apply to GRS 1915+105 in the obscured state, as will be discussed in more detail later. Explaining this result therefore remains non-trivial and is currently under discussion. In this work, I therefore limit myself to a phenomenological description of the observed spectral features.

3.5.1 On the inferred inclination of the reflecting region

One of the most intriguing results of this analysis is the relatively low inclination angle inferred consistently from both the relativistic line profile and the reflection modelling, with values of $i \sim 42°$. This is significantly lower than the inclination of $\sim 60°$–$70°$ commonly reported in the literature based on optical, radio, and previous X-ray studies (see the source overview). For this reason, we list below the most relevant measurements, together with the methods used to derive them, in order to enable a direct comparison.

Inclination from reflection (i)

A measurement of the disk inclination in GRS 1915+105 was obtained by Miller et al. (2013) through relativistic reflection modelling of *NuSTAR* spectra acquired during the “plateau” (hard) state on 2012 July 3. Their adopted model, `tbabs * kerrconv * (reflionx_hc + cutoffpl)`, consists of a power-law continuum with a high-energy cutoff (`cutoffpl`) illuminating an ionized accretion disk described by

`reflionx_hc`, an old constant-density reflection model that computes the ionization balance and produces both line and continuum reflection features. The reflection spectrum is convolved with the relativistic blurring kernel `kerrconv`, which performs full ray-tracing in the Kerr metric. This kernel explicitly includes the inner and outer disk emissivity indices (following Wilkins & Fabian 2012, with q_1 free and $q_2 = 0$), an emissivity break radius, the BH spin parameter a_*, and the disk inclination, which they restricted to lie within $65^\circ < i < 80^\circ$ based on prior jet kinematic studies (Fender et al. 1999). This model yielded a value of $i \simeq 72^\circ$. This approach differs significantly from the one adopted in this work. Here, I analyse data taken nearly a decade later, when GRS 1915+105 was in a deeply obscured, low-flux state characterised by strong and complex local absorption and a potentially altered disc–corona geometry, limiting a direct comparison between the inferred parameters. In addition, while Miller et al. (2013) relied exclusively on *NuSTAR* data, the present analysis combines *XMM-Newton* and *NuSTAR* observations, allowing the inclusion of the soft X-ray band, which provides additional constraints on absorption, ionization, and disc-related spectral features. Finally, this work adopts more recent reflection models, which incorporate updated atomic data and a self-consistent treatment of the illuminating continuum, potentially leading to systematic differences in the derived inclination. Consequently, the inclination constraints obtained here need not coincide with those reported by Miller et al. (2013).

Inclination from kinematic constraints

A refined estimate of the inclination of the binary system GRS 1915+105 has recently been provided by Reid & Miller-Jones (2023), who combined updated distance constraints with high-precision measurements of the proper motions of paired radio jet ejecta. In systems with symmetric approaching and receding jet components, the observed proper motions directly constrain the jet inclination once the source distance is known. Using their newly derived three-dimensional kinematic distance of $d = 9.4 \pm 0.6$ kpc, they re-analysed multiple jet-ejection episodes with reliable VLBA measurements and obtained a weighted mean inclination of $i = 64^\circ \pm 4^\circ$, slightly larger than earlier estimates based on parallax-only distances. This updated inclination is also consistent with the relatively low peculiar velocity (~ 20 km s^{-1}) found for the system, suggesting a formation channel with a low natal kick. However, the jet inclination of GRS 1915+105 reported by Reid & Miller-Jones (2023) is derived from proper motion measurements of symmetric radio ejecta observed over multiple outburst episodes, primarily between the late 1990s and early 2000s. These measurements are not simultaneous with the 2021 X-ray observations analysed in this work, and therefore represent a long-term, average jet geometry rather than the instantaneous configuration of the inner accretion flow. More recently, indeed, new VLA observations obtained in September–October 2023 revealed a dramatic and transient change in the jet geometry. By comparing the relative angular separations of the approaching and receding lobes, Rodríguez & Mirabel (2025) measured an inclination of $i = 87^\circ \pm 3^\circ$. This result indicates an increase of $\Delta i \simeq 17^\circ$ with respect to the historical value, occurring on a timescale shorter than a year. Interestingly, this was only a transient event, indeed the jet inclination returned in 2024 to values consistent with the historical range. Such a rapid change strongly suggests a temporary reorientation of the inner accretion flow, an the very high value implies that the jet axis was inclined by only $3^\circ \pm 3^\circ$ with respect to the plane of the sky during that epoch. Assuming that the jet axis is perpendicular to the accretion disc, this configuration corresponds to a line of sight nearly aligned with the plane of the disc itselTaken together, these results indicate that the orientation of the jet in GRS 1915+105 is not strictly fixed, but can vary on multi-year timescales. In this context, the inclination inferred from X-ray spectral modelling in this work is not necessarily inconsistent with jet-based estimates, but may instead reflect a temporally evolving geometry of the inner accretion–ejection

system during the 2021 re-brightening. While this interpretation is not unique, it offers a plausible framework in which the different inclination constraints can be reconciled.

Inclination constraints from reflection (ii)

In their systematic re-analysis of all available *NuSTAR* BH binaries, Draghis et al. (2024) derive the inclination of the inner accretion disk directly from relativistic reflection modelling. For each observation, they fit the spectra with several flavours of the RELXILL family, allowing the disk inclination to float freely and then computing its posterior probability distribution through dedicated MCMC runs. The final inclination is obtained by combining all individual posterior distributions with a Bayesian algorithm that weights each observation by its reflected-to-total flux ratio, thus giving more influence to spectra where reflection features—broad Fe K lines and the Compton hump—are most prominent. For GRS 1915+105, this approach leads to a broad and sometimes inconsistent set of inclination posteriors among independent observations, which the authors attribute to variable disk winds and absorption features affecting the blue wing of the Fe K line, a key region for inclination determination. Although the paper does not single out the observation I analysed for a dedicated discussion, this is included in the global dataset analysed.Within this framework, the authors measure an inclination from relativistic reflection modelling that is lower than the value of $\theta = 72^\circ \pm 1^\circ$ previously reported by Miller et al. (2013). However, when examining the inclination constraints obtained from individual observations within the same dataset, they note that the inclination inferred from the *NuSTAR* spectrum analysed by Miller et al. (2013) can reach higher values, consistent with the earlier result. This suggests that inclination estimates derived from reflection modelling may depend on the specific spectral state and data quality of a given observation, and that the values inferred from X-ray spectroscopy may not always correspond to a single, fixed geometric configuration and influenced by additional factors.

3.5.2 Comparison with XRISM/Resolve results

A useful point of comparison for the 2021 *XMM-Newton*+*NuSTAR* analysis presented in this chapter is provided by the first *XRISM*/Resolve spectrum of GRS 1915+105 in the obscured state (Miller et al. 2025), obtained on 2024 October 17. The aim of this comparison is not to establish a one-to-one correspondence between spectral parameters derived at different epochs, but rather to assess whether a coherent physical picture emerges across the obscured state. The *XRISM* spectrum was modelled using a combination of photoionized emission components and distant neutral reflection, with the latter described using the `mytorus` framework. Additional Gaussian components were included to account for broad emission underlying the Fe XXV He-α and Fe XXVI Ly-α complexes, whose centroids and widths are well constrained thanks to the high spectral resolution of Resolve (Miller et al. 2025). The best-fitting model yields a Cash statistic of $C = 3891$ for $\nu = 2933$ degrees of freedom and is not formally acceptable, although the main spectral features are well reproduced. The inferred continuum is dominated by thermal disc emission, consistent with a sub-Eddington, thermal-dominant state despite the presence of strong obscuration.

Crucially, the modelling of the neutral Fe Kα complex requires a combination of a relatively small emission radius and a very low inclination. The authors infer an inclination of $i \simeq 5^{+4}_{-2}$ deg for the region producing the neutral Fe Kα line. This value is strikingly different from the inclination of the binary system and jet ($i \simeq 64^\circ$–66°) and from that of the inner accretion disc inferred from relativistic reflection ($i \sim 60^\circ$). Such a discrepancy cannot be reconciled within a flat, planar disc geometry. Instead, Miller et al. (2025)

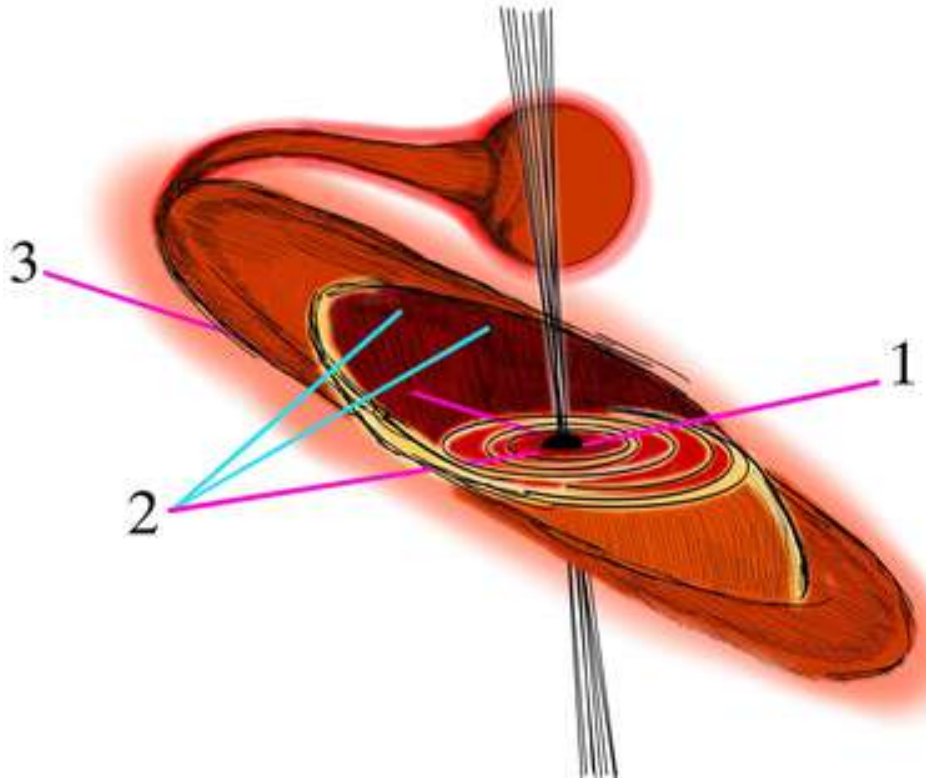

Figure 3.6: Schematic illustration of a warped accretion-disc geometry proposed by Miller et al. (2025) to explain the spectrum of GRS 1915+105 observed with Resolve. At Position 1, the central engine is directly visible and only partially obscured by disc winds. At Position 2, the central engine is blocked by a warp in the outer disc, while emission from the irradiated inner face of the warp remains observable. At Position 3, both the central engine and the irradiated disc surface are fully obscured. The warp is not phase-locked to the binary orbit, as its characteristic timescale is much longer than the orbital period of the system.

interpret this result as strong evidence for a warped accretion disc. In this configuration, the outer disc naturally occults the central engine, producing the observed obscuration, while the neutral Fe Kα emission arises from the inner face of the warp at low effective inclination (see Fig. 3.6). This scenario is further supported by recent *JWST* observations, which reveal an infrared flux approximately an order of magnitude higher than in earlier epochs, together with very strong infrared recombination lines, indicating an enhanced role of reprocessing during the obscured state.

In this context the relatively low inclination angles inferred from the reflection modelling in my work may naturally fit within the warped-disk scenario proposed by Miller et al. (2025). As a result, the inclination inferred from inner-disk reflection may differ from the inclination measured through optical, radio, or large-scale disk diagnostics.

3.6 Conclusions

In this chapter, I presented a phenomenological X-ray spectral analysis of GRS 1915+105 during its obscured state, based on quasi-simultaneous *XMM-Newton* and *NuSTAR* observations obtained during the 2021 re-brightening episode. The spectra are characterized by strong and complex absorption, together with prominent reflection features, indicating that part of the inner accretion flow remains visible despite the extreme obscuration.

A key result of this analysis is the measurement of a relatively low inclination angle, $i \sim 42°$, inferred consistently from both the relativistic Fe Kα line and the broadband reflection continuum. It is important to stress that the inclination derived from reflection modelling represents the effective inclination of the region dominating the reflected emission, rather than the orbital inclination of the binary system. Indeed the obtained value is significantly lower than the inclination of the binary system and radio jet reported in the literature, but similar to recent results obtained from *XRISM*/Resolve spectroscopy (Miller et al. 2025), could point toward reflection and line-emitting regions observed at substantially lower effective inclinations.

At the same time, the present analysis relies on a phenomenological spectral model, and the inferred parameters are subject to degeneracies. In addition, residual uncertainties in the intercalibration between *XMM-Newton* and *NuSTAR* may affect the detailed broadband spectral shape and the relative normalization of the different components, potentially influencing the constraints on reflection and absorption properties. While these degeneracies can bias inclination measurements, the statistical consistency between independent reflection components in the fit indicates that the low inclination found here is not solely driven by an unconstrained model. Nevertheless, the adoption of new more physically self-consistent models, capable of describing complex disk geometries, stratified absorbers, and reflection within a unified framework, may in the future reduce the need for two reflection components and provide more robust constraints on the structure of the inner accretion flow.

Future work is needed and will extend this study by applying a similar analysis to additional obscured-state observations of GRS 1915+105 obtained in 2019 and 2020 with quasi-simultaneous *XMM-Newton* and *NuSTAR*. A homogeneous treatment of multiple epochs will allow the temporal stability of the reflection geometry to be tested and will provide stronger constraints on the evolution of the inner accretion flow during the obscured phase.

4 Jet Modeling in MAXI J1535–571

In Chapters 2 and 3, I focused on one class of outflows from BH XRBs, namely accretion disk winds, discussing their observational properties and physical interpretation. In this chapter, I shift the attention to the other major form of outflow observed in these systems: relativistic ejections in the form of compact jets. In particular, this chapter introduces a theoretical code aimed at modeling the emission from steady, compact jets. The model provides a physically motivated description of jet dynamics and radiation processes, and will be used to interpret the broadband emission of the BH XRB MAXI J1535−571. Transient or discrete ejection events are not considered here, as they lie beyond the scope of this work.

4.1 Compact Jets

Jets are among the most powerful manifestations of energy release in astrophysical systems, spanning a vast range of spatial scales and source classes. From the parsec-scale radio lobes of AGNs to the transient and compact structures in XRBs, collimated outflows appear as a nearly ubiquitous product of accretion (Fender et al. 2004; Pe'er 2014). Despite their prevalence, the physical mechanisms governing their launching, acceleration and collimation remain only partially understood (Jacquemin-Ide et al. 2019). In XRBs, compact jets are observed predominantly in the radio to infrared regime (Russell & Fender 2010), and their emission is generally interpreted as synchrotron radiation from relativistic electrons spiralling around magnetic field lines (Han & Hjellming 1992; Corbel et al. 2001). These jets have been spatially resolved in only a few systems, such as GRS 1915+105 (Dhawan et al. 2000) and Cygnus X-1 (Stirling et al. 2001). In most cases, indeed, their compactness makes them unresolved, with characteristic extents of $\sim 10^{14}$–10^{15} cm in XRBs (Miller-Jones et al. 2012). Despite their small spatial scales, compact jets are capable of carrying away a substantial fraction of the accretion power and can dynamically interact with the surrounding environment (Malzac 2018). Theoretical models suggest that a large-scale vertical magnetic field anchored in the accretion flow, together with efficient mass-loading and angular momentum transport, are essential ingredients for jet formation (Jacquemin-Ide et al. 2019). While jets in XRBs are believed to be only mildly relativistic ($\Gamma \sim 1$–10), they are thought to share many physical properties with their highly relativistic counterparts in AGNs and Gamma-Ray Bursts (GRBs) with $\Gamma \geq 10$ or $\Gamma \geq 100$–1000 and distance up to $\sim 10^{23}$ cm (AGNs) and $\sim 10^{18}$ cm (GRBs), respectively (Mészáros & Rees 1997; Wijers et al. 1997; Alvarez et al. 2000).

The similarities in jet morphology across such a wide range of systems suggest a fundamental connection between accretion and ejection processes, making compact jets a critical probe of disk-jet coupling and

relativistic plasma physics. While it is well established that the observed jet emission is primarily produced by relativistic electrons or positrons, the exact composition of jets—whether predominantly leptonic or baryonic—remains uncertain. Concerning their launching mechanisms, various theoretical models have been developed to explain how outflows originate in the vicinity of accreting BHs, yet a comprehensive understanding of these processes is still missing.

In this context, significant progress has been achieved in recent years thanks to magnetohydrodynamic (MHD) and general relativistic magnetohydrodynamic (GRMHD) simulations. These numerical simulations self-consistently describe the dynamics of magnetized plasma in the strong gravitational field of a BH, allowing one to follow the formation, acceleration, and collimation of jets from first principles. Early and subsequent works have demonstrated that large-scale magnetic fields anchored in the accretion flow can efficiently extract energy and angular momentum from the disk and/or the rotating BH, naturally leading to the formation of relativistic outflows (e.g. McKinney 2006b; Hawley & Krolik 2006; Tchekhovskoy et al. 2011). More recent GRMHD studies have further explored the dependence of jet properties on BH spin, magnetic flux accumulation, and accretion regime, highlighting the role of magnetically arrested disks (MADs) in producing powerful, highly relativistic jets (e.g. Narayan & McClintock 2012; Tchekhovskoy et al. 2012; McKinney et al. 2012). While these simulations provide crucial insights into jet launching and large-scale dynamics, connecting their results to the observed radiative properties of compact jets in BH XRBs still requires simplified, semi-analytical emission models, which are the focus of this chapter.

4.1.1 Launching mechanisms

The Blandford–Payne Mechanism

The Blandford & Payne (1982) model provides a magnetohydrodynamic framework for launching and collimating astrophysical jets from a differentially rotating accretion disk. This mechanism requires: (i) a Keplerian disk with angular velocity $\Omega(r)$, (ii) a low-density ionized corona above and below the disk, and (iii) a large-scale poloidal magnetic field $\mathbf{B}_\mathrm{p}$ anchored in the disk.

Within the dense midplane of the disk the ram pressure of the plasma dominates over the magnetic pressure:

$$\rho\, v^2 \;\gg\; \frac{B^2}{8\pi}\,, \tag{4.1}$$

where ρ is the mass density, $v = \Omega\, r$ the orbital speed, and $B = |\mathbf{B}|$ the magnetic field intensity. In this regime the field lines are "frozen-in" and co-rotate with the plasma. In the tenuous corona, however, the magnetic pressure exceeds the ram pressure:

$$\frac{B^2}{8\pi} \;\gg\; \rho\, v^2\,, \tag{4.2}$$

so that the field controls the motion of the plasma. If the poloidal field lines are inclined by an angle $\theta < 60°$ with respect to the vertical axis, the component of the centrifugal force along the line of sight is sufficient to overcome gravity. Plasma then slides outward along the rigid "wire" of the field line under magnetocentrifugal acceleration, with acceleration

$$\mathbf{a}_\mathrm{cent} \;=\; \Omega^2\, R\, \hat{\mathbf{R}}\,, \tag{4.3}$$

where R is the cylindrical radius.

As the flow moves outward it crosses the Alfvén surface defined by

$$v = v_A = \frac{B}{\sqrt{4\pi\rho}}. \tag{4.4}$$

Inside this surface, the magnetic field dictates the plasma motion; beyond it, the inertia of the plasma begins to drag and twist the field lines, generating a toroidal component B_ϕ. This toroidal field produces a hoop-stress (magnetic tension),

$$T_{B_\phi} = \frac{B_\phi^2}{4\pi R} \tag{4.5}$$

and a magnetic pressure,

$$P_{B_\phi} = \frac{B_\phi^2}{8\pi}, \tag{4.6}$$

which together act to collimate the outflow into a narrow, bipolar jet.

The hoop-stress, also referred to as the *toroidal magnetic tension*, arises from the curvature of the toroidal field lines wrapped around the jet axis. In analogy to the tension in a stretched elastic band, it exerts an inward radial force that tends to reduce the radius of curvature, effectively "pinching" the jet towards its axis. Magnetic pressure, on the other hand, acts isotropically and pushes outward from regions of higher B_ϕ towards lower values. In the context of a jet, gradients in magnetic pressure along the poloidal direction contribute to accelerating the plasma outward, while radial gradients provide an additional collimating influence.

When acting together, hoop-stress dominates the radial confinement by pulling the plasma towards the jet axis, while magnetic pressure gradients provide a stabilizing balance and help guide the flow along the axis. This interplay of magnetocentrifugal acceleration, magnetic pressure, and magnetic tension is a key ingredient in producing the observed highly collimated, magnetically driven jets.

The Blandford–Znajek Mechanism

The Blandford & Znajek (1977) (BZ) mechanism describes how energy and angular momentum can be extracted from a rotating BH through magnetic fields. In the context of BH XRBs, this process offers a plausible explanation for the origin of relativistic jets, with analogous mechanisms also proposed to operate in AGNs.

The model assumes a rotating (Kerr) BH surrounded by a strong magnetic field, anchored by currents in the surrounding accretion disk. Due to the BH's spin, the spacetime around it is dragged—a relativistic effect known as frame dragging. When magnetic field lines thread the event horizon, this dragging causes them to twist, which in turn extracts energy from the BH's rotation.

This energy is carried outward by electromagnetic fields in the form of a *Poynting flux*, i.e. an outward transport of electromagnetic energy. The magnetic field lines are assumed to rotate with an angular velocity slower than that of the BH. If this condition is met, rotational energy can be transferred outward in the form of electromagnetic energy, stored in the toroidal and poloidal components of the field. Close to the BH, the energy is almost entirely electromagnetic; however, as the jet propagates, part of this Poynting flux is gradually converted into kinetic energy of the plasma, accelerating particles to relativistic speeds, and into radiation emitted along the jet. The power output of the jet depends on the strength of the magnetic field and

the BH's spin. A simplified expression for the extracted power is:

$$P_{\rm BZ} \propto \Phi_B^2 \Omega_{\rm H}^2, \tag{4.7}$$

where Φ_B is the magnetic flux through the horizon and $\Omega_{\rm H}$ is the angular velocity of the BH.

At larger distances, the rotation of the field lines creates a strong toroidal component of the magnetic field. This generates hoop stress (see the previous paragraph) that naturally collimates the outflow into a narrow, relativistic jet.

Unlike the Blandford–Payne mechanism, which relies on mass-loaded winds accelerated centrifugally from the accretion disk, the BZ mechanism extracts energy directly from the BH's spin. It can operate even in low-luminosity systems, as long as a force-free magnetosphere and sufficient magnetic flux are present.

The Blandford–Znajek (BZ) process is now a key ingredient in modern models of jet formation and is supported by both numerical MHD simulations (e.g., Komissarov 2001; McKinney 2006b; Hawley & Krolik 2006; Tchekhovskoy et al. 2011) and observations (Narayan & McClintock 2012; Zamaninasab et al. 2014). However, the Blandford–Payne (BP) mechanism (Blandford & Payne 1982) is also an important contributor and is frequently present in global general relativistic MHD simulations. These simulations typically show that outflows from accreting BHs consist of a magnetically dominated jet core powered by the BZ process and launched from the vicinity of the event horizon, together with a denser, slower outflow originating from the inner regions of the accretion disc and driven by the BP mechanism (McKinney 2006a; Tchekhovskoy et al. 2011; Liska et al. 2019). The relative contribution of these components depends on the magnetic flux threading the BH, the spin parameter a_*, and the disk's magnetization. Some simulations also show a gradual transition zone where centrifugal acceleration and magnetic pressure gradients work together, making it difficult to draw a sharp boundary between BP- and BZ-dominated regions (Yuan & Narayan 2014).

From an observational perspective, disentangling BZ and BP contributions is challenging. However, trends in jet power with both BH spin (favoring BZ; Narayan & McClintock 2012; Zamaninasab et al. 2014) and accretion rate (favoring BP) are observed; Fender et al. 2004 suggest that both mechanisms may operate simultaneously in many systems.

4.1.2 Acceleration mechanisms

Jets from compact objects can accelerate particles to relativistic energies through several mechanisms (see Matthews et al. (2020) for a review). Among the most studied is diffusive shock acceleration (DSA), where particles gain energy by repeatedly crossing shock fronts, experiencing a first-order Fermi process (Axford et al. 1977; Krymskii & Transkii 1977; Bell 1978; Blandford & Ostriker 1978; Marcowith et al. 2016). This mechanism predicts power-law energy distributions and is supported by both theoretical and observational evidence.

In this framework, the particle energy distribution can be written as $N(E) \propto E^{-p}$, where the index p characterizes the slope of the non-thermal population of accelerated particles (Longair 2011; Blandford & Eichler 1987). The value of p depends on the details of the acceleration process and on the plasma conditions. For weakly magnetized flows, the shock is mediated by self-generated magnetic turbulence that enables the efficient scattering and acceleration of particles through the Fermi process (Sironi et al. 2013). In this regime, the accelerated particles follow a power-law energy distribution with a slope of

$p \sim 2.5$, typically involving about 1–3% of the total particles and accounting for roughly 10% of the flow energy. The acceleration efficiency is comparable for electrons and ions, owing to strong pre-heating and near-equipartition between the two species. At higher magnetizations, the acceleration becomes less efficient and the resulting particle distributions steepen, with slopes $p \gtrsim 3$, as magnetic confinement weakens and the shock dynamics become increasingly dependent on the field orientation. Efficient acceleration is restricted to quasi-parallel (subluminal) configurations, whereas superluminal shocks suppress particle recrossing and yield predominantly thermal downstream populations (Marcowith et al. 2016).

An alternative acceleration channel is for example magnetic reconnections. (Parker 1957; Sweet 1958; Lyubarsky 2005). In reconnection regions, oppositely directed magnetic field lines converge and undergo resistive dissipation, forming X-points and magnetic islands where particles can be accelerated (Petschek 1964). Reconnection can drive first-order Fermi acceleration via converging inflows or by particle interactions with contracting islands and merging plasmoids (Loureiro et al. 2007; Ni et al. 2015). Numerical simulations, particularly particle-in-cell (PIC) models, reveal a variety of acceleration processes, with harder spectral indices typically ranging between $p \sim 1$ and $p \sim 2$ (Romanova & Lovelace 1992; Lyubarsky & Liverts 2008; Sironi & Spitkovsky 2014; Guo et al. 2015).

While some mechanisms operate in ordered magnetic geometries, others rely on turbulent reconnection, where particles experience stochastic acceleration reminiscent of a hybrid between first and second order Fermi processes (Comisso & Sironi 2018).

4.2 Radiation Processes in Compact Jets

In the following section, I move from the physical mechanisms of jet formation and particle acceleration to the discussion of the radiative processes that shape their observed spectra.

Relativistic jets in stellar mass compact objects emit across a wide range of frequencies, primarily due to synchrotron radiation produced by high-energy electrons spiralling in magnetic fields. The characteristic spectral shape observed from these jets arises from a combination of physical processes: synchrotron emission, synchrotron self-absorption, and radiative cooling.

4.2.1 Synchrotron Radiation and Spectral Features

I begin by describing synchrotron emission, which arises when relativistic electrons spiral around magnetic field lines, producing strongly beamed and intrinsically polarised radiation. Following Rybicki & Lightman (1979) and Longair (2011), each electron emits most of its power around a characteristic frequency $\nu_{\rm crit}$, which depends on its energy and the strength of the magnetic field. Due to relativistic aberration, the emitted radiation is confined within a narrow cone directed along the electron's instantaneous velocity vector. This cone has a half-opening angle of approximately $1/\gamma$, where γ is the Lorentz factor of the electron, resulting in strong beaming of the emission in the observer's frame (see Fig. 4.1).

For a single electron, the emitted spectrum peaks sharply at this frequency and declines rapidly at higher frequencies, forming a steep cutoff. At lower frequencies, $\nu \ll \nu_{\rm crit}$, the synchrotron emissivity follows a different behaviour: the spectral emissivity of a single electron scales as $j(\nu) \propto \nu^{1/3}$ (Rybicki & Lightman

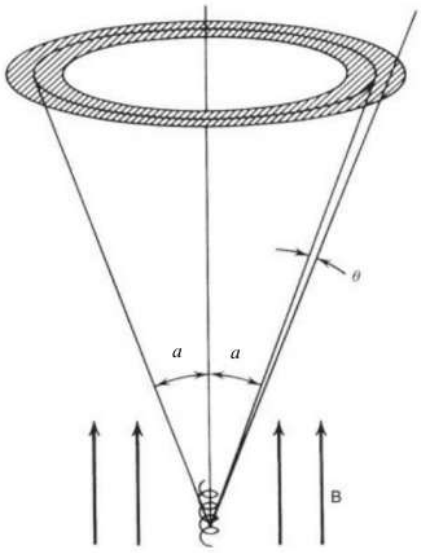

Figure 4.1: Synchrotron emission from an electron with pitch angle α is confined to the shaded region, corresponding to a cone with half-opening angle $\theta \sim \gamma^{-1}$. Figure from Rybicki & Lightman (1979).

1979). This low-frequency regime reflects the asymptotic form of the synchrotron spectrum, where the emitted power rises slowly with frequency before reaching its peak (see Fig. 4.3).

When considering a distribution of electron energies, this is typically modeled as a power-law $N(E)dE = \kappa E^{-p} dE$, p is the spectral index of the electron energy distribution and κ the normalisation (see Fig. 4.2).

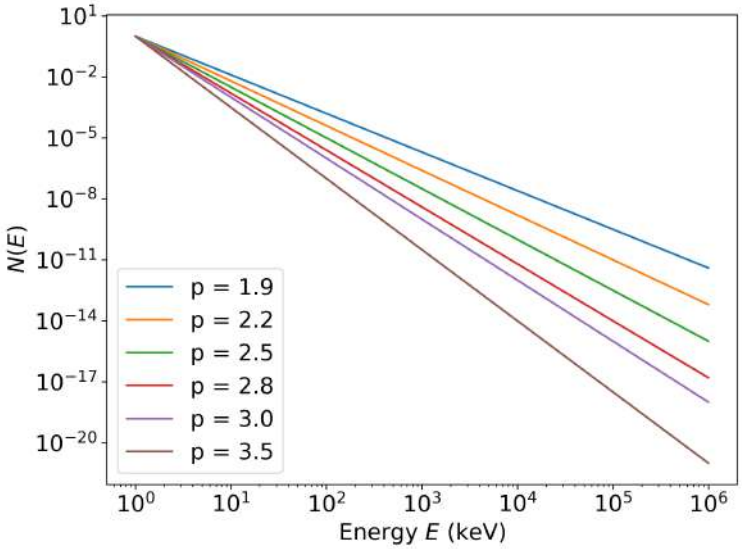

Figure 4.2: Electron energy distributions $N(E)\,dE = \kappa E^{-p}\,dE$ computed for a set of power-law indices $p = 1.9,\ 2.2,\ 2.5,\ 2.8,\ 3.0$, and 3.5. The curves are shown as a function of the electron energy in keV, covering the range 1 keV $\leq E \leq 10^6$ keV. Lower values of p correspond to harder particle spectra, while higher values produce steeper distributions dominated by low-energy electrons.

The resulting synchrotron spectrum from the ensemble of particles becomes a power-law of the form (Longair 2011):

$$J(\nu) \propto \kappa B^{(p+1)/2} \nu^{-(p-1)/2}, \tag{4.8}$$

where B is the magnetic field strength. The overall emission is thus shaped by both the slope of the electron energy and the magnetic environment.

4.2.2 Synchrotron Self-Absorption and Low-Frequency Turnover

At lower frequencies, synchrotron-emitting electrons can reabsorb part of their own radiation—a process known as synchrotron self-absorption. This effect becomes significant when the source becomes optically thick to its own emission, producing a spectral turnover. At a characteristic break frequency (ν_b), the spectrum transitions from the optically thick, self-absorbed regime to the optically thin domain. Physically, this break does not correspond to a sharply defined location in the jet, but rather emerges from the integrated contribution of multiple emission zones with varying optical depths along the outflow (Blandford & Königl 1979; Markoff et al. 2005). The region close to ν_b is thought to trace where a significant fraction of particles undergo acceleration from thermal to non-thermal distributions. Observationally, ν_b has been constrained from infrared to radio wavelengths, typically associated with regions located at $\sim$ 10–1000 r_g from the compact object during hard states (e.g., Markoff et al. 2000; Migliari et al. 2007; Gallo et al. 2007; Maitra et al. 2009). More recent studies have refined these constraints using multi-wavelength campaigns, highlighting the strong variability of ν_b across different sources and accretion states (e.g., Russell et al. 2013, 2014; Koljonen et al. 2015). In the optically thick regime, the flux density rises with frequency as (Longair 2011):

$$S_\nu \propto \nu^{5/2}, \tag{4.9}$$

which sets the local spectral slope of a homogeneous region. However, the broad-band spectra of compact jets cannot be explained by a single homogeneous zone. Instead, a continuous stratification of emission regions with different optical depths is required, so that their superposition naturally produces the broken power-law shape typically observed. In this picture, the low-frequency part of the spectrum is dominated by the outer, optically thick regions (Blandford & Königl 1979; Hjellming & Johnston 1988; Fender 2001) (see Fig. 4.4).

4.2.3 Radiative Cooling and the High-Frequency Break

At high frequencies, synchrotron-emitting electrons cool very efficiently through radiative losses. Since the synchrotron loss rate increases as the square of the electron Lorentz factor ($\dot{E} \propto \gamma^2$), the most energetic electrons lose energy on the shortest timescales. As a result, the high-energy tail of the electron population rapidly depletes, leading to a steepening of the emitted spectrum, commonly referred to as the synchrotron cooling break. For an injected power-law distribution of electrons, the spectral index changes from $\alpha = -(p-1)/2$ to $\alpha = -p/2$ above the cooling break frequency (Longair 2011) (see Fig. 4.4).

The location of the cooling break is determined by the balance between acceleration and cooling timescales, and it depends on physical parameters such as the magnetic field strength, the size of the emitting region, and the bulk Lorentz factor of the flow (e.g., Sari et al. 1998). Stronger magnetic fields or more compact emission regions generally shift the break to lower frequencies, since electrons cool more rapidly in these conditions.

It is important to distinguish this high-frequency cooling break from the low-frequency turnover associated with synchrotron self-absorption in compact jets. While the self-absorption break marks the transition from

optically thick to optically thin emission, the cooling break arises entirely within the optically thin regime and reflects intrinsic radiative losses of the electron population. Together, the two breaks define the overall broadband synchrotron spectrum of compact jets.

4.2.4 Integrated Jet Emission and Flat Radio Spectra

The combination of the low-frequency synchrotron self-absorption and the high-frequency radiative cooling effects described above leads to the characteristic flat or slightly inverted spectra observed in compact jets. In particular, the observed GHz-range emission can be interpreted as the superposition of multiple synchrotron-emitting regions distributed along the jet axis. Each region contributes a partially self-absorbed component with a turnover at a different frequency, and the cumulative effect of these overlapping components produces an overall spectrum that is flat ($\alpha \approx 0$) or mildly rising ($\alpha > 0$) (see Fig. 4.4):

$$S_\nu \propto \nu^\alpha, \quad \alpha \gtrsim 0. \tag{4.10}$$

It is worth noting, however, that adiabatic losses along an expanding jet would naturally tend to steepen the spectrum, leading to a more inverted shape than what is typically observed (see Fig. 4.5). The fact that compact jets instead display nearly flat spectra suggests the presence of continuous replenishment mechanisms,such as ongoing particle acceleration or energy injection along the jet, that compensate for these losses. This behaviour is elegantly captured by the seminal model of Blandford & Königl (1979), which interprets the broadband jet emission as the result of a stratified outflow in which each region becomes transparent at a different frequency. This framework has since become the standard reference for explaining the flat radio-to-infrared spectra of compact jets in both BH XRBs and AGN.

To summarize, the spectral properties of compact jets can be understood as the interplay between synchrotron emission, self-absorption, and radiative cooling, combined with relativistic effects and the stratified, multi-zone structure of the jet. Synchrotron radiation also predicts linear polarisation levels up to $\sim 10\%$ for self-absorbed and $\sim 72\%$ for optically-thin emission in the presence of ordered magnetic fields (Pacholczyk & Swihart 1967; Scheuer & Williams 1968; Longair 2011), although such high levels are seldom observed in XRBs (Fender 2003), possibly due to field disorder or multiple unresolved polarised components.

4.3 The Internal Shock Jet Emission Model: ISHEM

After discussing the radiative processes that govern the spectral properties of compact jets, I now turn to the ISHEM model. This code is specifically designed to reproduce such broadband jet spectra by coupling internal shock dynamics with synchrotron emission. In the following section, I outline the physical assumptions underlying the model and summarise the key improvements introduced in its most recent version, which I employ throughout this work.

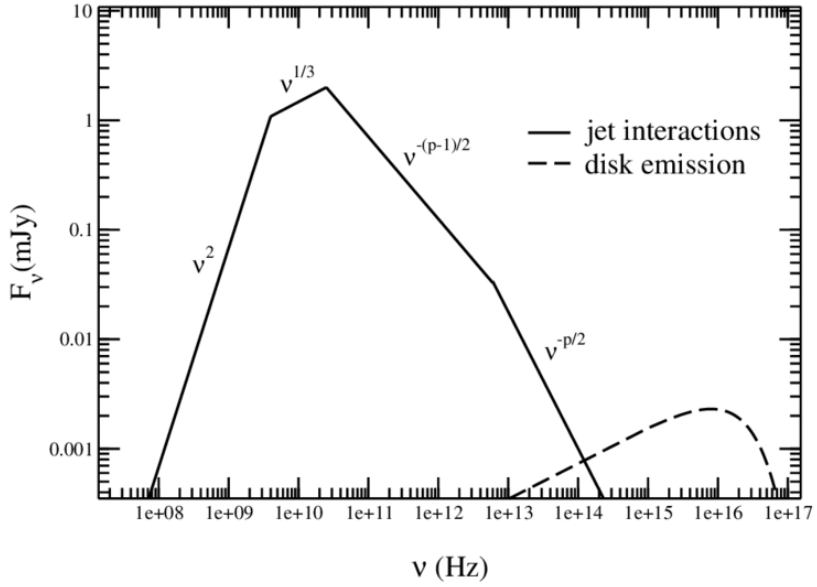

Figure 4.3: Schematic synchrotron spectrum of a compact jet (solid line), composed of the superposition of multiple self-absorbed synchrotron components. The spectrum corresponds to the peak of the emission phase ($t_{\rm peak} \sim t_{\rm cr} \sim 1$ yr) following the disruption of a solar-type star by a $10^7\,M_\odot$ BH at 1 Gpc. The break frequency $\nu_{\rm b}$ marks the transition between optically thick and thin synchrotron regimes, while $\nu_{\rm c}$ represents the cooling break caused by radiative losses. The dashed curve shows, for comparison, the expected thermal emission from the accretion disc. Adapted from Giannios & Metzger (2012).

4.3.1 Introduction

In my analysis of compact jets in BH XRBs, I employed the latest version of ISHEM (Malzac (2013, 2014) Malzac in prep.) a time-dependent simulation framework designed to track the dynamical and radiative evolution of relativistic outflows. ISHEM is based on the internal-shock scenario, in which fluctuations in the ejection velocity of plasma shells along the jet produce collisions at different distances from the BH. These shocks accelerate particles through the DSA mechanism discussed above, continuously replenishing the non-thermal electron population and compensating for adiabatic losses. The resulting synchrotron emission from these repeatedly energised particles naturally gives rise to the broadband spectra characteristic of compact jets.

A key ingredient in ISHEM is the assumption of a direct connection between accretion flow variability and jet emission. In practice, the X-ray PDS of the source is used as input to the model: the temporal fluctuations observed in X-rays are mapped onto fluctuations in the bulk velocity of the shells launched at the jet base. The jet velocity fluctuations are generated with the same shape and amplitude as the observed X-ray PDS. The subsequent collisions between faster and slower shells produce internal shocks, whose dynamics ultimately shape the jet's radiative output. Prior applications of ISHEM adopting this approach have successfully modeled the radio-to-IR SEDs of several BH XRBs, including GX 339–4 and MAXI J1836–194 (Drappeau et al. 2015, 2017; Péault et al. 2019; Bassi et al. 2020; Marino et al. 2020).

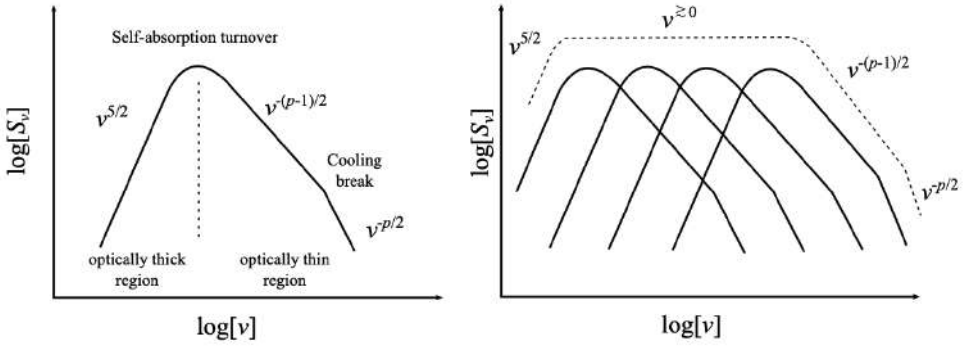

Figure 4.4: Synchrotron spectra produced by a power-law distribution of electrons, $N(E)\,dE = \kappa E^{-p}\,dE$. Left: example of a single synchrotron-emitting region, showing the characteristic transitions between the self-absorbed regime and the optically thin, cooling-dominated regime. Right: schematic illustration of how multiple such regions, each with its own turnover frequency, combine to form the flat composite spectrum typically observed in compact jets (dashed line). Figure adapted from the PhD thesis of T. Russell.

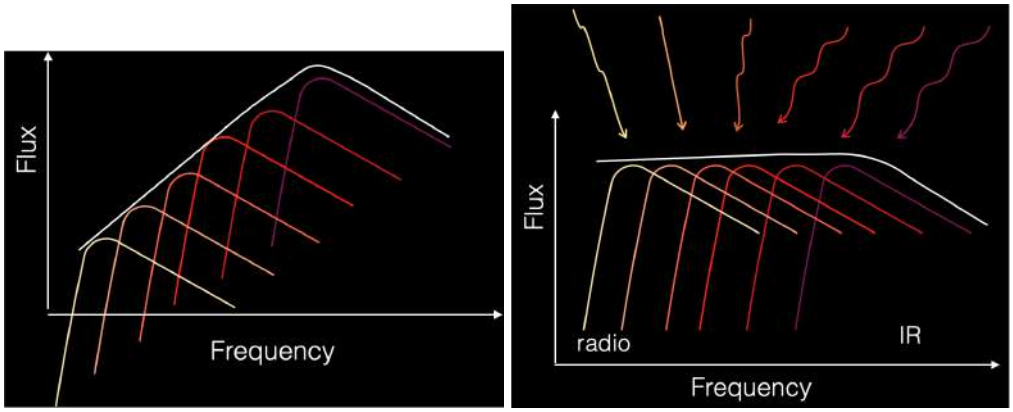

Figure 4.5: Left: schematic representation of the inverted synchrotron spectrum expected from an expanding jet in the absence of significant replenishment, where adiabatic losses steepen the emission at low frequencies. Right: observed flat spectrum produced in compact jets, where continuous energy injection or particle acceleration compensates for these losses, maintaining an approximately constant spectral slope along the jet.

4.3.2 Numerical Modeling and Geometry

In ISHEM the jet is discretized into cylindrical shells ejected at regular intervals with variable Lorentz factors. As particles traverse the shock front, their kinetic energy is partially converted into magnetic field energy and particle acceleration, giving rise to synchrotron radiation. Each shell is modeled as a cylinder whose radius expands along the jet axis according to a fixed geometry:

$$R(z) = r_b \left(\frac{z}{z_b}\right)^{\zeta} \tag{4.11}$$

where z denotes the position along the jet axis, and r_b and z_b correspond to the radius and height of the jet base. ζ sets the degree of collimation, typically $\zeta = 1$ for a conical jet (see 4.3.4 for more details). The radiative transfer is computed using a one-zone approximation for each cylinder, with angular dependence treated via an escape probability formalism. The radiation energy density $U_\mu(\nu)$ is evolved over time according to:

$$\frac{dU_\mu}{dt} = J(\nu) - A_\mu(\nu)U_\mu,$$

where A_μ includes both synchrotron self-absorption and photon escape, and $J(\nu)$ is the synchrotron source function. This numerical scheme is adapted from the BELM code (Belmont et al. 2008), offering a good balance between physical accuracy and computational efficiency (see Malzac in prep. for more details).

ISHEM consists of two main computational modules: `ShoGen` and `CoolSHEM`. The first module, `ShoGen`, generates the temporal sequence of shell ejections and constructs a hierarchical merging tree, tracking when and where collisions occur along the jet. The output from `ShoGen` is then passed to `CoolSHEM`, which solves the time-dependent radiative transfer and particle evolution equations for each collision, computing the emergent SED of the jet.

4.3.3 Kinetic Evolution and Radiative transfer

A major advancement of the `CoolSHEM` module in this new version is its detailed treatment of particle cooling. Earlier versions of ISHEM assumed purely adiabatic cooling and imposed a fixed power-law electron distribution. In contrast, `CoolSHEM` solves the coupled kinetic equations for electrons and photons, accounting for both synchrotron and synchrotron self-Compton (SSC) losses (Malzac in prep.). In the reference frame moving with the flow, the evolution over time of the lepton energy distribution is governed by a kinetic equation, following the formulation presented in Ghisellini et al. (1998):

$$\frac{\partial N}{\partial t} = \frac{\partial}{\partial \gamma}\left[\dot{\gamma}_c N + H\gamma^p \frac{\partial}{\partial \gamma}\left(\frac{N}{\gamma^p}\right)\right] + S(\gamma),$$

where N(γ) is the energy density, $\dot{\gamma}_c$ includes both radiative and adiabatic cooling, H accounts for synchrotron self-absorption, $p = \sqrt{\gamma^2 - 1}$ is the reduced particle momentum and $S(\gamma)$ represents the injection of accelerated particles at shocks.

Furthermore, the computational strategy has been refined compared to older versions of ISHEM. Rather than evolving radiative transfer for each shell individually, CoolSHEM applies a statistical sampling method: ejecta are grouped into branches based on their merger history, which can be evolved in parallel. This reduces computational cost while preserving spectral accuracy.

Another significant improvement is that CoolSHEM produces directly calibrated SEDs over a wide frequency range, eliminating the need for external fitting tools such as XSPEC. This allows for straightforward comparison with observational data across the radio to X-ray regime.

4.3.4 Jet Geometry and System Parameters

The geometry of the jet and its fundamental physical parameters play a central role in shaping its radiative properties because they determine how energy is dissipated and radiated along the outflow (Blandford & Königl 1979; Markoff et al. 2005). The ISHEM framework describes the jet using a well-defined set of parameters grouped into three main categories: particle distribution, system energetics, and jet geometry.

Particle Distribution Parameters

The injected population of relativistic particles follows a power-law energy distribution, expressed as $N(E) \propto E^{-p}$, where p is the spectral index (as I have described in the previous paragraphs). The parameter

$\gamma_{\rm min}$ sets the minimum Lorentz factor that the injected distribution needed to be accelerated. While particles with lower lorentz factors may still exist, their synchrotron emissivity is strongly suppressed, since the power radiated per electron is $P_{\rm sync} \propto \gamma^2$ (Rybicki & Lightman 1979; Longair 2011), making them largely irrelevant for the observed radiation. Furthermore, even if particles are initially injected at high energies, radiative and adiabatic losses inevitably shift a significant fraction of them toward lower lorentz factors, thereby repopulating the low-frequency part of the distribution. In this sense, $\gamma_{\rm min}$ should be regarded primarily as an injection parameter that sets the fraction of energy supplied to electrons that are radiatively efficient.

An important additional parameter is the acceleration efficiency, denoted by ξ_a, which defines the timescale over which particles gain energy relative to their gyro-period. Physically, ξ_a represents the inverse of the number of gyro-orbits required for a particle to double its energy. It is a dimensionless number ranging from 0 to 1, larger values of ξ_a correspond to more efficient acceleration, and hence higher maximum energies attainable by the particle population. This parameter is crucial for determining the location of the high-energy cutoff in the synchrotron spectrum and the onset of cooling effects. Indeed unlike older implementations, ISHEM no longer assumes a fixed $\gamma_{\rm max}$ for the electron population. Instead, the maximum energy that can be reached by the distribution of particles is computed self-consistently by equating the acceleration and cooling timescales.

Jet Power and Dynamical Parameters

The kinetic power of the jet, $P_{\rm jet}$, quantifies the amount of mechanical energy transported by the jet per unit time. It represents a fraction of the accretion power converted into bulk motion of relativistic plasma. The bulk lorentz factor Γ characterizes the relativistic motion of the plasma flow along the jet axis. Since the outflow velocity is always close to the speed of light, Γ does not simply represent the flow speed, but rather quantifies the degree of relativistic beaming and time dilation associated with the jet (Blandford & Königl 1979). The amplitude and timescale of the Γ fluctuations, that are linked to the variability of the accretion flow, determine the dissipation profile and ultimately shape the emergent broadband spectrum (Malzac 2014). Indeed as I described before, in the ISHEM framework, shells are ejected with fluctuations in Γ with a PDS that has the same shape and amplitude of the X-ray observed one. These fluctuations lead to collisions between faster and slower shells, dissipating kinetic energy and powering particle acceleration.

Jet Geometry and Expansion Profile

The third group concerns the jet geometry. The jet half-opening angle, ϕ_J, defines the angular width of the jet at the base—identified with the ejection region near the BH and the accretion flow. This angle is described by the relation:

$$\tan \phi_J = \frac{r_b}{z_b}, \tag{4.12}$$

I already introduced the key parameter ζ, which controls how the jet radius evolves with distance z from the compact object. The dependence of the jet radius on height is given by Eq. 4.11. This relation led to the definition an opening angle at any distance from the jet base. By setting z_r to the region where the bulk of the radio emission originates, one obtains the effective radio opening angle, which is the quantity typically inferred from radio observations:

$$\phi_r = \arctan\left(\frac{r_b}{z_r}\left(\frac{z_r}{z_b}\right)^{\zeta}\right). \tag{4.13}$$

In the case of a conical geometry ($\zeta = 1$), this angle is identical to the opening angle at the jet base, since the jet expands linearly with distance. If $\zeta > 1$, the jet expands faster than linearly, producing a broader and less stable outflow structure, which is expected to evolve toward a more collimated configuration with $\zeta \leq 1$ (Kaiser 2006). Conversely, $\zeta < 1$ corresponds to a parabolic geometry, in which the jet remains more confined and its radius increases sub-linearly with distance from the base (see Eq. 4.11 and Fig. 4.6).

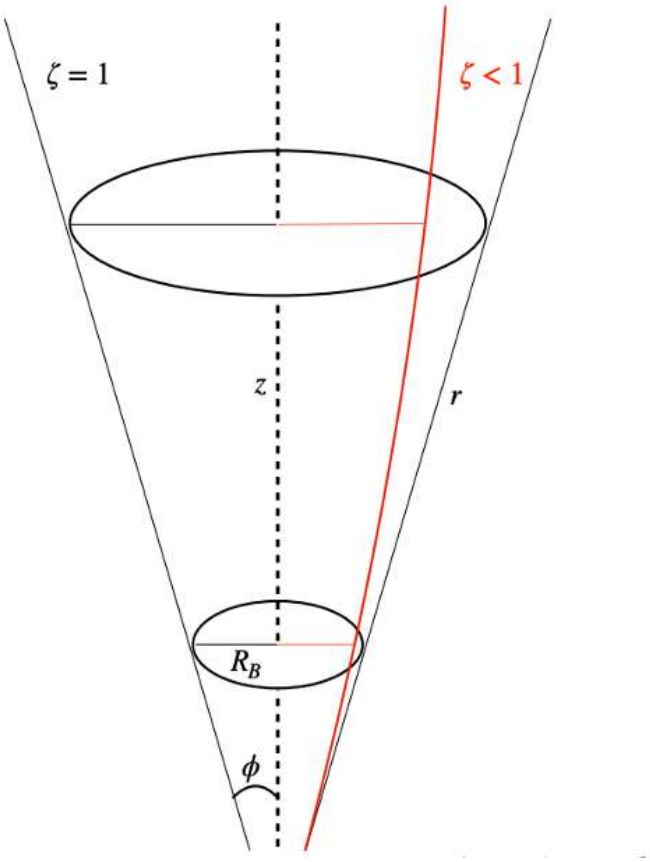

Figure 4.6: Schematic representation of the jet geometry for different values of the geometric parameter ζ, which controls the jet collimation profile. The black lines show the standard conical geometry ($\zeta = 1$), while the red curve illustrates a non-conical configuration ($\zeta < 1$), resulting in a more gradually expanding jet. Adapted from Marino et al. (2020).

Previous applications of ISHEM to BH XRBs typically assumed a conical geometry with ζ fixed to 1 by default (Drappeau et al. 2015; Péault et al. 2019; Bassi et al. 2020). However, Marino et al. (2020) examined how varying ζ impacts the radiative properties of the jet for a NS LMXB. Their study showed that reducing ζ (i.e., adopting a more parabolic shape) leads to a higher degree of collimation and consequently reduces adiabatic energy losses (see Fig. 4.6). In such configurations, the overall SED is modified: a more confined jet restricts the range of emitting regions along the axis, narrowing the range of self-absorbed synchrotron frequencies. The transition from the optically thick to the optically thin regime, visible as the low-frequency turnover in the SED, shifts to higher frequencies for more collimated jets (i.e. $\zeta < 1$). This feature marks the location of the terminal region of the compact jet, where most of the optically thick emission originates.

Moreover, in the ISHEM simulations, the maximum physical extent of the jet is determined by the distance that shells can propagate during the total simulation time, typically of the order of $c \cdot t_{\rm sim}$. Extending the simulation duration allows the shells to travel farther, thereby shifting the turnover frequency toward lower values. However, this variation affects only the optically thick portion of the SED, while the optically thin

(higher-frequency) part remains nearly unchanged. This behaviour contrasts sharply with the conical case ($\zeta = 1$), for which the simulated SED is largely independent of $t_{\rm sim}$. Such effects have also been confirmed in the updated version of ISHEM currently under development (Malzac in prep.).

4.4 MAXI J1535–571: Data Analysis and Jet Modelling with ISHEM

The primary objective of this work is to model the SED of J1535 across multiple observations using the most recent version of the ISHEM code, and to investigate whether the jet parameters exhibit any evolution over time. In doing so, I also explored a non-conical jet geometry, allowing the geometry parameter ζ to vary freely for the first time in a BH system. In the following sections, I present my analysis and discuss the resulting implications.

4.4.1 Source Overview

The Galactic BH XRB MAXI J1535–571 (hereafter J1535) was discovered in September 2017 during an outburst detected by the *MAXI/GSC* nova alert system (Negoro et al. 2017). This event triggered an extensive multi-wavelength campaign, with follow-up observations from radio to hard X-rays, which monitored the system for almost one year. The wealth of data collected during this period makes J1535 one of the best-studied transients of recent years, and it provided a unique opportunity to investigate the coupling between accretion and ejection in BH X-ray binaries (Tao et al. 2018; Russell et al. 2019; Baglio et al. 2018; Chauhan et al. 2019). Throughout the outburst, the source exhibited the full range of accretion states, including the hard-intermediate state (HIMS) and the soft-intermediate state (SIMS), as documented by Tao et al. (2018) and Nakahira et al. (2018).

Several studies have attempted to constrain the distance to J1535 using different methods, resulting in broadly consistent values. Neutral hydrogen absorption measurements obtained with the Australian Square Kilometre Array Pathfinder (ASKAP) place the system at $4.1^{+0.6}_{-0.5}$ kpc (Chauhan et al. 2019). Alternatively, spectral modelling with relativistic reflection and thin-disc components suggests a distance of $5.4^{+1.8}_{-1.1}$ kpc (Sridhar et al. 2019). Radio monitoring during the outburst revealed a rich phenomenology of compact and transient jet activity. In the bright hard state, compact jets were observed with the flat-to-inverted spectral shape typical of self-absorbed synchrotron emission (Russell et al. 2019). As the system evolved towards softer states, the compact jets quenched and the radio emission became dominated by rapid variability and intense flaring, marking the transition into the SIMS.

In my thesis work, I focus on the modelling of the broadband SED of J1535 during the phases dominated by compact jets. To this end, I make use of the most recent developments of the ISHEM code (Malzac, in prep.), which allows a physically motivated description of jet emission across multiple wavelengths. In addition, I explored the possible contribution of soft γ-ray emission within the ISHEM framework, in order to investigate whether compact jets can contribute to the high-energy radiation observed in this system. This approach complements previous studies, which first modelled the broadband SED of the compact jet using phenomenological fits (Russell et al. 2019 and see Fig. 4.7) and subsequently focused mainly on the behaviour of the transient ejecta in this source (Russell et al. 2020). In contrast, in this work I adopt a physically motivated framework, fitting the SEDs with the ISHEM jet model and thereby obtaining direct constraints on the physical conditions of the compact jet itself.

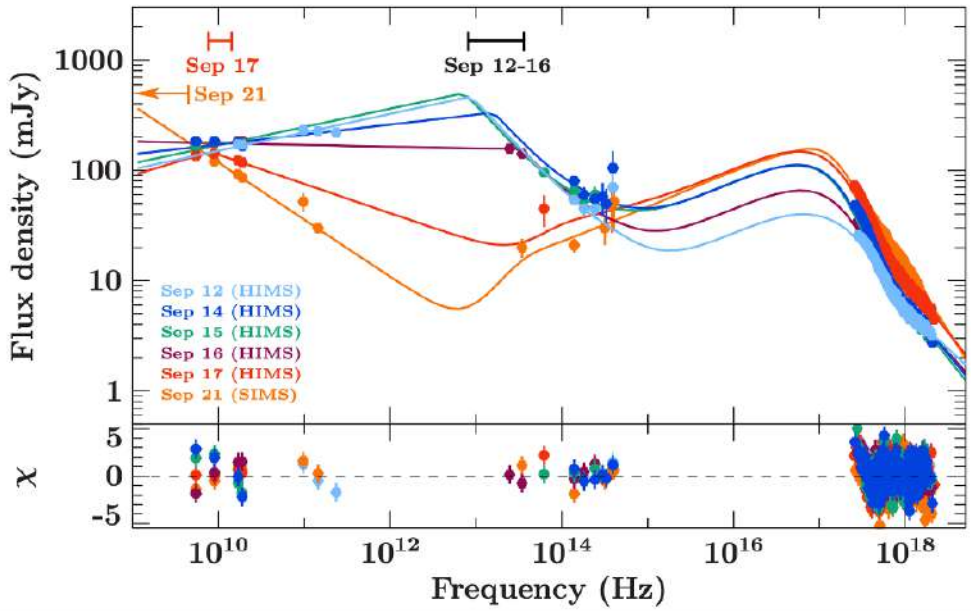

Figure 4.7: Phenomenological broad-band SED fits of MAXI J1535−571 during the rise of its 2017 outburst (figure adapted from Russell et al. 2020), covering the transition from the HIMS to the SIMS. Solid lines show the best-fitting models for each epoch (coloured by date). Fit residuals are displayed below. A marked change in the jet occurs on 17 September, when $\nu_{\rm break}$ dropped by nearly three orders of magnitude into the radio band. X-ray data are de-absorbed for display.

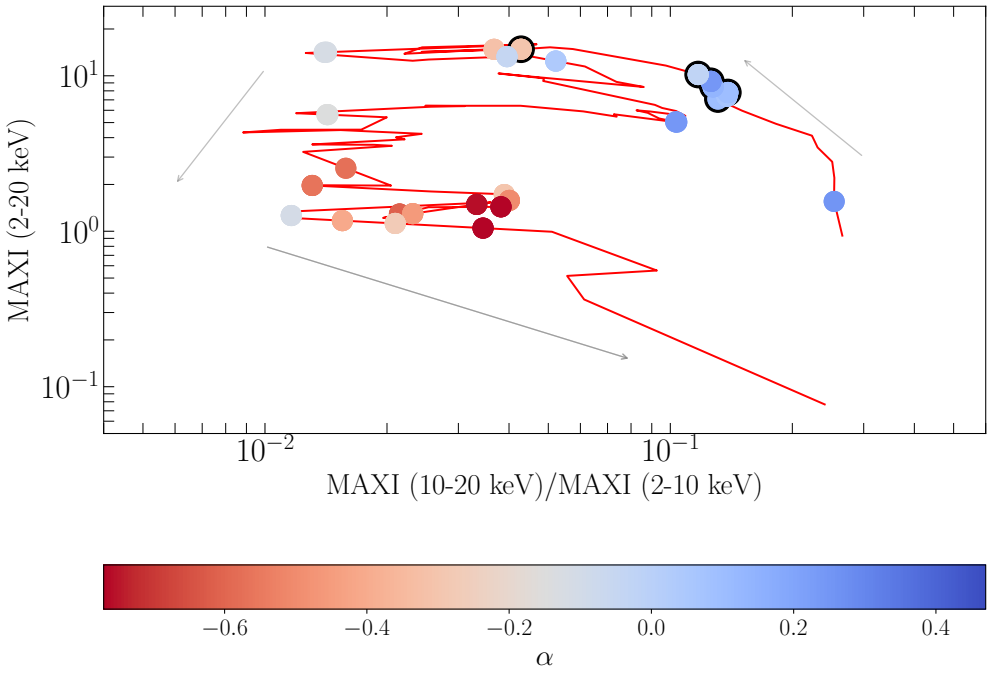

Figure 4.8: Readapted from Russell et al. (2019), the hardness-intensity diagram (HID) J1535 during its major outburst, where the hardness was determined from MAXI data. Only MAXI detections with a significance greater than 1.5σ are shown. Grey arrows indicate the overall evolution of the source. The overlaid circles represent radio observations, with the corresponding spectral index α. The color of the circles indicates the observed radio spectrum: blue represents a flat or inverted spectrum (associated with the compact jet), while red represents a steep spectrum (associated with the transient jet), as indicated by the color bar. The compact jet evolves into the transient jet as the source undergoes rapid X-ray spectral softening. The compact jet reappears during a brief return to the hard state, before vanishing again as the source softens rapidly, with the radio spectrum becoming steep. The black-marked points correspond to the observations analyzed in detail in this study.

4.5 Observations and data reduction

For this work, I made use of the multi-wavelength dataset presented by Russell et al. (2020), which covers the period between September 12 and September 21, 2017 (see Fig. 4.8). This campaign is particularly valuable because it provides strictly simultaneous coverage from the radio up to the optical bands, allowing me to reconstruct the broadband SED of the jet with unprecedented detail.

The radio observations were carried out with the Australia Telescope Compact Array (ATCA) at 5.5, 9.0, 17.0, and 19.0 GHz, while submillimeter measurements were obtained with the Atacama Large Millimeter/submillimeter Array (ALMA) at 97.5, 145, and 236 GHz (Russell et al. 2020). At shorter wavelengths, mid-IR data were collected with VISIR at the Very Large Telescope (VLT), and additional near-IR (NIR) observations were obtained with the Rapid Eye Mount (REM) telescope at frequencies of 1.39, 1.81, and 2.43×10^{14} Hz. Optical measurements were provided by the Las Cumbres Observatory (LCO), at 2.99, 3.12, 3.28, and 3.93×10^{14} Hz (Baglio et al. 2018).

The optical and IR fluxes had already been corrected for interstellar extinction by Baglio et al. (2018), who adopted an extinction based on an $N_{\rm H} = (3.84 \pm 0.03) \times 10^{22}\,{\rm cm}^{-2}$, derived from fitting the *Swift*/XRT spectrum obtained on 2017 September 11. This step is crucial, as it ensures that the intrinsic emission from the jet can be reliably compared with the model predictions.

The combination of these datasets provides a comprehensive view of the evolution of the compact jet as the source approached the soft state (see Fig. 4.8 and Tab. A1 in Russell et al. 2019). However, I decided to exclude the dataset corresponding to the SIMS from the modelling. As discussed by Russell et al. (2019), during the soft state the compact jet quenches and the emission becomes dominated by discrete ejecta, whereas ISHEM is specifically designed to model compact jet spectra. In the last observation, one VISIR data point was excluded from the fit. As shown in Fig. 1 of Russell et al. (2020), this point lies well above the expected jet contribution for this state and exhibits an upward trend. As such, it is most likely associated with emission from the accretion disk rather than the compact jet. We therefore treated it as an upper limit: although it does not directly trace the jet, it constrains the fit by requiring the simulated flux to remain below the observed value.

4.5.1 X-ray data

NICER

X-ray data are essential for constructing the PDS, which serve as a key input for the ISHEM simulations. I analysed X-ray observations obtained with the *Neutron Star Interior Composition Explorer* (*NICER*; Gendreau et al. 2016). In particular, I made use of five *NICER* pointings that were taken simultaneously with the radio observations, ensuring direct comparison with the jet emission at lower frequencies.

The reduction was performed using the *NICER* Data Analysis Software (NICERDAS, version 5), included in the *HEASoft* distribution (version 6.32). I applied the standard pipeline task `nicerl2` to produce Level 2 data, which involves calibration, screening, and standard filtering procedures. Following the instrument team's recommendations, I excluded detectors 14 and 34 from the analysis, as they are known to produce spurious signals. The parameter `detlist=launch` was used to select the standard set of detectors that were

operational at launch. Finally, to correct for non-source contributions, I applied the *SCORPEON* background model in its standard static configuration, generating a background spectrum file that accounts for both instrumental and diffuse components.

Swift/XRT

The *Neil Gehrels Swift Observatory* (*Swift*; Gehrels 2004) monitored J1535 with its X-ray Telescope (XRT) during the rise of the 2017 outburst, typically providing one pointing every 1–2 days. A detailed description of this monitoring campaign is presented in Tao et al. (2018).

For this work, I considered only the *Swift*/XRT observations closest in time to the ATCA radio data, within a temporal window of ± 0.5 days. The reduction was performed with the `xrtpipeline` task included in the *HEASoft* software package (version 6.32.1), adopting the most recent calibration files. To mitigate pile-up effects, I excluded the central region of the source point spread function (PSF) and instead extracted spectra using an annular region centred on the source with inner and outer radii of 24 and 47 arcseconds, respectively. The background spectrum was extracted from a nearby annulus of the same size.

These spectra were used to derive the X-ray fluxes and the resulting X-ray luminosities, which provided a physically motivated initial guess for one of the ISHEM input parameters (see Sec. 4.6.1). To derive the 0.5-10 keV fluxes, I perfomed spectral fits with the XSPEC package (version 12.13.1; Arnaud 1996), adopting a model consisting of comptonization component (`nthcomp`) plus a thermal disk emission (`diskbb`), both absorbed by the interstellar medium using `TBabs`, using the Wilms et al. (2000) abundances and the photoelectric cross-sections of Verner et al. (1996).

Then, assuming a BH mass of 10 $M_{\odot}$ and a distance of 4.1 kpc (Chauhan et al. 2019), I converted the best-fit unabsorbed fluxes into luminosities. These values, reported in Tables 4.3, are consistent with earlier estimates (e.g. Sreehari et al. 2019).

Swift/BAT

To extend the X-ray coverage to higher energies, I analysed archival data from the Burst Alert Telescope (BAT) onboard *Swift*, retrieved through the HEASARC public archive. The data reduction was carried out using the *BAT-IMAGER* software package (Segreto et al. 2010), which is specifically designed to process coded-mask instrument observations. This tool constructs all-sky images by modelling and subtracting the instrumental background, from which light curves and spectra of individual sources can be extracted.

For J1535, I produced light curves in three distinct energy bands (15–30 keV, 30–50 keV, and 50–196 keV), adopting a temporal resolution of one day (see Fig. 4.9). In addition, I extracted spectra in the 15–196 keV band, using logarithmic binning across six energy intervals and applying the official BAT response matrix (see Fig. 4.10).

The extracted spectra were analysed in XSPEC using the `cutoffpl` model, which is widely employed to describe the continuum shape of hard X-ray spectra in accreting BHs. From this analysis, I followed the temporal evolution of the photon index, which revealed significant spectral change only in the final observation, corresponding to the SIMS state. (see Fig. 4.11). Finally, I verified that the results were not affected by contamination from other sources within the BAT field of view, ensuring the reliability of the

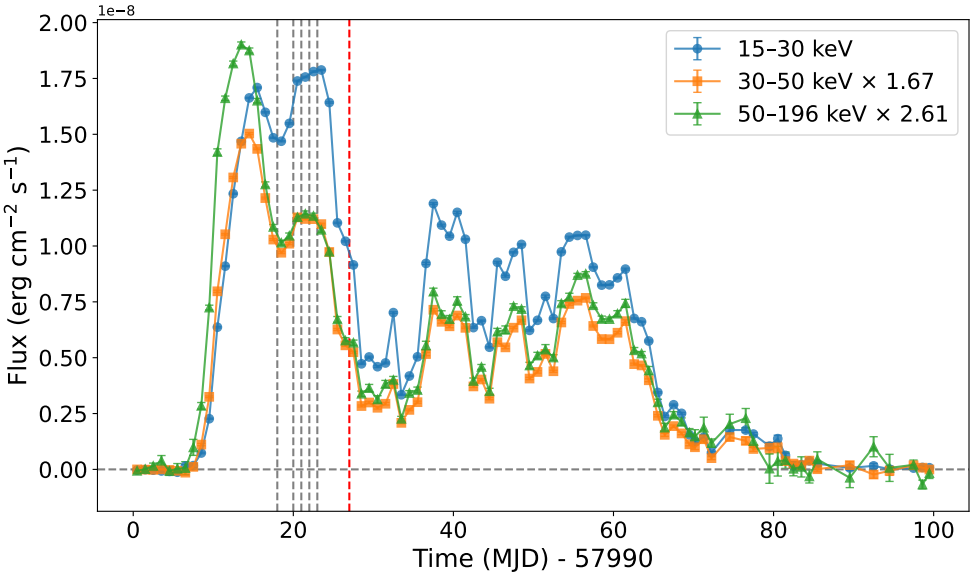

Figure 4.9: BAT light curves of MAXI J1535–571 in three energy bands: 15–30 keV (blue circles), 30–50 keV scaled by a factor of 1.67 (orange squares), and 50–196 keV scaled by a factor of 2.61 (green triangles). Vertical dashed black lines mark our observation dates (MJD 58008, 58010, 58011, 58012, and 58013), while the vertical dashed red line at MJD 58017 indicates the observation performed in the SIMS. Fluxes are expressed in erg cm^{-2} s^{-1}, and time is given as MJD – 57990.

extracted spectra.

4.5.2 Soft γ-ray data

To extend the spectral analysis of J1535 to the soft γ-ray domain and explore potential jet-related high-energy emission with ISHEM, I included data from the SPectrometer on board *INTEGRAL* (SPI; Roques et al. 2003). The instrument operates in the 20 keV–8 MeV energy range, making it well suited for studying the soft γ-ray tails of XRB spectra.

For this work, I incorporated the SPI observations presented by Rodi et al. (2022), corresponding to revolution 1860 (8–10 September 2017). This observation is nearly simultaneous with the first multiwavelength dataset analysed in this study, allowing a consistent comparison across the full radio–γ-ray SED. These data were used to test the possible contribution of non-thermal processes associated with the jet.

4.5.3 X-ray timing analysis

To investigate the fast variability properties of J1535 during the epochs analysed in this work, I performed a timing analysis using the XRONOS task `powspec` (Stella & Angelini 1992) to produce PDS. The event files were rebinned to a temporal resolution of $\Delta t = 0.02$ s, corresponding to a Nyquist frequency of $1/(2\Delta t) = 25$ Hz (Nyquist 1928). Power spectra were computed over segments of $N = 2048$ bins, giving a segment length of $T = N\Delta t = 41$ s and a frequency resolution of $\delta\nu = 1/T \simeq 0.02$ Hz. This configuration was applied uniformly across all observations to ensure consistency in the comparison of the timing properties.

Each PDS was initially calculated using the Leahy normalization (Leahy et al. 1983) and then converted to fractional rms^2 normalization to allow a direct interpretation in terms of intrinsic source variability. The

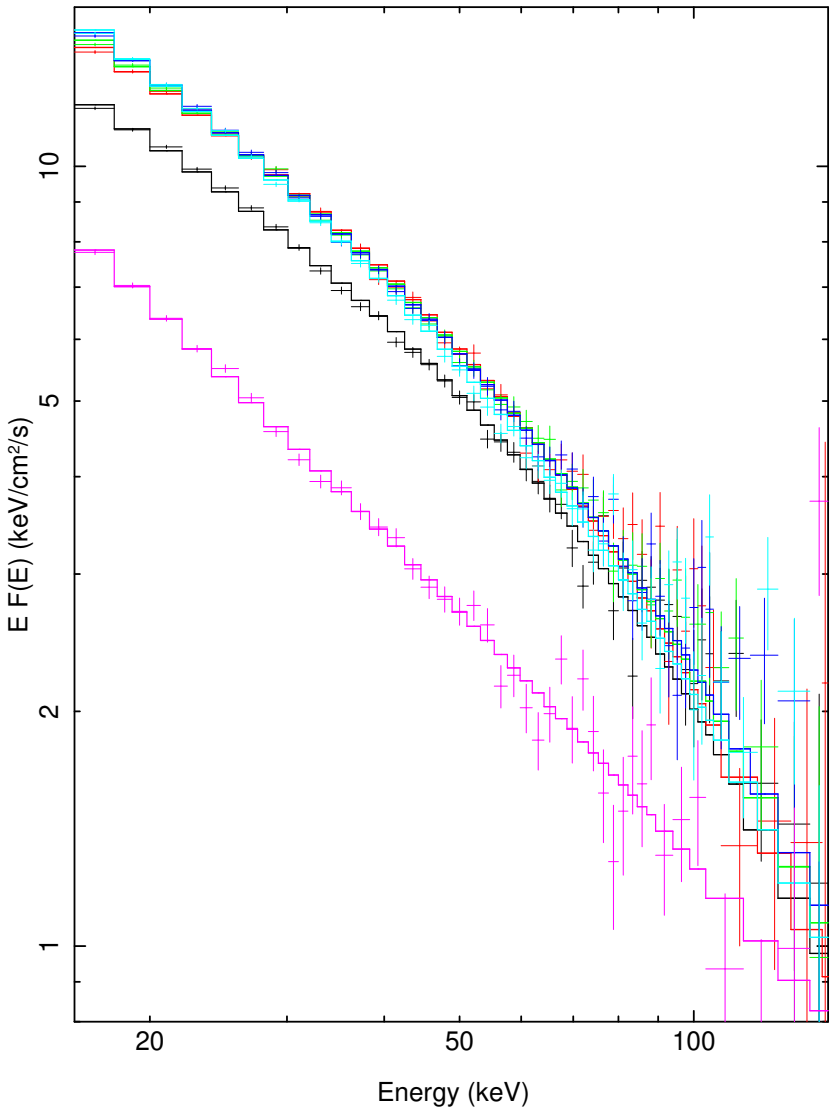

Figure 4.10: BAT spectra of MAXI J1535–571 corresponding to the same epochs as the light curves shown in Fig. 4.9. The spectra cover the 15–130 keV range and were extracted using logarithmic binning across six energy intervals. The colours indicate the different epochs: black (Obs 1), red (Obs 2), green (Obs 3), blue (Obs 4), cyan (Obs 5), and magenta (SIMS observation).

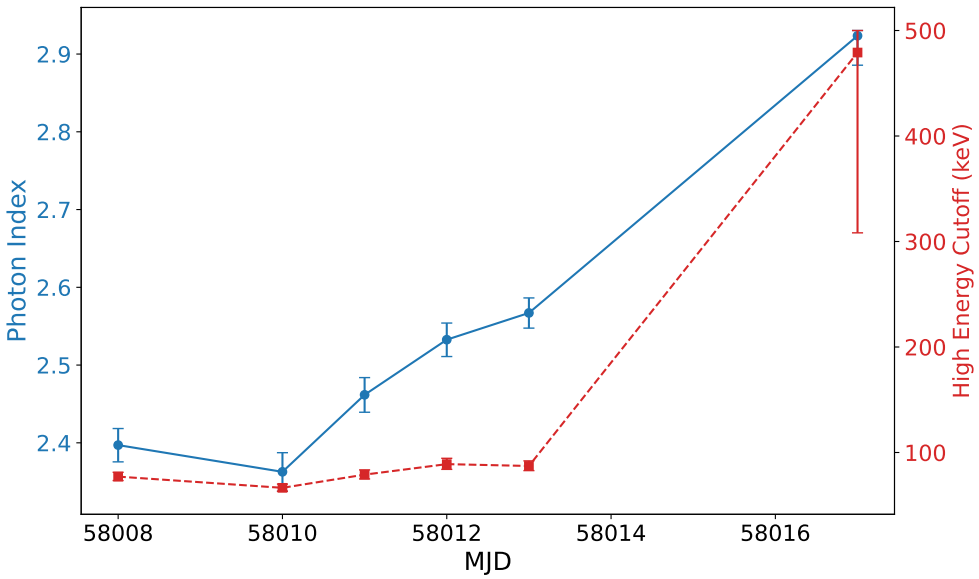

Figure 4.11: Evolution of the photon index (blue solid line, left axis) and high-energy cutoff (red dashed line, right axis) of the `cutoffpl` model for MAXI J1535−571, as a function of the MJD of each BAT spectrum corresponding to the same epochs as the light curves shown in Fig. 4.9. Error bars for both parameters represent the 90% confidence intervals.

Poisson noise level was estimated and subtracted following the prescription of Zhang et al. (1995). After subtraction, logarithmic rebinning in frequency was applied to enhance the visibility of broad features (see Fig. 4.12).

The resulting power spectra consistently revealed the presence of low-frequency QPOs in the ∼1–10 Hz range, characteristic of the hard-intermediate state. These findings are in agreement with those reported by Chen et al. (2022) and Chen & Wang (2024). Each PDS was modeled using a combination of Lorentzian components: broad Lorentzians to describe the broadband noise continuum and narrower ones to reproduce the QPO peaks.

The best-fit parameters derived from these models, including the centroid frequencies, widths, and amplitudes of the QPO components, were used as direct inputs for the ISHEM simulations. The corresponding results are summarized in Table 4.1.

4.6 Analysis of MAXI J1535−571 Using ISHEM

In this section, I present the application of ISHEM to MAXI J1535−571, describing the analysis procedure and the results obtained on the physical properties of its compact jet. The dataset used in this work consists of the five observations of J1535 I described before, obtained during its transition from the hard state into the soft state through the HIMS.

4.6.1 Fitting Procedure and Model Setup

The fitting procedure performed with ISHEM for each observation was carried out using a Markov Chain Monte Carlo (MCMC) approach, aimed at exploring the full parameter space and identifying the optimal set

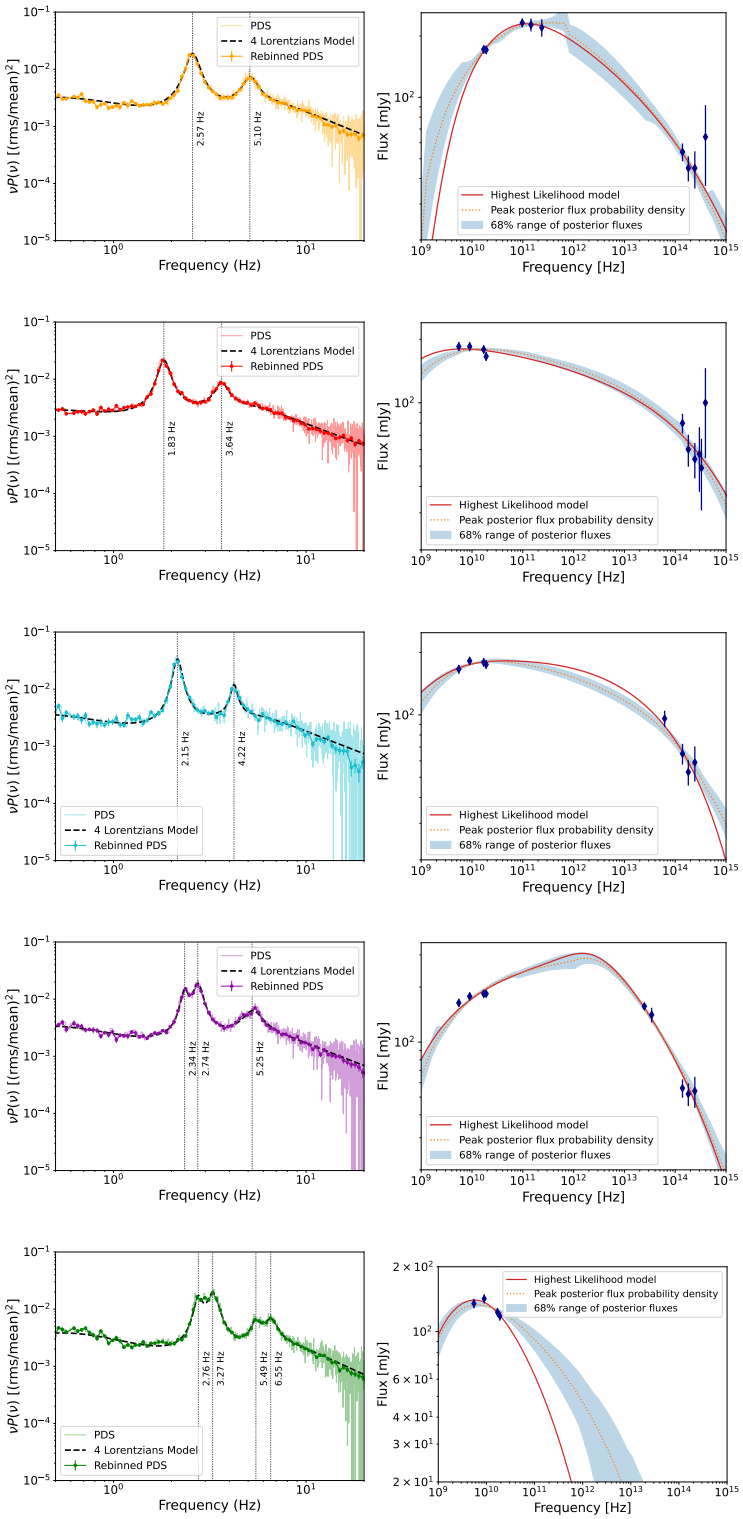

Figure 4.12: Noise-subtracted PDS (left panels) and corresponding SEDs (right panels) of MAXI J1535−571 for the five observations analysed. The PDS are shown in the νP_ν representation, with colour points corresponding to the logarithmically rebinned periodogram and the black dashed curves indicating the best-fit multi-Lorentzian models; vertical dashed lines mark the centroid frequencies of the detected QPOs. The SEDs are fitted with the ISHEM model assuming a parabolic jet geometry, with best-fit parameter values reported in Table 4.3.

Table 4.1: Best-fit parameters for the PDS of the five observations, modelled with multiple Lorentzian components. The Modified Julian Date (MJD) of each observation is included. Each Lorentzian is characterised by its central frequency (x_0), FWHM, and amplitude.

Obs.	MJD	Component	x_0 [Hz]	FWHM [Hz]	Amplitude
1	58008	Low-Frequency QPO	2.572 ± 0.009	0.459 ± 0.002	49 ± 3
		High-Frequency QPO	5.10 ± 0.03	1.0 ± 0.1	7.1 ± 0.5
		Broad Noise	(0)	0.91 ± 0.05	75 ± 4
		Additional Lorentzian	2.7 ± 0.4	8.8 ± 0.5	4.5 ± 0.4
2	58010	Low-Frequency QPO	1.828 ± 0.007	0.31 ± 0.02	77 ± 5
		High-Frequency QPO	3.60 ± 0.02	0.60 ± 0.08	11 ± 1
		Broad Noise	(0)	0.84 ± 0.05	105 ± 12
		Additional Lorentzian	3.7 ± 0.3	5.4 ± 0.3	5 ± 1
3	58011	Low-Frequency QPO	2.146 ± 0.009	0.23 ± 0.03	110 ± 12
		High-Frequency QPO	4.22 ± 0.02	0.38 ± 0.09	15 ± 2
		Broad Noise	(0)	0.72 ± 0.04	95 ± 7
		Additional Lorentzian	3.3 ± 0.3	7.5 ± 0.5	5.5 ± 0.6
4	58012	Low-frequency QPO	2.34 ± 0.02	0.23 ± 0.04	36 ± 6
		Low-frequency QPO	2.74 ± 0.01	0.32 ± 0.04	45 ± 5
		High-frequency QPO	5.25 ± 0.06	0.9 ± 0.3	5.3± 0.6
		Broad noise	(0)	0.80 ± 0.06	74 ± 4
		Additional Lorentzian	3.6 ± 0.6	7 ± 1	4.0 ± 0.5
5	58013	Low-frequency QPO	2.76 ± 0.04	0.30 ± 0.07	35 ± 4
		Low-frequency QPO	3.27 ± 0.03	0.50 ± 0.06	38 ± 3
		High-frequency QPO	5.49 ± 0.05	0.7 ± 0.3	5.0 ± 0.6
		High-frequency QPO	6.55 ± 0.08	1.2 ± 0.2	5 ± 0.4
		Broad noise	(0)	0.96 ± 0.05	75 ± 3
		Additional Lorentzian	6 ± 1	9 ± 2	2 ± 0.5

Table 4.2: Best-fit parameters of the ISHEM model for the five observations of J1535 for a parabolic geometry, excluding QPOs in the best-fit of the PDS and with $t_{\rm simu} = 1 \times 10^6$ s. The reported parameter uncertainties correspond to the 68% confidence intervals, derived from the marginalized posterior distributions by identifying the peak of the MCMC chain.

Parameter	**Obs 1**	**Obs 2**	**Obs 3**	**Obs 4**	**Obs 5**
$P_{\rm jet}$	$0.89^{+0.05}_{-0.3}$	$0.98^{+0.01}_{-0.30}$	$0.97^{+0.03}_{-0.40}$	$0.5^{+0.3}_{-0.2}$	$0.97^{+0.03}_{-0.40}$
Γ	5 ± 1	5 ± 1	5^{+2}_{-3}	$1.5^{+0.7}_{-0.2}$	11 ± 5
ϕ_J (°)	6^{+20}_{-2}	33 ± 10	30 ± 5	49^{+1}_{-12}	$49^{+0.6}_{-12}$
$\gamma_{\rm min}$	320^{+600}_{-20}	900^{+70}_{-130}	910^{+94}_{-150}	310^{+170}_{-100}	280 ± 150
p	2.9 ± 0.5	$2.2^{+0.5}_{-0.2}$	2.4 ± 0.5	$3.3^{+0.2}_{-0.8}$	$3.40^{+0.05}_{-0.50}$
ζ	$0.6^{+0.04}_{-0.1}$	0.73 ± 0.03	$0.70^{+0.03}_{-0.04}$	0.6 ± 0.3	$0.58^{+0.05}_{-0.04}$
χ^2/dof	2.3/2	9/3	4/1	18/2	4/2

Table 4.3: Best-fit parameters of the ISHEM model for the five observations of J1535 for a parabolic geometry, including QPOs in the best-fit of the PDS, with $t_{\rm simu} = 1 \times 10^6$ s and with the upper limit on ϕ_J increased to 90°. The table also reports the unabsorbed 0.5–10 keV flux for each observation. The reported parameter uncertainties correspond to the 68% confidence intervals, derived from the marginalized posterior distributions by identifying the peak of the MCMC chain.

Parameter	**Obs 1**	**Obs 2**	**Obs 3**	**Obs 4**	**Obs 5**
$P_{\rm jet}$	$0.8^{+0.2}_{-0.5}$	$0.93^{+0.07}_{-0.3}$	$0.96^{+0.04}_{-0.4}$	$0.8^{+0.2}_{-0.5}$	$0.96^{+0.04}_{-0.60}$
Γ	5 ± 1	5 ± 1	5 ± 2	$1.5^{+0.30}_{-0.02}$	7^{+6}_{-4}
ϕ_J (°)	10^{+28}_{-6}	66 ± 20	40^{+10}_{-30}	70^{+10}_{-14}	89^{+1}_{-11}
$z_r\,(R_g)$	2×10^8	3×10^5	6×10^5	3×10^7	4×10^6
ϕ_r (°)	$0.04^{+0.2}_{-0.03}$	7^{+74}_{-7}	2 ± 1	$0.3^{+0.2}_{-0.1}$	$0.5^{+0.6}_{-0.2}$
$\gamma_{\rm min}$	660 ± 230	990^{+6}_{-170}	980^{+20}_{-250}	250^{+150}_{-240}	220^{+240}_{-190}
p	2.8 ± 0.5	2.3 ± 0.4	2.6 ± 0.7	$2.9^{+0.5}_{-0.9}$	$3.20^{+0.04}_{-0.6}$
ζ	0.6 ± 0.1	0.71 ± 0.3	0.71 ± 0.03	0.61 ± 0.02	$0.53^{+0.04}_{-0.03}$
Flux (erg cm^{-2} s^{-1})	9.0×10^{-8}	9.0×10^{-8}	2.0×10^{-7}	3.5×10^{-7}	3.0×10^{-7}
χ^2/dof	3/3	6/3	4/1	8/2	2/2

of model parameters for reproducing the observed SEDs (Malzac, in prep., for further details). To ensure robust statistical convergence, I employed 30 walkers for a minimum of 2000 steps, resulting in at least 6×10^4 total simulations per observation. When parallelized over 30 CPUs, each MCMC run required approximately 50 hours to complete. This duration is longer than that reported by Malzac (in prep.) due to the extended simulation time and the inclusion of additional degrees of freedom related to the jet geometry parameter ζ. Parameter uncertainties were estimated at the 68% confidence level, derived from the marginalized posterior distributions around the peak of the MCMC chains.

For the analysis, I used the `CoolJet` code, a simplified implementation within the ISHEM framework optimized for fast SED modeling. `CoolJet` adopts the same physical treatment of particle acceleration and radiative processes as `CoolSHEM`, but it estimates the jet emission using a time-averaged dissipation profile along the jet, as predicted by the internal shock model. This approximation significantly accelerates the computation while retaining the essential physical accuracy, making it particularly efficient for comparison with observational data (see Malzac, in prep., for details).

To reduce the dimensionality of the MCMC parameter space and accelerate convergence, I initially fixed some parameters, such as the BH mass (10 $M_\odot$), while the available estimates of the distance (Sridhar et al. 2019; Chauhan et al. 2019) and inclination (Russell et al. 2019; Miller et al. 2018; Cooper et al. 2025) were used to constrain their initial ranges (3.6–7.2 kpc; < 76°, respectively). I restricted the slope of the particle energy distribution to the physically motivated range $p \in [1.9, 3.5]$ (Malzac, in prep.), which stabilized the fits and prevented unphysical solutions.

In the bright hard state, the jet power $P_{\rm jet}$ is typically expected to be of the same order as the X-ray luminosity, as both trace the accretion energy budget (Malzac 2018). Based on the flux estimated from the simultaneous *Swift*/XRT observations, I inferred an X-ray luminosity varying between $\sim 0.3\,L_{\rm Edd}$ and $\sim 0.6\,L_{\rm Edd}$. I therefore adopted a prior range of 0.3–1.0 $L_{\rm Edd}$ for the $P_{\rm jet}$ parameter.

For each observation, I generated the synthetic jet SED with ISHEM, using as input the best-fit model to the observed X-ray PDS. It is important to stress that if the X-ray QPO observed in the PDS of J1535 (see

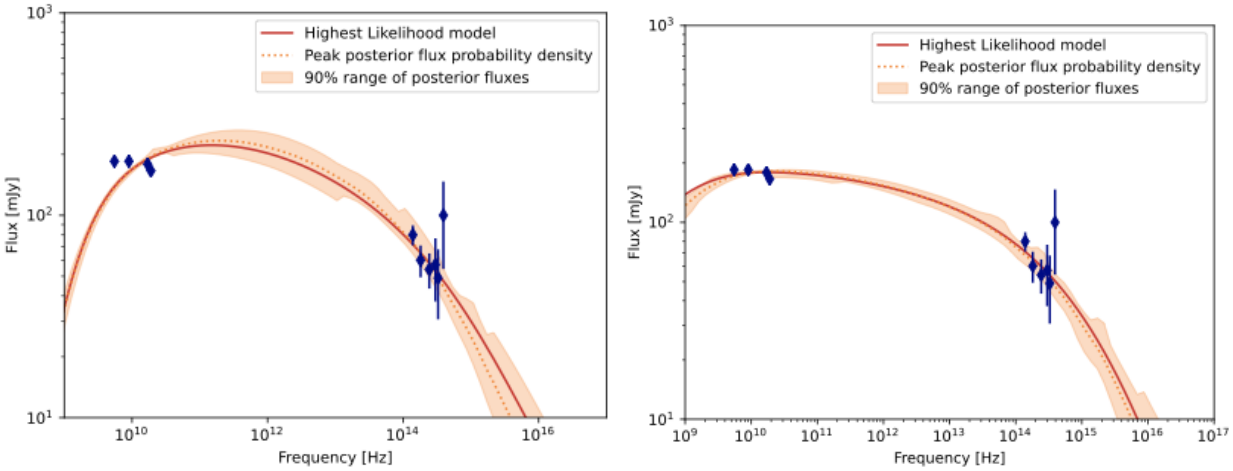

Figure 4.13: Comparison of ISHEM fits to the broadband SED of MAXI J1535–571 (Obs. 2, HIMS) using a parabolic jet geometry. Both panels adopt identical physical parameters, except for the simulation time, which is increased from $t_{\rm sim} = 10^5$ s (left) to 10^6 s (right). Extending the simulation time allows the outer shells to propagate farther, producing additional synchrotron emission at low frequencies and significantly improving the fit to the radio and sub-mm data.

Fig. 4.12 and Tab. 4.1) originates from a geometric effect, such as disk precession (Motta et al. 2015), it would not directly trace the intrinsic aperiodic variability of the accretion flow. Consequently, QPOs might play a negligible role in driving shell propagation and could, in principle, be excluded from the simulations.

For this reason, in my initial setup I excluded the QPO components from the PDS fits and assumed a conical jet geometry ($\zeta = 1$), consistent with previous applications of the code to BH systems (e.g. Drappeau et al. 2015; Péault et al. 2019; Bassi et al. 2020). In this configuration, the fits systematically converged toward very low inclination angles, implying a microblazar geometry inconsistent with current constraints for J1535. To avoid this unphysical solution, I fixed the inclination to $\theta = 10°$ (which defines the orientation of the jet axis relative to the line of sight), a value well within the observational upper limits (Russell et al. 2019; Cooper et al. 2025). However, this configuration resulted in very poor fit statistics, with reduced χ^2 values exceeding ~ 30.

Motivated by this outcome, I explored whether a non-conical jet geometry could provide a better description of the data. For the first time in the analysis of a BH XRB, I allowed the geometry parameter ζ to deviate from unity, adopting a prior range $\zeta \in [0.5, 1.0]$. This modification led to a significant improvement in the fit quality, with best-fit values of ζ in the range ~ 0.6–0.7 (see Tab. 4.2), indicating a mildly parabolic jet geometry.

I then investigated the combined effect of including the QPO components in the PDS fits and extending the upper limit on the jet opening angle up to 90° (see Tab. 4.3). I note that the opening angles reported here refer to the jet geometry at the base; a discussion of the effective opening angles evaluated at the radio-emitting region is presented in the Discussion. The inclusion of the QPOs, together with the relaxation of the opening-angle prior, does not alter the retrieved spectral parameters—most notably the value of ζ—but it does lead to an overall improvement in the fit quality. For this reason, in the following I refer to the results obtained from the fits that include all QPO components in the PDS.

By examining the evolution of the jet parameters across the different epochs, I find that quantities such as $P_{\rm jet}$, Γ, $\gamma_{\rm min}$, p, and ζ remain consistent within their 68% confidence intervals throughout the observations

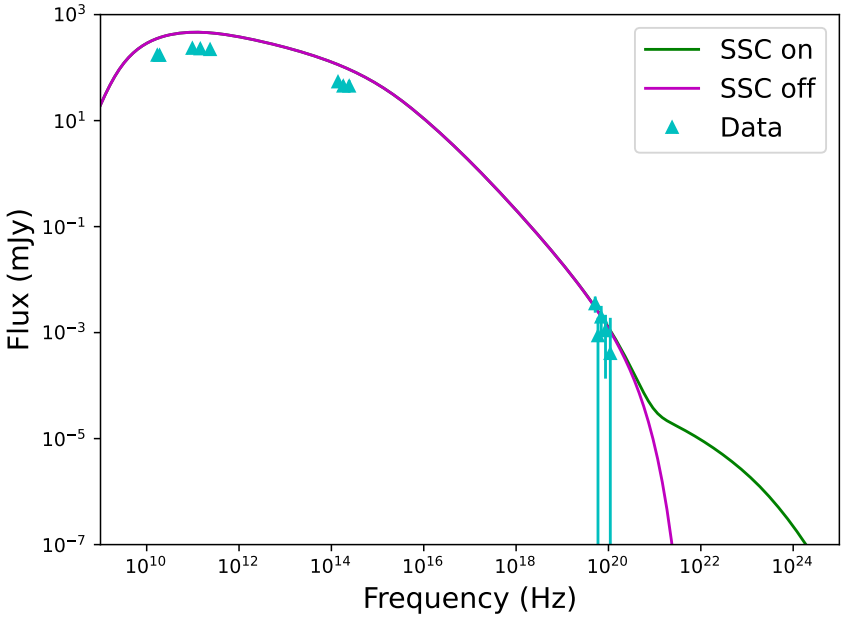

Figure 4.14: Simulated SED for Obs. 1 obtained with ISHEM, including the SPI data and without performing a fit. The figure shows how the inclusion of the SSC component affects the high-energy part of the spectrum, producing a significant excess only above the energy range covered by our SPI data ($E \gtrsim 450$ keV).

(see Tab. 4.3). In contrast, the jet opening angle ϕ_J shows a clear increase in the later epochs, indicating a systematic broadening of the outflow as the outburst progresses.

Figure 4.12 displays the resulting SEDs for each observation, with the best-fit ISHEM models overlaid. The corresponding parameter values are summarized in Table 4.3.

4.6.2 The Soft Gamma-ray Tail

To investigate a possible contribution of the jet at high energies, I included the soft γ-ray data from the *INTEGRAL*/SPI instrument in the fit of the first observation, following the same fitting procedure described in the previous section. In particular, the SPI spectrum was restricted to energies above 200 keV, as the emission below this threshold is reliably attributed to the accretion flow. This selection allowed the analysis to focus on the high-energy excess—often referred to as the "soft gamma-ray tail"—whose physical origin remains uncertain, being potentially associated either with non-thermal coronal processes or with the jet itself (e.g. Markoff et al. 2003; Bassi et al. 2020; Motta et al. 2021).

For this analysis, I activated the Compton-scattering module in ISHEM, which accounts for synchrotron self-Compton (SSC) emission, i.e. the up-scattering of synchrotron photons by the same population of relativistic electrons that produced them (Zdziarski et al. 2014). Although SSC emission is always present in jets, it is usually neglected in lower-energy analyses because it has a negligible impact on the radio-to-infrared bands and is computationally expensive to calculate (see Malzac, in prep.). However, I found that SSC emission dominates only in the γ-ray regime above the energy range covered by our SPI data, which extend up to 450 keV; for this reason, I disabled the SSC component in the present analysis. This effect is illustrated in Fig. 4.14.

In addition, I allowed the particle acceleration efficiency parameter, ξ_a, which is typically fixed to 0.1, to

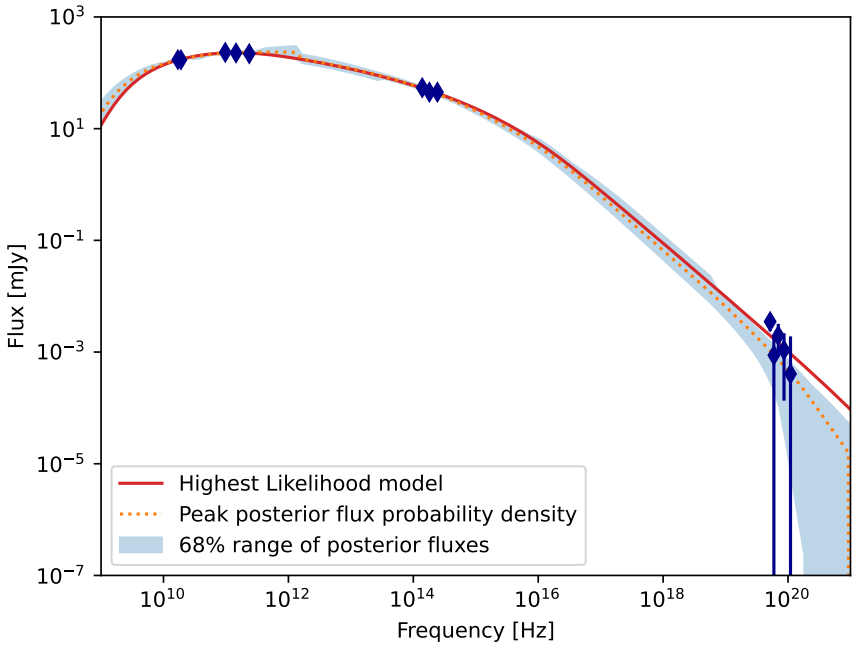

Figure 4.15: Resulting fit with ISHEM of the first observation including SPI data (Rodi et al. 2022) above 200 keV, used to investigate the soft γ-ray emission. The results indicate that jets contribute to the high-energy emission only when the slope of the injected particle distribution is $p < 2$, similar to the findings of Bassi et al. (2020).

vary freely. This parameter controls how efficiently particles are accelerated within internal shocks and plays a key role in determining the high-energy cutoff of the particle energy distribution.

The resulting fit (see Fig. 4.15 and Table 4.4) yielded parameters broadly consistent with those obtained without including the high-energy data (see Obs 1 in Table 4.3). The only notable difference concerns the slope of the injected particle distribution, for which I obtained a flatter index of $p = 1.9$, similar to previous studies of a BH XRB (e.g. Bassi et al. 2020).Such a value lies at the hard end of what standard DSA can produce, and remains noticeably lower than the particle slopes typically inferred for compact jets in XRBs ($p \sim 2.2$–2.8; e.g. Marcowith et al. 2016).

The fit also yielded a relatively high acceleration efficiency, $\xi_a \simeq 0.7$, which demands particularly efficient particle energization in the jet of J1535 during this phase of the outburst.

4.7 Discussion

4.7.1 Non-conical jet geometry

From my analysis of the radio-to-IR spectral domain, I found that the jet emission of J1535 is best reproduced by a non-conical jet geometry. Unlike the classical conical configuration, where the jet radius increases linearly with distance ($r \propto z$), the radius in this case follows a parabolic profile, $r \propto z^{\zeta}$, where z represents the distance along the jet axis and the parameter ζ indicates a progressively collimating structure ($\zeta < 1$). This configuration provides a better description of the broadband SED than the standard conical model, as discussed in the previous section. A similar parabolic geometry had been proposed for a NS LMXB by Marino et al. (2020), but my study represents the first application of such a geometry to a BH XRB.

Table 4.4: Best-fit ISHEM parameters for the first observation of J1535 with parabolic geometry, including SPI data above 200 keV. We used the same settings as in Table 4.3 ($t_{\rm simu} = 1 \times 10^6$ s, $\phi_J \leq 90°$, QPOs included), but in this case the acceleration efficiency parameter $\xi_{\rm acc}$ was treated as a free parameter. Reported uncertainties are 68% confidence intervals from the marginalized posteriors.

Parameter	Obs 1 (High Energy)
$\zeta_{\rm acc}$	$0.75^{+0.05}_{-0.03}$
$P_{\rm J}$	$0.8^{+0.2}_{-0.4}$
Γ	5 ± 1
$\phi_{\rm J}$ (°)	10^{+30}_{-6}
$\gamma_{\rm min}$	970^{+10}_{-350}
p	$1.90^{+0.10}_{-0.01}$
χ^2	6.5/6

One of the key differences between conical and parabolic jets lies in the behaviour of the opening angle ϕ_J as a function of the distance z (see Eq. 4.12). In a conical jet, ϕ_J remains constant at all distances, while in a parabolic geometry it decreases non-linearly with increasing distance from the jet base. To compare this configuration with the conical case, I estimated the effective opening angle ϕ_r at the distance where the radio emission is produced using Eq. 4.11,4.12,4.13 from Section 4.3 To this end, intermediate quantities are required. I first calculated z_b from Eq. 4.12, with jet base radius r_b fixed to $10\,r_g$ and ϕ_J given from the best-fit. Then I used an internal `ISHEM` routine to compute the characteristic distance z_r at which the bulk of the radio flux originates. With all the ingredients I the calculated the corresponding effective opening angle at the radio-emitting region using Eq. 4.13. The uncertainties on ϕ_r were estimated via a Monte Carlo approach. The input parameters ϕ_J and ζ were randomly sampled according to their measured uncertainties, assuming Gaussian or split-normal distributions in the presence of asymmetric errors. For each realization, z_b and ϕ_r were computed using Eqs. (1) and (3). The resulting distribution of ϕ_r was then used to derive the median value at 1σ confidence interval.

This procedure yielded frequency-dependent values of ϕ_r in the range of 0.04°–7° across the epochs, consistent with previous findings for XRB jets reported by Zdziarski et al. (2016), Marino et al. (2020), and Malzac (in prep.). Such narrow opening angles suggest a highly collimated outflow, as expected for a parabolic configuration.

The confinement of such a non-conical jet could be produced either through internal or external mechanisms. Internally, the jet may be collimated by a toroidal component of the magnetic field that increases along the jet axis, effectively reducing the opening angle (Heyvaerts & Norman 1989; Pudritz et al. 2006). However, Spruit (2010) questioned this possibility, arguing that the magnetic pressure associated with the toroidal field could instead promote expansion rather than confinement. Alternatively, external confinement could result from the interaction of the jet with the surrounding interstellar medium (Asada & Nakamura 2012), or from the influence of large-scale magnetic fields anchored in the accretion disk, which may provide additional pressure to collimate the flow (Spruit et al. 1997).

These results contrast with previous works on BH XRBs, where a conical geometry was generally sufficient to reproduce the observed emission. For example, applications of the ISHEM model to BH systems such as those studied by Péault et al. (2019) and Bassi et al. (2020) did not require deviations from the conical geometry, although some residuals in the radio band hinted that a flatter model could offer slight improvements. My analysis of J1535, however, provides the first clear evidence that a parabolic jet geometry

is required to reproduce its broadband SED. This result implies that the structural differences between jets in BH and NS XRBs may not be as pronounced as previously thought (Marino et al. 2020), suggesting that similar physical mechanisms could govern jet collimation across different types of compact objects.

4.7.2 Jet parameters variation

Here, I will alaways refer to the final parameter values reported in Table 4.3. The parameters obtained with ISHEM show some differences with respect to previous applications of earlier versions of the code to BH systems (Drappeau et al. 2015; Bassi et al. 2020). RegardingΓ, I encountered an issue in the penultimate observation: when left completely free, the fit converged to $\Gamma = 1$, implying a non-relativistic outflow. Such a result is physically inconsistent with the presence of a compact jet, as it would instead resemble a weakly collimated wind rather than a relativistic jet (Fender et al. 2004; Pe'er 2014). To avoid this unphysical outcome, I constrained the lower bound of Γ to 1.5 for that specific observation, obtaining a more reasonable set of parameters, albeit with a slightly worse χ^2 (see Table 4.3).

Overall, the derived values of Γ across the remaining observations, in the range $\Gamma = 5$–7, are higher than the upper limit of $\Gamma \sim 2$ predicted by the empirical $L_X \propto L_R^{0.7}$ correlation (Gallo et al. 2003). However, this does not necessarily contradict observations, since similar values were reported by Bassi et al. (2020), and it has been shown that this correlation does not exclude higher bulk Lorentz factors in BH XRBs (Heinz & Merloni 2004). Indeed, Miller-Jones et al. (2006) demonstrated that XRBs can produce relativistic jets with Γ up to ∼ 10, comparable to those observed in AGN, if the narrow observed opening angles are attributed to relativistic beaming rather than external confinement mechanisms such as magnetic or pressure-driven collimation. More recently, Zhang et al. (2025) report a candidate XRB jet with inferred $\Gamma > 5$, and further argue that the apparent difference between XRBs and blazar jets may largely arise from sample-selection biases.

Direct measurements of Γ remain rare and challenging, but several independent constraints exist. For example, Casella et al. (2010) inferred a lower limit of $\Gamma \geq 2$ for GX 339–4 from IR and X-ray time lags, while Tetarenko et al. (2019) derived $\Gamma \sim 2.6$ for Cyg X–1 through radio timing analysis. Similarly, Saikia et al. (2019) found bulk Lorentz factors in the range $\Gamma = 1.3$–3.5 for a sample of nine BH XRBs. Using the ISHEM model, Péault et al. (2019) showed that the Lorentz factor in MAXI J1836−194 decreases with spectral hardness, reaching values as high as $\Gamma \sim 16$ during intermediate states. Interestingly, in my analysis of J1535, the final HIMS observation yields a moderately relativistic outflow with Γ_J consistent with values up to ∼13 within the uncertainties, broadly comparable to the velocities inferred in J1836 during similar spectral conditions, suggesting that strong bulk acceleration may be a common feature of compact jets during transitional accretion phases in BH XRBs. This suggests that strong bulk acceleration may be a recurrent feature of compact jets during transitional accretion states in BH XRBs.

Furthermore, the parameters describing the particle distribution also differ significantly from those found in earlier ISHEM applications. In particular, I consistently found high minimum Lorentz factors for the accelerated particles, $\gamma_{\rm min} \sim 900$, compared to typical values of $\gamma_{\rm min} \sim 1$ reported in previous studies (Drappeau et al. 2015; Péault et al. 2019; Bassi et al. 2020). The slope of the injected electron distribution reaches $p \sim 3.2$ in the final observation, while in the other epochs similarly high values are reached through their upper limits, both steeper than the typical value close to $p \sim 2.0$ found in earlier works. It is important to note, however, that the updated version of ISHEM defines p as the slope of the *injected* particle distribution,

which subsequently steepens as electrons cool radiatively. Indeed, in previous implementations, RC was not included and p described the instantaneous distribution, leading to shallower inferred slopes. As a consequence of including RC in the present framework, the downstream particle distribution becomes significantly steeper due to cooling losses.

The relatively steep injection slope found here indicates that a substantial fraction of the energy is carried by high-energy electrons, which contribute prominently to the observed IR emission. This interpretation is supported by the consistently high values of $\gamma_{\rm min}$, consistent with the results of Malzac (in prep.), who demonstrated that a large minimum injection energy enhances the IR flux by compensating for relativistic boosting effects in this band. Therefore, my results reinforce the idea that efficient particle acceleration at high energies is necessary to reproduce the observed IR emission of J1535.

Another relevant aspect concerns the asymmetry observed in the posterior distributions of some parameters, which likely arises because the simulations have not yet reached a fully stationary regime. Overall, I did not find a clear correlation between the fitted parameters and the evolution of the source's spectral states. Constant fits to the parameter distributions are statistically consistent across all epochs, except for the jet opening angle ϕ_J, which exhibits a clear increasing trend with time; in this case, a linear fit provides a significantly better χ^2 than a constant one.

This behaviour has a direct physical impact on the SED. The fifth observation corresponds to the phase in which the jet is about to be quenched, and shows a shift of the spectral break from the IR to radio frequencies (Russell et al. 2020). My modelling naturally reproduces this evolution: while the other jet parameters remain broadly stable, an increase in ϕ_J alone is sufficient to move the jet break to lower frequencies. This effect is showed in Fig. 4.16, where I simulated SEDs with different opening angles while keeping all other jet parameters fixed.

These results indicate that the observed shift of the spectral break in the last observation does not require substantial changes in the intrinsic jet energetics or particle acceleration. Instead, it can be accounted for by a geometrical modification of the jet structure. This interpretation is reinforced by the broad similarity of the X-ray PDS across Obs. 1–5, which suggests that the variability driving the jet remained largely unchanged.

Finally, I note that only the final observation, corresponding to the SIMS, exhibited a marked spectral softening and was therefore excluded from the analysis, as this state is associated with the emergence of transient, discrete ejecta rather than a steady compact jet (see Fig. 4.10 and 4.11; see also the discussion in Russell et al. 2020).

Overall, these results suggest that the updated version of ISHEM, combined with a parabolic jet geometry, provides a robust framework for modelling the broadband SEDs of J1535. Nonetheless, further work is needed to better understand the origin of the asymmetries observed in the posterior distributions.

4.7.3 Jet contribution at high energies?

Rodi et al. (2022) investigated the spectral evolution of MAXI J1535−571 in the 100–400 keV band and identified a high-energy tail above $\sim$ 150 keV that does not follow the evolution of the thermal Comptonization flux. They interpreted this feature as potentially arising from a distinct physical component, possibly associated with the compact jet observed in the radio and IR bands. If this interpretation were correct, the detection of polarization in this energy range would provide strong evidence for a synchrotron origin. However, Cangemi

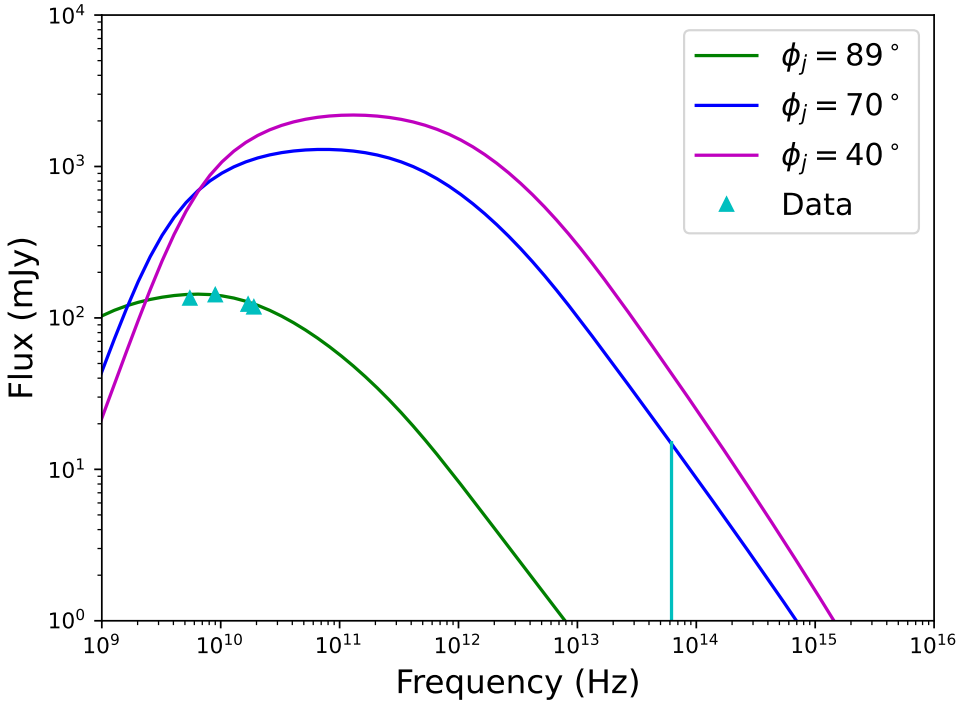

Figure 4.16: Effect of the jet opening angle on the modelled SED for Obs. 5. We computed a set of ISHEM simulations in which all jet parameters were held fixed to the best-fit values of Observation 5, while varying only the opening angle ϕ_J. Larger opening angles shift the jet break to lower frequencies, showing how geometric changes alone can account for the spectral evolution observed in the last epoch.

et al. (2023), who performed polarimetric observations of multiple sources in similar states, reported no significant polarization for J1535 in either the HIMS or SIMS states across different energy bands. They emphasized, however, that this non-detection is likely due to limited signal-to-noise above 300 keV rather than to an intrinsically unpolarized emission.

In my analysis, reproducing the soft γ-ray flux as jet emission requires a relatively hard injected particle slope of $p \approx 1.9$. Interestingly, a similar value was independently inferred for the discrete ejecta of J1535 by Chauhan et al. (2021), who reported a comparably hard spectrum during the radio flare. This close agreement may suggest a common acceleration mechanism operating in both the compact jet and the transient ejecta, potentially distinguishing J1535 from other BH XRBs in which steeper particle slopes are typically observed.

At the same time, the values of p inferred from fits that exclude the high-energy SPI data (see Tab. 4.3) are significantly steeper. If the compact jet were responsible for producing the γ-ray excess with $p \sim 1.9$, extrapolating the optically thin IR spectrum to higher energies would require a substantially flatter slope than implied by those lower-energy fits. Whether this tension reflects the presence of different acceleration zones within the jet, distinct electron populations (e.g. associated with synchrotron vs. SSC emission), or simply the limitations of the model in this regime remains uncertain. A more detailed investigation would be required, but this lies beyond the scope of the present work.

The best-fitting models also imply a high acceleration efficiency, with $\xi_a \approx 0.7$, sufficient to produce high-energy synchrotron or SSC emission. Nonetheless, the SSC contribution remains negligible over the relevant energy range, and the overall SED shape instead favours hybrid Comptonization in the corona as the more likely explanation for the observed flux.

Taken together, these results indicate that, although a jet-related origin of the high-energy tail cannot be entirely ruled out, the physical conditions required appear extreme. A coronal origin therefore remains the most plausible interpretation.

4.8 Conclusions

In this work I modelled the broadband SEDs of J1535 using the ISHEM framework, analysing five quasi-simultaneous multi-wavelength observations obtained during different spectral states of the outburst. This analysis provides new insights into the geometry and energetics of the compact jet in this system, and more broadly into the physics of jet–accretion coupling in BH XRBs. The main results can be summarised as follows:

- The jet geometry is best described by a parabolic profile, with $\zeta \sim 0.5$–0.7. This is remarkably similar to what has been reported in a NS system (Marino et al. 2020), suggesting that parabolic jets may be a common feature of accreting compact objects rather than specific to NS LMXBs. In addition, the fits consistently yield bulk Lorentz factors of $\Gamma \sim 5$–6 across multiple epochs, indicating that J1535 launches a moderately relativistic compact jet. This is a significant result, especially given the limited number of observational methods available to constrain this parameter in BH XRB jets.
- I do not find clear evidence for systematic evolution in most jet parameters across the five epochs. Notably, although the fifth observation corresponds to the onset of jet quenching—visible as a pronounced shift of the jet spectral break from the IR to the radio band—the main physical parameters of the jet remain broadly unchanged. The only quantity that shows a significant increase is the opening angle ϕ_J. This suggests that the dramatic spectral changes observed during the hard-to-soft transition may be driven primarily by geometrical modifications of the jet rather than by substantial variations in jet acceleration, energetics, or accretion-flow variability. This interpretation is consistent with the ISHEM modelling, the X-ray timing behaviour, and the limited spectral evolution seen in the BAT data. I also note that no pure hard-state observation is included in the dataset, since the multi-wavelength coverage begins after the source had already entered the HIMS.
- At high energies, I tested the jet contribution by including SPI data above 200 keV. While ISHEM can in principle reproduce the observed soft γ-ray flux, doing so requires extremely hard particle distributions and high acceleration efficiencies—conditions that appear physically demanding and challenge the plausibility of a jet-dominated origin for the excess emission. A more likely explanation remains Comptonization in the corona by a non-thermal electron population. Future polarimetric missions such as *COSI* (Sleator et al. 2019; Tomsick et al. 2023) will be essential to test the synchrotron scenario and establish the true origin of the high-energy tail.

Overall, this study demonstrates that incorporating a parabolic jet geometry into the ISHEM framework provides a robust and physically motivated description of the broadband emission in J1535. The results suggest that compact jets in BH systems may be more collimated and dynamically complex than previously thought, bridging the gap between NS and BH jet phenomenology. This work thus opens the path for future systematic studies aimed at testing the universality of jet geometries across different classes of compact objects.

Future directions for this research include applying ISHEM to a broader sample of BH systems such as MAXI J1348-630 and MAXI J1820+70 (in which polaritazion has been observed above 300 keV Cangemi et al. 2023), exploring alternative forms of variability input, and leveraging future polarimetric and γ-ray facilities to test the origin of high-energy jet emission. In this context, I have already started analysing MAXI J1820+070, which is of particular interest for jet studies given its exceptionally rich multi-wavelength coverage. In particular, I am focusing on the observation obtained during the hard state outburst on 12 April 2018 (Echiburú-Trujillo et al. 2024), which provides a nearly simultaneous broadband dataset including VLA and SMA radio measurements, sub-mm observations with ALMA, optical/infrared data from X-shooter and AAVSO, and X-ray coverage. Such a well-sampled SED, spanning from the radio to the X-ray band, represents an ideal test case for ISHEM, allowing us to place strong constraints on jet geometry, energetics, and spectral evolution.

5 Conclusions and Perspectives

This thesis has explored the physical properties and geometry of different forms of outflows in BH XRBs, focusing on their connection with the underlying accretion flow. I used a multi-wavelength and multi-technique approach, combining optical spectroscopy, X-ray spectral analysis, and time-dependent jet modelling. By focusing on three complementary manifestations of outflows—winds, obscuring structures, and relativistic jets—this work aimed at addressing some of the open questions regarding their presence, geometry, and evolution across different accretion states.

5.1 Summary of Results

In Chapter 2, optical spectroscopy of the BH XRB MAXI J1305–704 was used to investigate the presence of outflow signatures during its soft accretion state. The aim was to assess whether optical winds are systematically present in disk-dominated regimes, where winds are already well established at X-ray wavelengths. Although clear optical wind signatures could not be firmly identified, the analysis revealed absorption and emission features consistent with a complex and variable circumstellar environment. These results suggest that observational limitations, including sensitivity and temporal coverage, may play a significant role in limiting direct detections, while still remaining compatible with the presence of an optical outflow. This study contributes to the broader question of whether disk winds are ubiquitous in the soft state or instead dependent on viewing angle, ionization conditions, and launching radius.

Chapter 3 focused on the obscured spectral state of GRS 1915+105, a system characterized by extreme variability and sustained high accretion rates. Through phenomenological X-ray spectral modelling, this work provided new constraints on the geometry and origin of the obscuring material. The results favour a scenario in which the observed obscuration is most naturally explained by a warped accretion disk, rather than by a uniform absorber or a purely wind-driven structure. Such a configuration is consistent with theoretical expectations for systems accreting near the Eddington limit, where radiation-driven instabilities and relativistic effects can induce large-scale vertical distortions (Pringle 1996; Maloney et al. 1996). In this picture, geometrical effects associated with disk warping play a central role in shaping the observed X-ray phenomenology. This interpretation represents an important step forward in addressing open questions on the geometry and physics of accreting BH systems, and in understanding how complex disk structures can shape their observed X-ray phenomenology. Despite the consistency of this interpretation, some limitations

must be acknowledged. In particular, the spectral analysis relies on the combination of *XMM-Newton* and *NuSTAR* data, for which residual uncertainties in the intercalibration between the two instruments may affect the detailed shape of the broadband spectrum and the relative strength of spectral components. While these effects are not expected to alter the main qualitative conclusions, they can influence the precise determination of absorption properties and continuum parameters. Moreover, the adopted spectral modelling remains partly phenomenological, and alternative geometrical configurations cannot be entirely excluded. Future observations with improved spectral resolution and calibration will therefore be essential to further constrain the structure of the obscuring material and to test the warped-disk scenario more rigorously.

In Chapter 4, the broadband SED of MAXI J1535–571 was modelled using an updated version of the ISHEM code, allowing us to place new constraints on the physical and geometrical properties of its compact jet. By incorporating a parabolic jet geometry and relativistic effects, this study demonstrated that the observed multi-wavelength emission can be successfully reproduced with a jet that is more collimated than the traditionally assumed conical geometry, remarkably similar to that previously inferred in a NS system. This result suggests that parabolic jet geometries may represent a common outcome of accretion onto compact objects, rather than being specific to a particular class. The similarity between the inferred jet geometry in J1535 and that previously reported in NS systems further suggests that some aspects of jet formation may be largely independent of the nature of the compact object. This raises the possibility that the collimation and acceleration mechanisms are primarily governed by the properties of the accretion flow rather than by the presence of an event horizon. At the same time, differences in radiative efficiency, boundary layer physics, and magnetic field configurations in NS systems may still lead to observable differences in jet energetics and variability. Comparative studies between BH and NS XRBs will therefore be essential to assess the degree of universality of the accretion–ejection coupling.

In addition, the modelling provided one of the few observational constraints currently available on the velocity of steady compact jets in BH XRBs. By modelling jet during multiple epochs of the outburst decay, this work has addressed the long-standing question of how compact jets evolve as sources approach jet quenching. The results show that, despite the pronounced changes observed in the jet spectral properties, the underlying physical characteristics of the jet remain largely stable across the explored epochs. This finding suggests that the onset of jet quenching does not necessarily require substantial modifications in the jet energetics or particle acceleration processes. Instead, the analysis points to a change in jet geometry as the primary driver of the observed spectral evolution. In particular, the widening of the jet opening angle as the source approaches the hard-to-soft transition provides a natural explanation for the displacement of the jet spectral break and for the apparent suppression of jet emission. This result represents an important step forward in disentangling the physical mechanisms responsible for jet quenching, highlighting geometry as a key ingredient alongside accretion state changes. It is worth noting that J1535 does not exhibit a fully developed canonical hard state during the epochs considered here. This peculiarity may limit direct comparisons with more classical BH transients, and suggests that the inferred jet properties should be interpreted within the specific accretion regime explored in this source. Extending similar modelling to systems that undergo complete state transitions will be essential to assess the generality of these results. At high energies, this work has explored the long-debated question of whether compact jets can contribute significantly to the soft γ-ray emission in BH XRBs.

While a jet origin cannot be formally excluded based on spectral modelling alone, the required physical conditions appear extreme, favouring instead a scenario in which the high-energy tail is produced by Comptonization by a non-thermal electron population in the corona. This outcome reinforces the need

for observational diagnostics beyond spectroscopy to conclusively determine the origin of the high-energy emission. In this context, future polarimetric missions such as *COSI* (Sleator et al. 2019; Tomsick et al. 2023) will play a decisive role. Measurements of polarization degree and angle in the hard X-ray and soft γ-ray bands will provide a direct and unambiguous test of the synchrotron scenario, allowing jet-dominated and coronal models to be robustly distinguished.

Taken together, these results emphasize that outflows in BH XRBs cannot be described by a single, universal picture. Instead, winds, obscuring structures, and jets appear to be deeply interconnected phenomena whose properties depend on accretion state, luminosity, and geometry. From a broader perspective, the results presented in this thesis support an increasingly unified view in which the different forms of outflows observed in BH XRBs are not independent phenomena, but rather different manifestations of the same accretion–ejection coupling operating under different physical conditions. Winds, jets, and obscuring structures appear to dominate in different regions of the accretion parameter space, likely regulated by the mass accretion rate, disk geometry, and radiative feedback. In this framework, soft states favour the development of radiatively driven winds, while hard and intermediate states are associated with the presence of compact jets. At the highest luminosities, geometrical distortions such as disk warping may further modify the structure of the inner accretion flow, giving rise to obscured configurations. This suggests that geometry plays a central role in shaping the observed phenomenology, acting as a key link between accretion physics and the launching of outflows.

5.2 Future work and perspective

The results presented in this thesis naturally point toward a number of observational and theoretical developments that will be crucial to address the remaining open questions on the geometry and evolution of outflows in BH XRBs. In the coming years, a key priority will be to combine coordinated multi-wavelength campaigns with the capabilities of new and upcoming observatories, with the goal of directly testing the physical scenarios proposed in this work and placing them within a broader framework of accretion–ejection coupling.

- **Deep optical spectroscopy and coordinated multi-wavelength campaigns.** To overcome the limitations encountered in Chapter 2, deeper and more continuous optical spectroscopic observations combined with simultaneous high-resolution X-ray spectroscopy will be essential to capture transient wind signatures and better constrain outflow properties in soft states. A priority strategy will be the systematic coordination of X-ray, optical, infrared, and radio observations, allowing the structure and evolution of disk winds to be probed simultaneously across different accretion regimes. Facilities such as *XRISM*, already providing unprecedented spectral resolution in the X-ray band, and future missions like *Athena*, will be particularly powerful in bridging the gap between highly ionized "hot" winds detected in X-rays and the colder optical/infrared components. In this context, I am part of a collaboration with an accepted *XRISM* proposal aimed at connecting multi-phase outflows through coordinated observations. Extending these campaigns to eclipsing systems and sources undergoing state transitions will provide strong geometrical constraints and allow different disk regions to be probed through multiple emission lines.

- **Obscured states and transitional phases in GRS 1915+105 and similar systems.** As an immediate extension of Chapter 3, the additional *XMM+NuSTAR* observations obtained in 2019 and 2020 will be analysed to further investigate the nature and geometry of the obscured spectral state. A key priority will be to place these episodes within the broader long-term X-ray evolution of the source, identifying whether such configurations are linked to specific transitional phases, failed outbursts, or changes in accretion rate. In this context, recent observations with *XRISM*, as discussed in the dedicated chapter of this thesis, have already begun to provide new insights into the structure and physical conditions of the absorbing material through high-resolution spectroscopy. Future high-resolution X-ray spectroscopy with *Athena* will then offer a unique opportunity to systematically test warped-disk scenarios and to distinguish between geometrical and wind-driven origins of obscuration with unprecedented sensitivity. In this context, I am an active member of the *Athena* Working Groups on Compact Objects and on Transients and Multi-messenger Astrophysics, contributing to studies of the evolving inner regions of the accretion flow in stellar-mass BHs. In addition, X-ray polarimetry offers a complementary and largely unexplored diagnostic of the inner accretion geometry. Observations with *IXPE* can provide direct constraints on the orientation and structure of the scattering regions, helping to disentangle reflection, absorption, and geometrical effects in obscured configurations. In this context, polarimetric measurements during transitional or obscured phases could play a key role in probing the structure of the inner disk and its evolution.

- **Population studies of compact jets and new observational diagnostics.** A key next step will be to extend the updated ISHEM modelling to a larger sample of BH XRBs with well-sampled multi-wavelength coverage, including systems such as MAXI J1820+070 and MAXI J1348–630. In particular, I have already begun analysing MAXI J1820+070, a source of great interest for jet studies thanks to its exceptionally rich broadband dataset. I am focusing on the hard-state observation obtained during the 12 April 2018 outburst (Echiburú-Trujillo et al. 2024), which provides nearly simultaneous coverage from radio to X-rays, including VLA and SMA measurements, sub-mm data from ALMA, and optical/infrared observations with X-shooter and AAVSO. In contrast to MAXI J1535–571, for which a fully developed canonical hard state was not available during the epochs analysed in this thesis, MAXI J1820+070 offers the opportunity to study the jet under well-defined hard-state conditions. Such a well-sampled multi-wavelength SED represents an ideal benchmark for applying ISHEM. This will allow us to test whether parabolic jet geometries are a common feature among BH systems and to investigate how jet properties evolve across different outbursts and accretion states, particularly during transitions and jet quenching phases. In parallel, polarimetric observations will offer a powerful and largely unexplored diagnostic of jet and corona geometry. Measurements from missions such as *IXPE*, and future high-energy polarimeters, can help disentangle synchrotron and Comptonization contributions and provide direct constraints on magnetic field structure and emission regions. These efforts will be further strengthened by the next generation of facilities, including radio interferometers such as the SKA, which will enable detailed studies of jet evolution, and high-energy observatories such as CTA, which may probe particle acceleration at the highest energies.

Overall, the next stage of research will focus on building a coherent, multi-scale picture of accretion-driven outflows by combining coordinated multi-wavelength monitoring, high-resolution spectroscopy, and time-dependent physical modelling. Particular emphasis will be placed on transitional phases, obscured states, and failed outbursts, where rapid changes in geometry may reveal the physical links between winds, jets, and the inner accretion flow. The advent of a new generation of observational facilities—ranging from radio

interferometers such as the future SKA and enhanced ALMA capabilities, to wide-field X-ray and gamma-ray observatories including THESEUS and LHAASO, as well as next-generation Cherenkov telescopes such as the ASTRI Mini-Array—will provide unprecedented coverage of accreting compact objects across the electromagnetic spectrum. Such broad and coordinated coverage is precisely what is required to build well-sampled, truly simultaneous broadband SEDs, which are essential for applying physically motivated jet models such as ISHEM: a complete SED allows the jet spectral break, high-energy components, and their evolution across accretion states to be robustly constrained, thereby reducing modelling degeneracies and enabling a more reliable determination of jet geometry and energetics.

In addition, in this rapidly evolving multi-messenger and multi-wavelength landscape, compact jets are now emerging as potential accelerators up to PeV energies, and coordinated observations will be crucial to fully characterize their physics. These facilities will offer the opportunity to directly test jet models, constrain particle acceleration mechanisms, and place the results of this thesis within a broader and more complete physical framework.

Conclusions et perspectives

Cette thèse a exploré les propriétés physiques et la géométrie des différentes formes d'écoulements sortants dans les binaires X à trou noir (BH XRBs), en se concentrant sur leur lien avec le flot d'accrétion sous-jacent. J'ai adopté une approche multi-longueurs d'onde et multi-techniques, combinant spectroscopie optique, analyse spectrale en rayons X et modélisation temporelle des jets. En me concentrant sur trois manifestations complémentaires des écoulements sortants — vents, structures obscurcissantes et jets relativistes — ce travail visait à répondre à certaines questions ouvertes concernant leur présence, leur géométrie et leur évolution à travers les différents états d'accrétion.

5.3 Résumé des résultats

Dans le Chapitre 2, la spectroscopie optique du BH XRB MAXI J1305–704 a été utilisée pour étudier la présence de signatures d'écoulement sortant pendant son état d'accrétion mou. L'objectif était d'évaluer si des vents optiques sont systématiquement présents dans les régimes dominés par le disque, où les vents sont déjà bien établis aux longueurs d'onde X. Bien qu'aucune signature claire et non ambiguë de vent optique n'ait pu être identifiée, l'analyse a révélé des raies en absorption et en émission compatibles avec un environnement circumstellaire complexe et variable. Ces résultats suggèrent que les limitations observationnelles, notamment la sensibilité instrumentale et la couverture temporelle, peuvent jouer un rôle important dans la difficulté à détecter directement ces vents, tout en restant compatibles avec la présence d'un écoulement sortant optique. Cette étude contribue ainsi à la question plus générale de savoir si les vents de disque sont omniprésents dans l'état mou ou s'ils dépendent fortement de l'angle de visée, des conditions d'ionisation et du rayon de lancement.

Le Chapitre 3 s'est concentré sur l'état spectral obscurci de GRS 1915+105, un système caractérisé par une variabilité extrême et des taux d'accrétion durablement élevés. Grâce à une modélisation spectrale phénoménologique en rayons X, ce travail a permis d'apporter de nouvelles contraintes sur la géométrie et l'origine du matériau responsable de l'obscuration. Les résultats favorisent un scénario dans lequel l'obscuration observée s'explique plus naturellement par un disque d'accrétion déformé (warped disk), plutôt que par un absorbeur uniforme ou une structure uniquement liée à un vent. Une telle configuration est cohérente avec les attentes théoriques pour des systèmes accrétant près de la limite d'Eddington, où des instabilités induites par la radiation et des effets relativistes peuvent produire des déformations verticales

à grande échelle (Pringle 1996; Maloney et al. 1996). Dans ce cadre, les effets géométriques associés à la déformation du disque jouent un rôle central dans la phénoménologie observée en rayons X.

Cette interprétation représente une avancée importante pour répondre aux questions ouvertes sur la géométrie et la physique des systèmes à trou noir accrétants, et pour comprendre comment des structures de disque complexes peuvent façonner les propriétés observées en rayons X. Malgré la cohérence de ce scénario, certaines limites doivent toutefois être reconnues. En particulier, l'analyse spectrale repose sur la combinaison de données *XMM-Newton* et *NuSTAR*, pour lesquelles des incertitudes résiduelles d'intercalibration peuvent affecter la forme détaillée du spectre large bande et l'importance relative des différentes composantes spectrales. Bien que ces effets ne soient pas susceptibles de modifier les conclusions qualitatives principales, ils peuvent influencer la détermination précise des propriétés d'absorption et des paramètres du continuum. Par ailleurs, la modélisation spectrale adoptée reste en partie phénoménologique et des configurations géométriques alternatives ne peuvent être totalement exclues. De futures observations bénéficiant d'une meilleure résolution spectrale et d'une calibration améliorée seront donc essentielles pour contraindre davantage la structure du matériau obscurcissant et tester plus rigoureusement le scénario du disque déformé.

Dans le Chapitre 4, la distribution spectrale d'énergie large bande (SED) de MAXI J1535–571 a été modélisée à l'aide d'une version mise à jour du code ISHEM, permettant de placer de nouvelles contraintes sur les propriétés physiques et géométriques de son jet compact. En intégrant une géométrie de jet parabolique ainsi que des effets relativistes, cette étude a montré que l'émission multi-longueurs d'onde observée peut être reproduite avec succès par un jet plus collimaté que la géométrie conique traditionnellement supposée, remarquablement similaire à celle précédemment inférée dans un système à étoile à neutrons (NS). Ce résultat suggère que des géométries de jet paraboliques pourraient représenter une conséquence commune de l'accrétion sur des objets compacts, plutôt que d'être spécifiques à une classe particulière. La similarité entre la géométrie du jet déduite pour J1535 et celle observée dans les systèmes à NS suggère en outre que certains aspects de la formation des jets pourraient être largement indépendants de la nature de l'objet compact. Cela ouvre la possibilité que les mécanismes de collimation et d'accélération soient principalement gouvernés par les propriétés du flot d'accrétion plutôt que par la présence d'un horizon des événements. Néanmoins, des différences en termes d'efficacité radiative, de physique de la couche limite (boundary layer) et de configuration du champ magnétique dans les systèmes à NS pourraient conduire à des différences observables dans l'énergétique et la variabilité des jets. Des études comparatives entre BH et NS XRBs seront donc essentielles pour évaluer le degré d'universalité du couplage accrétion–éjection.

La modélisation a également fourni l'une des rares contraintes observationnelles actuellement disponibles sur la vitesse des jets compacts stationnaires dans les BH XRBs. En modélisant le jet à plusieurs époques pendant la phase de décroissance de l'outburst, ce travail s'est attaqué à la question de longue date de l'évolution des jets compacts à l'approche de leur extinction (jet quenching). Les résultats montrent que, malgré les changements marqués observés dans les propriétés spectrales du jet, les caractéristiques physiques sous-jacentes du jet restent largement stables au cours des époques considérées. Cela suggère que l'extinction du jet ne nécessite pas nécessairement des modifications substantielles de son énergétique ou des processus d'accélération des particules.

Au contraire, l'analyse indique qu'un changement de géométrie du jet constitue le principal moteur de l'évolution spectrale observée. En particulier, l'élargissement de l'angle d'ouverture du jet à mesure que la source s'approche de la transition dur-vers-mou fournit une explication naturelle du déplacement de la coupure spectrale du jet et de la suppression apparente de son émission. Ce résultat représente une avancée importante

dans la compréhension des mécanismes physiques responsables de l'extinction des jets, en soulignant le rôle central de la géométrie aux côtés des changements d'état d'accrétion. Il convient toutefois de noter que J1535 ne présente pas un état dur canonique pleinement développé durant les époques considérées. Cette particularité peut limiter les comparaisons directes avec des transitoires à trou noir plus classiques et suggère que les propriétés du jet déduites doivent être interprétées dans le cadre du régime d'accrétion spécifique exploré dans cette source. L'extension de cette modélisation à des systèmes traversant des transitions d'état complètes sera essentielle pour évaluer la généralité de ces résultats.

Aux hautes énergies, ce travail a exploré la question, débattue depuis longtemps, de savoir si les jets compacts peuvent contribuer de manière significative à l'émission en γ doux dans les BH XRBs. Bien qu'une origine liée au jet ne puisse être formellement exclue sur la seule base de la modélisation spectrale, les conditions physiques requises apparaissent extrêmes, favorisant plutôt un scénario dans lequel la composante de haute énergie est produite par Comptonisation d'une population d'électrons non thermiques dans la couronne. Ce résultat renforce la nécessité de diagnostics observationnels allant au-delà de la seule spectroscopie pour déterminer de manière concluante l'origine de l'émission de haute énergie. Dans ce contexte, de futures missions de polarimétrie telles que *COSI* (Sleator et al. 2019; Tomsick et al. 2023) joueront un rôle décisif. Les mesures du degré et de l'angle de polarisation dans les bandes des rayons X durs et des γ mous fourniront un test direct et sans ambiguïté du scénario synchrotron, permettant de distinguer de manière robuste les modèles dominés par le jet de ceux dominés par la couronne.

Pris ensemble, ces résultats soulignent que les écoulements sortants dans les BH XRBs ne peuvent être décrits par un schéma unique et universel. Au contraire, vents, structures obscurcissantes et jets apparaissent comme des phénomènes profondément interconnectés, dont les propriétés dépendent de l'état d'accrétion, de la luminosité et de la géométrie. Dans une perspective plus globale, les résultats présentés dans cette thèse soutiennent une vision de plus en plus unifiée, dans laquelle les différentes formes d'écoulements sortants observées dans les BH XRBs ne sont pas des phénomènes indépendants, mais plutôt différentes manifestations du même couplage accrétion–éjection opérant sous des conditions physiques variées. Les vents, les jets et les structures obscurcissantes semblent dominer dans différentes régions de l'espace des paramètres d'accrétion, probablement régulés par le taux d'accrétion, la géométrie du disque et le rétro-effet radiatif. Dans ce cadre, les états mous favorisent le développement de vents entraînés par la radiation, tandis que les états durs et intermédiaires sont associés à la présence de jets compacts. Aux luminosités les plus élevées, des déformations géométriques telles que le gauchissement du disque peuvent modifier la structure du flot interne et donner lieu à des configurations obscurcies. Cela suggère que la géométrie joue un rôle central dans la phénoménologie observée, constituant un lien essentiel entre la physique de l'accrétion et le lancement des écoulements sortants.

5.4 Travaux futurs et perspectives

Les résultats présentés dans cette thèse ouvrent naturellement la voie à un ensemble de développements observationnels et théoriques qui seront essentiels pour répondre aux questions encore ouvertes concernant la géométrie et l'évolution des écoulements sortants dans les BH XRBs. Dans les années à venir, une priorité sera de combiner des campagnes coordonnées multi-longueurs d'onde avec les capacités des observatoires actuels et futurs, afin de tester directement les scénarios physiques proposés dans ce travail et de les replacer dans un cadre plus large de couplage accrétion–éjection.

- **Spectroscopie optique profonde et campagnes coordonnées multi-longueurs d'onde.** Afin de surmonter les limitations rencontrées dans le Chapitre 2, des observations spectroscopiques optiques plus profondes et plus continues, combinées à une spectroscopie X à haute résolution simultanée, seront essentielles pour capturer des signatures transitoires de vents et mieux contraindre les propriétés des écoulements sortants dans les états mous. Une stratégie prioritaire consistera à coordonner systématiquement des observations en rayons X, optique, infrarouge et radio, afin de sonder simultanément la structure et l'évolution des vents et des jets à travers différents régimes d'accrétion. Des instruments tels que *XRISM*, qui fournit déjà une résolution spectrale sans précédent en rayons X, ainsi que les futures missions comme *Athena*, seront particulièrement puissants pour combler le fossé entre les vents fortement ionisés détectés en rayons X et les composantes plus froides observées en optique et en infrarouge. Dans ce contexte, je fais partie d'une collaboration impliquée dans une proposition acceptée avec *XRISM*, visant à relier les écoulements multi-phases grâce à des observations coordonnées. L'extension de ces campagnes à des systèmes éclipsants et à des sources en transition d'état fournira de fortes contraintes géométriques et permettra de sonder différentes régions du disque à travers de multiples raies d'émission.

- **États obscurcis et phases transitionnelles dans GRS 1915+105 et systèmes analogues.** En prolongement direct du Chapitre 3, les observations supplémentaires *XMM+NuSTAR* obtenues en 2019 et 2020 seront analysées afin d'étudier plus en détail la nature et la géométrie de l'état spectral obscurci. Une priorité sera de replacer ces épisodes dans le contexte de l'évolution X à long terme de la source, afin d'identifier si de telles configurations sont liées à des phases transitionnelles spécifiques, à des outbursts avortés ou à des variations du taux d'accrétion. La future spectroscopie X à haute résolution avec *Athena* offrira une opportunité unique de tester systématiquement les scénarios de disque déformé et de distinguer entre des origines géométriques ou liées aux vents de l'obscuration. Dans ce cadre, je suis membre actif des groupes de travail *Athena* sur les objets compacts et sur les transitoires et l'astrophysique multi-messagers, contribuant à l'étude de l'évolution des régions internes du flot d'accrétion autour des trous noirs stellaires. En outre, la polarimétrie en rayons X constitue un diagnostic complémentaire encore largement inexploré de la géométrie interne de l'accrétion. Les observations avec *IXPE* peuvent fournir des contraintes directes sur l'orientation et la structure des régions diffusantes, aidant à démêler les effets de réflexion, d'absorption et de géométrie dans les configurations obscurcies. Des mesures polarimétriques durant les phases transitionnelles ou obscurcies pourraient ainsi jouer un rôle clé pour sonder la structure verticale du disque interne et son évolution.

- **Études de population des jets compacts et nouveaux diagnostics observationnels.** Une étape clé consistera à étendre l'application du code ISHEM mis à jour à un échantillon plus large de BH XRBs disposant d'une couverture multi-longueurs d'onde bien échantillonnée, incluant des systèmes tels que MAXI J1820+070 et MAXI J1348–630. Cela permettra de tester si les géométries de jets paraboliques sont une caractéristique commune des systèmes à trou noir et d'étudier l'évolution des propriétés des jets au cours de différents outbursts et états d'accrétion, en particulier durant les transitions et les phases d'extinction des jets. Parallèlement, les observations polarimétriques offriront un diagnostic puissant et encore largement inexploré de la géométrie du jet et de la couronne. Les mesures provenant de missions telles que *IXPE*, ainsi que de futurs polarimètres à haute énergie, permettront de distinguer les contributions synchrotron et Compton et de fournir des contraintes directes sur la structure du champ magnétique et les régions d'émission. Ces efforts seront encore renforcés par la prochaine génération d'instruments, notamment les interféromètres radio tels que le SKA, qui permettront des

études détaillées de l'évolution des jets, ainsi que les observatoires de haute énergie comme CTA, capables de sonder l'accélération des particules aux énergies les plus élevées.

Dans l'ensemble, la prochaine étape de ces recherches visera à construire une vision cohérente et multi-échelle des écoulements sortants entraînés par l'accrétion, en combinant un suivi coordonné multi-longueurs d'onde, une spectroscopie à haute résolution et une modélisation physique dépendant du temps. Une attention particulière sera portée aux phases transitionnelles, aux états obscurcis et aux outbursts avortés, où des changements rapides de géométrie peuvent révéler les liens physiques entre vents, jets et régions internes du flot d'accrétion.

L'avènement d'une nouvelle génération d'installations observationnelles — allant des interféromètres radio tels que le futur SKA et les capacités accrues d'ALMA, aux observatoires à grand champ en rayons X et en γ comme THESEUS et LHAASO, ainsi qu'aux télescopes Cherenkov de nouvelle génération tels que l'ASTRI Mini-Array — offrira une couverture sans précédent des objets compacts accrétants sur l'ensemble du spectre électromagnétique. Dans ce paysage en rapide évolution, à la fois multi-messagers et multi-longueurs d'onde, les jets compacts émergent désormais comme de potentiels accélérateurs de particules jusqu'à des énergies de l'ordre du PeV, et des observations coordonnées seront essentielles pour en caractériser pleinement la physique. Ces infrastructures offriront l'opportunité de tester directement les modèles de jets, de contraindre les mécanismes d'accélération des particules et d'inscrire les résultats de cette thèse dans un cadre physique plus large et plus complet.

A Publications

A.1 List of refereed publications

- **C. Miceli**, D. Mata Sánchez, A. Anitra, T. Muñoz-Darias, T. Di Salvo, R. Iaria, A. Marino, W. Leone, M. Del Santo, M. Armas-Padilla, N. Degenaar, J. M. Miller, M. Reynolds (2024), A&A, 684, A67, 7 pp., *Soft-state optical spectroscopy of the Black Hole MAXI J1305–704*. doi: 10.1051/0004-6361/202348482.

- A. Anitra, **C. Miceli**, T. Di Salvo, R. Iaria, N. Degenaar, J. M. Miller, F. Barra, W. Leone, L. Burderi (2024), A&A, 690, A148, 11 pp., *X-ray view of emission lines in optical spectra: Spectral analysis of the two low-mass XRB systems Swift J1357.2−0933 and MAXI J1305–704*. doi: 10.1051/0004-6361/202348907; arXiv: 2409.11988.

- A. Anitra, D. Mata Sánchez, T. Muñoz-Darias, T. Di Salvo, R. Iaria, **C. Miceli**, M. Armas-Padilla, J. Casares, J. M. Corral-Santana (2023), A&A, 679, A145, 6 pp., *Hβ spectroscopy of the high-inclination black hole transient Swift J1357.2−0933 during quiescence*. doi: 10.1051/0004-6361/202346909; arXiv: 2310.12636.

- R. Iaria, T. Di Salvo, A. Anitra, **C. Miceli**, F. Barra, W. Leone, L. Burderi, A. Sanna, A. Riggio (2024), A&A, 683, A79, 16 pp., *Confirmation of the presence of a CRSF in the NICER spectrum of X 1822−371*. doi: 10.1051/0004-6361/202345888; arXiv: 2401.03698.

- R. Iaria, T. Di Salvo, A. Anitra, **C. Miceli**, W. Leone, C. Maraventano, F. Barra, A. Riggio, A. Sanna, A. Manca, L. Burderi (2024), A&A, 686, A216, 7 pp., *The puzzling orbital residuals of XTE J1710−281: Is a Jovian planet orbiting the binary system?*. doi: 10.1051/0004-6361/202449299; arXiv: 2404.11203.

- G. Mastroserio, B. De Marco, M. C. Baglio, F. Carotenuto, S. Fabiani, T. D. Russell, F. Capitanio, Y. Cavecchi, S. Motta, D. M. Russell, M. Dovčiak, M. Del Santo, K. Alabarta, A. Ambrifi, S. Campana, P. Casella, S. Covino, G. Illiano, E. Kara, E. V. Lai, G. Lodato, A. Manca, I. Mariani, A. Marino, **C. Miceli**, P. Saikia, A. W. Shaw, J. Svoboda, F. M. Vincentelli, J. Wang (2025), ApJ Lett., 978(2), L19, 17 pp., *X-Ray and Optical Polarization Aligned with the Radio Jet Ejecta in GX 339−4*. doi: 10.3847/2041-8213/ad9913; arXiv: 2408.06856.

- W. Leone, L. Burderi, T. Di Salvo, A. Anitra, A. Sanna, A. Riggio, R. Iaria, F. Fiore, F. Longo, M. Ďuríšková, A. Tsvetkova, C. Maraventano, **C. Miceli** (2025), A&A, 701, A50, 16 pp., *Time*

domain astrophysics with transient sources: Delay estimate via Cross Correlation Function techniques. doi: 10.1051/0004-6361/202453054; arXiv: 2506.04014.

- R. Iaria, T. Di Salvo, A. Anitra, F. Barra, A. Sanna, C. Maraventano, **C. Miceli**, W. Leone, L. Burderi (2025), *A mysterious feature in the NICER spectrum of 4U 1820−30: A gravitationally redshifted absorption line?*. arXiv: 2511.20499.

A.2 Atel

- M. Del Santo, A. Segreto, **C. Miceli** (2025), The Astronomer's Telegram, No. 17139, *Swift observations of the new outburst of the BH transient 4U 1630−472*.
  Available online: https://www.astronomerstelegram.org/?read=17139
- C. Salvaggio, Sara E. Motta, M. C. Baglio, R. Fender, M. Del Santo, **C. Miceli**, A. Ingram, M. Ewing, A. Beri (2026) The Astronomer's Telegram, No. 17638, *The black hole X-ray binary GS 1354-64 in transition from the hard to the soft state*

A.3 Proposal

- **PI: C. Miceli**, CoIs: M. Del Santo, S.E. Motta, T.D. Russell, M. C. Baglio, A. Marino, A. Segreto, A. D'A'ı, C. Pinto, E., Ambrosi, F. Pintore (2024), Neil Gehrels Swift Observatory monitoring of a black hole transient in outburst.
- A. Anitra, **C. Miceli**, M. C. Baglio, M. M. Messa, A. Marino, T. Di Salvo (2025), Unveiling warped disc geometry in SAX J1808.4-3658 with VLT/X-SHOTER spectroscopy.

A.4 List of publications in preparation

- **C. Miceli**, J. Malzac, M. Del Santo, D. M. Russell, T. D. Russell, M. C. Baglio, A. Marino, J. Rodi, A. Segreto, *Evidence for a parabolic jet geometry in MAXI J1535−571 from ISHEM modelling*.
- **C. Miceli** et al., *Peculiar obscured Spectral State in GRS 1915+105: XMM+NUSTR anlysis*

Bibliography

Abbott, B. P., Abbott, R., Abbott, T. D., et al. 2016, Phys. Rev. Lett., 116, 061102

Abbott, R., Abbott, T. D., Abraham, S., et al. 2020, Phys. Rev. Lett., 125, 101102

Abbott, R., Abbott, T. D., Acernese, F., et al. 2023, Physical Review X, 13, 041039

Abramowicz, M. A., Czerny, B., Lasota, J. P., & Szuszkiewicz, E. 1988, ApJ, 332, 646

Abramowicz, M. A. & Igumenshchev, I. V. 2001, ApJ Lett., 554, L53

Agol, E. & Krolik, J. H. 2000, ApJ, 528, 161

Altamirano, D., Belloni, T., Linares, M., et al. 2011, ApJ Lett., 742, L17

Alvarez, H., Aparici, J., May, J., & Reich, P. 2000, A&A, 355, 863

Anitra, A., Miceli, C., Di Salvo, T., et al. 2024, A&A, 690, A148

Antonucci, R. 1993, Annual Review of Astronomy and Astrophysics, 31, 473

Appenzeller, I., Fricke, K., Fürtig, W., et al. 1998, The Messenger, 94, 1

Applegate, J. H. 1992, ApJ, 385, 621

Armas Padilla, M., Ueda, Y., Hori, T., Shidatsu, M., & Muñoz-Darias, T. 2017, MNRAS, 467, 290

Armas Padilla, M., Wijnands, R., Altamirano, D., et al. 2014, MNRAS, 439, 3908

Arnaud, K. A. 1996, in Astronomical Society of the Pacific Conference Series, Vol. 101, Astronomical Data Analysis Software and Systems V, ed. G. H. Jacoby & J. Barnes, 17

Asada, K. & Nakamura, M. 2012, ApJ Lett., 745, L28

Astropy Collaboration, Price-Whelan, A. M., Lim, P. L., et al. 2022, ApJ, 935, 167

Athulya, M. P. & Nandi, A. 2023, MNRAS, 525, 489

Axford, W. I., Leer, E., & Skadron, G. 1977, in International Cosmic Ray Conference, Vol. 11, International Cosmic Ray Conference, 132

Baade, W. & Minkowski, R. 1954, ApJ, 119, 215

Baade, W. & Zwicky, F. 1934, Proceedings of the National Academy of Science, 20, 259

Baglio, M. C., Russell, D. M., Casella, P., et al. 2018, ApJ, 867, 114

Balakrishnan, M., Miller, J. M., Reynolds, M. T., et al. 2021, ApJ, 909, 41

Balbus, S. A. 2005, in Astronomical Society of the Pacific Conference Series, Vol. 330, The Astrophysics of Cataclysmic Variables and Related Objects, ed. J. M. Hameury & J. P. Lasota, 185

Bambi, C. 2025, Symmetry, 17, 1393

Basak, R., Zdziarski, A. A., Parker, M., & Islam, N. 2017, MNRAS, 472, 4220

Bassi, T., Del Santo, M., D'Aı, A., et al. 2019, MNRAS, 482, 1587

Bassi, T., Malzac, J., Del Santo, M., et al. 2020, MNRAS, 494, 571

Begelman, M. C. & McKee, C. F. 1983, ApJ, 271, 89

Bell, A. R. 1978, MNRAS, 182, 147

Belloni, T., Homan, J., Casella, P., et al. 2005, A&A, 440, 207

Belloni, T., Klein-Wolt, M., Méndez, M., van der Klis, M., & van Paradijs, J. 2000, A&A, 355, 271

Belloni, T., Parolin, I., Del Santo, M., et al. 2006, MNRAS, 367, 1113

Belmont, R., Malzac, J., & Marcowith, A. 2008, Mem. Soc. Astron. Ital., 79, 228

Blandford, R. & Eichler, D. 1987, Phys. Rep., 154, 1

Blandford, R. D. & Begelman, M. C. 1999, MNRAS, 303, L1

Blandford, R. D. & Königl, A. 1979, ApJ, 232, 34

Blandford, R. D. & Ostriker, J. P. 1978, ApJ Lett., 221, L29

Blandford, R. D. & Payne, D. G. 1982, MNRAS, 199, 883

Blandford, R. D. & Znajek, R. L. 1977, MNRAS, 179, 433

Bouchet, L., del Santo, M., Jourdain, E., et al. 2009, ApJ, 693, 1871

Bradt, H. V., Rothschild, R. E., & Swank, J. H. 1993, A&AS, 97, 355

Brigitte, M. & Svoboda, J. 2025, arXiv e-prints, arXiv:2504.10981

Brocksopp, C., Corbel, S., Fender, R. P., et al. 2005, MNRAS, 356, 125

Buisson, D. J. K., Fabian, A. C., Barret, D., et al. 2019, MNRAS, 490, 1350

Burderi, L., Di Salvo, T., Riggio, A., et al. 2010, A&A, 515, A44

Burrows, D. N., Hill, J. E., Nousek, J. A., et al. 2005, Space Sci. Rev., 120, 165

Cangemi, F., Rodriguez, J., Belloni, T., et al. 2023, A&A, 669, A65

Casares, J. & Jonker, P. G. 2014, Space Sci. Rev., 183, 223

Casares, J., Muñoz-Darias, T., Torres, M. A. P., et al. 2022, MNRAS, 516, 2023

Casella, P., Belloni, T., & Stella, L. 2005, ApJ, 629, 403

Casella, P., Maccarone, T. J., O'Brien, K., et al. 2010, MNRAS, 404, L21

Castro Segura, N., Knigge, C., Long, K. S., et al. 2022, Nature, 603, 52

Chadwick, J. 1932, Nature, 129, 312

Chakrabarti, S. & Titarchuk, L. G. 1995, ApJ, 455, 623

Chandrasekhar, S. 1931, ApJ, 74, 81

Chandrasekhar, S. 1960, Radiative Transfer (New York: Dover Publications)

Charles, P. A. & Coe, M. J. 2006, in Compact stellar X-ray sources, ed. W. H. G. Lewin & M. van der Klis, Vol. 39 (Cambridge University Press), 215–265

Chauhan, J., Miller-Jones, J. C. A., Anderson, G. E., et al. 2021, PASA, 38, e045

Chauhan, J., Miller-Jones, J. C. A., Anderson, G. E., et al. 2019, MNRAS, 488, L129

Chen, W.-C. & Podsiadlowski, P. 2019, ApJ Lett., 876, L11

Chen, X. & Wang, W. 2024, arXiv e-prints, arXiv:2402.11293

Chen, X., Wang, W., You, B., et al. 2022, MNRAS, 513, 4875

Churazov, E., Gilfanov, M., & Revnivtsev, M. 2001, MNRAS, 321, 759

Church, M. J. & Bałucińska-Church, M. 2004, MNRAS, 348, 955

Comisso, L. & Sironi, L. 2018, Phys. Rev. Lett., 121, 255101

Contopoulos, J. & Lovelace, R. V. E. 1994, ApJ, 429, 139

Cooper, A. J., Matthews, J. H., Carotenuto, F., et al. 2025, MNRAS, 541, 3518

Coppi, P. S. 1999, in Astronomical Society of the Pacific Conference Series, Vol. 161, High Energy Processes in Accreting Black Holes, ed. J. Poutanen & R. Svensson, 375

Corbel, S., Coriat, M., Brocksopp, C., et al. 2013, MNRAS, 428, 2500

Corbel, S., Fender, R. P., Tzioumis, A. K., et al. 2000, A&A, 359, 251

Corbel, S., Kaaret, P., Jain, R. K., et al. 2001, ApJ, 554, 43

Coriat, M., Corbel, S., Prat, L., et al. 2011, MNRAS, 414, 677

Cúneo, V. A., Muñoz-Darias, T., Sánchez-Sierras, J., et al. 2020, MNRAS, 498, 25

D'Aì, A., di Salvo, T., Ballantyne, D., et al. 2010, A&A, 516, A36

Dauser, T. e. a. 2014, MNRAS, 444, L100–L104

Davis, S. W., Blaes, O. M., Hubeny, I., & Turner, N. J. 2005, ApJ, 621, 372

De Marco, B., Ponti, G., Muñoz-Darias, T., & Nandra, K. 2015, MNRAS, 454, 2360

De Marco, B., Zdziarski, A. A., Ponti, G., et al. 2021, A&A, 654, A14

Del Santo, M., Belloni, T. M., Tomsick, J. A., et al. 2016, MNRAS, 456, 3585

Del Santo, M., Malzac, J., Belmont, R., Bouchet, L., & De Cesare, G. 2013, MNRAS, 430, 209

Del Santo, M., Malzac, J., Jourdain, E., Belloni, T., & Ubertini, P. 2008, MNRAS, 390, 227

della Valle, M., Benetti, S., Cappellaro, E., & Wheeler, C. 1997, A&A, 318, 179

Dhawan, V., Mirabel, I. F., & Rodríguez, L. F. 2000, ApJ, 543, 373

Di Marco, A., La Monaca, F., Poutanen, J., et al. 2023, ApJ Lett., 953, L22

di Salvo, T., Burderi, L., Riggio, A., Papitto, A., & Menna, M. T. 2008, in American Institute of Physics Conference Series, Vol. 1068, A Decade of Accreting MilliSecond X-ray Pulsars, ed. R. Wijnands, D. Altamirano, P. Soleri, N. Degenaar, N. Rea, P. Casella, A. Patruno, & M. Linares, 33–37

Di Salvo, T., D'Aí, A., Iaria, R., et al. 2009, MNRAS, 398, 2022

Di Salvo, T., Goldoni, P., Stella, L., et al. 2006, ApJ Lett., 649, L91

Di Salvo, T., Papitto, A., Marino, A., Iaria, R., & Burderi, L. 2023, arXiv e-prints, arXiv:2311.12516

Di Salvo, T., Robba, N. R., Iaria, R., et al. 2001, ApJ, 554, 49

Di Salvo, T. & Sanna, A. 2022, in Astrophysics and Space Science Library, Vol. 465, Astrophysics and Space Science Library, ed. S. Bhattacharyya, A. Papitto, & D. Bhattacharya, 87–124

Di Salvo, T., Sanna, A., Burderi, L., et al. 2019, MNRAS, 483, 767

Díaz Trigo, M. & Boirin, L. 2016, Astronomische Nachrichten, 337, 368

Díaz Trigo, M., Parmar, A. N., Boirin, L., Méndez, M., & Kaastra, J. S. 2006, A&A, 445, 179

Done, C. & Gierliński, M. 2003, MNRAS, 342, 1041

Done, C., Gierliński, M., & Kubota, A. 2007, A&ARv, 15, 1

Doroshenko, V., Poutanen, J., Tsygankov, S. S., et al. 2022, Nature Astronomy, 6, 1433

Draghis, P. A., Miller, J. M., Costantini, E., et al. 2024, ApJ, 969, 40

Drappeau, S., Malzac, J., Belmont, R., Gandhi, P., & Corbel, S. 2015, MNRAS, 447, 3832

Drappeau, S., Malzac, J., Coriat, M., et al. 2017, MNRAS, 466, 4272

Dubus, G., Hameury, J. M., & Lasota, J. P. 2001, A&A, 373, 251

Duchêne, G. & Kraus, A. 2013, ARA&A, 51, 269

Echiburú-Trujillo, C., Tetarenko, A. J., Haggard, D., et al. 2024, ApJ, 962, 116

Eggleton, P. P. 1983, ApJ, 268, 368

Egron, E., di Salvo, T., Burderi, L., et al. 2011, A&A, 530, A99

Einstein, A. 1916, Annalen der Physik, 354, 769

Esin, A. A., McClintock, J. E., & Narayan, R. 1997, ApJ, 489, 865

Espinasse, M. & Fender, R. 2018, MNRAS, 473, 4122

Event Horizon Telescope Collaboration, Akiyama, K., Alberdi, A., et al. 2022, ApJ Lett., 930, L12

Event Horizon Telescope Collaboration, Akiyama, K., Alberdi, A., et al. 2019, ApJ Lett., 875, L1

Fabian, A. C., Iwasawa, K., Reynolds, C. S., & Young, A. J. 2000, PASP, 112, 1145

Fabian, A. C. e. a. 1989, MNRAS, 238, 729–736

Fabrika, S. 2004, Astrophysics and Space Physics Reviews, 12, 1

Falcke, H., Körding, E., & Markoff, S. 2004, A&A, 414, 895

Fender, R. 2003, Astrophysics and Space Science, 288, 79

Fender, R. & Belloni, T. 2004, ARA&A, 42, 317

Fender, R., Belloni, T., & Gallo, E. 2005, Astrophysics and Space Science, 300, 1

Fender, R. & Muñoz-Darias, T. 2016, in Lecture Notes in Physics, ed. F. Haardt, V. Gorini, U. Moschella, A. Treves, & M. Colpi, Vol. 905 (Springer, Berlin, Heidelberg), 65–100

Fender, R. P. 2001, MNRAS, 322, 31

Fender, R. P., Belloni, T. M., & Gallo, E. 2004, MNRAS, 355, 1105

Fender, R. P., Garrington, S. T., McKay, D. J., et al. 1999, MNRAS, 304, 865

Ferreira, J. 1997, A&A, 319, 340

Ferreira, J., Petrucci, P.-O., Henri, G., Saugé, L., & Pelletier, G. 2006, A&A, 447, 813

Ferrigno, C., Bozzo, E., Del Santo, M., & Capitanio, F. 2012, A&A, 537, L7

Fiocchi, M., Bazzano, A., Ubertini, P., & Jean, P. 2006, ApJ, 651, 416

Fomalont, E. B., Geldzahler, B. J., & Bradshaw, C. F. 2001, ApJ, 558, 283

Frank, J., King, A., & Raine, D. J. 2002, Accretion Power in Astrophysics, 3rd edn. (Cambridge, UK: Cambridge University Press)

Fuchs, Y., Rodriguez, J., Mirabel, I. F., et al. 2003, A&A, 409, L35

Gallo, E., Degenaar, N., & van den Eijnden, J. 2018, MNRAS, 478, L132

Gallo, E., Fender, R. P., & Pooley, G. G. 2003, MNRAS, 344, 60

Gallo, E., Fender, R. P., & Pooley, G. G. 2004, Nuclear Physics B Proceedings Supplements, 132, 363

Gallo, E., Migliari, S., Markoff, S., et al. 2007, ApJ, 670, 600

Gallo, L. C., Miller, J. M., & Costantini, E. 2023, arXiv e-prints, arXiv:2302.10930

Galloway, D. K., Johnston, Z., Goodwin, A., & Heger, A. 2019, in IAU Symposium, Vol. 339, Southern Horizons in Time-Domain Astronomy, ed. R. E. Griffin, 121–126

Gandhi, P., Bachetti, M., Dhillon, V. S., et al. 2017, Nature Astronomy, 1, 859

Gandhi, P., Borowski, E. S., Byrom, J., et al. 2025, MNRAS, 537, 1385

García, J., Dauser, T., Reynolds, C. S., et al. 2013, ApJ, 768, 146

García, J. A., Steiner, J. F., McClintock, J. E., et al. 2015, ApJ, 813, 84

García, J. A., Tomsick, J. A., Sridhar, N., et al. 2019, ApJ, 885, 48

García, J. e. a. 2014, ApJ, 782, 76

Gehrels, N. 2004, in American Institute of Physics Conference Series, Vol. 727, Gamma-Ray Bursts: 30 Years of Discovery, ed. E. Fenimore & M. Galassi, 637–641

Gendreau, K. C., Arzoumanian, Z., Adkins, P. W., et al. 2016, in Society of Photo-Optical Instrumentation Engineers (SPIE) Conference Series, Vol. 9905, Space Telescopes and Instrumentation 2016: Ultraviolet to Gamma Ray, ed. J.-W. A. den Herder, T. Takahashi, & M. Bautz, 99051H

Ghez, A. M., Salim, S., Weinberg, N. N., et al. 2008, ApJ, 689, 1044

Ghisellini, G., Haardt, F., & Svensson, R. 1998, MNRAS, 297, 348

Giacconi, R. 1974, in IAU Symposium, Vol. 64, Gravitational Radiation and Gravitational Collapse, ed. C. Dewitt-Morette, 147

Giacconi, R., Gursky, H., Paolini, F. R., & Rossi, B. B. 1962, Phys. Rev. Lett., 9, 439

Giannios, D. & Metzger, B. D. 2012, in International Journal of Modern Physics Conference Series, Vol. 8, International Journal of Modern Physics Conference Series, 253–258

Gierliński, M., Done, C., & Page, K. 2008, MNRAS, 388, 753

Gierliński, M., Zdziarski, A. A., Poutanen, J., et al. 1999, MNRAS, 309, 496

Gilfanov, M. 2010, in Lecture Notes in Physics, ed. T. Belloni, Vol. 794 (Berlin, Heidelberg: Springer Berlin Heidelberg), 17–51

Gilfanov, M., Churazov, E., & Revnivtsev, M. 1999, A&A, 352, 182

Gillessen, S., Eisenhauer, F., Trippe, S., et al. 2009, ApJ, 692, 1075

GRAVITY Collaboration, Abuter, R., Amorim, A., et al. 2019, A&A, 625, L10

Greene, J. E., Strader, J., & Ho, L. C. 2020, ARA&A, 58, 257

Guo, F., Liu, Y.-H., Daughton, W., & Li, H. 2015, ApJ, 806, 167

Gusinskaia, N. V., Deller, A. T., Hessels, J. W. T., et al. 2017, MNRAS, 470, 1871

Haardt, F., Maraschi, L., & Ghisellini, G. 1994, ApJ Lett., 432, L95

Han, X. & Hjellming, R. M. 1992, ApJ, 400, 304

Harrison, F. A., Craig, W. W., Christensen, F. E., et al. 2013, ApJ, 770, 103

Hasinger, G. & van der Klis, M. 1989, A&A, 225, 79

Hawking, S. W. 1975, Communications in Mathematical Physics, 43, 199

Hawley, J. F. & Krolik, J. H. 2006, ApJ, 641, 103

Heger, A., Fryer, C. L., Woosley, S. E., Langer, N., & Hartmann, D. H. 2003, ApJ, 591, 288

Heinz, S. & Merloni, A. 2004, MNRAS, 355, L1

Hewish, A., Bell, S. J., Pilkington, J. D. H., Scott, P. F., & Collins, R. A. 1968, Nature, 217, 709

Heyvaerts, J. & Norman, C. 1989, ApJ, 347, 1055

Hjellming, R. M. & Johnston, K. J. 1988, ApJ, 328, 600

Holt, S. S., Boldt, E. A., Kaluzienski, L. J., & Serlemitsos, P. J. 1975, Nature, 256, 108

Homan, J. & Belloni, T. 2005, Astrophysics and Space Science, 300, 107

Homan, J., Wijnands, R., van der Klis, M., et al. 2001, ApJS, 132, 377

Horne, K. & Marsh, T. R. 1986, MNRAS, 218, 761

Ingram, A., van der Klis, M., Middleton, M., et al. 2016, MNRAS, 461, 1967

Ingram, A. R. & Motta, S. E. 2019, New Astron. Rev., 85, 101524

Jacquemin-Ide, J., Ferreira, J., & Lesur, G. 2019, MNRAS, 490, 3112

Jain, C., Dutta, A., & Paul, B. 2007, Journal of Astrophysics and Astronomy, 28, 197

Jayasinghe, T., Stanek, K. Z., Kochanek, C. S., et al. 2020, Monthly Notices of the Royal Astronomical Society, 493, 4045

Jerkstrand, A. 2017, in Handbook of Supernovae, ed. A. W. Alsabti & P. Murdin (Cham, Switzerland: Springer International Publishing), 795–842

Jiménez-Ibarra, F., Muñoz-Darias, T., Armas Padilla, M., et al. 2019, MNRAS, 484, 2078

Kaaret, P., Feng, H., & Roberts, T. P. 2017, ARA&A, 55, 303

Kaastra, J. 1999, Iron Line Spectroscopy of Clusters of Galaxies, Chandra Proposal ID 01800303

Kaiser, C. R. 2006, MNRAS, 367, 1083

Kalemci, E., Tomsick, J. A., Rothschild, R. E., et al. 2006, ApJ, 639, 340

Kallman, T. & Bautista, M. 2001, ApJS, 133, 221

Kara, E., Steiner, J. F., Fabian, A. C., et al. 2019, Nature, 565, 198

Kaur, R., Kaper, L., Ellerbroek, L. E., et al. 2012, ApJ Lett., 746, L23

Kennea, J., Miller, J. M., Beardmore, A., Degenaar, N., & Reynolds, M. T. 2012, The Astronomer's Telegram, 4071, 1

Kerr, R. P. 1963, Phys. Rev. Lett., 11, 237

Khargharia, J., Froning, C. S., Robinson, E. L., & Gelino, D. M. 2013, AJ, 145, 21

Kippenhahn, R. & Weigert, A. 1990, Stellar Structure and Evolution, Astronomy and Astrophysics Library (Berlin, Heidelberg: Springer-Verlag)

Kippenhahn, R., Weigert, A., & Weiss, A. 2013, Stellar Structure and Evolution, Astronomy and Astrophysics Library (Springer)

Koljonen, K. I. I., Russell, D. M., Fernández-Ontiveros, J. A., et al. 2015, ApJ, 814, 139

Komissarov, S. S. 2001, MNRAS, 326, L41

Kong, L.-D., Ji, L., Santangelo, A., et al. 2024, A&A, 686, A211

Körding, E. G., Jester, S., & Fender, R. 2006, MNRAS, 372, 1366

Kraft, R. P., Mathews, J., & Greenstein, J. L. 1962, ApJ, 136, 312

Krawczynski, H., Muleri, F., Dovčiak, M., et al. 2022, Science, 378, 650

Krolik, J. H., McKee, C. F., & Tarter, C. B. 1981, ApJ, 249, 422

Krymskii, G. F. & Transkii, I. A. 1977, in International Cosmic Ray Conference, Vol. 3, International Cosmic Ray Conference, 300

Kubota, A. & Done, C. 2004, MNRAS, 353, 980

Kubota, A., Makishima, K., & Ebisawa, K. 2001, ApJ Lett., 560, L147

Kubota, A., Tanaka, Y., Makishima, K., et al. 1998, PASJ, 50, 667

Lasota, J.-P. 2001, New Astron. Rev., 45, 449

Lattimer, J. M. & Prakash, M. 2004, Science, 304, 536

Leahy, D. A., Elsner, R. F., & Weisskopf, M. C. 1983, ApJ, 272, 256

Lee, J. C., Reynolds, C. S., Remillard, R., et al. 2002, ApJ, 567, 1102

Lewin, W. H. G., van Paradijs, J., & van den Heuvel, E. P. J. 1996, Space Sci. Rev., 77, 375

Lin, D., Remillard, R. A., & Homan, J. 2007, ApJ, 667, 1073

Liska, M., Tchekhovskoy, A., Ingram, A., & van der Klis, M. 2019, MNRAS, 487, 550

Longair, M. S. 2011, High Energy Astrophysics, 3rd edn. (Cambridge, UK: Cambridge University Press)

Loureiro, N. F., Schekochihin, A. A., & Cowley, S. C. 2007, Physics of Plasmas, 14, 100703

Luketic, S., Proga, D., Kallman, T. R., Raymond, J. C., & Miller, J. M. 2010, ApJ, 719, 515

Lyubarsky, Y. & Liverts, M. 2008, ApJ, 682, 1436

Lyubarsky, Y. E. 2005, MNRAS, 358, 113

Maitra, D., Markoff, S., Brocksopp, C., et al. 2009, MNRAS, 398, 1638

Maloney, P. R., Begelman, M. C., & Pringle, J. E. 1996, ApJ, 472, 582

Malzac, J. 2013, MNRAS, 429, L20

Malzac, J. 2014, MNRAS, 443, 299

Malzac, J. 2018, arXiv e-prints, arXiv:1804.03451

Malzac, J., Petrucci, P. O., Jourdain, E., et al. 2006, A&A, 448, 1125

Marcel, G., Ferreira, J., Clavel, M., et al. 2019, A&A, 626, A115

Marcel, G., Ferreira, J., Petrucci, P.-O., et al. 2022, A&A, 659, A194

Marcel, G., Ferreira, J., Petrucci, P.-O., et al. 2018a, A&A, 617, A46

Marcel, G., Ferreira, J., Petrucci, P.-O., et al. 2018b, A&A, 615, A57

Marcowith, A., Bret, A., Bykov, A., et al. 2016, Reports on Progress in Physics, 79, 046901

Marino, A., Del Santo, M., Cocchi, M., et al. 2019, MNRAS, 490, 2300

Marino, A., Malzac, J., Del Santo, M., et al. 2020, MNRAS, 498, 3351

Markoff, S., Falcke, H., & Fender, R. 2000, in American Astronomical Society Meeting Abstracts, Vol. 197, American Astronomical Society Meeting Abstracts, 84.01

Markoff, S., Nowak, M., Corbel, S., Fender, R., & Falcke, H. 2003, New Astron. Rev., 47, 491

Markoff, S., Nowak, M. A., & Wilms, J. 2005, ApJ, 635, 1203

Martin, R. G., Nixon, C. J., Pringle, J. E., & Livio, M. 2019, NewA, 70, 7

Mastroserio, G., De Marco, B., Baglio, M. C., et al. 2025, ApJ Lett., 978, L19

Mata Sánchez, D., Muñoz-Darias, T., Casares, J., et al. 2018, MNRAS, 481, 2646

Mata Sánchez, D., Muñoz-Darias, T., Casares, J., Huertas-Company, M., & Panizo-Espinar, G. 2023, MNRAS, 524, 338

Mata Sánchez, D., Muñoz-Darias, T., Cúneo, V. A., et al. 2022, ApJ Lett., 926, L10

Mata Sánchez, D., Rau, A., Álvarez Hernández, A., et al. 2021, MNRAS, 506, 581

Matsuoka, M., Kawasaki, K., Ueno, S., et al. 2009, PASJ, 61, 999

Matt, G., Perola, G. C., & Piro, L. 1991, A&A, 247, 25

Matthews, J. H., Bell, A. R., & Blundell, K. M. 2020, New Astron. Rev., 89, 101543

McClintock, J. E., Shafee, R., Narayan, R., et al. 2006, ApJ, 652, 518

McKee, C. F. & Ostriker, J. P. 1977, ApJ, 218, 148

McKinney, J. C. 2006a, MNRAS, 367, 1797

McKinney, J. C. 2006b, MNRAS, 368, 1561

McKinney, J. C., Tchekhovskoy, A., & Blandford, R. D. 2012, MNRAS, 423, 3083

Meier, D. L. 2005, Astrophysics and Space Science, 300, 55

Méndez, M. & van der Klis, M. 1997, ApJ, 479, 926

Mészáros, P. & Rees, M. J. 1997, ApJ Lett., 482, L29

Mezcua, M. 2017, International Journal of Modern Physics D, 26, 1730021

Miceli, C., Mata Sánchez, D., Anitra, A., et al. 2024, A&A, 684, A67

Middleton, M., Done, C., Gierliński, M., & Davis, S. W. 2006, MNRAS, 373, 1004

Migliari, S., Fender, R. P., Rupen, M., et al. 2004, MNRAS, 351, 186

Migliari, S., Miller-Jones, J. C. A., & Russell, D. M. 2011, MNRAS, 415, 2407

Migliari, S., Tomsick, J. A., Markoff, S., et al. 2007, ApJ, 670, 610

Mihara, T., Nakajima, M., Sugizaki, M., et al. 2011, PASJ, 63, S623

Miller, J. M. 2007, ARA&A, 45, 441

Miller, J. M., Balakrishnan, M., Reynolds, M., et al. 2019a, The Astronomer's Telegram, 12771, 1

Miller, J. M., Balakrishnan, M., & Reynolds, M. T. e. a. 2020, ApJ, 904, 30

Miller, J. M., Gendreau, K., Ludlam, R. M., et al. 2018, ApJ Lett., 860, L28

Miller, J. M., Gu, L., Raymond, J., et al. 2025, ApJ Lett., 995, L14

Miller, J. M., Parker, M. L., & Fuerst, F. e. a. 2013, ApJ, 775, L45

Miller, J. M., Raymond, J., Fabian, A., et al. 2006, Nature, 441, 953

Miller, J. M., Raymond, J., Fabian, A. C., et al. 2016, ApJ Lett., 821, L9

Miller, J. M., Raymond, J., Kallman, T. R., et al. 2014, ApJ, 788, 53

Miller, M. C., Lamb, F. K., Dittmann, A. J., et al. 2019b, ApJ Lett., 887, L24

Miller, M. C., Lamb, F. K., Dittmann, A. J., et al. 2021, ApJ Lett., 918, L28

Miller-Jones, J. C. A., Fender, R. P., & Nakar, E. 2006, MNRAS, 367, 1432

Miller-Jones, J. C. A., Moin, A., Tingay, S. J., et al. 2012, MNRAS, 419, L49

Miller-Jones, J. C. A., Tetarenko, A. J., Sivakoff, G. R., et al. 2019, Nature, 569, 374

Mirabel, I. F. & Rodríguez, L. F. 1994, Nature, 371, 46

Mitsuda, K., Inoue, H., Koyama, K., et al. 1984, PASJ, 36, 741

Mitsuda, K., Inoue, H., Nakamura, N., & Tanaka, Y. 1989, PASJ, 41, 97

Morihana, K., Sugizaki, M., Nakahira, S., et al. 2013, PASJ, 65, L10

Motta, S., Williams, D., Fender, R., et al. 2019, The Astronomer's Telegram, 12773, 1

Motta, S. E. & Belloni, T. M. 2024, A&A, 684, A209

Motta, S. E., Casella, P., Henze, M., et al. 2015, MNRAS, 447, 2059

Motta, S. E., Kajava, J. J. E., Giustini, M., Williams, D. R. A., & Del Santo, M. 2021, MNRAS, 503, 152

Motta, S. E., Rouco Escorial, A., & Kuulkers, E. e. a. 2017, MNRAS, 471, 1797

Muñoz-Darias, T., Casares, J., Mata Sánchez, D., et al. 2016, Nature, 534, 75

Muñoz-Darias, T., Fender, R. P., Motta, S. E., & Belloni, T. M. 2014, MNRAS, 443, 3270

Muñoz-Darias, T., Jiménez-Ibarra, F., Panizo-Espinar, G., et al. 2019, ApJ Lett., 879, L4

Muñoz-Darias, T., Motta, S., & Belloni, T. M. 2011, MNRAS, 410, 679

Muñoz-Darias, T. & Ponti, G. 2022, A&A, 664, A104

Nakahira, S., Shidatsu, M., Makishima, K., et al. 2018, PASJ, 70, 95

Narayan, R., Kato, S., & Honma, F. 1997, ApJ, 476, 49

Narayan, R. & McClintock, J. E. 2012, MNRAS, 419, L69

Narayan, R. & Yi, I. 1995, ApJ, 444, 231

Nayakshin, S. 2000, ApJ, 534, 718

Naylor, T. 1998, MNRAS, 296, 339

Negoro, H., Ishikawa, M., Ueno, S., et al. 2017, The Astronomer's Telegram, 10699, 1

Negoro, H., Tachibana, Y., Kawai, N., et al. 2018, The Astronomer's Telegram, 11828, 1

Neilsen, J., Altamirano, D., Homan, J., et al. 2021, The Astronomer's Telegram, 14792, 1

Neilsen, J., Cackett, E., Remillard, R. A., et al. 2018, ApJ Lett., 860, L19

Neilsen, J., Lee, J. C., & Remillard, R. 2009, in Chandra's First Decade of Discovery, ed. S. Wolk, A. Fruscione, & D. Swartz, 49

Neilsen, J., Petschek, A. J., & Lee, J. C. 2012, MNRAS, 421, 502

Neilsen, J., Remillard, R. A., & Lee, J. C. 2011, ApJ, 737, 69

Nelemans, G. & Jonker, P. G. 2010, New Astron. Rev., 54, 87

Nelson, L. A. & Rappaport, S. 2003, ApJ, 598, 431

Newman, E. T., Couch, E., Chinnapared, K., et al. 1965, Journal of Mathematical Physics, 6, 918

Ni, L., Kliem, B., Lin, J., & Wu, N. 2015, ApJ, 799, 79

Nowak, M. A. 1995, PASP, 107, 1207

Nyquist, H. 1928, Transactions of the American Institute of Electrical Engineers, 47, 617

Oppenheimer, J. R. & Snyder, H. 1939, Physical Review, 56, 455

Oppenheimer, J. R. & Volkoff, G. M. 1939, Physical Review, 55, 374

Özel, F. & Freire, P. 2016, ARA&A, 54, 401

Pacholczyk, A. G. & Swihart, T. L. 1967, ApJ, 150, 647

Pacini, F. 1967, Nature, 216, 567

Paczyński, B. 1971, ARA&A, 9, 183

Paizis, A., Farinelli, R., Titarchuk, L., et al. 2006, A&A, 459, 187

Panizo-Espinar, G., Armas Padilla, M., Muñoz-Darias, T., et al. 2022, A&A, 664, A100

Panizo-Espinar, G., Armas Padilla, M., Muñoz-Darias, T., et al. 2022, Astronomy & Astrophysics, 664, A100

Parker, E. N. 1957, J. Geophys. Res., 62, 509

Parra, M., Petrucci, P. O., Bianchi, S., et al. 2024, A&A, 681, A49

Péault, M., Malzac, J., Coriat, M., et al. 2019, MNRAS, 482, 2447

Pe'er, A. 2014, Space Sci. Rev., 183, 371

Petschek, H. E. 1964, in NASA Special Publication, Vol. 50, The Physics of Solar Flares, ed. W. N. Hess (Washington, D.C.: NASA), 425–439

Pinto, C., Mehdipour, M., Walton, D. J., et al. 2020, MNRAS, 491, 5702

Ponti, G., Bianchi, S., De Marco, B., et al. 2019, Monthly Notices of the Royal Astronomical Society

Ponti, G., Bianchi, S., Muñoz-Darias, T., et al. 2015, MNRAS, 446, 1536

Ponti, G., Fender, R. P., Begelman, M. C., et al. 2012, MNRAS, 422, L11

Ponti, G., Muñoz-Darias, T., & Fender, R. P. 2014, MNRAS, 444, 1829

Pottschmidt, K., Wilms, J., Nowak, M. A., et al. 2003, A&A, 407, 1039

Poutanen, J. & Coppi, P. S. 1998, Physica Scripta Volume T, 77, 57

Poutanen, J. & Svensson, R. 1996, ApJ, 470, 249

Pringle, J. E. 1981, ARA&A, 19, 137

Pringle, J. E. 1996, MNRAS, 281, 357

Proga, D. 2002, in Astronomical Society of the Pacific Conference Series, Vol. 255, Mass Outflow in Active Galactic Nuclei: New Perspectives, ed. D. M. Crenshaw, S. B. Kraemer, & I. M. George, 309

Proga, D. 2003, ApJ, 585, 406

Proga, D., Stone, J. M., & Kallman, T. R. 2000, ApJ, 543, 686

Psaltis, D., Belloni, T., & van der Klis, M. 1999, ApJ, 520, 262

Psaradaki, I., Costantini, E., Mehdipour, M., & Díaz Trigo, M. 2018, A&A, 620, A129

Pudritz, R. E., Rogers, C. S., & Ouyed, R. 2006, MNRAS, 365, 1131

Rappaport, S., Verbunt, F., & Joss, P. C. 1983, ApJ, 275, 713

Ravishankar, B. T., Tilak, K., Athulya, M. P., et al. 2021, The Astronomer's Telegram, 14811, 1

Reid, M. J. & Miller-Jones, J. C. A. 2023, ApJ, 959, 85

Remillard, R. A. & McClintock, J. E. 2006, ARA&A, 44, 49

Reynolds, C. S. 2014, Space Sci. Rev., 183, 277

Reynolds, C. S. & Nowak, M. A. 2003, Phys. Rep., 377, 389

Rhoades, C. E. & Ruffini, R. 1974, Phys. Rev. Lett., 32, 324

Rodi, J., Jourdain, E., & Roques, J. P. 2022, ApJ, 935, 25

Rodríguez, L. F. & Mirabel, I. F. 2025, ApJ, 986, 108

Rogantini, D., Homan, J., Plotkin, R. M., et al. 2025, A persistent disk wind and variable jet outflow in the neutron-star low-mass X-ray binary GX 13+1

Romanova, M. M. & Lovelace, R. V. E. 1992, A&A, 262, 26

Roming, P. W. A., Kennedy, T. E., Mason, K. O., et al. 2005, Space Sci. Rev., 120, 95

Roques, J. P., Schanne, S., von Kienlin, A., et al. 2003, A&A, 411, L91

Russell, D. M. & Fender, R. P. 2010, arXiv e-prints, arXiv:1001.1244

Russell, D. M., Markoff, S., Casella, P., et al. 2013, MNRAS, 429, 815

Russell, T. D., Lucchini, M., Tetarenko, A. J., et al. 2020, MNRAS, 498, 5772

Russell, T. D., Soria, R., Miller-Jones, J. C. A., et al. 2014, MNRAS, 439, 1390

Russell, T. D., Tetarenko, A. J., Miller-Jones, J. C. A., et al. 2019, ApJ, 883, 198

Rybicki, G. B. & Lightman, A. P. 1979, Radiative Processes in Astrophysics (New York, NY: John Wiley & Sons)

Saikia, P., Russell, D. M., Bramich, D. M., et al. 2019, ApJ, 887, 21

Sánchez-Sierras, J. & Muñoz-Darias, T. 2020, A&A, 640, L3

Sanna, A., Méndez, M., Altamirano, D., et al. 2014, MNRAS, 440, 3275

Sari, R., Piran, T., & Narayan, R. 1998, ApJ Lett., 497, L17

Scheuer, P. A. G. & Williams, P. J. S. 1968, ARA&A, 6, 321

Segreto, A., Cusumano, G., Ferrigno, C., et al. 2010, A&A, 510, A47

Shakura, N. I. & Sunyaev, R. A. 1973, A&A, 24, 337

Shapiro, S. L., Lightman, A. P., & Eardley, D. M. 1976, ApJ, 204, 187

Shapiro, S. L. & Teukolsky, S. A. 1983, Black Holes, White Dwarfs, and Neutron Stars: The Physics of Compact Objects (New York, NY: John Wiley & Sons)

Shaw, A. W., Charles, P. A., Casares, J., & Steeghs, D. 2017, in 7 years of MAXI: monitoring X-ray Transients, ed. M. Serino, M. Shidatsu, W. Iwakiri, & T. Mihara, 45

Shidatsu, M., Ueda, Y., Nakahira, S., et al. 2013, ApJ, 779, 26

Sibgatullin, N. R. & Sunyaev, R. A. 2000, Astronomy Letters, 26, 699

Sincell, M. W. & Krolik, J. H. 1998, Advances in Space Research, 21, 113

Sironi, L. & Spitkovsky, A. 2014, ApJ Lett., 783, L21

Sironi, L., Spitkovsky, A., & Arons, J. 2013, ApJ, 771, 54

Sleator, C. C., Zoglauer, A., Lowell, A. W., et al. 2019, Nuclear Instruments and Methods in Physics Research A, 946, 162643

Smak, J. 1981, Acta Astronomica, 31, 395

Soria, R., Wu, K., & Hunstead, R. W. 2000, ApJ, 539, 445

Spencer, R. E. 1979, Nature, 282, 483

Spruit, H. C. 2010, in Lecture Notes in Physics, Vol. 794: The Jet Paradigm, ed. T. Belloni (Berlin Heidelberg: Springer-Verlag), 233–263

Spruit, H. C., Foglizzo, T., & Stehle, R. 1997, MNRAS, 288, 333

Sreehari, H., Ravishankar, B. T., Iyer, N., et al. 2019, MNRAS, 487, 928

Sridhar, N., Bhattacharyya, S., Chandra, S., & Antia, H. M. 2019, MNRAS, 487, 4221

Steeghs, D. & Casares, J. 2002, ApJ, 568, 273

Steeghs, D., McClintock, J. E., Parsons, S. G., et al. 2013, ApJ, 768, 185

Stella, L. & Angelini, L. 1992, in Data Analysis in Astronomy, ed. V. di Gesu, L. Scarsi, R. Buccheri, & P. Crane, 59–64

Stirling, A. M., Spencer, R. E., de la Force, C. J., et al. 2001, MNRAS, 327, 1273

Strüder, L., Briel, U., Dennerl, K., et al. 2001, A&A, 365, L18

Sundqvist, J. O. & Owocki, S. P. 2013, MNRAS, 428, 1837

Suwa, F., Negoro, H., Nakahira, S., et al. 2012, The Astronomer's Telegram, 4035, 1

Sweet, P. A. 1958, in IAU Symposium, Vol. 6, Electromagnetic Phenomena in Cosmical Physics, ed. B. Lehnert, 123

Tananbaum, H., Gursky, H., Kellogg, E., Giacconi, R., & Jones, C. 1972, ApJ Lett., 177, L5

Tao, L., Chen, Y., Güngör, C., et al. 2018, MNRAS, 480, 4443

Tarter, C. B., Tucker, W. H., & Salpeter, E. E. 1969, ApJ, 156, 943

Tauris, T. M. & van den Heuvel, E. P. J. 2006, in Compact Stellar X-ray Sources, ed. W. H. G. Lewin & M. van der Klis, Vol. 39 (Cambridge, UK: Cambridge University Press), 623–665

Tchekhovskoy, A., McKinney, J. C., & Narayan, R. 2012, in Journal of Physics Conference Series, Vol. 372, Journal of Physics Conference Series (IOP), 012040

Tchekhovskoy, A., Narayan, R., & McKinney, J. C. 2011, MNRAS, 418, L79

Tetarenko, A. J., Casella, P., Miller-Jones, J. C. A., et al. 2019, MNRAS, 484, 2987

Tetarenko, B. E., Dubus, G., Lasota, J. P., Heinke, C. O., & Sivakoff, G. R. 2018, MNRAS, 480, 2

Titarchuk, L., Soffitta, P., Seifina, E., et al. 2025, A&A, 704, A87

Tohline, J. E. 2002, ARA&A, 40, 349

Tomaru, R., Done, C., & Mao, J. 2023, MNRAS, 518, 1789

Tombesi, F., Cappi, M., Reeves, J. N., et al. 2010, A&A, 521, A57

Tomsick, J. A., Kalemci, E., Kaaret, P., et al. 2008, ApJ, 680, 593

Tomsick, J. A., Sleator, C. C., Zoglauer, A., & et al. 2023, Astroparticle Physics [arXiv: 2308.12362]

Torres, M. A. P., Callanan, P. J., Garcia, M. R., et al. 2002, ApJ, 569, 423

Torres, M. A. P., Jonker, P. G., Casares, J., Miller-Jones, J. C. A., & Steeghs, D. 2021, MNRAS, 501, 2174

Ueda, Y., Inoue, H., Tanaka, Y., et al. 1998, ApJ, 492, 782

van der Klis, M. 1989, ARA&A, 27, 517

van der Klis, M. 2004, arXiv e-prints, astro

van der Klis, M. 2006, Advances in Space Research, 38, 2675

van Dokkum, P. G., Bloom, J., & Tewes, M. 2012, L.A.Cosmic: Laplacian Cosmic Ray Identification, Astrophysics Source Code Library, record ascl:1207.005

van Straaten, S., van der Klis, M., & Méndez, M. 2003, ApJ, 596, 1155

Veledina, A., Muleri, F., Dovčiak, M., et al. 2023, ApJ Lett., 958, L16

Verbunt, F. & Zwaan, C. 1981, A&A, 100, L7

Verner, D. A., Ferland, G. J., Korista, K. T., & Yakovlev, D. G. 1996, ApJ, 465, 487

Vink, J. S., Higgins, E. R., Sander, A. A. C., & Sabhahit, G. N. 2021, MNRAS, 504, 146

Virtanen, P., Gommers, R., Burovski, E., et al. 2020, scipy/scipy: SciPy 1.5.3, Zenodo

Wang, J., Mastroserio, G., Kara, E., et al. 2021, ApJ Lett., 910, L3

Wang, Z., Archibald, A. M., Thorstensen, J. R., et al. 2009, ApJ, 703, 2017

Weisskopf, M. 2022, in AAS/High Energy Astrophysics Division, Vol. 19, AAS/High Energy Astrophysics Division, 301.01

White, N. E. & Holt, S. S. 1982, ApJ, 257, 318

White, N. E., Stella, L., & Parmar, A. N. 1988, ApJ, 324, 363

Wijers, R. A. M. J., Rees, M. J., & Meszaros, P. 1997, MNRAS, 288, L51

Wijnands, R. 2001, Advances in Space Research, 28, 469

Wilkins, D. R. & Fabian, A. C. 2012, MNRAS, 424, 1284

Wilms, J., Allen, A., & McCray, R. 2000, ApJ, 542, 914

You, B. 2024, in Proceedings of the 45th COSPAR Scientific Assembly, Vol. 45, 1537

Yuan, F. 2001, MNRAS, 324, 119

Yuan, F. & Narayan, R. 2014, ARA&A, 52, 529

Zamaninasab, M., Clausen-Brown, E., Savolainen, T., & Tchekhovskoy, A. 2014, Nature, 510, 126

Zdziarski, A. A. & De Marco, B. 2020, ApJ Lett., 896, L36

Zdziarski, A. A., Gierliński, M., Mikołajewska, J., et al. 2004, MNRAS, 351, 791

Zdziarski, A. A., Paul, D., Osborne, R., & Rao, A. R. 2016, MNRAS, 463, 1153

Zdziarski, A. A., Pjanka, P., Sikora, M., & Stawarz, Ł. 2014, MNRAS, 442, 3243

Zdziarski, A. A., Poutanen, J., Paciesas, W. S., & Wen, L. 2002, ApJ, 578, 357

Zhang, S. N., Cui, W., & Chen, W. 1997, ApJ Lett., 482, L155

Zhang, W., Jahoda, K., Swank, J. H., Morgan, E. H., & Giles, A. B. 1995, ApJ, 449, 930

Zhang, X., Yu, W., Carotenuto, F., et al. 2025, arXiv e-prints, arXiv:2504.11945

Życki, P. T., Done, C., & Smith, D. A. 1999, MNRAS, 309, 561